

University of Nottingham
UK | CHINA | MALAYSIA

Department of Mechanical, Materials and Manufacturing Engineering

Faculty of Engineering

NUMERICAL SIMULATIONS TO ASSESS THE PERFORMANCE OF SCOOP BASED LUBRICATION DEVICES FOR USE IN AERO-ENGINES

ARUN PRABHAKAR, BEng (Hons)

Thesis submitted to the University of Nottingham

for the degree of Doctor of Philosophy

September 2018

Abstract

In civil aircraft aero engine bearing chambers it is sometimes difficult to feed oil to bearings using the traditional under-race or targeted jet approaches. In such situations one proposed solution is that of a scoop delivery system. Published experimental investigations into scoop performance show that scoop collection efficiency (the percentage of oil delivered by the scoop system to its destination compared to that supplied by the feed jet) is a function of many operational and geometric parameters. However even with high speed imaging it is impossible to experimentally determine in detail the factors that most contribute to reduction in capture efficiency and it is here particularly that a Computational Fluid Dynamics (CFD) investigation has value.

In the work of this thesis CFD investigations using ANSYS FLUENT are used to investigate the performance of scoop based lubrication devices. The computational domain, a 2D slice through the chosen scoop system, is discretized utilizing ANSYS Meshing. The Volume of fluid (VOF) model is used to model the multiphase flow of oil and air in the system and the RNG k-ε turbulence model is employed to account for the effects of turbulence. Comparison of numerical results with experimental results indicate good agreement. Results achieved from analytical modelling also support the results obtained from CFD and experiments. The effect of vortex shedding from the tip of scoops and different scoop geometries on the capture efficiency have also been investigated. A computationally efficient model for assessing the performance of scoops has been developed in this PhD.

List of Publications

Published

1. Arun Prabhakar, Yousif Abdalla Abakr and Kathy Simmons, 2018. **Numerical Investigations to Assess the Impact of Shaft Speed on the Performance of Scoop Devices** In: ASME Turbo Expo 2018: Turbomachinery Technical Conference and Exposition. **(GT2018-76177)**
2. Arun Prabhakar, Yousif Abdalla Abakr and Kathy Simmons, 2017. **Effect of Vortex Shedding on the Performance of Scoop Based Lubrication Devices** In: ASME Turbo Expo 2017: Turbomachinery Technical Conference and Exposition.**(GT2017-63444)**
3. Paloma Paleo Cageo, Kathy Simmons, Arun Prabhakar and Budi Chandra, 2017, **Assessment of the oil scoop capture efficiency in high speed rotors** Journal of Engineering for Gas Turbines and Power. **(doi:10.1115/1.4040812)**

Writing in Progress

4. Arun Prabhakar, Yousif, Abdalla Abakr and Kathy Simmons, 201x, **Effect of geometry and operating conditions on scoop capture efficiency**- intended to be submitted to ASME Journal of Turbomachinery

Acknowledgements

I acknowledge the support from God till date and for making this PhD a possibility.



I am very grateful to the Faculty of Engineering at the University of Nottingham Malaysia Campus for awarding me the Dean's Excellence PhD Scholarship which fully funded my tuition fees and maintenance expenses without which I would have not been able to pursue my PhD.

I would like to express my deep gratitude to Professor Yousif Abdalla Abakar and Dr. Kathy Simmons who have provided endless support and motivation throughout the whole duration of my PhD. I have learned considerable amount of valuable things from them even outside academics. Professor Yousif had been a mentor since my undergraduate days and has never failed to keep motivating me during the most stressful times and has been one of the reasons for me to pursue a PhD. Dr. Kathy's role as a mentor commenced since the start of my PhD. During the first year of my PhD she had given me the opportunity to visit the UK campus and observe the experiments associated with my project. This opportunity enhanced my research experience and elevated my understanding of the project significantly. Towards the latter part of my PhD, both my supervisors supported me considerably towards acquiring the rare opportunity of undertaking a post-doctoral fellowship with the University of Nottingham.

The PhD was carried under the Gas Turbines Transmissions Research Centre (G2TRC) at the University of Nottingham. I sincerely thank the support from G2TRC. I wish to acknowledge the help provided by Dr. Budi Chandra and Dr. Paloma Paleo Cageao for sharing their experimental results which was essential to validate my numerical results. Assistance provided by Mr. Bob Stables and Dr. Graham Johnson in giving expertise advice on the technical and experimental aspects of the project is greatly appreciated.

I would like to thank my post-doctoral supervisor, Professor Hervé Morvan who has been a great source of inspiration and support, especially for giving me the opportunity to carry out post-doctoral research under him. My sincere gratitude goes to Dr. Stephen Ambrose who is the Computational Fluid Dynamics (CFD) team lead in the G2TRC. I received lot of guidance and advice in the writing of my thesis from him. Furthermore I have learned numerous amount of new CFD techniques from him and my skills were strengthened considerably over a short time period while working with him.

I would like to thank my examiners Professor Steve Pickering and Dr. Henk Versteeg for examining my thesis and giving valuable feedback to improvise the thesis.

My dearest friends Sanmouga, Sean, Denesh, Senthil, Vishnu, Kanesan , Shivaharan, Rajeevnath, Gaurav, Soudamini, Tshaiya, Indusha, Thibbadarshini, Thavamalar, Rajmeela, Sakthi, Chakaravarthi, Roshini, Malaka, Aaniya, Rohit, Remon, Aruthiran, Dilukshan, Lakshan, Reminton, Hamad, Silmy, Zuhair, Sam Anna, Rumesh, Siva, Mathulah, Nikesh, Poongothai, Manivannan, Srikanth, Abarajithan, Hari and Skanda Nathan have played a very important part in providing me motivational and emotional support during the times I really needed it. I also would like to specially thank the families of Sean, Thibbadarshini, Skanda Nathan and Rajeevnath who have accommodated me on numerous occasions and given me the feeling of being in a “Home away from Home” during my PhD days.

I am very thankful to Dr. Tissa, Dr. Jiin and the Graduate school for investing lot of time in training me during the course of the PhD. They have shared their valuable knowledge and experiences. I am also grateful for the administrative support from Ms. Yogeswary, Ms. Shikin and Mrs. Muna from the Faculty of Engineering at University of Nottingham Malaysia Campus.

Finally yet most importantly, I dedicate this PhD to my parents, Prabhakar and Sathiyavani. More than the fact of Dad being a Naval Engineer himself, it was rather his innovative and captivating ways of handling problems that inspired me to follow his footsteps. I still remember the good old days as a kid when I was fond of breaking open and examining toys (which slowly progressed to household appliances). Dad had always considered this as part of my learning curve and never discouraged this despite his strict disciplinary rules at home. After realizing my interests, he had started to enlighten me with various science kits starting from the age of

nine. When I was a bit older, he introduced me to his engineering tools and taught me several mechanical processes (drilling, assembling and painting). By the time I graduated from high school, I was acquainted with many tools and had a head-on lead when I commenced my degree in Mechanical Engineering. Mom had a special role in providing me continuous mental strength and the extra pampering I needed till date especially during childhood days when I was a below average student in academics. Both my parents have helped me develop an attitude towards accepting failures as positive elements of life and have always instigated me to not give up on ambitions and interests. Teachings and moral values that I inherited from them have driven me up to this level today. Sincere thanks “Appa and Amma”! I would like to thank my sister Archana for standing by and encouraging me throughout.

Contents

Nomenclature ..... **xix**

Glossary ..... **xxi**

1 Introduction **1**

1.1 Overview 1

1.2 Background 1

1.3 Limitations and gaps in existing work on scoops 5

1.4 Aims and Objectives 6

1.5 Thesis Structure 6

2 Literature Review **8**

2.1 Introduction 8

2.2 CFD modelling of jets 9

2.3 Turbulence modelling involving complex geometries in rotating flows. 20

2.4 Multiphase flow modelling of rotating flows 22

2.5 Vortex Shedding 25

2.6 Numerical and experimental work on scoops 30

2.6.1 Numerical modelling of scoops. 30

2.6.2 Experimental investigation of scoop devices 35

2.7 CFD modelling strategy recommendations based on literature review 36

2.8 Summary of literature review 40

3 CFD Methodology 41

3.1 Introduction 41

3.2 Geometry development 42

3.3 Numerical Grid 44

3.4 Numerical Modelling 45

3.4.1 Governing Equations 45

3.4.2 Multiphase Modelling 46

3.4.3 Discretization 48

3.4.4 Pressure-Velocity Coupling 51

3.4.5 Turbulence 53

3.4.6 Sliding Mesh 59

3.4.7 Boundary, Initial Conditions and reference values 59

3.4.8 Convergence 61

3.4.9 Material Properties 62

3.5 Data Analysis and Post Processing 63

3.5.1 Numerical Data 63

3.5.2 Post Processing 63

3.6 Computational Resources 63

3.7 Chapter summary 63

4 Analytical and numerical investigations to assess effect of shaft speed on capture efficiency 65

4.1 Overview 65

4.2 Analytical study of scoops 65

4.2.1 Shaft speeds below VR_{thr} 68

4.2.2 Shaft speeds above VR_{thr} 71

4.2.3 Key conclusions of analytical study 78

4.3 CFD Geometry and Boundary conditions 79

4.4 Grid and time dependence studies 82

4.4.1 Grid details and Grid dependence studies 82

4.4.2 Time dependence studies 96

4.4.3 Adopted grid 96

4.5 Computational Resources and HPC scaling study 96

4.6 CFD analysis of the effect of shaft speed on capturing efficiency 97

4.7 Significance of 2D studies 107

4.8 Chapter conclusions on the effect of shaft speed on capture efficiency 109

5 Effect of geometry and operating conditions on scoop capture efficiency 110

5.1 Overview 110

5.2 Effect of constriction gap 111

5.3 Effect of varying the jet velocity. 115

5.4 Effect of jet angle 120

5.5 Effect of differential pressure 123

5.6 Effect of Number of Scoops 128

5.7 Chapter conclusions 132

6 Effect of vortex shedding on the performance of scoop based lubrication devices 134

6.1 Overview 134

6.2 Vortex shedding from scoops 135

6.3 Geometry optimization to minimize vortex shedding effects 143

6.4 Chapter conclusions 147

7 Conclusions 148

7.1 Attainment of objectives 148

7.2 Conclusions on the effect of shaft speed on capture efficiency presented in chapter 4 148

7.3 Conclusions on the effect of geometry and operating conditions on scoop capture efficiency presented in chapter 5 149

7.4 Conclusions on the effect of vortex shedding on the capture efficiency presented in chapter 6 150

7.5 Contribution to science and novelty in work 150

7.6 Future Work 151

References 152

8 Appendix 158

8.1 Post-Processing and exporting images using FLUENT while running on high performance computing (HPC) 158

8.2 MATLAB codes 167

8.2.1 Analytical modelling calculations (iterative calculations and plots)..... 167

8.2.2 MATLAB Post-processing code for FLUENT data..... 171

8.3 Experimental Paper with published results for validation. 177

List of Figures

Figure 1.1 Bi-direction scoop design patented by Fisher [4] 2

Figure 1.2 Key dimensions (right) of scoop being investigated and the trajectory of oil after being captured by scoops[5] 3

Figure 1.3 Top- Schematic diagram of experimental setup. Bottom- Oil scoop test module: side view (left) and front view (right). 1-Front chamber, 2-Scoop chamber, 3- Oil jet injector, 4-Front chamber exit and 5-Scoop chamber drain [5] 4

Figure 2.1Illustration of the break up process of a liquid jet emerging from a nozzle into ambient air[8]..... 9

Figure 2.2 Experimental visualization of a kerosene jet exiting into a cross flow of air[9]. 9

Figure 2.3 Stability curve for a jet exiting from a nozzle showing the variation of break up length as a function of the jet exit velocity[11]. 10

Figure 2.4 Contour of volume fraction at mid-plane showing the break up for swirl atomizer 3D jet with different grid sizes. From left to right 56, 29 and 9μm cell sizes[14]. 13

Figure 2.5 From top to bottom: Full 3D, 3D symmetric and 2D axis-symmetric model[15]. 14

Figure 2.6 Breakup of droplets for the three cases (3D, 3D symmetric and 2D axis-symmetric) investigated by Khosla et al[15] showing very similar results. 15

Figure 2.7 Breakup of droplet for different cell sizes in the 2D axis symmetric case of Khosla et al [15] investigations. 16

Figure 2.8 Tip of jet forming a umbrella like shape[17]. 17

Figure 2.9 CFD geometry used in the work of Guo et al [19]. Dimensions are in mm. 18

Figure 2.10 Modelling of oil droplets using the VOF model with a coarse mesh[29] 23

Figure 2.11 Formation of eddy from the trailing edge in a gear teeth[29]..... 24

Figure 2.12 Illustration of scoops and blades of a VAWT rotating about a vertical axis. 26

Figure 2.13 Growth of a vortex and subsequent separation of the vortex from the leading edge of the blade shown using PIV results of Ferreira[34] 27

Figure 2.14 Velocity vectors produced by Mclaren using CFD in the vicinity of the turbine blades in a VAWT[35] 28

Figure 2.15 CFD results of Li et al using 2.5D URANS and 2.5 LES models on a static turbine blade[36]. 29

Figure 2.16 Scoop assembly setup used in the work of Prasad et al [40]. 31

Figure 2.17 CFD domain and boundary conditions used in the work of Prasad et al [40] 32

Figure 2.18 Splashing of oil when sliced by scoops using implicit VOF model[40]. 32

Figure 2.19 Hexahedral mesh used in the CFD study of Korsukova et al [41]. 33

Figure 2.20 Volume fraction contours of oil as observed in the work of Korsukova et al. showing the formation of droplets as a result of the slicing process of the oil jet[41] 34

Figure 3.1 Geometry of fluid flow domain in 3D 42

Figure 3.2 2D CFD domain of scoops simplified from a 3D domain 43

Figure 3.3 Numerical Grid with 401,283 cells using a core cell size of 0.26mm 44

Figure 3.4 Algorithm for CFD solvers[55] 51

Figure 3.5 Mesh showing scoop moving on rotating zone (red color), jet fixed (blue color) on stationary zone(green color) and the interface between the two zones. 59

Figure 4.1 Geometry of scoops at point of slicing oil jet. 66

Figure 4.2 Shaft speeds below VR_{thr} 68

Figure 4.3 Shaft speeds above VR_{thr} 71

Figure 4.4 Strike angle vs. shaft speed 73

Figure 4.5 $\Theta_{capture}$ vs. shaft speed 74

Figure 4.6 Effect of shaft speed on C_x 75

Figure 4.7 Collision points graphically illustrated for various shaft speeds with jet velocity= 22.381 m/s and jet angle=64.2^o 76

Figure 4.8 Collision points graphically illustrated for various jet angles with jet velocity= 22.381 m/s and shaft speed=5000rpm. 77

Figure 4.9 CFD geometry and boundaries 79

Figure 4.10 Section of capture efficiency which is considered to be steady state 81

Figure 4.11 Grids shown in the vicinity of the scoop which were used for grid dependency studies 83

Figure 4.12 Chosen locations for velocity analysis and sample velocity plot shown for location 2 88

Figure 4.13 Moment on rotating walls of scoops a) vs. number of rotations b) values after achieving convergence 90

Figure 4.14 Oil Residence mass a) vs. number of rotations b) values after achieving convergence 92

Figure 4.15 Capture Efficiency a) versus number of rotations b) values after achieving convergence 94

Figure 4.16 Slicing of oil jet for different grid sizes (red denotes 100% oil and blue 100% air). 95

Figure 4.17 HPC scaling plot 97

Figure 4.18 Mass flow rate from the 6 scoops at 10000rpm with a jet velocity of 22.381m/s 98

Figure 4.19 Capture efficiency vs. number of rotations at 10000rpm with a jet velocity of 22.381m/s 98

Figure 4.20 Sequence of oil volume fraction contours illustrating the slicing and capturing process at 10000rpm with a jet velocity of 22.381m/s (red denotes 100% oil and blue 100% air) 99

Figure 4.21 Oil being centrifuged out as the scoop rotates (red denotes 100% oil and blue 100% air). 100

Figure 4.22 Capture Efficiency(from CFD, analytical study and experiments[5]) vs. shaft speed 101

Figure 4.23 Oil loss at 500rpm (red denotes 100% oil and blue 100% air) 102

Figure 4.24 C_x at strike point for a jet velocity of 22.381m/s and a jet angle of 64.2^o 103

Figure 4.25 Collision points in CFD a) 5000rpm b) 7500rpm c) 10000rpm (red denotes 100% oil and blue 100% air) 103

Figure 4.26 Illustrative image showing jet pluming a)CFD(red denotes 100% oil and blue 100% air) b)Experimental visualization[5] 104

Figure 4.27 Jet deflected from the theoretical path at 1000rpm (red denotes 100% oil and blue 100% air) 106

Figure 4.28 Consideration of jet diameter, *d*, for theoretical analysis 106

Figure 4.29 Tetrahedral grid of 3D scoops domain 107

Figure 5.1 Constriction gap and Jet angle 110

Figure 5.2 Effect of constriction gap on capture efficiency. Experimental data is obtained from[5] 112

Figure 5.3 Volume fraction and pressure contours of oil after the slicing process of oil jet shown for the three gaps at 7500rpm at the same time instant. 113

Figure 5.4 Scoops at the same time instant after capturing oil at 7500rpm shown using volume fraction contours of oil. 114

Figure 5.5 Geometry of single tandem jet that are 10^{o} circumferentially apart. 115

Figure 5.6 Capture Efficiency vs. shaft speed for varying jet velocity shown for CFD and experiments[5]. 117

Figure 5.7 Oil droplets centrifuged outwards significantly at 500rpm following slicing of oil jet shown using volume fraction contours of oil..... 118

Figure 5.8 Near jet view at 500rpm and 10000rpm after the slicing of jet at approximately the same position (red denotes 100% oil and blue 100% air). 119

Figure 5.9 Residence mass of oil for 500rpm and 10000rpm 120

Figure 5.10 Effect of jet angle on the capture efficiency shown for CFD and experiments[5] 121

Figure 5.11 Distribution of oil droplets close to the scoop outlet highlighted for the three jet angles at the same time instant at 7000rpm a) 54.2^{o} b) 59.2^{o} a) 64.2^{o}(red denotes 100% oil and blue 100% air)..... 122

Figure 5.12 Absolute pressure contours indicating low pressure region at scoop outlets with a differential pressure of 0.18 bar (right). 124

Figure 5.13 Capture efficiency vs. differential pressure for a shaft speed of 7500rpm, jet velocity of 22.381, jet angle of 64.2^{o} and constriction gap of 2mm. 125

Figure 5.14 Ingestion of oil into scoop outlet using various differential pressures at a shaft speed of 7500rpm and a constriction gap of 2mm(red denotes 100% oil and blue 100% air) 126

Figure 5.15 Volume fraction contours of oil without differential pressure (left) and with a differential pressure of 0.18bar (right). 127

Figure 5.16 Theoretical capture efficiency for a jet velocity of 20m/s and a jet angle of 64.2^{o} 128

Figure 5.17 Capture efficiency vs. number of scoops for a jet velocity of 6m/s, a jet angle of 64.2^{o} and constriction gap of 4mm. 129

Figure 5.18 Oil volume fraction contours using 1 scoop just after impact with scoop 130

Figure 5.19 Pressure contours indicating low pressure at scoop tips due to vortex formation. 131

Figure 6.1 Experimental test on a wedge (left)[5] and CFD slicing of oil jet showing the formation of plume at the tip of jet after slicing using volume fraction contours of oil (right). 135

Figure 6.2 Vortex shedding progression highlighted for a scoop at 10000 rpm 136

Figure 6.3 Vorticity increasing progressively with shaft speed 137

Figure 6.4 Pressure data from vertex point behind scoop tip at 10000rpm 139

Figure 6.5 PSD plot using total pressure data at 10000rpm..... 140

Figure 6.6 Characteristic length, *L,* for an inclined flat plate as used in the work of Lam & Wei [71]..... 140

Figure 6.7 Top-Absolute pressure contours exhibiting low pressure regions close to the scoops tips. Bottom- Gauge pressure illustrating the pluming effect..... 142

Figure 6.8 Velocity vectors at the tip of the scoop indicating a swirl 142

Figure 6.9 Volume fraction contours (red- oil and blue-air) showing formation of plume at tip of jet which eventually gets stretched out and is uncaptured by the proceeding scoop..... 143

Figure 6.10 Volume fraction contours of oil, Total pressure and Vorticity contours for sharp tip (top row) and blunt tip (bottom row) at 7500rpm..... 144

Figure 6.11 Capture efficiency for three different tip geometries of scoop..... 145

Figure 6.12 Volume fraction contours of oil (left) and vorticity contours (right) for the progression of oil jet slicing process using a reverse jet configuration. 146

List of Tables

Table 2.1 Adopted modelling strategy 37

Table 3.1 Non-dimensionalized velocity, U* 58

Table 3.2 Material Properties 62

Table 4.1 Threshold ratios for different jet angles 70

Table 4.2 Boundary Conditions 80

Table 4.3 Grid information 83

Table 4.4 Calculated average GCI values based on velocity magnitude for each of the grids 88

Table 4.5 Calculated average GCI values based on moment for each of the grids 90

Table 4.6 Calculated average GCI values based on oil residence mass for each of the grids. 93

Table 4.7 Calculated relative errors and average GCI values based on capture efficiencies for each of the grids 94

Table 5.1 Tested experimental casses for investigations on varying the jet velocity[5] 116

Table 5.2 Tested experimental cases for investigations on varying the jet angle[5] 121

Table 6.1 Sampling frequency, $f_{s,}$ for each case 138

Table 6.2 Shaft speeds with associated vortex shedding frequencies and Strouhal numbers 141

Nomenclature

Symbol	Description	SI Unit
F	Force	kg/ms^{-2}
f	Frequency	Hz
g	Acceleration due to free fall	ms^{-2}
h	Cell size	m
k	Turbulent kinetic energy per unit mass	m^2/s^2
L	Characteristic length	m
R	Radius of scoop	m
Re	Reynolds number	
r	Ratio of cell size between two grids	
St	Strouhal number	
t	Time	s
P	Pressure	N/m^2
U	Velocity	m/s
C_X.	Distance between scoop tip and point of jet impingement	m
$\dot{m}$	Mass flow rate	kg/s
N_{Scoops}	Number of Scoops	
u_i	Velocity. Subscript *i*= x direction, *j*=y direction, *k*=*z* direction	m/s
VR	Velocity ratio between scoop tip and jet	
V_{jet}	Velocity of jet	m/s
x_i	Direction. Subscript *i*= x direction, *j*=y direction, *k*=*z* direction	

y^+	Non dimensional wall distance used in the context of turbulence	
α	Volume fraction	
ε	Turbulence dissipation rate of k	m^2/s^3
θ_{jet}	Jet angle	Degrees or Radians
ρ	Density	kg/m^3
μ	Dynamic viscosity	*kg/ms*
σ	Surface tension	Nm^{-1}
τ_w	Wall shear stress	N/m^2
ζ	Vorticity	$1/s$
ω	Angular speed	rad/s

Glossary

CFD	Computational Fluid Dynamics
CFL	Courant-Lewy-Friedrich
G2TRC	Gas Turbines Transmissions Research Centre
GCI	Grid Convergence Index
HPC	High Performance Computing
PISO	Pressure-Implicit with Splitting of Operators
RANS	Reynolds-Averaged Navier-Stokes
SIMPLE	Semi-Implicit Method for Pressure-Linked Equations
SIMPLEC	Semi-Implicit Method for Pressure-Linked Equations Consistent
SPH	Smoothed Particle Hydrodynamics
UDF	User-Defined Function
URF	Under Relaxation Factors
VOF	Volume of Fluid
VAWT	Vertical Axis Wind Turbines

1 Introduction

1.1 Overview

In this thesis Computational Fluid Dynamics (CFD) is used to assess the performance of scoop devices that are intended to deliver lubrication to bearings in aero-engines. In depth analysis is conducted to study the contributing factors that cause depletion in the capture efficiency under various operating conditions and scenarios.

1.2 Background

The shafts in aero-engines rotate at speeds in the order of several thousand revolutions per minute. The bearing assemblies on which these shafts are supported, require continuous lubrication to ensure smooth operation. Frictional forces arising due to shaft speeds aggravate wear on bearing assemblies while generating heat simultaneously. Hence reliable lubrication and scavenging systems are essential to regulate the temperature and minimize the effects of wear in the bearing assembly and associated bearing chambers. The components of the aero-engine located in the vicinity of the bearings, make the bearings almost inaccessible, thus the process of delivering lubricant, to cool and lubricate bearings, becomes a difficult task. In order to overcome the challenges pertaining to the lubrication process in aero-engines, cutting edge systems are currently in the process of being developed.

Scoop based lubrication systems have the potential to be effective systems to lubricate the bearings in aero-engines where direct lubrication is not possible. The concept of scoop delivery systems is not new; a NASA technical memorandum from 1980 surveying lubrication of rolling element bearings includes an axial scoop system where an oil jet is targeted axially at a channel that delivers oil to under-race feed holes at a different axial locations [1] but technology development has been relatively slow as in most cases a scoop delivery system is not necessary. An early scoop design for a gas turbine shaft is described in the 1987 patent of Kovaleski [2]; the invention described is a scoop system that directs specific proportions of oil axially, forward and rearward from the scoop to lubricate bearings located on opposite sides of the scoop itself. Over the years, scoop geometry design has evolved in order to meet the increasingly crucial requirements of gas turbines for higher stage loadings and consequently higher operating

speeds. The 2002 patent of Fisher et al [3], collects oil in scoops and delivers it to a series of axial grooves. The scoop design patented by Fisher in 2004 [4] is shown in Figure 1.1. It is very similar in design to that being investigated in the work presented in this thesis although in the patented concept oil is delivered alternately axially left and right and is also split above the scoop and below giving 4 different paths whereas in the design investigated here the requirement is for as much oil as possible to be collected under the scoop.

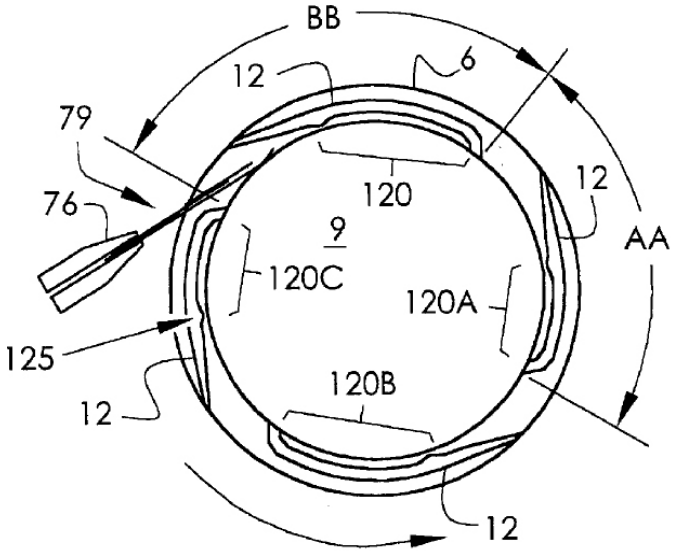


Figure 1.1 Bi-direction scoop design patented by Fisher [4]

Figure 1.2 shows two of the geometrical dimension associated with the scoop geometry being investigated in this thesis which are the jet angle, θ_{jet}, and the constriction gap, d_c. Lubrication oil from the jet is delivered to scoops that rotate on a shaft with a speed of ω at an angle, θ_{jet}, to the radial direction. The shaft speed, ω, for the work in this thesis is in the range of 500rpm to 10000rpm. The oil from the jet is delivered at a velocity V_{jet} to the scoops. The oil jet is sliced by the scoops as they rotate. Once the oil is sliced by the scoop, the initial momentum of the oil from the oil jet, drives the oil towards the constriction gap and subsequently to the scoop outlet where oil is delivered to bearings as shown in Figure 1.2. If the momentum of the oil from the jet is not sufficient, centrifugal forces from the scoop may overcome the momentum of the oil and eventually lead to oil being centrifuged away from the constriction gap without being captured.

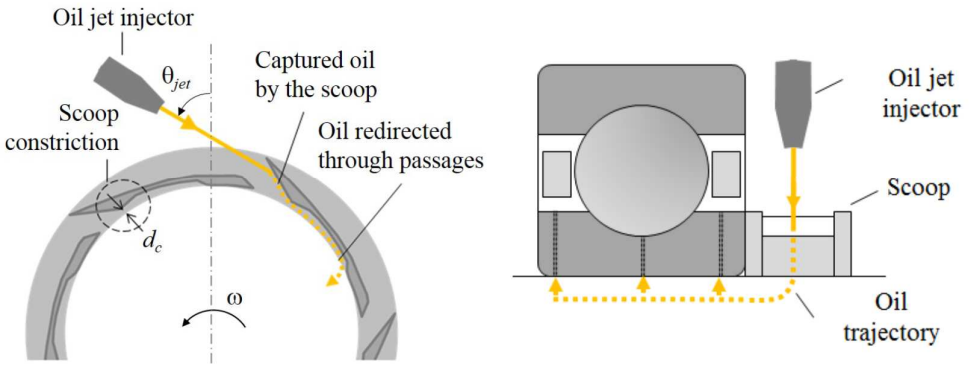


Figure 1.2 Key dimensions (right) of scoop being investigated and the trajectory of oil after being captured by scoops[5]

An important parameter that quantifies the performance of scoops is the capture efficiency which is the ratio of the amount of oil captured by the scoop to the amount of oil delivered to the scoop over a given time period. In order to determine the capture efficiency of the scoops experimental studies have been conducted on the geometry being investigated for this thesis[5] by researchers from the Gas Turbines Transmissions Research Centre(G2TRC). A schematic diagram and an image of the experimental setup is shown in Figure 1.3. Oil from an inlet pump is delivered to the oil jet at a flow rate that is measured at regular intervals into a chamber where the scoops rotate. Oil that is captured by the scoops is directed from the outlet of the scoops into the front chamber (indicated by number 1 in Figure 1.3) where it is drained out and measured. The oil acquired from front chamber is analyzed with respect to the inlet flow rate of oil to determine the capture efficiency of the scoops. The front chamber from which oil is drained out represents the location where oil is delivered to bearings in an aero-engine.

As oil is sliced by the scoops, there is a quantity of oil that is not captured, as a result of centrifugal effects and other factors. This uncaptured oil is drained out from the scoop chamber (indicated by number 2 in Figure 1.3). Oil that has been uncaptured from the scoop chamber and the quantity of oil that has been measured from the front chamber are re-fed together into an oil reservoir from which oil is drawn by the inlet pump, that eventually feeds oil to the oil jet nozzle.

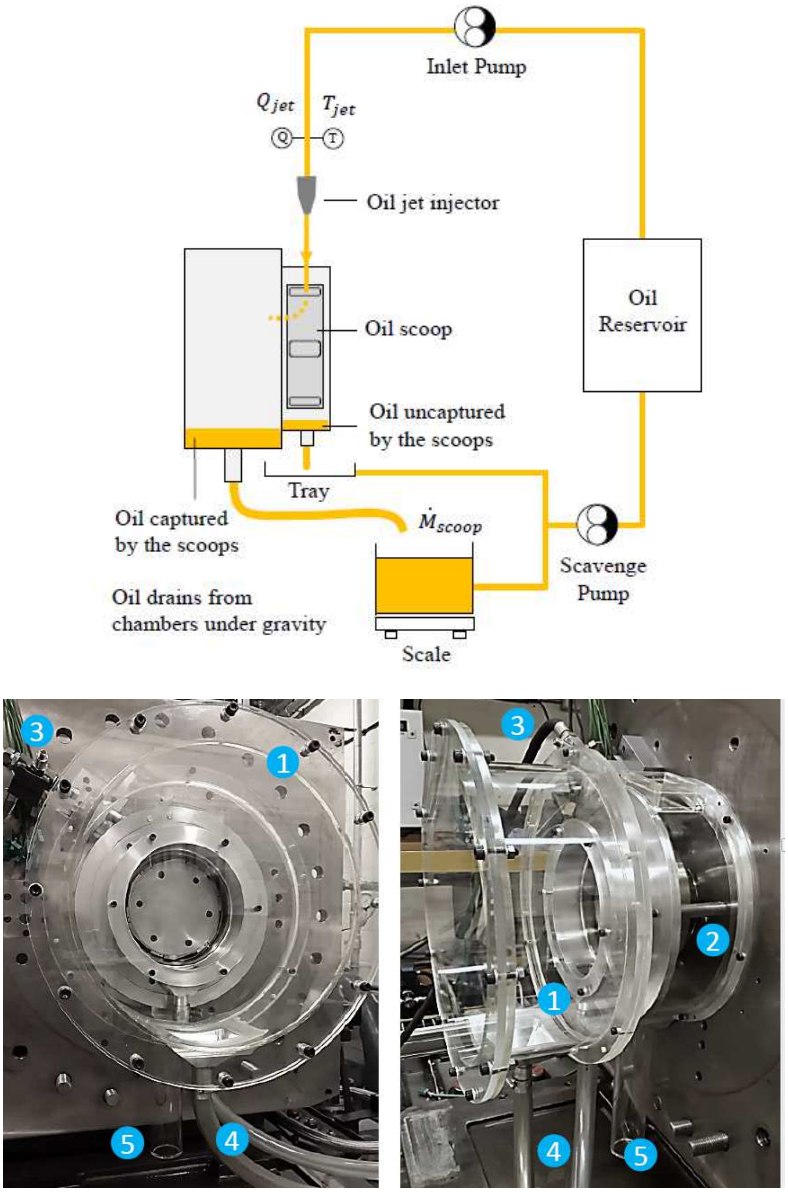


Figure 1.3 Top- Schematic diagram of experimental setup. Bottom- Oil scoop test module: side view (left) and front view (right). 1-Front chamber, 2-Scoop chamber, 3-Oil jet injector, 4-Front chamber exit and 5-Scoop chamber drain [5]

Based on experimental results, it is observed that the capture efficiency, which is the ratio of the amount of oil captured to the amount of oil supplied to the scoops, depends on several

design variables such as shaft speed, oil jet velocity, and jet angle and the constriction gap. It is also dependant on other factors such as the losses incurred due to the slicing event of the oil jet and losses caused by centrifugal forces. Rotating scoops induce a highly turbulent air flow in the scoop chamber. Although it is impractical to quantify the intensity of turbulence in the scoop chamber experimentally, a highly turbulent flow is evident from visualizations that show uncaptured oil being driven forcefully along the walls of the scoop chamber casing to the scoop chamber drain (indicated by number 5 in Figure 1.3). The geometry of the scoop and associated cavities in the scoop contribute towards such a turbulent flow of air in the scoop chamber.

Although experimental tests conducted on the scoop geometry are able to quantify the capture efficiency of scoops, in depth reasoning of associated oil losses have not been made from experimental tests and visualizations. One of the main reasons for this is the limited amount of optical and visual access that is available in the scoop chamber. At high shaft speeds, where a fully turbulent air flow drives the oil along the walls of the scoop chamber, almost complete visual access of the scoops is lost through the transparent walls of the casing. Hence experimental investigations use a borescope camera embedded within the scoop chamber to gain some level of visual access. At high shaft speeds even the visualizations acquired from the borescope camera suffer from clarity issues due to intense splashing effects of oil caused by the slicing of the oil jet. It is here that CFD studies have the potential of providing in depth reasoning for oil loses occurring from scoops. Limited amount of CFD studies have been conducted on scoop devices by past researchers and this PhD thesis presents work conducted in-depth on the scoop device that has been experimentally assessed by researchers at the G2TRC.

1.3 Limitations and gaps in existing work on scoops

Literature review presented in Chapter 2 has clearly suggested that there are several gaps in the modelling of scoop devices using CFD. There are several gaps that were not investigated experimentally due to limitations and complexity involved. Theses gaps and limitations in experiments lay the foundation for this PhD research.

The gaps and limitations are:

1. Researchers have investigated the effect of various parameters on the capture efficiency. However most of them have not done an in-depth analysis of the contributing reasons for the change in the capture efficiency due to the variation in the parameters. The PhD will fill this gap and detailed reasoning and analysis will be made from the observations in CFD results
2. The effect of the number of scoops and differential pressure across scoops on the capture efficiency has not been investigated yet and this has been done during the PhD.
3. None of the researchers reviewed have identified that vortex shedding from the tip of scoops contribute to decreased capture efficiency at higher speeds. The PhD work includes studies about the vortex shedding behaviour and also estimating the associated vortex shedding frequencies and Strouhal numbers in scoop devices.
4. Parametric studies on optimizing the shape of the scoops are also done in order to show the performance of scoops with alternate shapes and configurations.

1.4 Aims and Objectives

The aim of this PhD is to predict the performance of a scoop device using CFD as accurately as possible. The objectives of the project are as follows:

- Develop a CFD model that is capable of predicting the capture efficiencies of scoop devices with sufficient accuracy while being computationally efficient.
- Assessing the effects of design variables such as shaft speed, oil jet speed, jet angle and constriction gap on the capture efficiency of scoop devices using CFD.
- Provide qualitative insight into factors both geometric and functional that affect scoop performance.

1.5 Thesis Structure

Chapter 1 gives an introduction to scoops devices and discusses the experimental work on the scoop device that has been assessed for the validation work in this thesis by previous researchers. Then the limitations and gaps identified from literature review in Chapter 2 are highlighted. Finally, the aim and objectives for the PhD are stated in this chapter.

Chapter 2 presents a review of work carried out by previous researchers in the areas concerning the CFD modelling of scoops. The review has been split into parts. An adopted modelling strategy is chosen based on the literature review and presented in a table towards the end of the chapter.

Chapter 3 highlights the CFD methodology used in the thesis. The creation of geometry, numerical grid, numerical models and post-processing details are included in this chapter.

Chapter 4 presents the numerical assessment of the effect of shaft speed on the capture efficiency of scoops. Analytical modelling is carried out before CFD studies are presented. The chapter includes grid dependency studies. The significance of 2D modelling is highlighted in this chapter. The chapter contains content that have been published in the Journal of Turbomachinery[5] and ASME Turbo Expo 2018 proceedings[6].

Chapter 5 comprises of investigations that were carried out to assess the performance of the scoops due to variation in the design variables and operating conditions. These include the effect of the jet angle, constriction gap, differential pressure and number of scoops on the capture efficiency.

Chapter 6 presents the vortex shedding phenomena observed in scoop devices. The effect of vortex shedding on the capture efficiency is presented in detail. Vortex shedding frequencies are estimated in this chapter. The chapter contains content that have been published in the ASME Turbo Expo 2017 proceedings[7].

Chapter 7 presents a summary of the conclusions from all the chapters and highlights the contribution to the science from this PhD work. Recommendation for future work are also made in this chapter.

2 Literature Review

2.1 Introduction

This chapter presents the literature used to obtain information to derive a CFD modelling strategy for scoops. To the best of the author's knowledge, only very little literature is available on modelling of scoop devices using CFD. Hence the literature review is split into different aspects based on the information presented in chapter 1, section 1.2 and in depth review of each aspect is presented. The findings of the review are put together and the most appropriate models that satisfy all the aspects are adopted to model scoop devices. The aspects reviewed include:

1. Modelling of a jet.
   Modelling of turbulence in rotating flow involving complex geometries. This aspect is reviewed after considering the complex shape of the scoops to be investigated.
2. Appropriate multiphase modelling for highly turbulent rotating flows.
3. Modelling of vortex shedding from scoop devices. This aspect was reviewed after preliminary simulations and experimental results indicated the formation of vortices that affected the capture efficiency.

Relevant work conducted by researchers on scoops using both CFD and experimentally are also reviewed in this Chapter.

2.2 CFD modelling of jets

Lubrication to the scoop is fed by oil jets from a nozzle that are directed towards rotating scoops that slice the oil jet as explained in chapter 1, section 1.2 . A liquid jet that exits from a nozzle into a gaseous domain is subjected to a break up at a distance from the nozzle exit. The break up distance is illustrated in Figure 2.1 for a jet that exits into ambient air[8]. A similar break up process is also expected for a liquid jet entering into a gaseous domain with a cross flow as shown in Figure 2.2[9]. However there is a deflection in the trajectory of the jet as it enters into a cross flow.

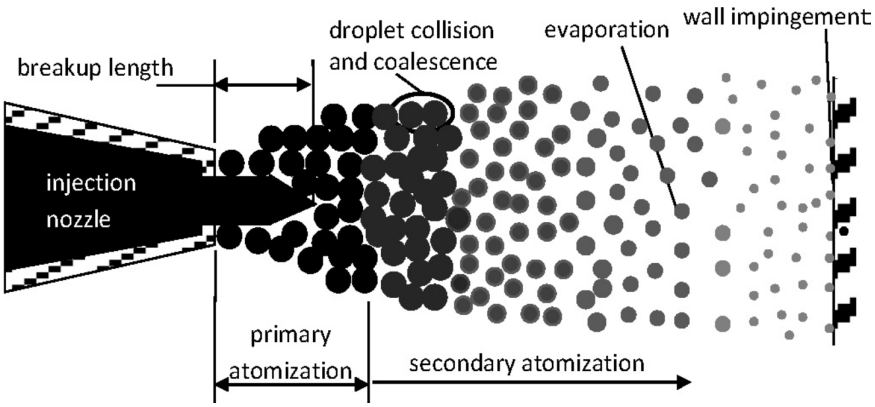


Figure 2.1Illustration of the break up process of a liquid jet emerging from a nozzle into ambient air[8].

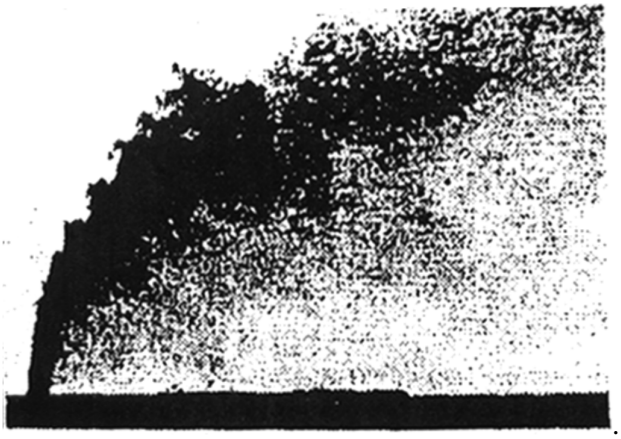


Figure 2.2 Experimental visualization of a kerosene jet exiting into a cross flow of air[9].

The length at which a jet breaks up is dependent on a number of factors such as the jet velocity, jet diameter, density of the liquid jet and air, surface tension between the liquid jet and gaseous

environment and disturbances associated with turbulence at the nozzle exit and cross flow[10]. Hence several experimental and theoretical efforts have been devoted towards studying the breakup of liquid jets exiting into a gaseous environment in different conditions. Experimental studies have found a relationship between the break up length and the jet exit velocities for both laminar and turbulent liquid jets. Figure 2.3 shows the variation of break up length as a function of the jet exit velocity[11]. It is observed that between the laminar and the turbulent region there exists a peak beyond which there is a small transition region where the break up length decreases as the jet velocity increases. Beyond the transition region, the breakup length begins to increase linearly similarly to the laminar regime as the jet velocity is increased.

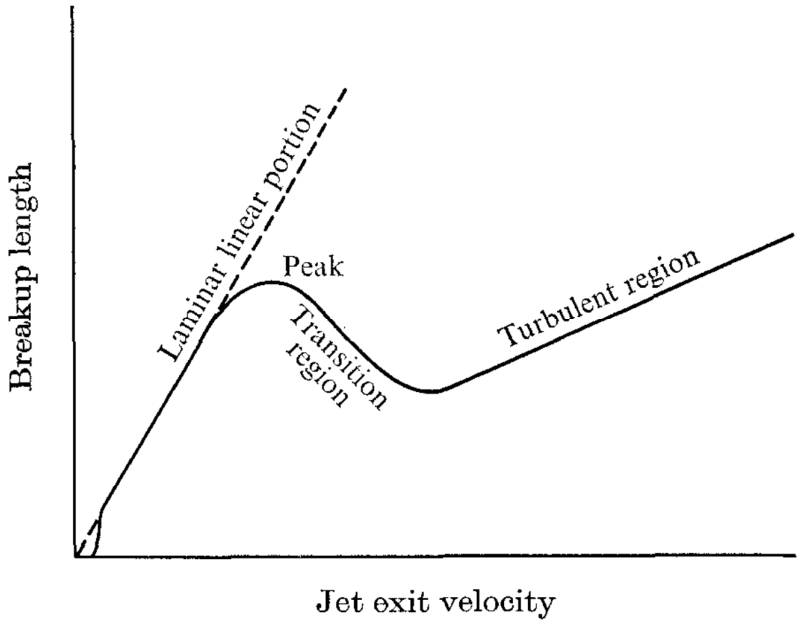


Figure 2.3 Stability curve for a jet exiting from a nozzle showing the variation of break up length as a function of the jet exit velocity[11].

The Reynolds numbers of the jet investigated in this thesis lie in the range of 1000 and 17000 as evaluated in chapter 3, section 3.4.5. Most of the cases investigated in the thesis involve a turbulent jet(s) and the disturbance caused by turbulence makes it impractical to theoretically determine the breakup length for the jet(s) used in the studies. Hence experimental visualizations[5] that were conducted on the geometry being assessed were used as a guide to determine whether there will break up of the jet before it is sliced by the scoop. Based on visualizations[5] it is evident that for all the cases investigated experimentally the jet is not

close to the point at which break up takes place. This is because the distance between the jet nozzle and the point at which a scoop slices a jet, is significantly smaller than the break up length. Hence breakup of the oil jet prior to the scoop slicing is not anticipated for any of the cases investigated using CFD in this thesis.

The flow of oil from the jets is in the turbulent regime and hence careful consideration has to be given in choosing an appropriate multiphase model and turbulent model that simulates the flow of oil from the jet into the scoops. Jet studies have been reviewed in this section to select the most appropriate multiphase and turbulence model for the jet.

Grosshans et al [12] have analyzed the breakup of a liquid jet numerically in 3D by using the Volume of Fluid(VOF) multiphase model and Large Eddy Simulations(LES) was used to model the effects of turbulence. The effects of surface tension are captured using the Continuum Surface Force (CSF) model. The geometry used in their model has a domain in the form of a cuboid. The dimensions of the cuboid in units are 16 x 16 x 55d_{nozz} . The inlet velocity of the jet was at 500m/s. Walls were imposed with no-slip and zero-gradient velocity conditions. In order to conduct grid sensitivity, they developed three grids with uniform cell sizing. Cell sizes of 0.05d_{nozz}, 0.1d_{nozz} and 0.2d_{nozz} are assessed. They observed that the coarsest grid (cell size=0.2d_{nozz}) causes the high numerical diffusion and also leads to damping of turbulence. This eventually results in the spray not widening to the same extent as seen with finer grids. However, the spread is similar for the two finer grids. Comparison of the centerline velocities of the three grids indicates a maximum difference of 4% between the coarse grid and the fine grid. The researchers state that the velocity of the jet could be considered as grid independent, but when observing the qualitative results of the spread of the jet that did not appear to be grid independent. Hence they have emphasized that the VOF model is sensitive to the grid resolution.

Part of their study also involves assessment of the jet breakup process. They studied the effect of the liquid to gas ratio parameter on the breakup process of the jet. It was observed that when the liquid to gas density ratio is high (this was assessed for the range of 10 to 30), the breakup of the jet is low. This is because the liquid droplets, which are denser compared to the gas, tend to be less influenced by the turbulent eddies in the domain. However, when the density of the liquid droplets is lower, they can be subject to aerodynamic drag because of the gas density

and can undergo secondary breakup. This also supports as to why jet break up is not observed in experimental visualizations of the tests used for validation of results this thesis. The ratio of oil to air density is close to 800 in the experiments conducted on the geometry used in this thesis[13].

Fuster et al [14] also emphasize the necessity of selecting an appropriate grid resolution in order to accurately capture the break up and disintegration of a jet in 3D. They have used the VOF model with an adaptive mesh refinement (AMR) on their octree mesh used for simulations. Piecewise-linear geometrical reconstruction scheme is used to construct the interface between the two phases in the flow. Despite the capability of the scheme to preserve a sharp interface and be accurate close to second-order, they point out that the scheme is not strictly mass-conservative. However, the conservation errors, using this scheme, for the most complex problems have accounted for less than 0.01%. Prior to conducting simulation of realistic cases, the adopted modelling strategy was validated for a simple case using the temporal viscous Linear Theory (LT). They state the high uncertainty involved in experimental measurements, make it less appealing to conduct validation studies in atomization experiments. After validating the adopted model, a swirl atomizer jet was simulated in 3D. The density of the liquid jet was 1000 kg/m^3 and the gas phase was 35.92kg/m^3. The viscosity of the liquid phase was $8x10^{-3}$Pa.s and the gas phase was $2.87x10^{-4}$Pa.s. The surface tension between the phases was 0.432 N/m. A jet velocity of 20m/s and inlet diameter of 0.4mm were used. A uniform 3D grid was used to assess the effect of grid density for three grids using cell sizing of $0.140d_{inlet}$, $0.070d_{inlet}$ and $0.023d_{inlet}$. Figure 2.4 shows the influence the grids have on the jet break up process and disintegration of the jet into smaller droplets. It is clearly observed from the study on the necessity of having a small cell size (such as $0.023d_{inlet}$) especially when the jet is turbulent.

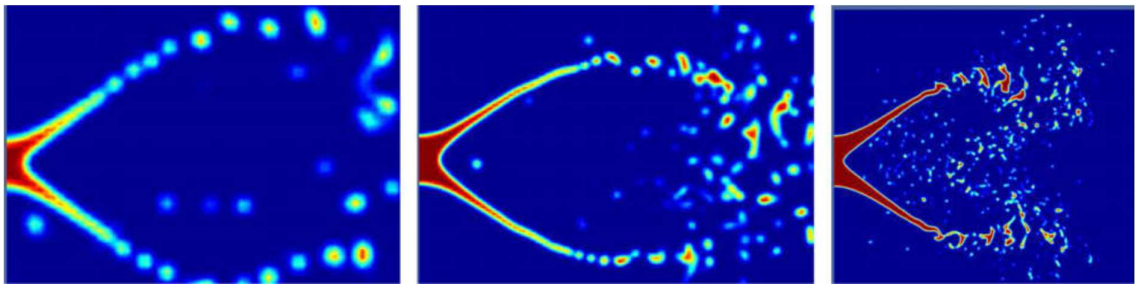


Figure 2.4 Contour of volume fraction at mid-plane showing the break up for swirl atomizer 3D jet with different grid sizes. From left to right 56, 29 and 9µm cell sizes[14].

It has been shown by Khosla et al [15] that the simulated breakage of a droplet in a cross flow can be successfully carried out using a 2D axis-symmetric model. They used the VOF model to simulate the breakup of a single 600 micron diameter ethanol drop in a gas cross-flow in both 3D and 2D and compare their results. The results of their CFD study is validated against existing experimental data for liquid drop breakup. A cell size of 10 microns was used in the grids. The study assessed 3 cases: a) a full 3D model with 7 million cells b) 3D grid with symmetry boundary condition with 2 million cells and a 2D axis symmetric grid with 100, 000 cells. Figure 2.5 shows the 3 geometrical models of an ethanol droplet in their associated domains and Figure 2.6 shows the results of the breakup of the droplets for the 3 cases.

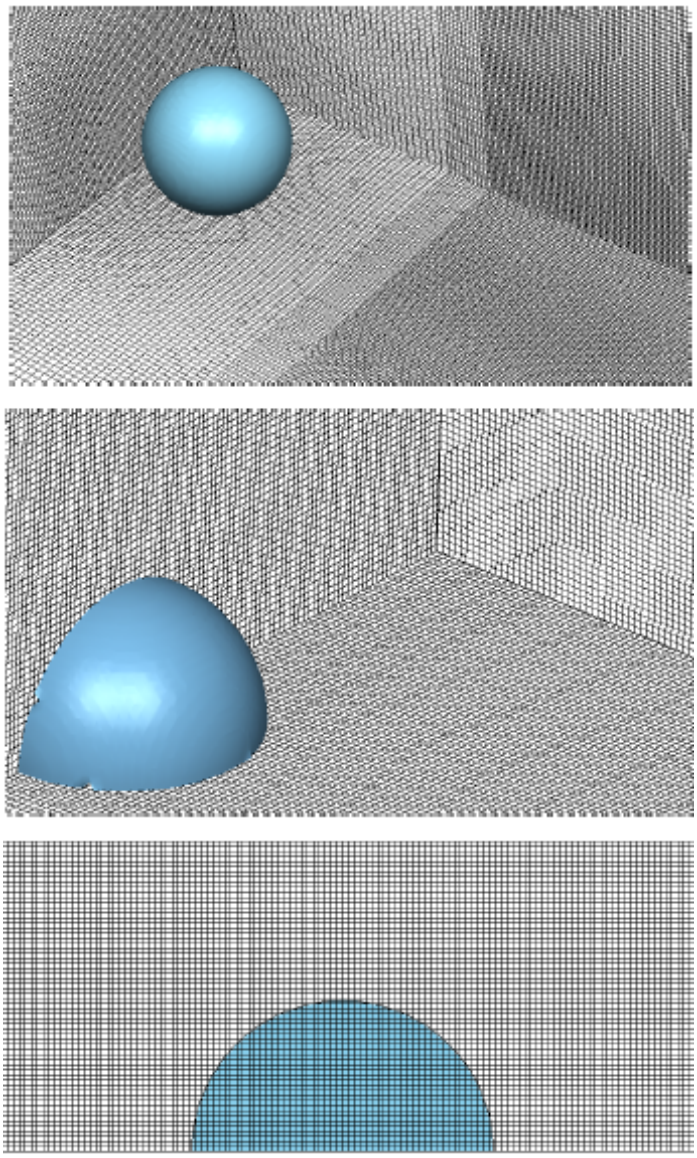


Figure 2.5 From top to bottom: Full 3D, 3D symmetric and 2D axis-symmetric model[15].

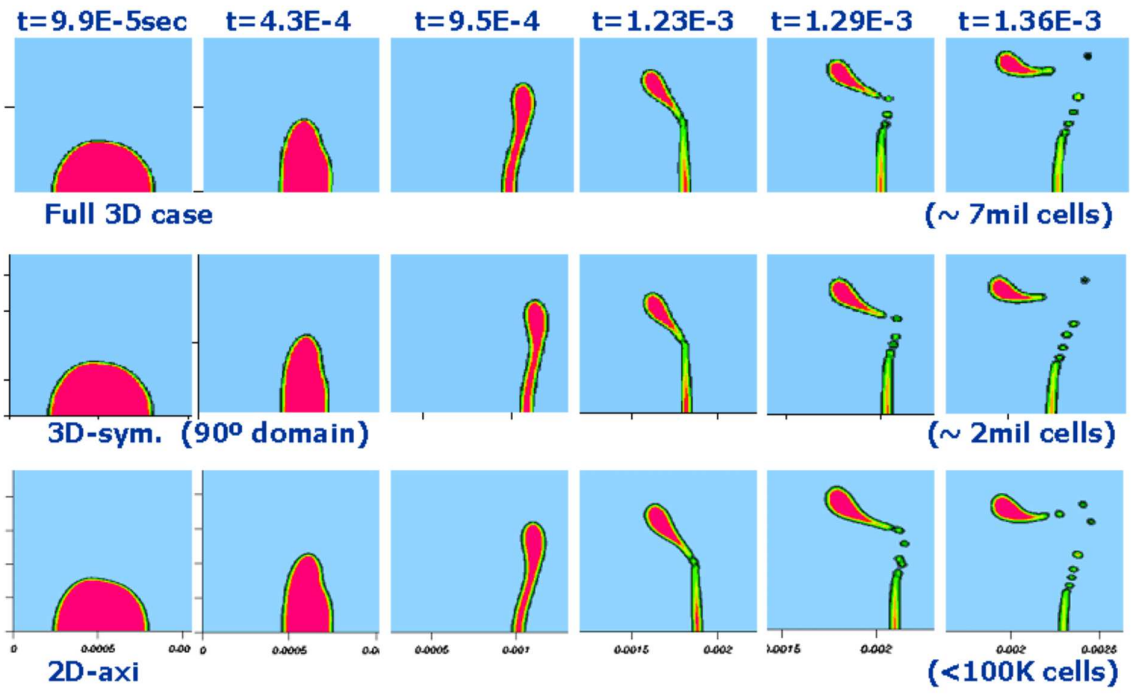


Figure 2.6 Breakup of droplets for the three cases (3D, 3D symmetric and 2D axis-symmetric) investigated by Khosla et al[15] showing very similar results.

Further investigations included grid independence studies carried out on the 2D axis-symmetric case. Cells size of 5, 10, 12.7 and 30 microns were used for this. Figure 2.7 shows the break up process of the droplet for different grid resolutions. Bulk of the break up behavior of the initial droplet seems to be resolved in a similar way for all the grids, however subsequent break up into smaller droplets is only resolved well when using a fine grid. This once again indicates the necessity of an adequately fine grid when resolving a multiphase flow using the VOF model.

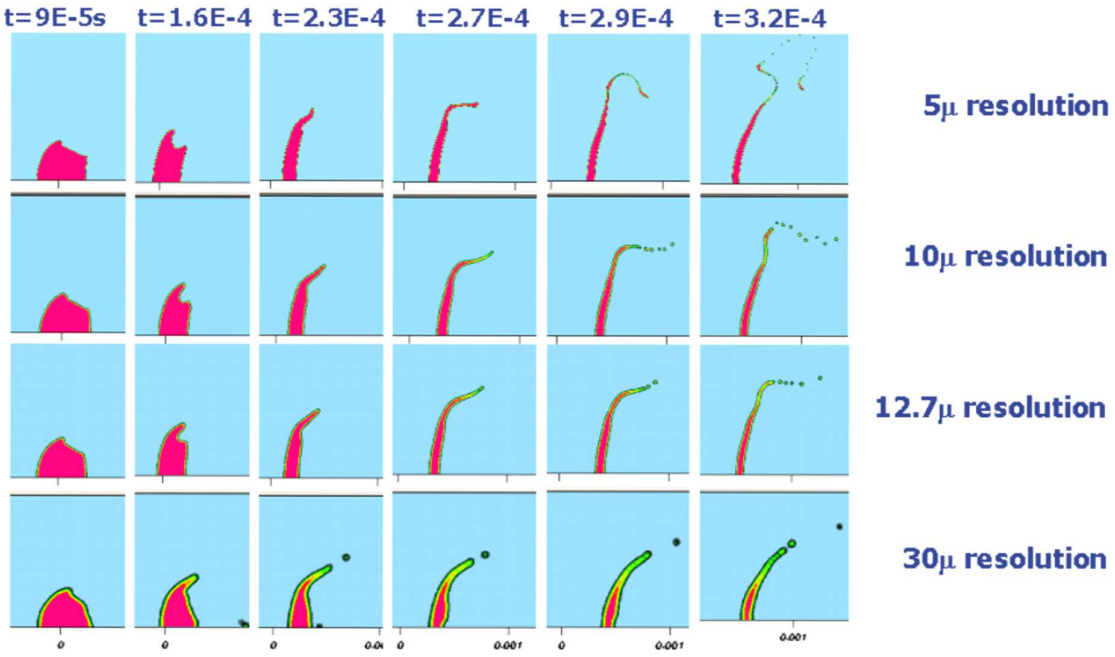


Figure 2.7 Breakup of droplet for different cell sizes in the 2D axis symmetric case of Khosla et al [15] investigations.

Studies conducted by Reddy and Banerjee [16][17] also utilize the VOF model in order to look at the primary atomization of a 2D planar liquid jet that is emanating into a quiescent gaseous environment. Simulations were carried out in 2D using a structured Cartesian grid. The interface advection was carried out using the Operator split scheme with Eulerian implicit-Lagrangian explicit method. Surface tension was modelled using the CSF model. Validation of the solver against a published bench mark case was carried out for the chosen models prior to conducting simulations. The ratio of liquid to gas density and viscosity used in the simulations were 30 and 100 respectively. Reynolds numbers of the assessed liquid jets were in the range of 2100 to 3500 which fall into the range of the jet Reynolds numbers being assessed for this thesis. It is seen from CFD, as the jet emerges from the tip of the jet nozzle it is subjected to high shear as it encounters the stationary gas phase. The tip of the jet begins to form into the shape of an umbrella, as shown in Figure 2.8, which eventually stretches out and breaks into ligaments and droplets. The 2D results have also been compared to a similar 3D study of a diesel jet where the disintegration of liquid jet is very similar qualitatively. In order to observe droplet pinching from the ligaments a sufficiently fine mesh is essential as stated in their study. It was also seen that some of the droplets that were formed were entrained to a

recirculating flow that was induced by the jet. At high Reynolds number the flow structures in the vortices are believed to interact with the small droplets that are formed. Various grid resolutions (coarse and fine) were used to show the significant differences in the ligaments formation process and atomization of droplets. Conclusions made from their observations favor the use of a fine grid in order to capture realistic droplet formation.

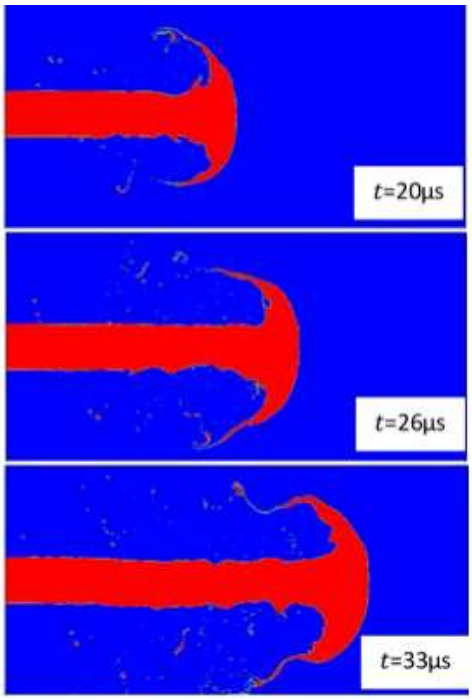


Figure 2.8 Tip of jet forming a umbrella like shape[17].

Further research involving highly turbulent water jets in air were conducted by Anirban et al [18]. In their study they use a structured grid that is created using the mesh generation software GAMBIT. The jet is simulated in a 2D axis-symmetrical domain. The domain was 1000mm x 500mm. The Reynolds number of the jet was 19,000 which is close to the highest jet Reynolds number investigated in this thesis. The Eulerian multiphase model was used and the effects of turbulence was captured using standard k-ϵ model with standard wall conditions. Water was set as the secondary phase in the model. QUICK schemes was used for the discretization schemes for the momentum and Volume fraction while turbulent kinetic energy and dissipation rate were solved using second order upwind. SIMPLE algorithm was used for Coupling of pressure-velocity. A time step size of 10^{-5}s was used. Under-relaxation factors were set at

default values for the CFD code, FLUENT. The results indicate that the simulation accurately predicts the characteristics of the flow (volume fraction of the phases and the velocity) to be expected from experimental results. However, it is to be noted, that well away from the centerline of the jet, where the flow is comprised of sparse (dispersed) droplet flow with water mist, the Eulerian model is no longer valid. This is because of the continuum hypothesis assumption made when using the Eulerian model which assumes there is a smooth change in physical variable in the domain. However, it was concluded that there is an advantage of using the Eulerian model to assess the performance and behavior of jets only if the focus is on the main jet region.

Guo et al[19] assessed the performance of turbulence models for a 2D submerged confined jet in a single phase flow. The turbulence models included the standard k-ϵ model, RNG k-ϵ model, low Reynolds number k-ϵ model and the Reynolds Stress model (RSM). The setup of the geometry and boundary conditions are shown in Figure 2.9.

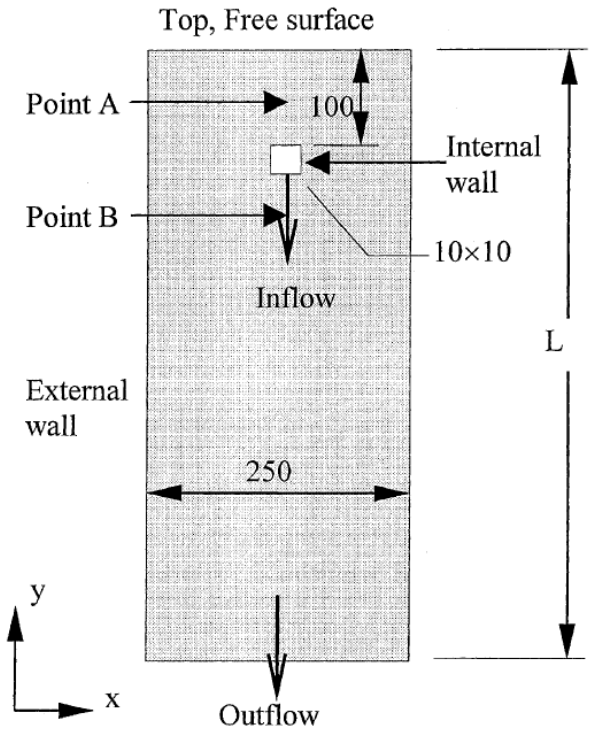


Figure 2.9 CFD geometry used in the work of Guo et al [19]. Dimensions are in mm.

A jet Reynolds number of 1.16 x 10^4 similar to the Reynolds number of the jet used in some cases of this thesis is assessed. Water was used as the working fluid in the simulations. PISO algorithm was used for the pressure correction so that the number of iterations needed for convergence is reduced. A quadratic, fully implicit backward scheme was used for temporal discretization. Time steps of 0.01s were used after being identified as sufficiently small enough to give time-step independent results. Prior to conducting simulation, the performance of three type of grids were assessed: Uniform rectangular grid, non-orthogonal grid and non-uniform rectangular grid. All the grids used quadrilateral cells. Uniform grid was found to be inappropriate as the y+ at the interior walls was different from the exterior walls. Non-orthogonal grid was also found to be unsuitable as grid independent solutions were not attainable for all the turbulence models. Finally, two non-uniform rectangular grids were developed. For the standard k-ϵ model, RNG k-ϵ model and the Reynolds Stress model a grid with y+ values in the range of 15 to 250 was constructed. For the low Reynolds number, a grid with low y+ values in the range of 1-5 was constructed. This was done because the low Reynolds number model solves up to the wall and a linear velocity distribution is assumed near the wall cells where the laminar sub-layer is present. Hence the near wall nodes should have a y+ value close to 1. Fluctuations in the velocity are monitored at point A and B. Their results were compared with experimental results using the Strouhal number for the dominant frequency identified in the velocity fluctuations at the points (A and B). The dominant frequency was estimated using the aid of a Power spectral density (PSD) plot of the velocity fluctuation at the points. From this work the key points that have to be taken are the necessity of a non-uniform quadrilateral grid in order to achieve grid independent solutions and the applicability of the three turbulence models that were assessed in the study to model jets.

Hajikandi and Mansoori [20] carried out similar work to that of Guo et al[19] on a 2D axisymmetric confined jet with back pressure to assess five turbulence models. The Five turbulence models were the standard k-ϵ model, RNG k-ϵ model, Realizable k-ϵ, standard k-ω and SST k-ω model. The SIMPLE scheme was used for the pressure-velocity coupling and simulations were carried out using a second order upwind scheme for the convective terms. A rectangular grid comprising of quadrilateral elements was utilized. Experiments were also conducted on a similar model. Several comparisons including the spread of the jet and center line velocity distribution obtained using CFD were made with experimental results. It was

concluded that the RNG k-ϵ model had outperformed all of the other models that were assessed in terms of accuracy and agreement with experimental results. It was also stated the RNG k-ϵ model needed more computational effort per iteration compared to other models and needed more iterations to convergence due to the strong non-linear terms existing in the transport equations.

Based on the work reviewed in this section conclusions about the grid size, the appropriate turbulence model, which seems to be the RNG k-ϵ and the multiphase VOF model which is applicable to the modelling of a liquid jet exiting into a gaseous environment are made. The findings are used to choose the adopted modelling strategy presented in Table 2.1.

2.3 Turbulence modelling involving complex geometries in rotating flows.

The scoops rotate in the range of 500 rpm to 10,000rpm and create a complicated air flow due to their complex geometry. The Reynolds numbers evaluated for these rotational speeds are in the range of 57,000 to 760,000 as discussed in chapter 3, section 3.4.5. Hence a relevant turbulence model capable of modelling the air flow is essential. This section presents work of previous researchers that deal with the modelling of a turbulent flow involving a complex geometries.

Jafarzadeh et al [21] investigated the complex flow arising in a high speed centrifugal water pump rotating at 13,000rpm. Although the working fluid is water in their work, the relevancy to the work in this thesis lies in the modelling of the complex components involved in the centrifugal pump and the associated rotational speed of 13000rpm which is close to the highest rotational speed investigated in thesis. Three different turbulent models: standard k-ϵ, RNG k-ϵ and RSM models were assessed. ANSYS FLUENT was used to conduct their study.

For the analysis the segregated solver was chosen for the analysis over the coupled solver as the coupled solver is more appropriate for high compressible flows where the flow and energy equation are coupled and hence convergence can be achieved faster. They have also stated that the coupled solver requires almost 2 times more memory capacity than the segregated solver. For the pressure-velocity coupling the SIMPLE scheme was selected over the SIMPLEC scheme as it was felt that the SIMPLE scheme was more appropriate considering the complexities involved in the flow being investigated and the quality of the grid.

It is evident from the results that all the turbulence models assessed, provide acceptable results when compared with available experimental results. However, it was observed that the RNG k-ϵ and RSM models have results in closer agreement with experiments. With regards to computation they have seen that the RNG k-ϵ needs lesser memory compared to the RSM model. The RSM model requires 50-60% more computational time per iteration compared to the k-ϵ models. This is because the RSM model solves seven additional transport equations whereas the k-ϵ models (including RNG) solve only two equations. The RNG k-ϵ model takes 10-15% more computational time compared to the standard k-ϵ model due to the extra terms and functions in the transport equations.

With regards to the convergence of the models, it is stated that the standard k-ϵ is known to be slightly over diffusive in certain cases whereas the RNG k- ϵ model can handle similar situations where high rates of strain are present by reducing the turbulent viscosity. However, since diffusion has an advantage of better numerical stability, the RNG k- ϵ model is more susceptible to instability in steady state solutions. It is stated that this should not be seen as a disadvantage because this makes the model more responsive to physical instabilities such as a time-dependent turbulent vortex shedding. Based on the investigations conducted by Jafarzadeh et al, they concluded that the RNG k- ϵ model produced results that had the best agreement with experimental results. Important key points to be taken from their work include the accuracy of the RNG k-ϵ model in predicting the turbulent flow of such a complex geometry and the use of the SIMPLE segregated solver which is essential when modelling complex geometries as the one that will be modelling in this thesis.

Wei-lin et al[22] modelled the rotating cavities in aero-engine compressors using CFD. For the work in this thesis, the geometry involves a rotating cavity beneath each scoop. The Reynolds number of the rotating flow was in the range of $2x10^5$ and $5x10^5$ which is the range of the Reynolds numbers investigated in this thesis. The SIMPLE algorithm of FLUENT was utilized for the pressure-velocity coupling. The RNG k-ϵ model and the Spalart-Allmaras(SA) one equation turbulence models were used in the study and for computations a hexahedral mesh was used. Using appropriate comparisons made from literature they conclude that the RNG k-ϵ model is more appropriate to model the flow in the rotating cavities. They have also been able to visualize vortex behaviors arising in the flow.

The work done by Turner[23], Webb[24], Li and Versteeg[25], Rapley[26] and Gorla et al[27][28] demonstrated the successful use of the RNG k-ϵ model in highly turbulent multiphase flows involving gear lubrication with promising results. Their work involved rotational speeds of gears in the range of 1200rpm-13000rpm. It is also interesting to observe that work done by Li was done in 2D and some of the cases done by Rapley were also done in 2D and the results obtained show very good agreement with experimental results. Many of these cases were done using standard wall conditions. This eliminates the requirement for a very low y+ value in the near wall region and hence the overall grid size may be smaller. A key conclusion from these studies is that the RNG k-ϵ model is capable of capturing complex flows and swirls involving complex geometries (spur and bevel gears as in these studies) with adequate accuracy.

Based on the literature reviewed in this section the key points to be concluded are:

- RNG k-ϵ model is the most appropriate model when considering the accuracy, capability of modelling complex turbulent flow with complex geometries.
- The applicability of the standard wall functions when the RNG k-ϵ model in order to eliminate the necessity of a very y+ value in the regions close to the wall while producing accurate results.
- The necessity of the SIMPLE segregated solver which is essential when modelling complex geometries.
- The use of quadrilateral cells (hexahedral cells in the case of a 3D simulation) which is used by researchers in most of the relevant studies reviewed under modelling of turbulent flows using complex geometries.

2.4 Multiphase flow modelling of rotating flows

It is appropriate to look into work conducted by previous researchers in this area due to the similarity of windage effects that are induced in rotating scoops. Hence the oil jet used to deliver lubricant to scoops is exposed to high windage forces. Therefore an appropriate multiphase model for this scenario has to be chosen. Multiphase flow in scoop based lubrication systems have been modelled using CFD by previous researchers and it will be presented in section 2.6 of this chapter where past work of literature in the context of scoops will be

discussed. Literature discussed in this section will only present studies of other similar multiphase flows involving high windage such include lubrication of gears rotating at high-speeds and the flow in bearing chambers of an aero-engines.

Arisawa et al.[29] modelled the churning and windage loss (flow loss) in high speed gears. The rotational speeds of the input and output gears are 9500rpm and 9200rpm in their study. The associated Reynolds numbers of the air flow calculated using the gear radius as the characteristic length are 226,000 and 240,000 for the input and output gear respectively. The Reynolds numbers of the air flow in their study are in the range of the Reynolds numbers of the air flow investigated in this thesis. The Volume of Fluid method (VOF) was used to simulate the acceleration of oil droplets, considering the model's advantage in simulating the behavior of oil droplets. A hexahedral body fitted mesh is used for the numerical grid in the studies. FLOW-3D was used to conduct the CFD study. Since the VOF model is very dependent on the Courant–Friedrichs–Lewy (CFL) condition for the numerical stability and accuracy, a coarse mesh which allows the use of larger time-step that satisfies the CFL condition was used. This effectively reduced the computational time in comparison to a fine grid which requires a smaller time-step to satisfy the CFL condition. The use of a coarse grid is justified by stating, that it does not significantly introduce errors in the modelling of oil droplets which contribute to churning losses, as the droplets are summed up in CFD with the same velocity, compared to the realistic scenario of several droplets with different sizes but of the same velocity. This is illustrated in Figure 2.10.

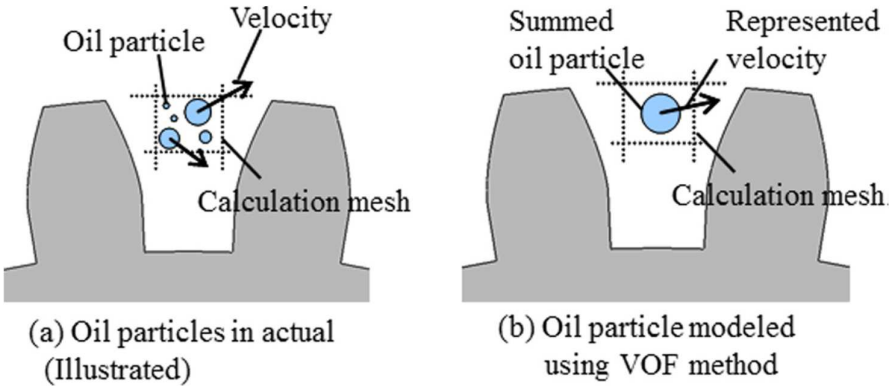


Figure 2.10 Modelling of oil droplets using the VOF model with a coarse mesh[29]

A turbulence model was not used in this study. For the solver a variable time-stepping was used so that the Courant number was kept below 0.45. The effects of gravity due to the amount of oil present after accumulation in the domain was taken into account as the gravitational effects could not be ignored any more. An experiment performed to validate the results of the CFD showed good agreement between the trend in the results of CFD and experimental investigations. Although a turbulence model was not used it was observed that the flow loss due to windage effects predicted by CFD follows a relatively same trend with experiments. They have also predicted that swirls and eddy as shown in Figure 2.11 can be expected in an actual system. Promising results from their CFD study indicate the applicability of the VOF model for flow involving Reynolds numbers close to 700,000 and hence for the work in this thesis.

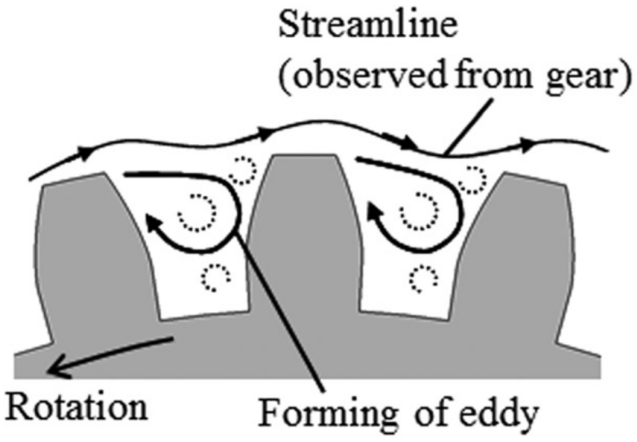


Figure 2.11 Formation of eddy from the trailing edge in a gear teeth[29]

Studies by Concli et al[30][31][32][33] involved the simulation of splashing and churning losses for gears that rotate up to speeds that correspond with Reynolds number of 150,000 for air, using the VOF model. The Reynolds numbers of air for some of the cases investigated are within the range of Reynolds numbers for the work in this thesis. A CFD study was carried out using ANSYS Fluent with no turbulence modelling. A domain comprising of hexahedral cells was used. It is stated that a tetrahedral domain is avoided due to the fact that cell skewness can be affected leading to reduced solution accuracy and convergence. The geo-reconstruct scheme was used for interface construction and the SIMPLE scheme for pressure-velocity coupling. The results of the simulations are in very good agreement with corresponding experiments. The

studies of Concli et al. show the ability of the VOF model to predict oil splashing behavior that may take place when a scoop slices the oil jet in the simulations carried out in the research work presented in this thesis.

Based on the work reviewed in this section of past researchers who have investigated flows with Reynolds numbers comparable to that being investigated in this thesis, some of the conclusions that can be drawn are:

- The Volume of Fluid (VOF) multiphase model available in ANSYS FLUENT is capable of simulating the flow of oil and air in a system with good accuracy.
- The geo-reconstruct scheme is the most appropriate scheme used by researchers for the representation of interfaces when using the VOF model
- The SIMPLE scheme for pressure-velocity coupling is used by researchers when a complex geometry such as gears are involved when studying a multiphase CFD problem.

2.5 Vortex Shedding

It was identified that vortices that were shed from the tip of scoops led to decreased capture efficiencies of scoops. This phenomena of vortex shedding is presented in Chapter 6 of this thesis. Hence relevant literature was reviewed to aid the understanding of the vortex shedding behavior from scoops in this section.

Scoops rotate around an axis that can be compared to the rotation of turbine blades in a Vertical Axis Wind Turbine (VAWT) as shown in Figure 2.12. It is evident from literature that vortex shedding is observed from the turbine blades that rotate about a vertical axis. Hence the same phenomena can be anticipated from rotating scoops around a vertical axis.

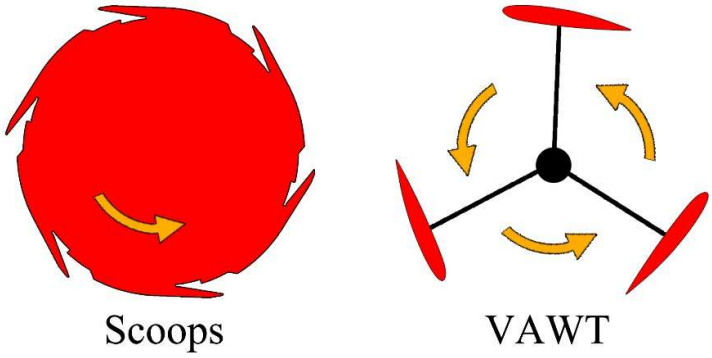


Figure 2.12 Illustration of scoops and blades of a VAWT rotating about a vertical axis.

The formation of vortices from turbine blades in a VAWT is illustrated in the thesis of Ferreira[34]. The separation of vortex from the tip of turbine blades was studied experimentally. Particle Image Velocimetry (PIV) was used to develop the phase averaged vortex structures. Figure 2.13 shows part of the results developed using PIV to elucidate the growth and separation of the vortices from the turbine blade.

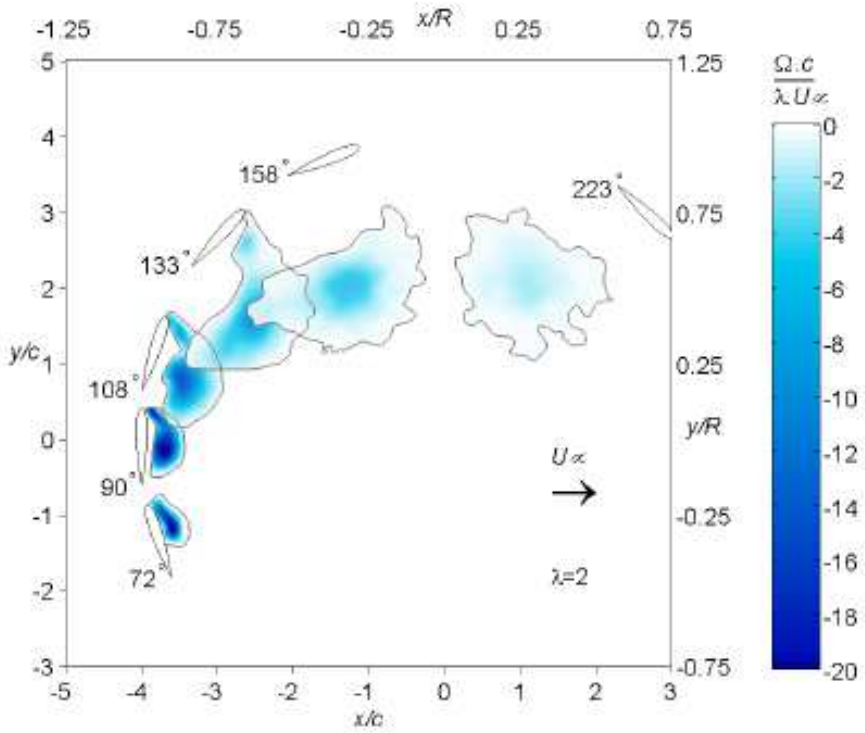


Figure 2.13 Growth of a vortex and subsequent separation of the vortex from the leading edge of the blade shown using PIV results of Ferreira[34]

It was observed that the vortex has a linear growth in terms of size from 72^{o} to around 110^{o}. The growth rates reduce thereafter and the vortex begins to separate from the tip of the leading edge. After the detachment of the vortex from the leading edge, the vortex is subjected to diffusion and its vorticity begins to diminish. The same progression of vortex shedding from the tip of a scoop is also seen in CFD results presented in Figure 6.2 in Chapter 6.

In the thesis of Mclaren numerical and experimental investigations were performed on the unsteady loading of high solidity VAWTs[35]. Simulations were conducted using NACA 0015 blade. Velocity vectors which were produced as part of the numerical investigations illustrate the direction of the velocities in the vortex arising close to the edge of the turbine blades. Figure 2.14 shows the velocity vectors produced using CFD. It was observed that the vortex exhibit a swirling motion. This also reflects on CFD results of velocity vectors visualized at the tip of scoops as shown in Figure 6.8 in Chapter 6.

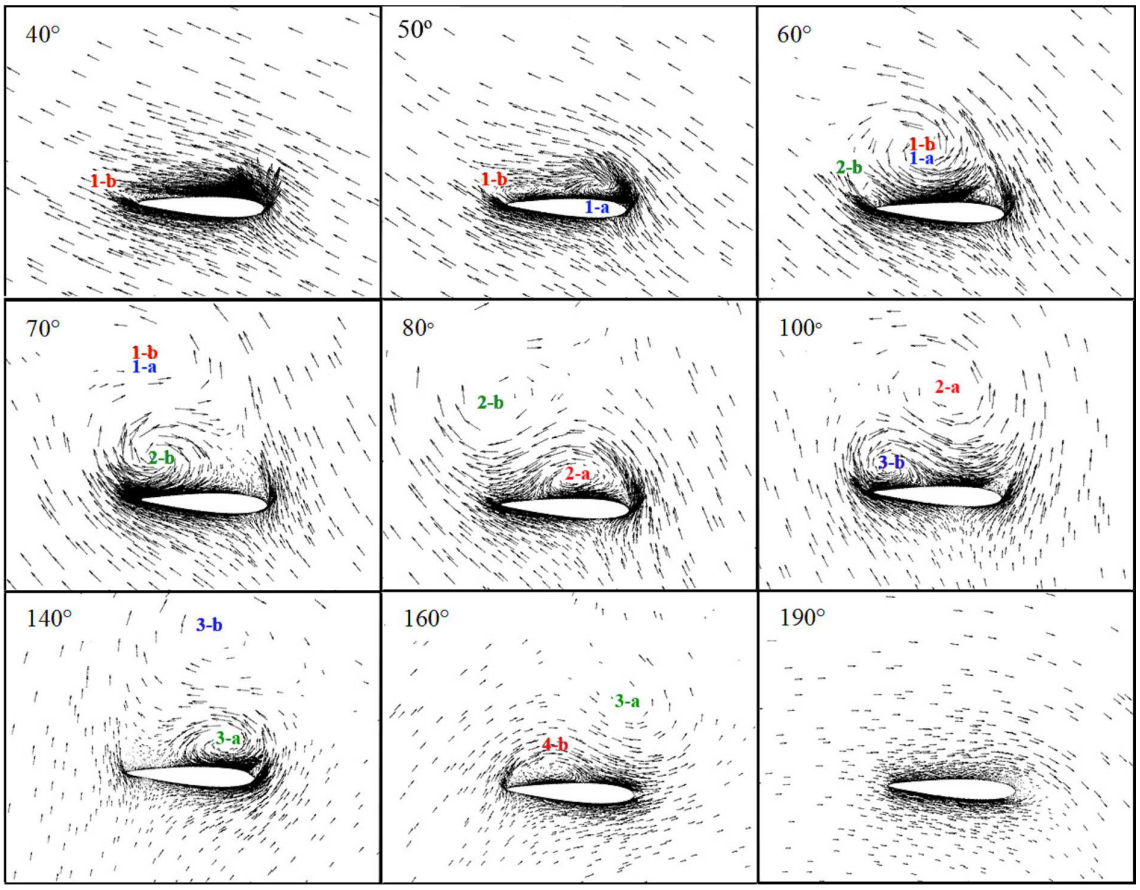


Figure 2.14 Velocity vectors produced by Mclaren using CFD in the vicinity of the turbine blades in a VAWT[35]

The CFD study conducted by Li et al. showed the formation of vortices from a static turbine blade at different pitch angles[36]. The study illustrated that the intensity of the vortices varies according to the pitch angle. In their study the employed the SST k-ω to solve the Unsteady Reynolds Averaged Navier-Stokes (URANS) equations. 2D URANS, 2.5D URANS and 2.5D LES are used to simulate the effects of turbulence. The results for various angles of attack, α, and turbulence models are shown in Figure 2.15. The study concludes that the 2D URANS turbulence model has a poor accuracy in vortex modelling and fails to predict the aerodynamics characteristics of the VAWT accurately. Negative pressure coefficients were evident in the vicinity of the vortices at higher angles of attack which essentially means that negative gauge pressures could be present in the vortices. Based on results presented in Chapter 6, from Figure 6.7 it is seen that at the tip of scoops a region of lower absolute pressure (negative total

pressure) relative to the surroundings is present and is similar to the negative pressures seen in vortices near the blades of a VAWT in the study of Li et al.

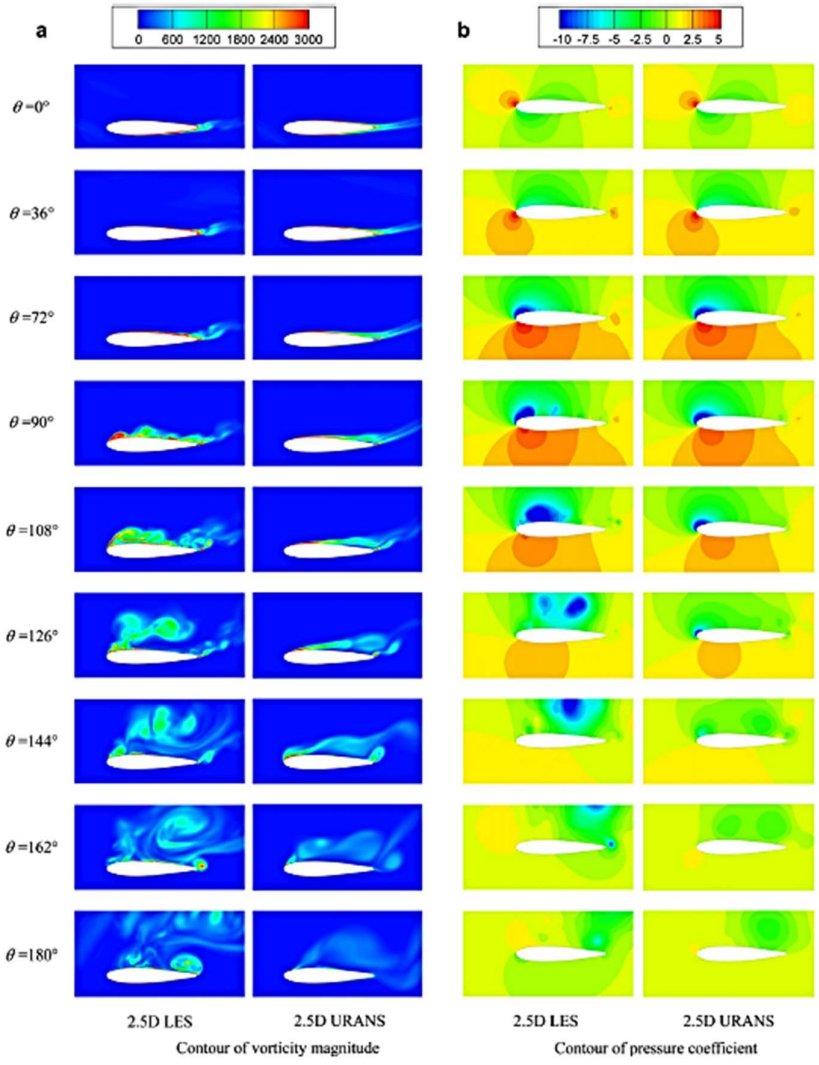


Figure 2.15 CFD results of Li et al using 2.5D URANS and 2.5 LES models on a static turbine blade[36].

Chen and Lian[37] in their study numerically analyzed the performance of a H-rotor vertical axis wind turbine in 2D. The associated flow separation and vortical flows were studied. The RNG k-ϵ model was used to account for turbulence and the SIMPLE scheme for the pressure-velocity coupling. A sliding mesh technique was used to handle the rotation of the blades in the system. The CFD was validated with available experimental results that show the applicability of the modelling strategy using the RNG k-ϵ model to predict the formation of

vortices. CFD investigations in this thesis initially commenced without knowledge of vortex shedding that affected the capture efficiency of scoops. Until the identification of vortex shedding from the tip of scoops all the investigations were carried out using the RNG k-ϵ model and hence it was convincing to learn from literature of the applicability of the RNG k-ϵ model to pursue in depth research about vortex shedding from scoops.

Two important variables in the context of vortex shedding is the frequency of vortex shedding, f and the associated Strouhal number, St given by:

$$St = \frac{fL}{U} \tag{2.1}$$

Where L is the characteristic length and U is the velocity of the free stream

As shown in the studies of Lam and Leung [38] and Sondak and Dorney [39], in order to estimate the vortex shedding frequency either the pressure or the velocity fluctuations along with the time-history at a point(s) where the vortices are being shed should be monitored. The data should then be converted into a Power Spectral Density (PSD) plot using a Fast Fourier Transform (FFT). From the PSD plots the dominant frequencies can be identified. As stated by Sondak and Dorney [39] it is very likely that there are several other peaks corresponding to blade rotation that may also emerge. In order to identify the peak corresponding to the vortex shedding frequency, the blade rotational speed should be known. When the vortex shedding frequency is estimated, the associated Strouhal number can be calculated once the characteristic length, l, and the velocity of the free stream, U, is known.

2.6 Numerical and experimental work on scoops

2.6.1 Numerical modelling of scoops.

One of the earliest work on scoops is that of Prasad et al[40] who assessed the performance of scoops using experiments and CFD. Minimal details of their experiment are mentioned in their paper. The scoop assembly comprising of 3 scoops and two jets spaced 180^o apart circumferentially is shown in Figure 2.16. The CFD domain of their study is shown with relevant boundary conditions in Figure 2.17. A structured hexahedral domain is used to

discretize the CFD domain. For CFD ANSYS FLUENT is used with the implicit-VOF model along with the k-ϵ realizable model with standard wall conditions to model turbulence. The Pressure based solver with the SIMPLE scheme was used in their study. The momentum, continuity and turbulence equations are solved using second order upwind schemes. The effects of gravity are not taken into account. The sliding mesh model was used to simulate rotating scoops. The tip of the scoops have an average speed of Mach 0.3 and jet has a Reynolds number of 13000 in average for their investigations which is in the range of the jet Reynolds number being studied in this thesis. At the inlets of the oil jet a mass flow boundary condition is used corresponding to the jet velocity required by them.

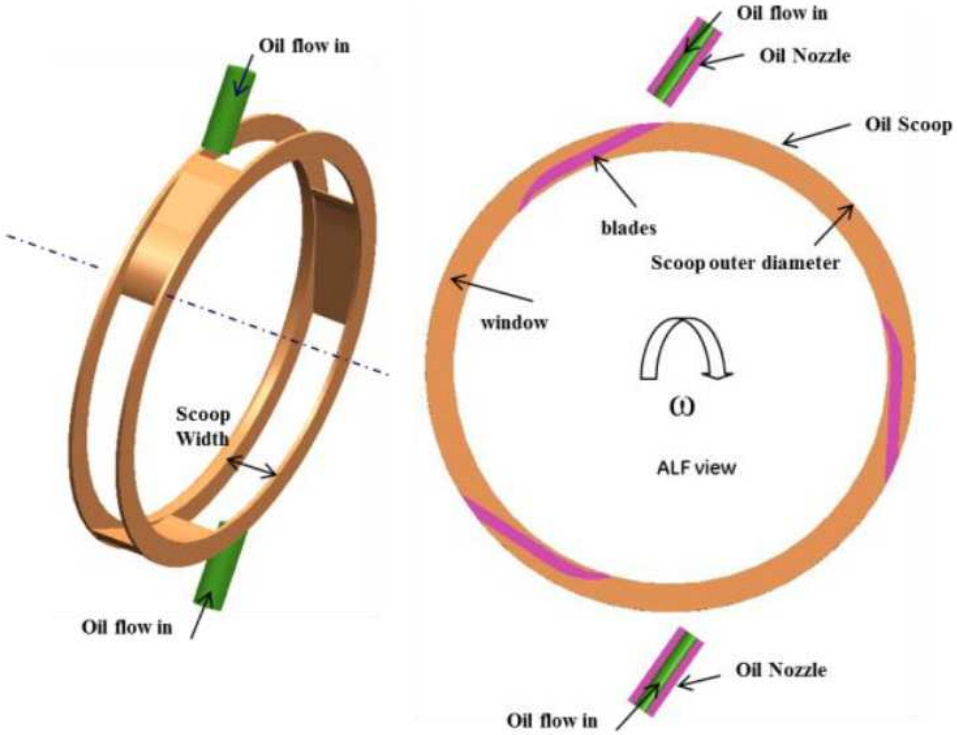


Figure 2.16 Scoop assembly setup used in the work of Prasad et al [40].

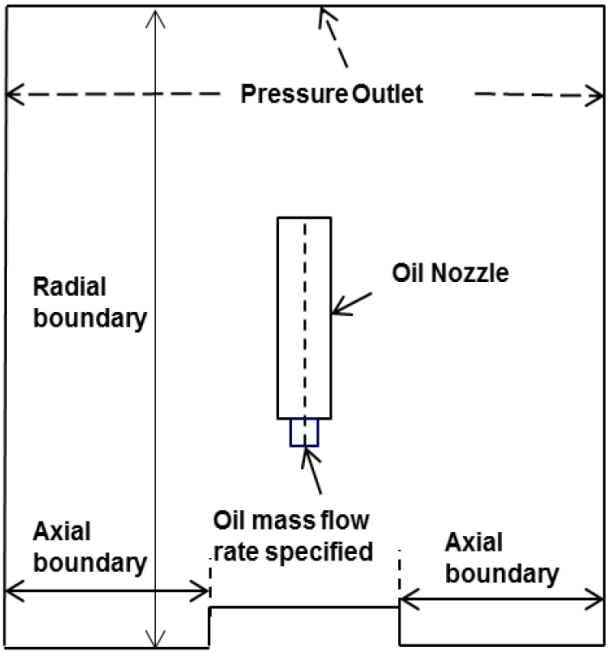


Figure 2.17 CFD domain and boundary conditions used in the work of Prasad et al [40]

From their results it is evident that the oil jet, as shown in Figure 2.18, is not resolved well. No ligaments or droplets are seen in during the slicing process of the oil jet and does not represent the actual slicing process that are seen from other experimental visualizations [5]. This problem is associated with the use of the implicit VOF model which cannot capture the splashing process of oil accurately as compared .to the explicit VOF model.

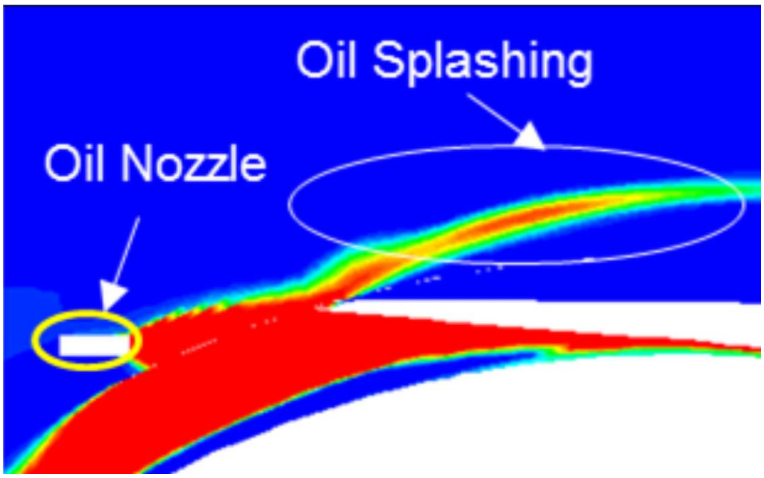


Figure 2.18 Splashing of oil when sliced by scoops using implicit VOF model[40].

The parameters that have been investigated in their study include the effect of oil flow rate, scoop width, scoop outer diameter, effect of shaft speed and effect of time step. However for each of the parameters they investigated, they have conducted simulation only at 3(4 for shaft speed) different values of the investigated parameters. One of the vital conclusions, relevant for the work in this thesis, that is drawn from their study is the existence of an optimum shaft speed for a constant jet velocity where maximum capture efficiency can be obtained. They claim that their experimental results are with 2% with CFD results for the capture efficiency of the scoops.

In the work of Korsukova et al. [41]they use CFD and Smoothed Particle Hydrodynamics(SPH) to assess the performance of a scoop geometry comprising of 6 scoops. Simulations are done both in 2D and 3D. The VOF model with the geo-reconstruct scheme is used to track the interface between the phases and SST k-ω is employed to model turbulence. The CSF model is used to model the effects of surface tension. A hexahedral mesh is created using ANSYS ICEM for their studies in 3D as shown in Figure 2.19. The hexahedral mesh was created from the extrusion of the grid comprising of quadrilateral elements that was used for 2D simulations. The grid used in 2D consisted of 400,000 elements and the 3D grid had 5.6 million elements.

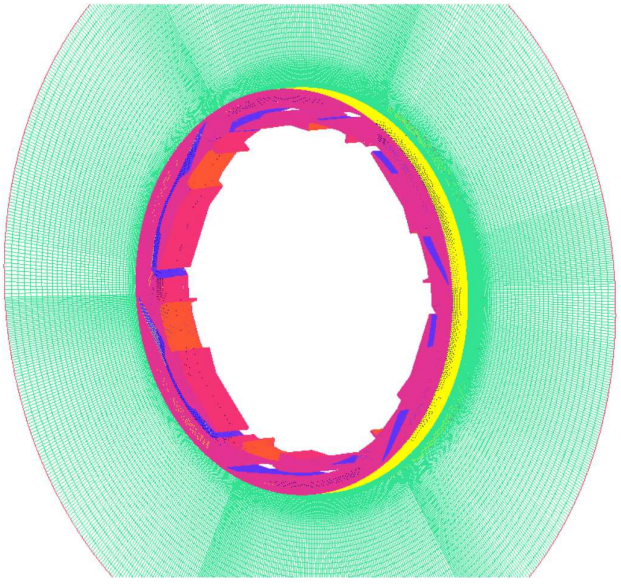


Figure 2.19 Hexahedral mesh used in the CFD study of Korsukova et al [41].

In their study they have assessed the performance of scoops at the shaft speeds between 0 to 10000rpm.

The slicing process of the oil in their CFD results is somewhat similar to that observed in the experimental visualizations although the size of the resulting droplets from slicing are bigger compared to what is seen in experiments[5]. Figure 2.20 shows the oil droplets using the volume fraction contours that are formed as a result of the scoops slicing the oil jet. The bigger droplets compared to that of experiments is associated with the coarse element size used in the vicinity of the oil jet and the tip of the scoops.

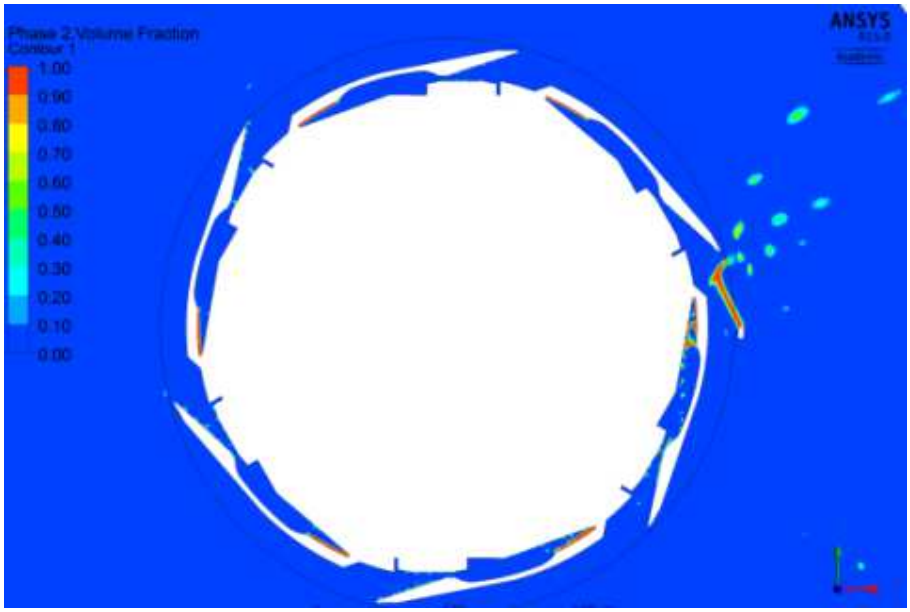


Figure 2.20 Volume fraction contours of oil as observed in the work of Korsukova et al. showing the formation of droplets as a result of the slicing process of the oil jet[41]

Two important conclusions that they draw about the capturing process of oil by the scoops are:

- Following the slicing process of the oil jet by a scoop a plume is formed at the tip of the jet that lowers the capture efficiency for the proceeding scoop.
- Oil that is captured by the scoops initially sticks to the walls of the scoop pockets, but as the scoops rotate the oil, is centrifuged outwards leading to decrease the capture efficiency.

These conclusions made from their study are used to support CFD results presented in this thesis in Chapters 4, 5 and 6. Korsukova et al. have produced results that are within 15% from experimental results.

In studies involving 2D CFD investigations carried out by Simmons et al.[42], the same numerical methodology as in [41] was applied. In this study the performance of tandem oil jets at four different angles was assessed. It was observed that the steeper jet gave a better capture efficiency for the scoops. On investigating the impact of a pulsed oil jet on the oil capture efficiency, it was observed that the oil capture efficiency improved. However, the study stated that despite the evident benefits of using a pulsed oil jet, the complications of implementing such a configuration practically outweigh the benefits.

Yaguo et al. [43] also conducted CFD studies using the numerical methodology used in [41]. A hexahedral grid was selected for the study. The effect of shaft speed and oil jet flow rate for 4 different values was investigated. A conclusion relevant from their study for this thesis in the high shaft speed range, the capture efficiency of the scoops decreased as the shaft speed increased for a constant jet velocity. A similar conclusion is made in Chapter 4 of this thesis where the effect of capture efficiency is investigated for a constant jet velocity. In chapter 4 an insight into factors affecting the capture efficiency are highlighted, which haven't been identified in literature.

2.6.2 Experimental investigation of scoop devices

In-depth experimental studies were carried out by Paloma et al [5] at the Gas Turbine Transmission Research Centre(G2TRC) on a scoop geometry that is simplified for the work in this thesis. The CFD results produced in this thesis will be validated against experimental results produced by them. The parameters investigated by them include jet to scoop velocity ratio, scoop constriction gap (a dimension that will be discussed later in Chapter 5 of in this thesis), shaft speed and jet angle. Detailed information of the geometry and experimental setup are given in their paper which is presented in Appendix section 8.3. This section will highlight some of their key results which are beneficial for the work in this thesis. They are as follows:

- For a fixed jet velocity, there exists an optimum shaft speed at which maximum capture efficiency is obtained. For the geometrical setup and conditions they investigated to

assess the effect of shaft speed on the capture efficiency, they have identified that the velocity ratio, *VR*, at which maximum capture efficiency is obtained is 0.44. Velocity ratio, *VR*, is ratio of the velocity of the scoop tip to the velocity of the oil jet.

- For a constant velocity ratio, *VR,* that significant higher than the velocity ratio at which optimum efficiency is obtained, it is found that the most radial jet which makes a low angle with respect to the vertical axis give the highest capture efficiency. There is an improvement of 11% in the capture efficiency between the steepest (larger angle to the vertical than a radial jet) and the most radial jet.
- At a constant shaft speed, jet velocity and a jet angle, it is observed that a variation in the constriction gap doesn't give a significant change in the capture efficiency. However the capture efficiencies when using a wider gap are slightly higher when compared to using a small gap.
- The pluming(distortion of the jet tip) of the oil jet is observed following the slicing of a scoop using high speed visualizations and also tests conducted on a wedge like structures that have similar geometry to the tip of a scoops.

Observations and results found experimentally from the work of Paloma et al will be used to validate and support CFD results and conclusions from CFD presented in this thesis. Quantifying and assessing oil losses experimentally is quite difficult because of limited amount of visual access that is available and also the complexity of installing visualization equipment. For the high shaft speeds investigated in the experimental study it is noted that the quality of movies acquired from camera and visualizations done with a borescope are obscured due to excessive splashing of oil. This is where CFD studies have value and fill in the gaps that are associated with experimental investigations.

2.7 CFD modelling strategy recommendations based on literature review

With the aid of the foregoing literature review on the various aspects concerning the modelling of scoops, a modelling strategy was chosen after careful consideration. It is also to be noted that several case studies were conducted during the course of the First year of the PhD in order to assess the performance of some methods mentioned in literature. For example, the performance of the Eulerian model to model jets was assessed. Prior to conducting simulation on the actual scoop geometry selected for this Thesis, dimensionally scaled down 2D and 3D

scoop geometries were also assessed, with a low grid size that could be run on a workstation with 4 CPU cores with ease. These findings have been presented in the first and second year progress [44][45] and also aided in choosing the adopted modelling strategy for the work in this PhD. The chosen modelling strategy is shown in Table 2.1.

Table 2.1 Adopted modelling strategy

	Chosen method/model
Domain	A 2D domain is chosen. The justification for a 2D domain over a 3D domain is: • Decreased computational costs • Numerous studies have shown and proved that it is applicable to the aspects that were reviewed in the context of scoops modelling. Many of the CFD studies in 2D have been validated with experimental results and have shown promising results[15][16][17][18] [19] [25] [26] [46] [36] [37][41] [42]. All these studies give a lot of confidence to choose a 2D domain over a 3D one. • Several different geometries and configurations can be assessed during the course of the PhD. With a 3D domain, only few geometries can be assessed due to the increased computational time for simulations and costs.
Multiphase Model	It is very evident from all the aspects that were investigated that the most applicable multiphase model for the modelling is the explicit VOF model. The Geometric reconstruction scheme will be used to construct the interface between the phases. Relevant and validated studies in the aspects reviewed for scoops modelling support this modelling choice[12] [14] [15] [47] [25][29] [48] [30][31][32][33] [46] [40] [41] [42] [43]. Another potential model is the Eulerian model. This model was not chosen despite its increased accuracy over the VOF because of the computational costs involved. The computational efforts required using The Eulerian model are two times higher. This suggests why only limited literature is available with the use of the Eulerian model in the aspects that were reviewed for the modelling of scoops.

Turbulence modelling	The RNG k-ϵ model is chosen to model the effect of turbulence. This is because of the following advantages: ability to model rotational flows and swirls with adequate accuracy, modelling of jets, rotating cavities, complicated geometries and multiphase flows[20] [11] [49] [22] [23] [24] [25] [26] [27][28] [48]. It also requires less computational time compared to other models which solve more equations[21]. The RNG k-ϵ model can be used with a coarser grid in comparison with k-ω models. This is because the RNG k-ϵ with standard wall functions only needs y+ values in the range of 30-60 near the wall, whereas the k-ω model requires y+ values of less than 1. Turbulence intensity and viscosity ratio values can be kept at default values of the solver as seen from researchers who successfully used the default values in the absence of experimental data for those values. Another potential model that is applicable in the modelling of scoops with similar advantages as the RNG k-ϵ is the SST k-ω. This was not chosen because of the increased computational efforts required and also the necessity of a finer grid.
Surface tension	Continuum Surface Force (CSF) model by Brackbill et al[50] will be used to model the surface tension effects between the air and oil phase. It is the most widely and well validated model used in the studies that were reviewed for multiphase modelling[12][16][17][41] [42] [43].

Numerical Grid	1. Element type- A quadrilateral type grid is chosen to model the domain: • Almost all the fluid flow problems reviewed in literature with validated results use either a quadrilateral (for 2D) or hexahedral (unstructured or structured for 3D). • Requires lesser number of cells compared to when using a triangular(tri) cells • Accuracy and the quality of the grid is far better using the quadrilateral grid. Convergence of solutions are also better using a quadrilateral grid[30][31][32][33]. 2. Element sizing- When the VOF multiphase model is used, the dependence of the solution depends heavily on the grid sizing. From literature it is quite evident that a fine mesh is needed to accurately resolve the oil droplet break up process in jets. Using the guidelines investigated by researchers[12] [14] [15] [47] [16][17] [48], the element size used in the grid will be below $0.1d_{inlet}$, where d_{inlet} is the diameter of the inlet. In-depth grid dependency studies will also be done for cell sizes below $0.1d_{inlet}$ to achieve grid independent results. The grid will be refined to achieve y+ values in the range of 30-60 near the walls, which is essential for the turbulence model to be applicable.
Modelling of rotating components	The sliding mesh model will be used, based on the work and well validated studies done by researchers, involving rotating components and complicated geometries [21] [37] [40] [41] [43]. The mesh will be conformal at the interface in order to reduce interpolation errors between the zones and help to achieve quicker solution convergence as indicated by Castelli et al.[51].
Solver	Time Steps will be chosen in such a way that they satisfy the CFL condition. This is to ensure numerical stability and accuracy. First order explicit time-stepping will be used.[40]. SIMPLE scheme will be used for the pressure-velocity coupling considering its use in most of the studies for the various aspects that were reviewed[21] [52] [53][54] [22] [30][31][32][33] [46]. Furthermore it is also relevant to use the SIMPLE scheme when the flow is complex [21]. Under-relaxation factors will be kept at default values of the solver.

2.8 Summary of literature review

This chapter presents the relevant work done by previous researcher with regards to the aspects in the context of modelling scoop based lubrication devices. The aspects include: modelling of a jet, modeling of turbulence in rotating flows, modelling of multiphase flows in a rotating flow and vortex shedding. A number of models, techniques and observations from the work of past researchers were drawn from the literature review that will facilitate and help to validate the research work carried out in this thesis. Conclusions and observations from the experimental work conducted on the geometry being investigated in this thesis is also presented in this chapter. Detailed information about the experimental setup and test matrix are presented in Appendix section 8.3. A modelling strategy is adopted based on the findings of previous researchers and presented in Table 2.1. CFD work in this thesis will be based on the adopted modelling strategy presented in the Table 2.1.

3 CFD Methodology

3.1 Introduction

This chapter outlines the methodology used for the Computational Fluid Dynamics (CFD) work in this thesis. In CFD there are 3 major elements:

1) Pre-Processing- This step involves the creating/simplification of the geometry and generating a numerical grid that will be used by the CFD solver. These two steps are done using a CAD software (PTC Creo and ANSYS Design modelling is used here) and a mesh generator (ANSYS Meshing is used here).
2) Solving- Governing equations of fluid flow is solved on the numerical grid with the aid of a solver. ANSYS FLUENT is used in this thesis.
3) Post-Processing- The data acquired from the solver has to be analysed using a suitable post-processor. FLUENT, CFD-Post, MATLAB, Movie maker and MS Excel are used for post-processing of data.

3.2 Geometry development

The CAD geometry of the scoops was extracted from the geometry that was assessed experimentally[5]. The geometry was simplified in 3D using PTC Creo by removing bolts, holes and other unnecessary features. The fluid domain from the CAD geometry was extracted using ANSYS Design modeler with the Boolean tool. The extracted fluid domain is shown in Figure 3.1. A zone that represented the domain in which the oil jets (jets cannot be seen in the image as it is inside the zone) were housed was added in addition to the fluid domain of the scoops.

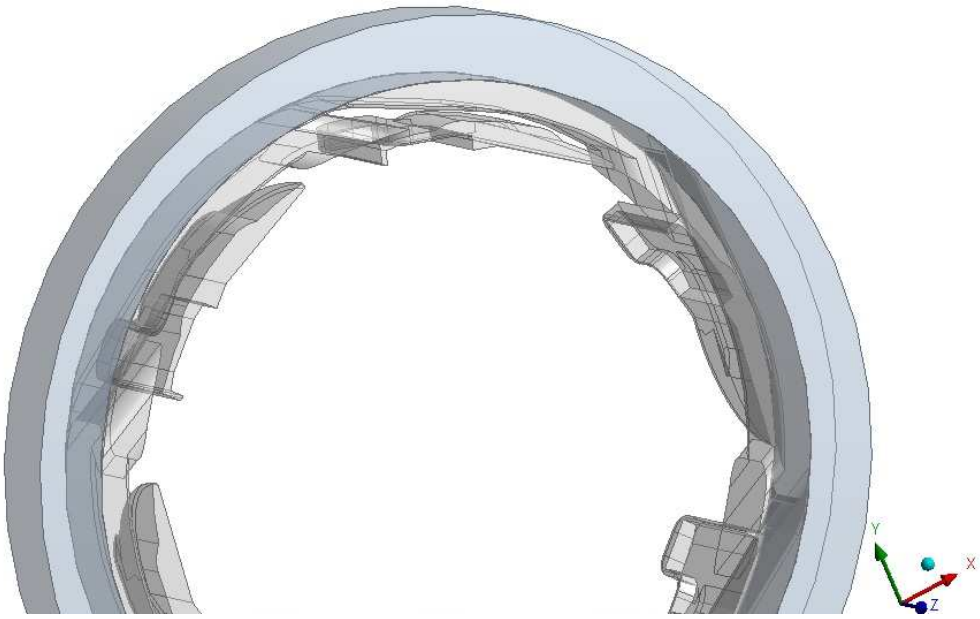


Figure 3.1 Geometry of fluid flow domain in 3D

The 3D geometry of the scoops was then simplified to a 2D geometry using ANSYS design modeler as shown in Figure 3.2, with 3 zones in the fluid domain. As justified in Table 2.1, the main reasons behind choosing a 2D geometry is to reduce computational costs and also maximize the number of cases that can be investigated during the course of the PhD. Boundaries, Boundary conditions and additional constraints imposed in the domain will be shown and discussed in Chapter 4.

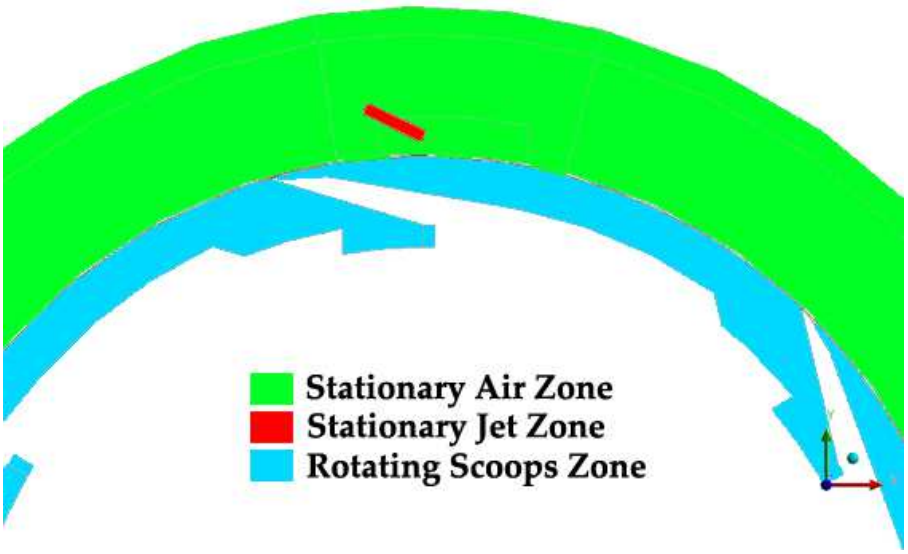


Figure 3.2 2D CFD domain comprising of 3 zones, simplified from a 3D domain

3.3 Numerical Grid

The 2D geometry created for CFD simulation is discretized using ANSYS meshing. Cell sizes below 0.35mm were used to create the grids as indicated from literature. In the near wall regions cell sizing were adopted to suit the requirement of the turbulence model that is used. This was done by imposing sizing functions at the edges of the walls in the domain.

Several grids were created in order to assess the dependency of the solution on the grid. A grid that is developed using a core cell sizing of 0.26mm is shown in Figure 3.3. All the grids used have been generated while adhering to the quality requirements for a grid that should be used in CFD. The main parameters that are used to assess the quality of a grid are aspect ratio and orthogonal quality.

In depth details about the quality of the grid and grid independence will be discussed in the Chapter 4 after the introduction of other concepts and variables that will be used in grid independence studies.

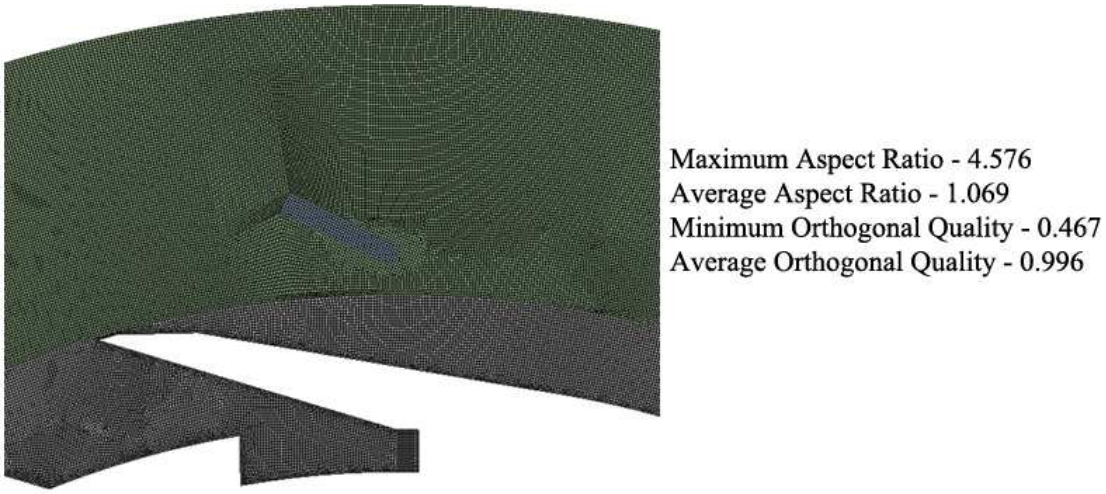


Figure 3.3 Numerical Grid with 401,283 cells using a core cell size of 0.26mm and associated mesh metrics

3.4 Numerical Modelling

3.4.1 Governing Equations

Fluid flow can be represented using the set of mathematical equations known as the Navier-Stokes (NS) equations. For a Cartesian grid the equations can be written as follows:

$$\frac{\partial \rho u_i}{\partial t} + \frac{\partial \rho u_i u_j}{\partial x_j} = -\frac{\partial P}{\partial x_i} + \frac{\partial}{\partial x_j}\left(\mu\left(\frac{\partial u_i}{\partial x_j} + \frac{\partial u_j}{\partial x_i}\right)\right) + \rho g_i + F_i + S_m \quad \textbf{(3.1)}$$

F_i and S_m represent external forces and source terms respectively, g is the acceleration due to free-fall.

The momentum equations are used to describe the variation of momentum with time and space. However it should be noted that the equation is not mass conservative and hence the continuity equation has to be taken into account and is given by:

$$\frac{\partial \rho}{\partial t} + \frac{\partial \rho u_i}{\partial x_i} = 0 \quad \textbf{(3.2)}$$

The Navier-Stokes equations cannot be solved analytically and hence the equations have to be solved numerically at discrete points in the flow domain which is often represented by a numerical grid after the discretization process of the geometry. The numerical approach of solving these equations is known as Computational Fluid Dynamics (CFD).

In this thesis the commercial CFD solver ANSYS FLUENT is utilized to solve the numerical equations. FLUENT uses a finite-volume method by using the numerical grid which is divided into cells and finite volumes. The NS equations are integrated over the cells and volumes which result in a series of equations that are linearized and solved algebraically with the aid of a solver. There are two types of solvers available in FLUENT: a pressure based solver and a density based solver. The solvers are discussed in section 3.4.4 of this chapter.

3.4.2 Multiphase Modelling

3.4.2.1 Volume of Fluid (VOF)

The two phases (air and oil) in the flow have been modelled using the Volume of fluid (VOF) model which solves the continuity equation for each of the phases. Air is chosen as the primary phase (phase p) and oil as the secondary phase (phase q). The continuity equation for the VOF model solves the volume fraction of the oil phase using the equation:

$$\frac{1}{\rho_{oil}}\left(\frac{\partial}{\partial t}(\alpha_{oil}\rho_{oil}) + \nabla.(\alpha_{oil}\rho_{oil}\vec{u})\right) = S_{\alpha_{oil}} + \sum_{p=1}^{n}(\dot{m}_{pq} - \dot{m}_{qp}) \quad \textbf{(3.3)}$$

$\dot{m}_{pq} - \dot{m}_{qp}$ represents the mass exchange between the phases when there is evaporation or condensation. However in this thesis phase changes are not considered and hence $\dot{m}_{pq} - \dot{m}_{qp} = 0$. In order to calculate the volume fraction of the p phase the following equation is used.

$$\alpha_{air} = 1 - \alpha_{oil} \quad \textbf{(3.4)}$$

The effective material property of the mixture, ψ_{mixture}, is calculated using:

$$\psi_{mixture} = \sum_{i=1}^{2}\psi_i\alpha_i \quad \textbf{(3.5)}$$

For example the density of the mixture, $\rho_{mixture}$ and viscosity of the mixture, $\mu_{mixture}$ are calculated as follows:

$$\rho_{mixture} = (1 - \alpha_{air})\rho_{oil} + \alpha_{air}\rho_{air} \quad \textbf{(3.6)}$$

$$\mu_{mixture} = (1 - \alpha_{air})\mu_{oil} + \alpha_{air}\mu_{air} \quad \textbf{(3.7)}$$

3.4.2.2 Interface interpolation

There are four schemes available in ANSYS FLUENT in order to formulate the face fluxes when using the VOF model. They are:

1. The Geometric Reconstruction Scheme
2. Modified High Resolution Interface Capturing (HRIC) scheme
3. Compressive Scheme
4. The Compressive Interface Capturing Scheme for Arbitrary Meshes (CICSAM)

The method chosen for the work in this thesis is the geometric reconstruction scheme. This method is chosen based on recommendation by ANSYS FLUENT theory guide as it offers the highest accuracy compared to other schemes[55]. It has also been used in previous work concerning modelling of multiphase flow between oil and air[48]. The scheme utilizes a linear piecewise approach. The approach assumes that the interface in a cell between the air and oil phases has a linear slope. Hence a linear shape in the cell is used for the calculation of advection of fluid through the cell faces. The steps involved in the geometric reconstruction scheme are as follows:

1. Using the volume fraction and its derivatives, the position of the linear interface is constructed.
2. The quantity of advecting fluid is calculated using the linear interface that was calculated and the components of the velocity(normal and tangential)
3. The volume fraction in each cell is calculated using the balance of fluxes calculated in the previous step.

3.4.2.3 Surface Tension Modelling

The continuum surface force(CSF) model proposed by Brackbill et.al[50] is used to model the surface tension between the air and oil phases. Surface tension is modelled in terms of the pressure jump across the surface. The volume force as a result of this is added into the momentum equation as a source term.

The volume force for surface tension calculated using the CSF model can be written as follows:

$$F_{vol} = \sigma_{air_oil}\left(\frac{\rho_{mixture} y_{air} \nabla \alpha_{air}}{0.5(\rho_{air} + \rho_{oil})}\right) \quad \textbf{(3.8)}$$

Where, $\sigma_{air_oil} = 0.031 N/m$ and y_{air} is the curvature from the surface normal.

Although surface tension is modelled in this thesis for improved accuracy, it should be noted that the Weber number (ratio between inertial force and surface tension force) for the jet is in the range of 50 to 4000 which is shows that the effects of surface tension are insignificant. Hence the discrepancies in modelling the surface tension in a 2D and 3D domain are negligible.

3.4.3 Discretization

3.4.3.1 Spatial Discretization

The NS equations have to be integrated over a control volume (cells). Following integration the equations are discretized. The unsteady conservation equation for transport of a variable quantity, ϕ, that is integrated over a control volume, V, is given by:

$$\int_V \frac{\partial \rho \phi}{\partial t}.dV + \oint \rho\, \phi \vec{u}.d\vec{A} = \oint \Gamma_\phi\, \nabla \phi d\vec{A} + \int_V S_\phi\, dV \quad \textbf{(3.9)}$$

The discretized equations can be written as:

$$\frac{\partial \rho \phi}{\partial t} V + \sum_{f}^{N_{faces}} \rho_f \vec{u}_f \phi_f . \vec{A}_f = \sum_{f}^{N_{faces}} \Gamma_\phi \nabla \phi_f . \vec{A}_f + S_\phi V \quad \textbf{(3.10)}$$

In general the discretized equation are non-linear and can be linearized to solve for ϕ a particular cell, p. The linear equations can be expressed as:

$$a_p \phi = \sum_{ab} a_{nb} \phi_{nb} + b \quad \textbf{(3.11)}$$

Where, a_p is the coefficient of the variable in the cell p, a_{nb} is the coefficient for a neighboring cell to cell p and b is the constant corresponding to any source terms that are introduced.

Linear algebraic equations are written for each cell in the numerical grid which eventually results in a set of algebraic equations for which a matrix of coefficients can be written. FLUENT solves these equations using a Gauss-Seidel linear equation solver and an algebraic multigrid (AMG) method. The values of the variable quantities are stored in the center of cells. In order to calculate the values at the faces an approximation must be used. There are 4 different types of approximations that are available to use in FLUENT: First order upwind, Second Order Upwind, power law and Quadratic Upwind Interpolation for Convective Kinetics (QUICK). The work in the thesis uses Second Order Upwind for spatial discretization of most of the variables. This was chosen after considering work that was done in the past for similar applications[41] with results that were produced with sufficient accuracy. Power law and QUICK schemes are higher order approximations and were not used in order to minimize computational resources required for simulations.

3.4.3.2 Temporal Discretization

Following literature review the explicit VOF model is chosen to simulate the multiphase flow of air and oil. When using the explicit VOF scheme volume fraction values from both the current and the previous time-step is required.

The interpolation of the values from both the time steps is as follows

$$\frac{{\alpha_{oil}}^{n+1}\rho_{oil}{}^{n+1} - {\alpha_{oil}}^{n}\rho_{oil}{}^{n}}{\rho_{oil}} + \sum_{f} \rho_{oil}{u_f}^{n}\,{\alpha_{oil,f}}^{n} = \left(\sum_{p=1}^{n}(\dot{m}_{pq} - \dot{m}_{qp}) + S_{\alpha_{oil}}\right)V \qquad \textbf{(3.12)}$$

Where n+1 is the current time step and n is the previous time step.

When using the explicit VOF model the numerical stability is subjected to the Courant Friedrichs Lew condition(CFL)[56].

The condition states that the time step, t, is subjected to the following constraint.

$$t \leq \frac{CFL.\,h_{min}}{u_{max}} \qquad \textbf{(3.13)}$$

Where h_{min} is the smallest cell size in the domain, u_{max} is the highest velocity in the domain and CFL is the Courant number. It is good practice to keep the courant number below 1 to minimize errors in the solution[57]. In this thesis for almost all the cases investigated, the Courant number has been kept lower than 1 (or close to 1 if above 1) throughout the whole simulation. It is not possible to keep the courant number always lower than 1, as occasionally the velocity in some cells (particularly very small cells) may increase above the predicted maximum velocity in the domain.

3.4.4 Pressure-Velocity Coupling

There are two solvers available to use in ANSYS FLUENT. They are:

1. Pressure based solver
2. Density based solver

The density based solver is not chosen because:

- It is only appropriate when the flow is considered as compressible. The flow investigated in this thesis is not in the regime where compressibility effects have to be taken into account.
- The multiphase model that is used in this thesis restricts the use of the density based solver in FLUENT.

Hence, the pressure based solver is utilized in this thesis to solve the governing equations (continuity and momentum) which are in the linear form as shown in equation **(3.11)**. The pressure-based solver can be used either with a segregated algorithm or a coupled algorithm. The algorithms for the different solvers are shown in Figure 3.4.

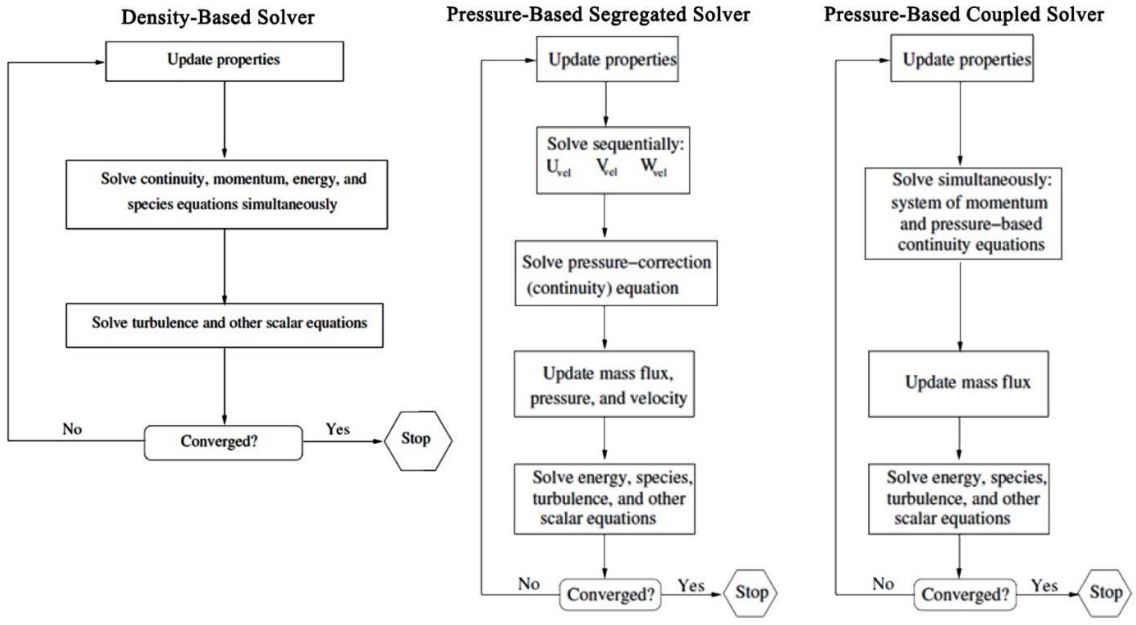


Figure 3.4 Algorithm for CFD solvers[55].

There are four types of pressure-based algorithms available in FLUENT and these are categorized as follows:

1. Segregated algorithms:
    - Semi-Implicit Method for Pressure-Linked Equations(SIMPLE)
    - Semi-Implicit Method for Pressure-Linked Equations Consistent(SIMPLEC)
    - Pressure-Implicit with Splitting of Operators(PISO)
2. Coupled algorithm- Coupled

For this thesis the Semi-Implicit Method for Pressure-Linked Equations (SIMPLE) segregated algorithm will be used. This is chosen based on literature review as explained in Table 2.1.

When using the segregated solver, an initial pressure is guessed based on the previous iteration's values. When the simulation is started initially, the values stated by the user are used (this process of the user stating values is called initialization of the variables). The pressure is used to calculate the velocity. However the velocity calculated in this step does not necessarily satisfy the continuity equation. Hence a pressure correction is essential to calculate an updated pressure field and then correct the velocity field such that it satisfies the continuity equation.

This correction of pressure is usually done with the use of an under-relaxation factor (URF). The corrected pressure, P can be written as follows:

$$P = P^* + URF.P' \tag{3.14}$$

Where, P^* is the initial guess, P' is the correction to the pressure and URF is the under-relaxation factor which is between 0 and 1. The value of the under-relaxation factors in FLUENT can be changed by the user. URF plays a role in increasing the numerical stability by preventing a massive change in the value of a variable between two consecutive iterations. However it should be noted that when URF values are reduced with the intention of increasing numerical stability, the time taken for the solution to achieve convergence in the residuals (residuals will be highlighted later on in the chapter) will take longer. Under relaxation values are not changed and will be kept at default values of FLUENT for this thesis.

3.4.5 Turbulence

Turbulence in fluid dynamics is the nature of a flow field to fluctuate in a stochastic manner. In order to model the flow field while considering the effects of turbulence, the flow field, for example velocity, can be represented by $u(t) = u + u'(t)$.

When the fluctuating terms are taken in account in the flow equation, the mathematical mean of the NS equations change into a form known as the Reynolds Average Navier-Stokes (RANS) equations. They can be expressed as follows:

$$\frac{\partial \rho}{\partial t} + \frac{\partial \rho u_i}{\partial x_i} = 0 \tag{3.15}$$

$$\frac{\partial \rho u_i}{\partial t} + \frac{\partial \rho u_i u_j}{\partial x_j} = -\frac{\partial P}{\partial x_i} + \frac{\partial}{\partial x_j}\left(\mu \frac{\partial u_i}{\partial x_j} - \rho \overline{u_\iota' u_j'}\right) + \rho g_i + F_i + S_m \tag{3.16}$$

The terms $\frac{\partial}{\partial x_j}(-\rho \overline{u_\iota' u_j'})$ on the right hand side of equation **(3.16)** are new unknowns and are called the Reynolds stresses. The extra unknowns that have been introduced into the NS equations have to be solved using a turbulence model. There are number of different turbulence models that have been developed over the recent decades. The Reynolds Stress Model (RSM) solves all the unknowns that have been introduced alongside an additional equation that solves the kinetic energy dissipation rate, ϵ. Due to the 7 additional equations that have to be solved, the computational costs involved in using the RSM model is significantly higher compared to using two or four equation turbulence models. It is practical to choose a turbulence model that solves lesser number of equations and hence requires less computational effort as well as predicts turbulence with sufficient accuracy. In order to choose the correct turbulence model, a literature review was conducted on the available models and their applicability to the work being presented in the thesis. Potential models included the standard k-ϵ, Realisable k-ϵ, RNG k-ϵ, standard k-ω and the SST k-ω. With reference to Table 2.1 it was identified that the RNG k-ϵ model was the most appropriate model to be used for the work in this thesis.

It is important to consider turbulence for the work done in this PhD due to the Reynolds number associated with the flow that characterizes the flow in this work in the turbulent regime. The Reynolds number for the jet, Re_{jet} and air, Re_{air} are given by:

$$Re_{jet} = \frac{\rho_{oil} V_{jet} d_{nozzle}}{\mu_{oil}} \quad \textbf{(3.17)}$$

$$Re_{air} = \frac{\rho_{air} V_{tip} R}{\mu_{air}} \quad \textbf{(3.18)}$$

Where, ρ_{oil} and ρ_{air} are the densities of oil and air respectively, V_{jet} is the velocity of the oil jet at the exit, V_{tip} is the velocity at the tip of a scoop, R is radius of the scoop, μ_{oil} and μ_{air} are the dynamic viscosities of oil and air respectively and d_{nozzle} is the diameter of the jet nozzle. It is calculated that the Reynolds number of the jet is in the range of 1000 to 17000 and the air is in the range of 57,000 to 760,000 for the tests that were carried out experimentally. and will be used for validation in CFD. For all the tests carried out, it was found that the Reynolds numbers associated with the air flow was in the turbulent regime (Re>4000). Hence the use of a turbulence model was essential.

The turbulence model that will be used in this thesis is a two equation model. It is developed on the assumption of the Boussinesq hypothesis which will be introduced before describing about the model.

3.4.5.1 Boussinesq hypothesis

The Boussinesq hypothesis states that the Reynolds stresses are proportional to the mean rates of deformation (strain)[58]. The assumption of the hypothesis is that turbulence is isotropic. Although this assumption may not be true always, for most industrial problems the reduction in accuracy from this assumption is outweighed by the reduction in computational costs by implementing the assumption[24].

The hypothesis can be written as follows:

$$-\rho\overline{u_i{}'u_j{}'} = \mu_t\left(\frac{\partial u_i}{\partial x_j}+\frac{\partial u_j}{\partial x_i}\right)-\frac{2}{3}\rho k\delta_{ij} \quad \textbf{(3.19)}$$

Where μ_t is the turbulent viscosity and differs in value based on the turbulence model that is used. *k* is the turbulent kinetic energy and is given by:

$$k = \frac{1}{2}\left(\overline{u'^2}+\overline{v'^2}+\overline{w'^2}\right) \quad \textbf{(3.20)}$$

δ_{ij} is called the Kronecker delta and has the following values:

$$\delta_{ij} = \begin{cases} 1 \text{ if } i = j \\ 0 \text{ if } i \neq 0 \end{cases} \quad \textbf{(3.21)}$$

3.4.5.2 RNG k-ε model

The RNG k-ε model is chosen for use in this thesis based on literature review. The model is derived based on the two equation standard k-ε model that was proposed by Launder and Spalding[59]. The RNG k-ε model as implemented by Yakhot et al[60] is described here.

In the standard k-ε model two additional transport equations for k and ε are solved. The equations are comprised of several constants. The transport equations for k and ε are used to calculate the turbulent viscosity, μ_t:

$$\mu_t = \rho C_\mu \frac{k^2}{\varepsilon} \quad \textbf{(3.22)}$$

For the RNG k-ε model $C_\mu = 0.0845$ by default and the value is suitable for many engineering flow problems.

The RNG k-ε is devised using the Renormalization Group theory and is made using the following adjustments to the classical model (standard k-ε model):

- Inclusion of the R_ε term that enhances the accuracy for highly strained flow
- The effect of swirl can be taken into account for turbulence modelling which increases the accuracy when swirl flows are modelled
- All the k-ε models are developed to use in flows with high- Reynolds number. However the RNG model uses an analytically derived formula for effective viscosity, μ_{eff} that is capable of modelling flow with low-Reynolds number flows. In order to make effective use of this, correct treatment of the near-wall regions have to be made.

The transport equation for the RNG k-ε model are as follows:

$$\frac{\partial}{\partial t}(\rho k) + \frac{\partial}{\partial x_i}(\rho k u_i) = \frac{\partial}{\partial x_j}\left[\alpha_k \mu_{eff} \frac{\partial k}{\partial x_j}\right] + G_k + G_b - \rho\varepsilon - Y_M + S_k \qquad \textbf{(3.23)}$$

$$\frac{\partial}{\partial t}(\rho\varepsilon) + \frac{\partial}{\partial x_i}(\rho\varepsilon u_i) = \frac{\partial}{\partial x_j}\left[\alpha_\varepsilon \mu_{eff} \frac{\partial \varepsilon}{\partial x_j}\right] + C_{1\varepsilon}\frac{\varepsilon}{k}(G_k + C_{3\varepsilon}G_b) - \rho C_{2\varepsilon}\frac{\varepsilon^2}{k} - R_\varepsilon + S_\varepsilon \qquad \textbf{(3.24)}$$

Similar to the standard k-ε model once the transport equation of the RNG k-ε model are solved, μ_{eff} can be calculated. Then $\mu_t = \mu_{eff} - \mu$ is calculated and μ_t will be used in equations **(3.15)** and **(3.16)** .

Terms in the RNG k-ε model

- The constants $C_{1\varepsilon} = 1.42$ and $C_{1\varepsilon} = 1.68$ are in FLUENT by default.
- $G_k$is the production of turbulent kinetic energy due to the mean velocity gradients.G_b is the generation of turbulent kinetic energy due to buoyancy.
- Y_M is the contribution of the fluctuating dilatation in compressible turbulence to the overall dissipation rate.
- S_k and S_ε are user-defined source terms.
- R_ε is the term that considers rapid strains in the flow and is given by

$$R_\varepsilon = \frac{C_\mu \rho \eta^3 \left(1 - \frac{\eta}{\eta_o}\right) \varepsilon^2}{(1 + \beta \eta^3) k} \quad \textbf{(3.25)}$$

Where $\eta = Sk/\varepsilon$, $\eta_o = 4.38$ and $\beta = 0.012$ and $S = \sqrt{2S_{ij}S_{ij}}$ and $S_{ij} = \frac{1}{2}\left(\frac{\partial u_i}{\partial x_j} + \frac{\partial u_j}{\partial x_i}\right)$

- α_k and α_ε are the inverse effective Prandtl numbers and they are calculated using an analytical formula associated with the RNG theory as follows:

$$\left|\frac{\alpha - 1.3929}{\alpha_0 - 1.3929}\right|^{0.6321} + \left|\frac{\alpha - 2.3929}{\alpha_0 - 2.3929}\right|^{0.3679} = \frac{\mu_{mol}}{\mu_{eff}} \quad \textbf{(3.26)}$$

Where μ_{mol} is the molecular viscosity and $\alpha_0 = 1$ for high Reynolds number flows$\left(\frac{\mu_{mol}}{\mu_{eff}} \ll 1\right)$.

Usually $\alpha_k = \alpha_\varepsilon \approx 1.393$

3.4.5.3 Wall Treatment in turbulence modelling

In the region close to the wall where the boundary layer is present, there is a viscous sublayer in which the viscous forces dominate the inertial forces. Hence the turbulence model, RNG k-ε is not valid in this region as the flow is laminar. Hence a model in addition to the turbulence model is essential to predict the flow in the boundary layer. Alternatively a very fine mesh also could be used. The use of a fine mesh will eventually increase computational costs. Models used to consider the effects of walls are called wall functions. The standard wall function is implemented in this thesis. In the context of wall functions one of the most important variables is y+ which is the non-dimensionalized distance from the wall and is given by

$$y^+ = \frac{\rho u_r y}{\mu} \quad \textbf{(3.27)}$$

Where, y is the distance from the wall to the cell centroid and $u_r$is the friction velocity and is given by

$$u_r = \sqrt{\frac{\tau_w}{\rho}} \tag{3.28}$$

However FLUENT uses a different equation in order to define the non-dimensionalized distance,y*, from the wall. Both y* and y+ give very similar values in regions close to the wall. y* is given by

$$y^* = \frac{\rho C_\mu{}^{0.25} k_p{}^{0.5} y_p}{\mu} \tag{3.29}$$

Where k_p is the turbulent kinetic energy at a node P near the wall, $C_\mu = 0.0845$ and y_p is the distance from the center of node P to the wall.

Using $y^*$the non-dimensionalized velocity U* can be calculated based on Table 3.1.

Table 3.1 Non-dimensionalized velocity, U*

For y*<11.225	For y*>11.225
$U^* = y^*$	$U^* = \frac{1}{k}\ln(Ey^*)$ Where *k* is the von Karman constant= 0.4187and *E*=9.793

The flow velocity, u_p, near a node P can then be found using:

$$u_p = U^* \frac{\tau_w}{\rho C_\mu{}^{0.25} k_p{}^{0.5}} \tag{3.30}$$

Wall functions are used to determine the velocity and also other scalar quantities associated with the flow near the wall.

3.4.6 Sliding Mesh

The sliding mesh technique is used to simulate rotating scoops. The scoops are constructed on a zone which rotates. The interface between the rotating zone and the stationary zone needs to be connected to achieve fluid motion through the interfaces of the zones. Figure 3.5 shows the stationary and rotating zones which are part of the CFD domain. The jet (shown in blue) is in a fixed position and placed in the stationary zone (shown in green). The scoops that rotate are placed on a rotating zone (shown in red) which is imposed with a rotational velocity corresponding to the shaft speed. The interface between the two zones is shown in Figure 3.5. In depth details of the sliding mesh theory are stated in the theory guide[55].

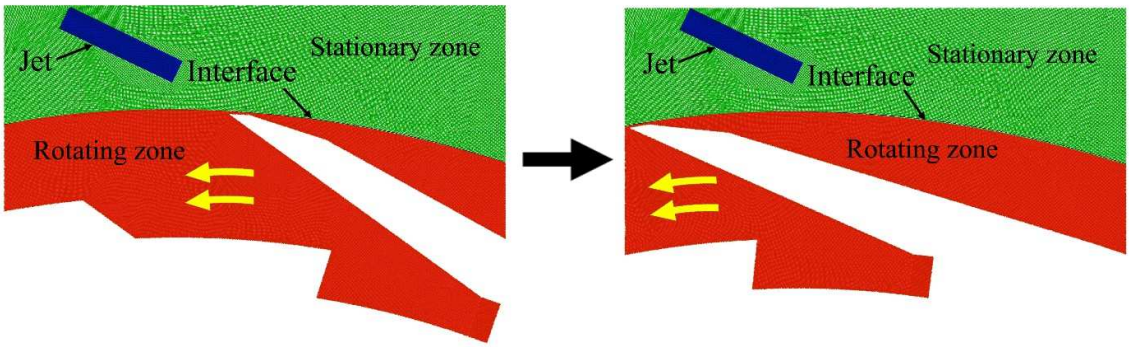


Figure 3.5 Mesh showing scoop moving on rotating zone (red color), jet fixed (blue color) on stationary zone(green color) and the interface between the two zones.

3.4.7 Boundary, Initial Conditions and reference values

Boundary conditions are constraints that are imposed at locations in the CFD domain that do not vary with time (unless specified by the user to vary with time). Initial conditions are variable values specified a point in space, but the values can change with time.

For example:

- At a rotating wall, the rotational velocity is specified as 10000rpm. This is a boundary condition as the rotational velocity is constant throughout the simulation.
- In a cell right above a rotating wall, when a single phase simulation is commenced, the cell is initialized with a velocity of, *u,* since the velocity in the cell is unknown. As the

simulation progresses the value of the velocity in the cell can change depending on the influence of the boundary layer and turbulence induced by the rotating walls. The velocity u adjacent to the wall is an initial value (condition) as it can change as the simulation progresses. The velocity magnitude , u, is chosen as the tip velocity of the scoop.

3.4.7.1 Boundary Conditions

There are four types of boundary conditions used in this thesis as explained in this section.

Wall

At wall boundaries, due to the no slip shear condition that is imposed, the velocity of the fluid takes the value of the velocity of the wall. If the wall is stationary, the velocity of the fluid adjacent to the wall will be 0. If the wall is moving axially or rotating, then the velocity of the fluid adjacent to the wall will be equal to the velocity of the wall. The walls of the scoops are specified as rotating walls with a rotational velocity corresponding to the shaft speed and the walls of the jet housing are stationary walls.

Pressure Outlet

A pressure outlet is used at boundaries where the flow rate of the phases is not known but the pressure is known. The gauge pressure (relative to the operating pressure) is stated at the pressure outlet. The operating pressure in the domain is set 101,325 Pa, hence the absolute pressure at pressure outlet is at 101,325 because the gauge pressure is set at 0. The values of the turbulence intensity and turbulence viscosity ratio are stated at pressure outlet. Turbulence intensity is at 5% and turbulence viscosity ratio is at 10 based on values chosen by users for similar applications[41]. Using the values of the pressure and turbulent quantities, calculations are carried out using the nodes adjacent to the pressure-outlet boundaries to estimate the mass-flux through the boundaries.

Velocity Inlet

The condition is used at the oil jet inlet(s) where the velocity of the oil jet is specified. The volume fraction of the oil jet is at 1. Turbulence intensity is at 5% and turbulence viscosity ratio is at 10 based on values chosen by users for similar applications[41].

Interface

Technically this isn't a boundary condition but the end of a zone in the fluid domain which is adjacent to another zone. Interfaces have to be specified under boundary conditions section in FLUENT for two zones that are adjacent to each other so that connectivity between the zones is achieved and fluid can flow across the zones. The interfaces between two zones are made conformal (cell sizing same on either side of the interfaces). This is to ensure convergence in the numerical results and also increased accuracy.

3.4.7.2 Initial Conditions

At t=0, when the simulation begins the domain is initialized with values stated at the inlet for the whole domain. Single phase simulations are run initially and after convergence in the moment is achieved, two phase simulations are run using the converged stated of the single phase. Prior to running a two phase simulation, the domain is patched with a volume fraction for the oil phase with 0 values. This is done to mimic the real scenario, where there is no oil in the domain prior to oil being fed into the domain.

3.4.8 Convergence

Convergence in the solutions in the simulations are determined using two methods:

1. Monitoring the scaled residuals, R^{ϕ}, until they have reached acceptable values of 10^{-5}. ANSYS FLUENT theory guide suggests that the default values for convergence of10^{-3} is sufficient. However this was lowered to 10^{-5} for better accuracy in the solutions. The residuals are calculated from the imbalance of equation **(3.11)** for each of the cell and then summed for the whole domain.

The scaled residual for the flow of a variable, ϕ, is given by:

$$R^{\phi} = \frac{\sum_{cells\ P} \left| \sum_{nb} a_{nb} \phi_{nb} + b - a_p \phi_p \right|}{\sum_{cells\ P} \left| a_p \phi_p \right|} \tag{3.31}$$

Residuals, R^{ϕ}, are considered as converged once they reach values of 10^{-4} for the respective flow variables.

2. Monitoring variables such as the velocity field, moment on the rotating walls, residence mass of oil and capture efficiency of the scoops. These variables and their convergence will be presented more in detail in Chapter 4 under grid independence studies.

3.4.9 Material Properties

The properties of oil and air used in the simulations are stated in Table 3.2. The properties are chosen based on the air and oil properties used in experimental tests[5] carried out on similar geometry presented in this thesis.

Table 3.2 Material Properties

	Air	**Oil**
Density(kg/m^3)	1.225	924
Dynamic Viscosity(kg/ms)	1.789×10^{-5}	0.025

3.5 Data Analysis and Post Processing

3.5.1 Numerical Data

Numerical data acquired from FLUENT are post processed mainly using MATLAB and Excel. A code is written in MATLAB to conduct numerical integration of the data and calculate the capture efficiency of the scoops. The code is presented in Appendix section 8.2.2.

3.5.2 Post Processing

Post processing is done using FLUENT, CFD-Post and Microsoft movie maker. Graphical contour images were developed using FLUENT during the simulations with the aid of predefined scenes and execute commands. Post-processing and acquiring graphical images from FLUENT are presented in appendix section 8.1. Images output from FLUENT were compiled together using Microsoft Movie maker to develop animations. This method of post-processing using FLUENT and Microsoft Movie maker to create animations is time-efficient and saves lot of disk space because case and data files do not have to be saved often. The time required in reading large case and data files using CFD post is eliminated this way. However CFD-Post was also used to do some post-processing of certain variables but not to create animations.

3.6 Computational Resources

Simulations were carried out using a high performance computing facility (HPC) at the University of Nottingham. FLUENT was run in parallel using 40 computer nodes for each simulation. Each node consists of Two Intel Xeon E5 2670, 2.60 GHz (Sandy Bridge) Processors and 32Gbytes of RAM, with each processor providing 8 cores. An HPC scaling study presented in Chapter 4 was done in order to make optimal use of the HPC.

3.7 Chapter summary

This chapter presents the CFD methodology used for the work done in this thesis. The chapter starts by giving details of the CFD domain that was extracted from the CAD model of the experimentally assessed geometry. A brief introduction to the numerical grid that will be used is also presented. Detailed numerics and quality of the grids used for grid independency studies

will be presented in chapter 4 after introduction of variables used for the studies. The chapter discusses the governing equations that are solved by the CFD solver, ANSYS FLUENT and the methods used to solve the equations. The importance of using a turbulence model for this thesis is highlighted and the RNG k-ϵ model is chosen to model the effects of turbulence in this thesis. The Volume of Fluid (VOF) model which is used in this thesis for modelling the flow of the air and oil phases is presented in this chapter. The types of boundary and initial conditions used in the thesis are explained in detail in this chapter. Details of post-processing data acquired from ANSYS FLUENT is also discussed. The computation resources used are explained finally in this chapter.

4 Analytical and numerical investigations to assess effect of shaft speed on capture efficiency

4.1 Overview

In order to gain an understanding of the performance of the scoop system at different speeds and jet angles, an analytical modeling of the system was carried out. Part of this chapter discusses the analytical study. The chapter then presents details of the CFD geometry, boundary conditions, grid and time dependence studies, HPC scaling studies and in-depth analysis of the CFD results.

4.2 Analytical study of scoops

Figure 4.1 shows the geometry of the scoops at the instant at which a scoops slices the oil jet. The figure shows associated dimensions and angles at this instant. The figure is described as follows:

- The jet is assumed as a thin line positioned at a radial distance R+ h_{axis} from the centre, O, of the scoops. The jet makes an angle, θ_{jet} to the vertical axis as shown in the figure.
- The angle between two consecutive scoops is $\theta_2 + \theta_4$. This is calculated using equation **(4.1)** and is dependent on the number of scoops.
- A and B are the cutting points of the jet path in the circle formed by the outer radius of the scoop.
- R_R is the minimum radial distance from the centre, O, to the inlet of the scoop constriction. This imposes the constraint for the lowest jet angle, θ_{jet}.
- R_{jet} is the perpendicular distance from the centre, O, to the jet.
- θ_5 is the angle the proceeding scoop's tip, C, makes with the horizontal axis as shown. This will be used to define the strike angle later in section 4.2.2. Angles θ_1 and θ_3 are required to calculate θ_5.

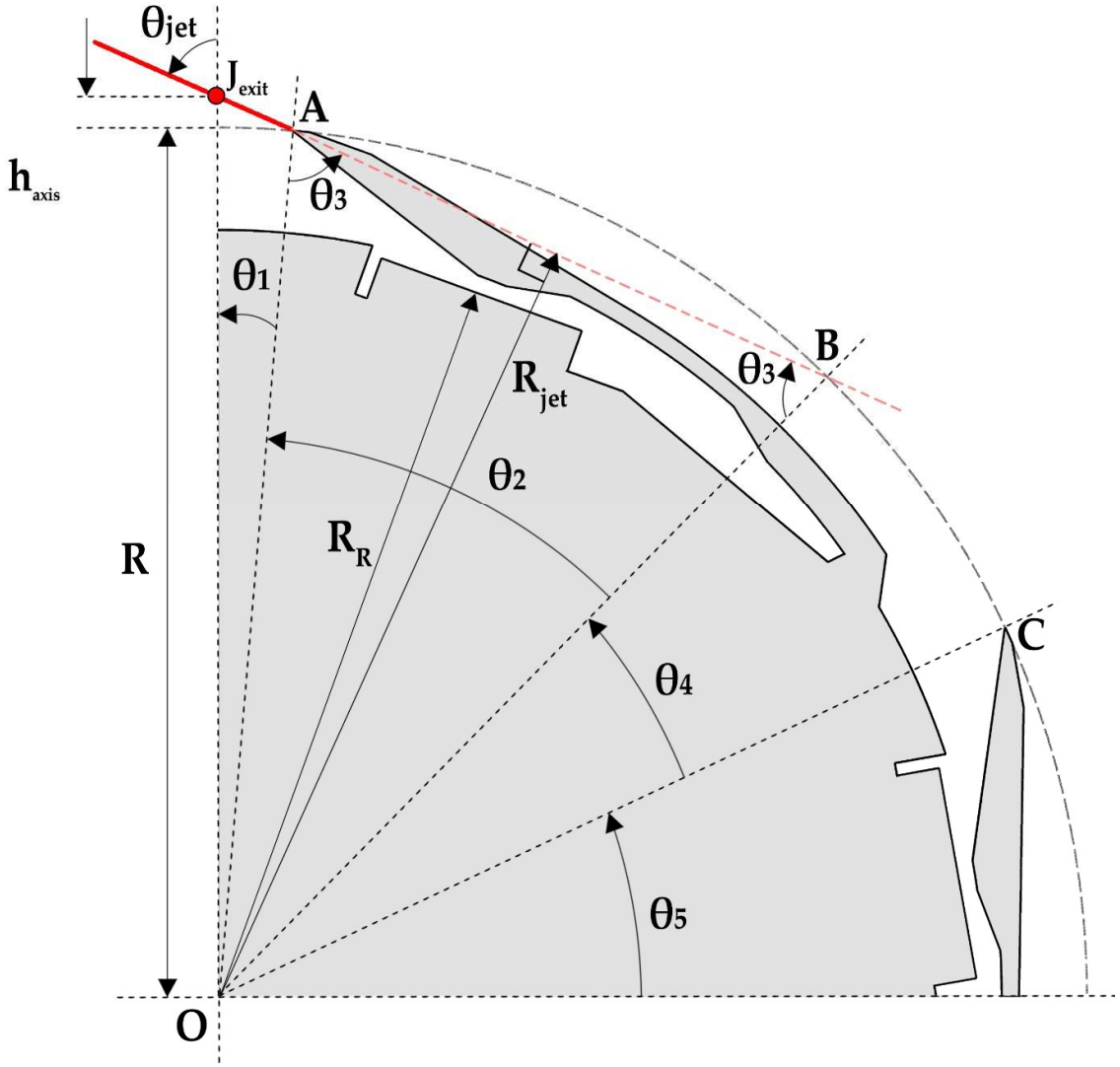


Figure 4.1 Geometry of scoops at point of slicing oil jet.

Equations **(4.1)**-**(4.6)** are used to calculate the dimensions associated with Figure 4.1.

$$\theta_2 + \theta_4 = \frac{2\pi}{N_{Scoops}} \tag{4.1}$$

$$Cos\left(\frac{\theta_2}{2}\right) = \frac{(R + h_{axis})\sin\theta_{jet}}{R} \tag{4.2}$$

$$AB = 2R \sin\left(\frac{\theta_2}{2}\right) \tag{4.3}$$

$$\theta_3 = \sin^{-1}\left(\frac{(R + H_{axis}) * \sin(\theta_{jet})}{R}\right) \tag{4.4}$$

$$\theta_1 = \theta_3 - \theta_{jet} \tag{4.5}$$

$$\theta_5 = \frac{\pi}{2} - \frac{2\pi}{N_{Scoops}} - \theta_1 \tag{4.6}$$

It is expedient to use the concept of the velocity ratio VR, the ratio of the scoop tip speed to the jet speed:

$$VR = \frac{\omega R}{V_{jet}} \tag{4.7}$$

The velocity ratio at which the following scoop and the jet meet at B at the same time can be defined as the threshold value VR_{thr}. Velocity ratios below VR_{thr} give rise to an angle,θ_{Loss}, through which a scoop rotates without capturing portions of the jet.Velocity ratios above VR_{thr} will result in the following scoop impacting with the jet at a strike point located in the path AB. Hence, it can be identified that for a fixed jet velocity there are two phases of rotational speeds, 0 to ω_{thr} through which capture efficiencies vary and speeds above ω_{thr} where 100% capture is theoretically possible.

4.2.1 Shaft speeds below VR_{thr}

With reference to Figure 4.2 when the rotational speed of the shaft is low relative to the velocity of the jet, the oil jet will travel through B before the next scoop reaches B. From the instant the jet passes through B till it gets sliced by the proceeding scoop at B, the tip of the proceeding scoop will rotate through a loss angle, θ_{Loss}. During this period of time, portions of the jet will be uncaptured until the tip of the scoop reaches B and slices it. At low rotational speeds the proceeding scoop will slice the jet two times, first at B and then at A. It should be noted at low rotational speeds the point of impact of the jet and the scoop is always at B. The positions of the scoops at the instant when the previous scoop slices the oil jet at A is shown in a lighter color in Figure 4.2.

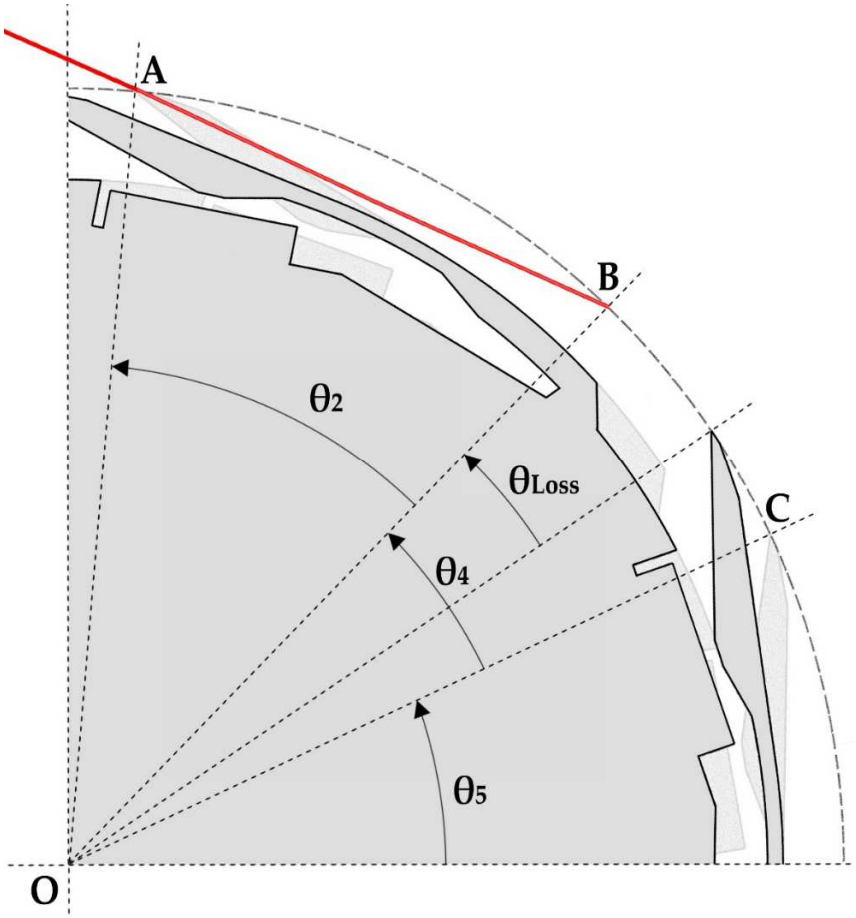


Figure 4.2 Shaft speeds below VR_{thr}

θ_{loss} illustrated in Figure 4.2 can be calculated using:

$$\theta_{loss} = \theta_4 - \frac{2R\omega}{V_{jet}} sin\left(\frac{\theta_2}{2}\right) \quad \textbf{(4.8)}$$

The volume of oil lost as the next scoop rotates to B, in phase 1 is estimated using

$$vol_{lost} = V_{jet} A_{jet} \frac{\theta_{Loss}}{\omega} \quad \textbf{(4.9)}$$

Where A_{jet} is the cross-sectional area of the jet.

In this phase (VR < VRthr) the oil capture efficiency is given by:

$$\eta = \frac{\frac{2\pi}{N_{scoops}} - \theta_{loss}}{\frac{2\pi}{N_{scoops}}} \quad \textbf{(4.10)}$$

In order to identify the range of rotational speeds in phase 1 and phase 2, it is necessary to calculate the threshold velocity ratio. This is obtained by equating the time taken for the jet to travel from A to B with the time taken for the scoop to rotate through θ_4. It is found that

$$VR_{thr} = \frac{\theta_4}{2sin\left(\frac{\theta_2}{2}\right)} \quad \textbf{(4.11)}$$

The geometry studied in this chapter uses a 6-scoop geometry with a jet angle of $\theta_{jet} = 64.2^o$, a jet velocity of $V_{jet} = 22.381 m/s$. Using these values, it can be shown for the geometrical setup in the theoretical analysis, VR_{thr} is 0.44 and ω_{thr} is 934rpm. Different jet angles will give rise to different threshold velocity ratios and for comparison, values of VR_{thr} are tabulated in Table 4.1 for the investigated geometry and jet velocity. It is seen at larger jet angles (less radial jet) threshold velocity ratios are higher and also the radius above which the jet passes

tangentially above the rotor is greater. table 4.1 also presents the perpendicular distances from the origin to the jet, R_{jet}, for the different jet angles that were investigated. For the minimum possible jet angle, $R_{jet} = R_R$ which corresponds to the inner radius of the rotor and for the maximum jet angle that can be used, $R_{jet} = R$, which corresponds to the outer radius of the scoop.

Table 4.1 Threshold ratios for different jet angles

Jet angle, $\boldsymbol{\theta_{jet}}$ (degrees)	Perpendicular distance from origin,O, to jet, $\boldsymbol{R_{jet}}$(in terms of rotor radius, R_R)	$\boldsymbol{VR_{thr}}$
53.7(min)	R_R	0.03
58.2	$1.06R_R$	0.07
61.2	$1.09R_R$	0.23
64.2	$1.11R_R$	0.44
67.2	$1.14R_R$	0.72
70.2	$1.17R_R$	1.42
74.4(max)	$1.20R_R = R$	2.27

4.2.2 Shaft speeds above VR_{thr}

For velocity ratios above VR_{thr} the proceeding scoop strikes the oil jet on path AB, with the tip of the scoop making an angle Φ with reference to B as shown in Figure 4.3. The positions of the scoops at the instant when the previous scoop slices the oil jet at A is shown in a lighter color in Figure 4.3. At the instant the jet strikes the next scoop, the distance between the tip of the scoop, Z, and the point of impact is given by C_X. After the impact the scoop continues to rotate from Z to A where it slices the jet. From the instant when the jet strikes the scoop till the instant the scoop slices the jet, it rotates through an angle, $\theta_{capture}$. At velocity ratios above the threshold ratios, the scoop slices the oil jet only once at A. It is also expected that theoretically the capture efficiency is 100% in this phase because there are no uncaptured portions of the jet.

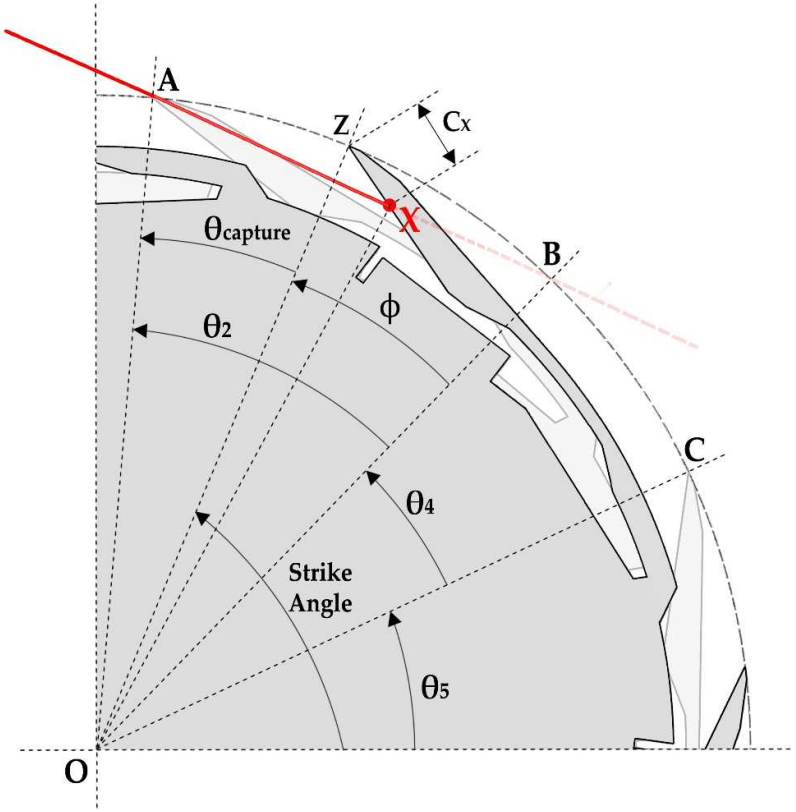


Figure 4.3 Shaft speeds above VR_{thr}

The point, X, at which the oil jet strikes the base of the scoop, lies in the path of the jet AB. The angle through which the proceeding scoop has rotated before the jet strikes the scoops is is $\theta_4 + \phi$. An iterative approach to calculating ϕ can be implemented by equating the time taken for the jet to travel from A to X, t_{AX} with the time taken for the scoop to rotate through angle $\theta_4 + \phi$ which is t_Z.

$$t_{AX} = t_Z = \frac{\theta_4 + \phi}{\omega} \tag{4.12}$$

ϕ is solved by iteration in MATLAB and the code is given in the appendix section 8.3.1.

With reference to Figure 4.3, strike angle is defined as $\theta_4 + \theta_5 + \Phi$

$$Strike\ angle = \theta_4 + \theta_5 + \Phi. \tag{4.13}$$

The strike angle is defined with reference to the positive x-axis and is used to illustrate collision points graphically in Figure 4.7 and Figure 4.8.

Using the dimensions associated with the geometry investigated in this thesis and a jet velocity of 22.381 m/s the values for strike angle are calculated and plotted against shaft speed for various jet angles in Figure 4.4. For a particular jet angle it can be seen that as the shaft speed is increased towards the threshold shaft speed corresponding to the jet angle, the strike angle remains constant. During this phase, capture efficiencies are below 100%. As the shaft speeds are increased beyond the threshold shaft speed, the strike angle increases. During the phase where the shaft speeds operate at velocity ratios above the threshold velocity ratio, the jet impacts the scoop at an angle greater than $\theta_4 + \theta_5$ with reference to Figure 4.3. From Figure 4.4 it can also be seen that at shaft speeds operating well above the threshold velocity ratio, that more radial jets (i.e: lower θ_{jet} values and lower radial distances, $\boldsymbol{R_{jet}}$,from the center)

have a greater striker angle compared to steeper jets(higher θ_{jet} values and larger radial distances, $\boldsymbol{R_{jet}}$,from the center).

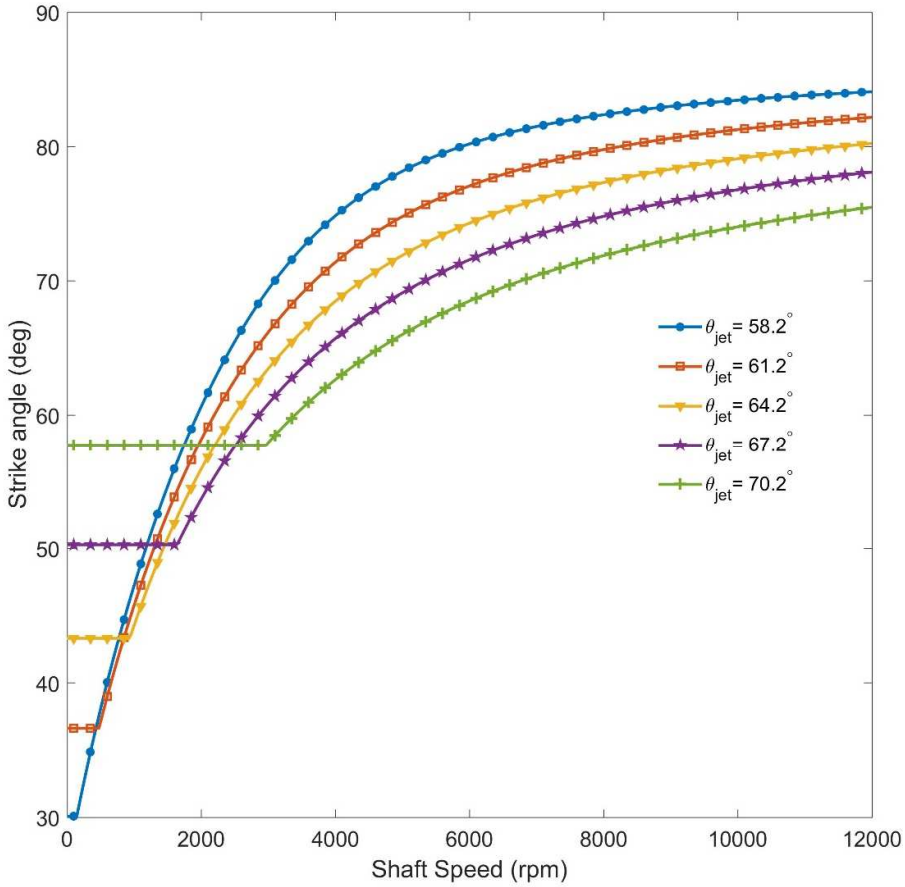


Figure 4.4 Strike angle vs. shaft speed

The angle through which a scoop is in contact with the oil jet after impact is denoted as $\theta_{capture}$ in Figure 4.3. As the strike angle increases, $\theta_{capture}$ becomes smaller and thus the amount of oil being captured by each scoop is reduced for each slicing event. In theory this has no effect on the capture efficiency as all the oil is still captured, but in smaller segments. However, in practice there is a loss associated with each slicing event as shown in [7].

Figure 4.5 shows $\theta_{capture}$ versus shaft speed for the configuration investigated for a range of jet angles. For shaft speeds that operate below the threshold shaft speed, the capture angle is given by θ_2 with reference to Figure 4.3. This corresponds to the constant value seen in Figure 4.5 for a particular jet angle as the shaft speed is increased towards the threshold shaft speed.

Beyond the threshold shaft speed, the capture angle decreases below θ_2. It is seen from Figure 4.5, for jet with lower values of R_{jet}(smaller jet angles), the capture angles are lower compared to jets with higher values of R_{jet}(larger jet angles).

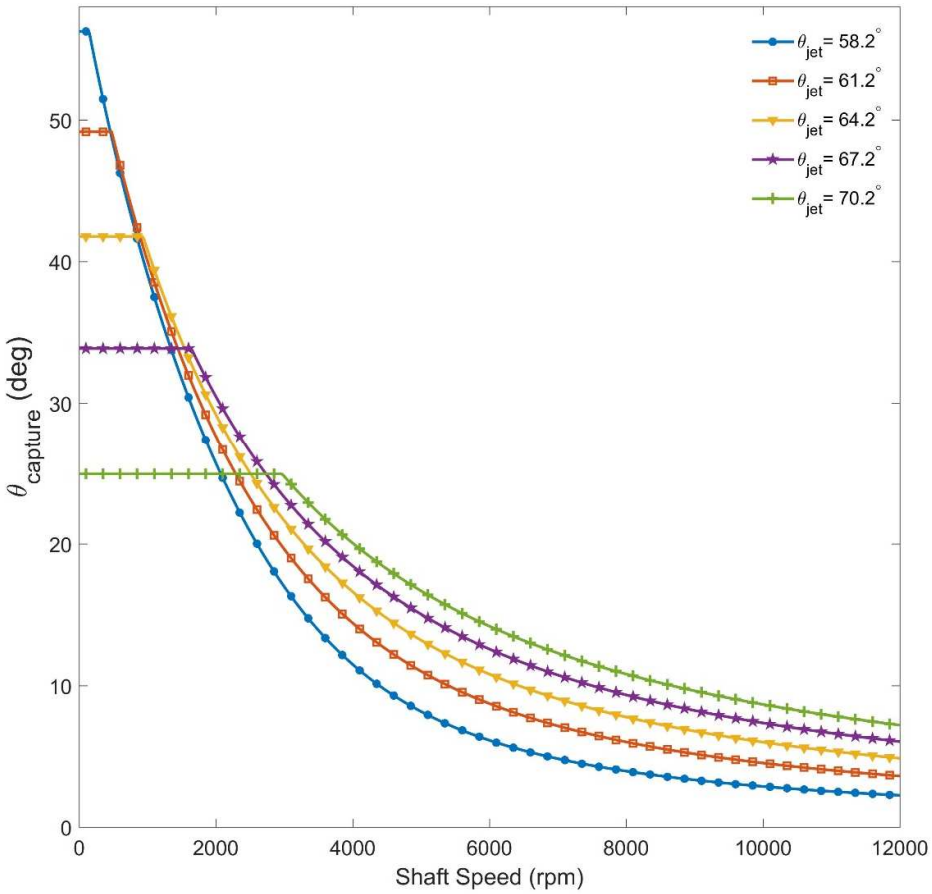


Figure 4.5 $\Theta_{capture}$ vs. shaft speed

C_X, which is the distance from the tip of the scoop to the point of impact, at the instant of striking is plotted against the shaft speed in Figure 4.6. Figure 4.6 shows that more radial jets impact at a larger value of C_X and if we assume that they lose less momentum since the impact point is closer to the outlet, we would infer better capture efficiency in such cases. C_X reduces with increasing shaft speed and this could infer reduced capture efficiency at higher shaft speeds as more oil initially within the scoop envelope could lose momentum and move out of the scoop because of centrifugal effects.

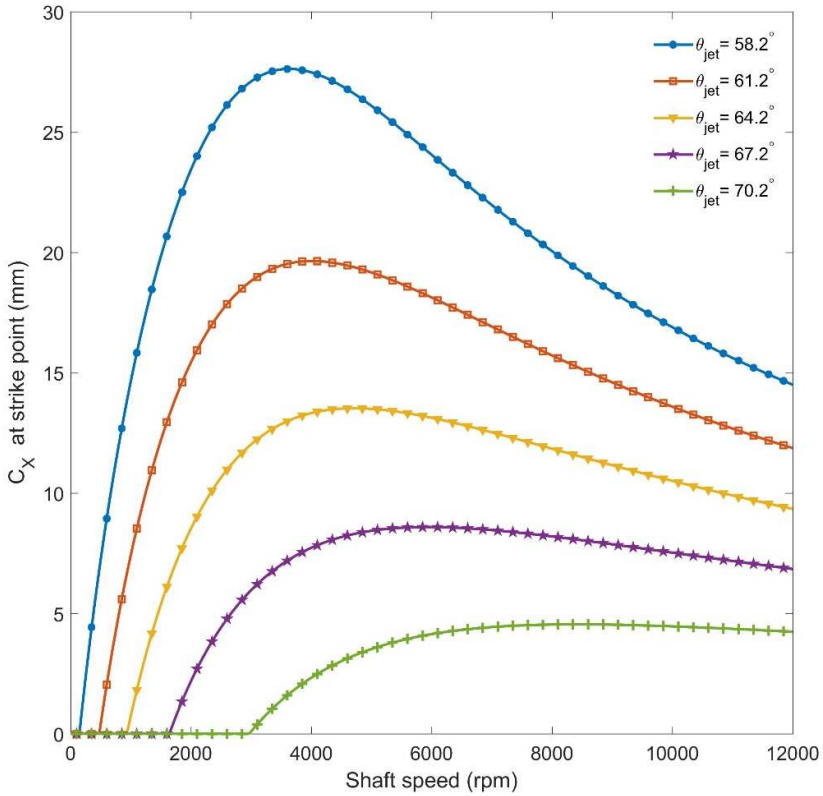


Figure 4.6 Effect of shaft speed on C_x

Graphical images, shown in Figure 4.7 are produced to scale to illustrate the collision points for shaft speeds above ω_{thr} for a jet angle of 64.2° and a jet velocity of 22.381m/s. The circle circumscribed by the outer radius of tip of the scoop is shown in the images. It can be seen that as the shaft speeds are increased towards the higher shaft speeds, C_x gradually decreases and the strike point is more closer to the outlet of the scoop.

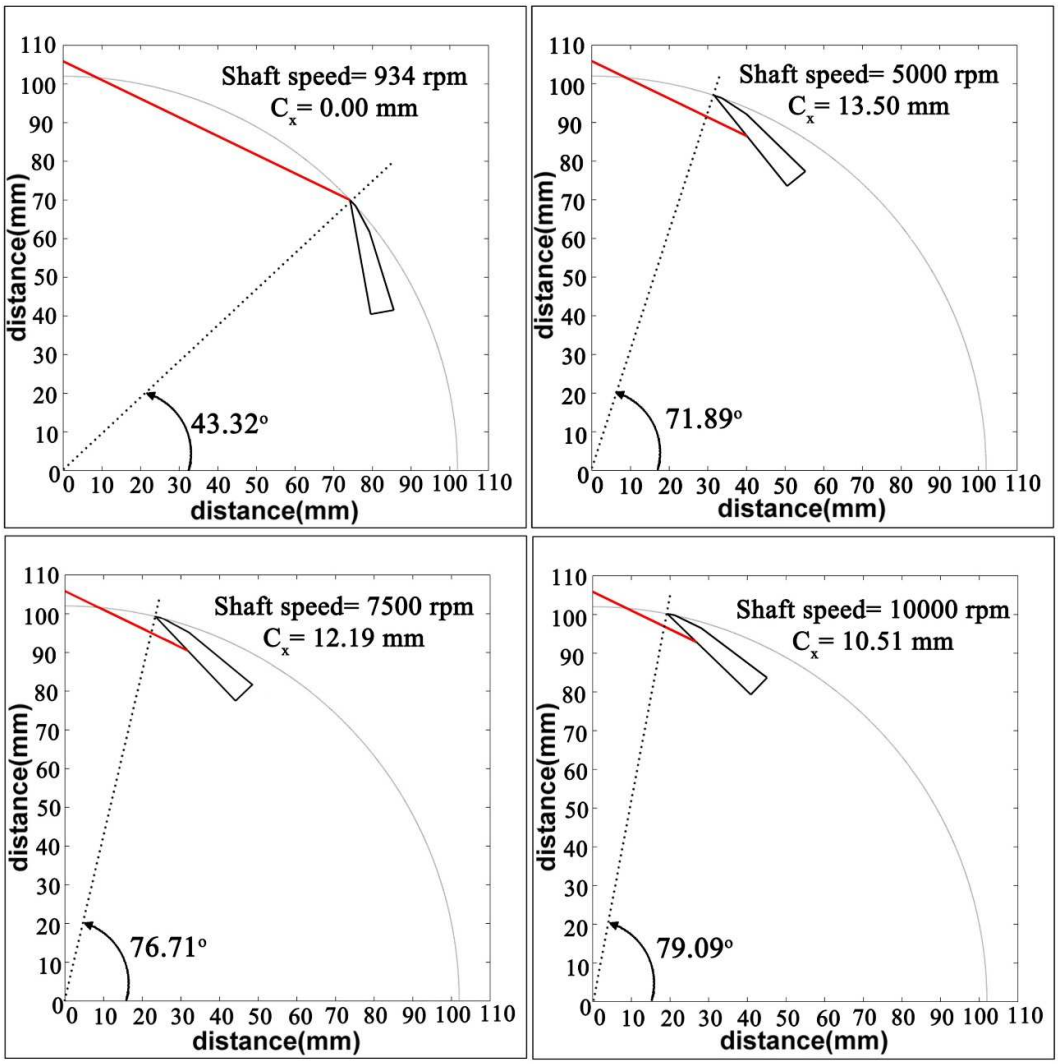


Figure 4.7 Collision points graphically illustrated for various shaft speeds with jet velocity= 22.381 m/s and jet angle=64.2°.

Figure 4.8 shows the graphical images for the collision points for a range of jet angles at a constant shaft speed of 5000rpm. It can be seen that for lower values of the jet angle, θ_{jet}(lower R_{jet}), the length C_x is greater which means that the oil jet strikes more inboard of the scoop. At higher values of θ_{jet} (higher R_{jet}) the jet strikes the scoop closer to the tip. Oil that rebounds from the scoop is not necessarily uncaptured as it will travel inboard to the inner sleeve and provided its inwards momentum is greater than the outwards centrifugal force, it is still captured. The effect of the change in C_X is therefore complex.

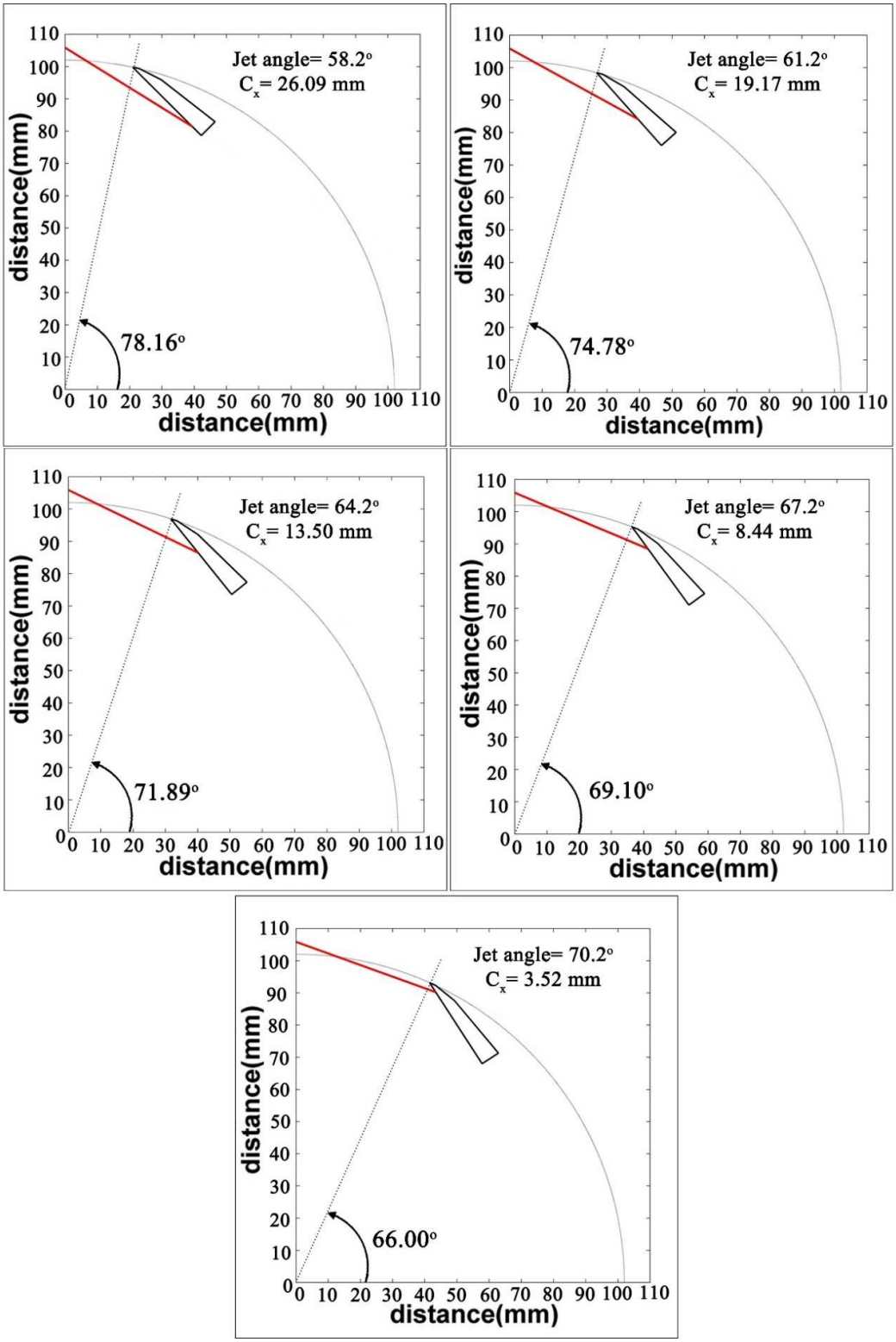


Figure 4.8 Collision points graphically illustrated for various jet angles with jet velocity= 22.381 m/s and shaft speed=5000rpm.

4.2.3 Key conclusions of analytical study

- For a constant jet velocity and a jet angle, there exists a threshold shaft speed beyond which theoretically 100% capture efficiency can be obtained. For the CFD work presented in this chapter the jet angle and jet velocity used for CFD simulations are 64.2^{o} and 22.381m/s respectively. The threshold shaft speed for this configuration is calculated analytically as 934rpm.
- For jet angles lower than 67.2^{o}, as the shaft speed is increased beyond 5000rpm, the strike point of the jet with the scoop moves closer towards the tip of the scoop.
- For jet with lower perpendicular distance to the centre, O, it is expected that for shaft speeds well above the threshold shaft speed, the strike point is closer to the outlet of the scoop with larger C_x values at the instant of striking compared to when using jets with a larger perpendicular distance to the centre, O.

4.3 CFD Geometry and Boundary conditions

The simplified 2D geometry presented in Chapter 3 was used for the numerical study presented in this thesis. The geometry preserves most of the vital features present on the experimentally investigated scoop lubrication system such as the constriction gap of the scoop and scoop angle.

The oil jet has been modelled as an inlet with the same "nozzle diameter" as was used in the experiments. The upstream feed for the nozzle from the actual system is excluded in the simplified geometry. The CFD geometry and boundaries is shown in Figure 4.9.

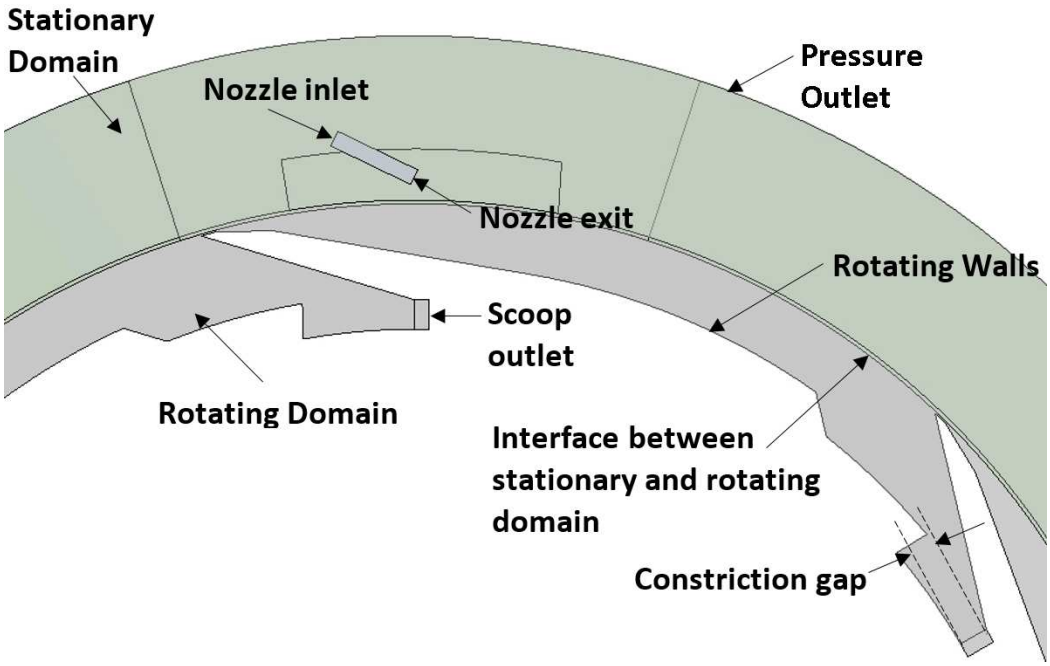


Figure 4.9 CFD geometry and boundaries

Boundary conditions have been implemented for the simulations such that they replicate as closely as possible the conditions under which experimental studies were performed. A pressure outlet shown in Figure 4.9 in the stationary domain is chosen, instead of a wall, for the following reasons:

- In 2D simulations when droplets are produced after the slicing events they are centrifuged outwards. If a wall is used for the boundary, the flow of the droplets will be considerably dominated by gravitational effects in a 2D simulation compared to a 3D one. This is because in 2D simulation the droplets are actually considered as

extruded in the axial direction (z-axis) and will be treated like films as they flow along a wall. However, this is not the case in experiments. In order to avoid this incorrect modelling of droplets, a wall is not used for that boundary.

- Since the 2D case is a simplification of a 3D case, the case should take into account and give allowance for locations where oil droplets are lost in a 3D case. In a 3D case oil droplets can also move in the axial direction (z-axis) after the slicing event and they are eventually not captured. In order to consider this, it is preferable to use a pressure outlet than a wall, as the inclusion of a wall, will mean that oil droplets that collide with it, can be recaptured if they fall back leading to higher capture efficiencies. Capture efficiencies predicted using CFD simulations presented in this chapter indicate that the 2D case already over predicts the capture efficiency compared to experimental data.

The radial distance of the pressure outlet is chosen such that it coincicdes with the radius of the outer casing used in the experiments. A parametric study on the radial distance of the pressure outlet to ensure that changing the distance does not have an effect on the capture efficiency.

The boundary conditions used for the simulations in this chapter are given in Table 4.2. The scoop outlet gauge pressure is set as 0Pa which physically means that the outlet is at the atmospheric pressure(operating pressure).The values for the jet turbulent intensity and viscosity ratios are chosen based on what past researchers have used for similar applications[41].

Table 4.2 Boundary Conditions

Parameter	Value
Operating pressure	101325 Pa
Oil jet velocity	22.38 m/s
Oil jet turbulent intensity	5%
Oil jet turbulent viscosity ratio	10
Oil jet inlet gauge pressure	0 Pa
Scoop outlet gauge pressure	0 Pa

The mass flow rate of the oil phase was monitored using the aid of surface monitors, at every time step. The monitors were imposed at the inlet of the oil jet and the outlets of each scoop in

the system. The results from the surface monitors were processed using MATLAB and the capture efficiency was calculated using:

$$\text{Efficiency} = \frac{\sum_{i_{steady}}^{i_{last}} \dot{m}_{outlet}\, t_i}{\sum_{i_{steady}}^{i_{last}} \dot{m}_{inlet}\, t_i} \tag{4.14}$$

where i_{last} is the number of time steps used for each simulation, i_{steady} is the time step beyond which the efficiency is considered to have achieved pseudo steady state and t_i is time step value. A sample plot of the capture efficiency vs. number of rotations is shown in Figure 4.10. The section which is used to estimate the value of the capture efficiency after it has achieved pseudo steady stated is marked in the plot.

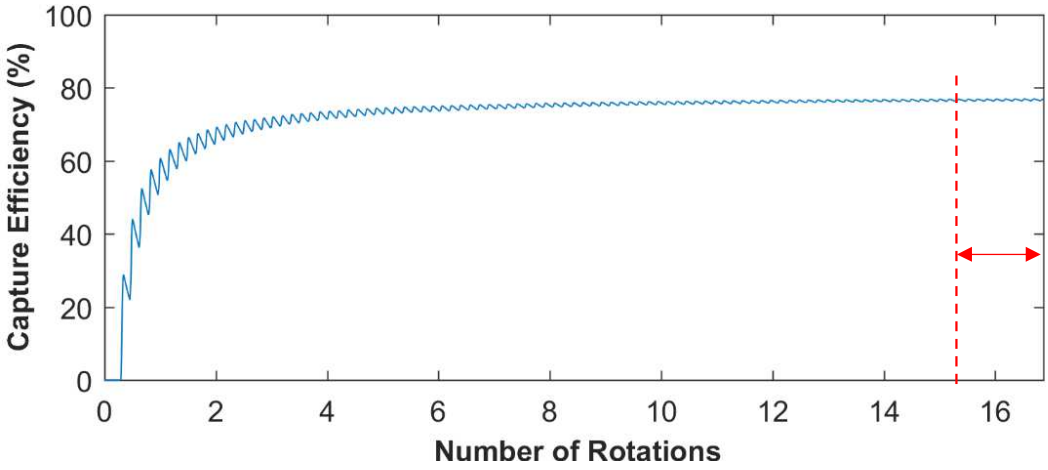


Figure 4.10 Section of capture efficiency which is considered to be steady state

Time Stepping

An explicit scheme is adopted to solve the continuity equation, and as this scheme has to satisfy the CFL condition it is highly sensitive to the time step. The CFL condition is governed by the size of the smallest cells and the highest velocities in the domain. At rotational speeds above 2150 rpm, the tip of the scoop has a greater tangential velocity than the oil jet. Aiming for a Courant number of 1 or less, for shaft speeds lower than ω=2150 rpm, the jet velocity and typical cell size near the jet was used to choose the time step. For shaft speeds greater than ω=2150rpm, the cell size near the scoop tip and the tip speed were used. The number of time

steps needed for the simulations was based on the desire that the scoop rotor should rotate sufficient number of rotations so that the capture efficiency has achieved convergence. This was chosen following examination of the capture efficiency plots.

4.4 Grid and time dependence studies

4.4.1 Grid details and Grid dependence studies

Sufficient amount of time was dedicated towards discretizing the CFD domain and conducting grid dependence studies. In depth grid dependency studies were conducted for all the cases that were investigated. It is highly desirable to obtain a grid that doesn't give changes in solution when the cell density is changed. In this thesis only one case of grid dependence study for a shaft speed of 10000rpm, jet velocity of 22.381m/s, jet angle of 64.2^{o} and a constriction gap of 4mm is presented. It should be noted that a similar approach was applied for all the cases.

The geometry was discretized using quadrilateral type cells due to the advantage of aligning them with the flow. For all the grids that were developed using ANSYS a method called mapped face meshing was utilized. This method aligns the cells in the domain with the edges (walls) in the geometry. This is essential to ensure that the cells are in line with the flow direction and lead to better accuracy in the solution. Cells were clustered and a high density was used close the walls to ensure that y+ values were in the range of 20-40 for both the air and oil phase which is crucial for the use of the standard wall function. For all the grids that were generated the maximum aspect ratio is less than 5 and the minimum orthogonal quality is above 0.40. For CFD the maximum aspect ratio is recommended to be lower than 10 and the minimum orthogonal quality should be above 0.20. Table 4.3 gives information about the grids that were generated to conduct grid dependence studies. $h_{M1,}$ $h_{M2,}$ h_{M3} and h_{M4} are the sizes of the cells used in the grid. r_{M1M2}, r_{M2M3} and r_{M3M4} are the ratio between the core cell sizing between two grids.

Table 4.3 Grid information

	M1	M2	M3	M4
Core cell size(mm)	h_{M1}=0.338	h_{M2}= 0.260	h_{M3}=0.200	h_{M4}=0.153
Ratio of cell size between grid, *r*		r_{M1M2}=1.3	r_{M2M3}=1.3	r_{M3M4}=1.3
Number of Cells	200,103	401,283	621,300	1,000,161
Maximum Aspect Ratio	5.678	4.576	4.347	3.104
Average Aspect Ratio	1.085	1.069	1.046	1.068
Minimum Orthogonal Quality	0.424	0.467	0.406	0.610
Average Orthogonal Quality	0.993	0.996	0.998	0.996

Figure 4.11 shows the four grids in the vicinity of the scoop which illustrates increasing grid density from grid M1 towards M4.

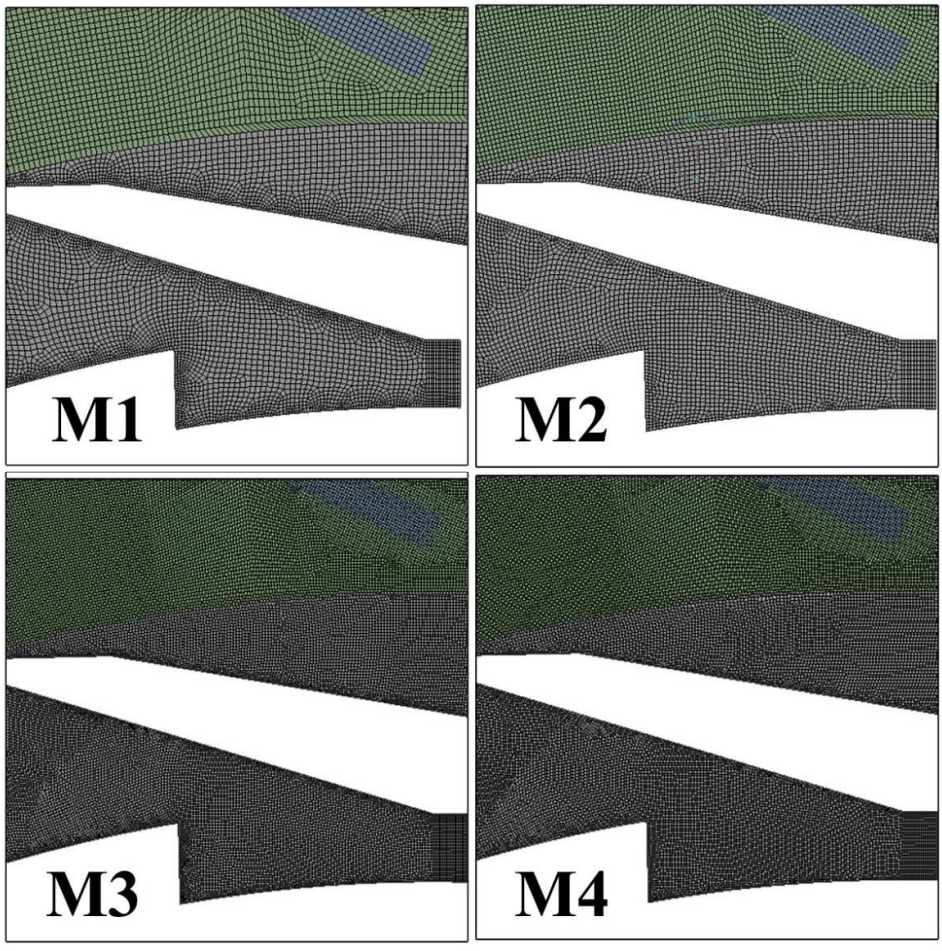


Figure 4.11 Grids shown in the vicinity of the scoop which were used for grid dependency studies

The GCI method which is based on the Richardson Extrapolation (RE) method for estimating discretization error is used in this thesis to evaluate the discretization error. The method has been used in several papers that were published[61][62][63] and is recommended by the Journal of Fluids Engineering[64]. Hence, it is chosen for the study. The GCI method is outlined as follows:

1. A grid with a core cell size of h is used for the first grid which is coarse. The core cell size used for the coarse grid M1 is 0.338mm. Subsequent grids were developed by refining the coarse grid. The refinement factor $r = h_{coarse}/h_{fine}$ is chosen as 1.3 and is kept constant between two consecutive grids used in the study.
   For two dimensional geometries:

$$h = \left[\frac{1}{N}\sum_{i=1}^{N}(A_i)\right]^{1/2} \quad \textbf{(4.15)}$$

   Where A_i is the area of the i^{th} cell, and N is the total number of cells used for the computations.

   Four significantly different sets of grids were generated comprising of only quadrilateral type cells.

2. Simulations were run and a variable, Φ, relevant to the study was chosen to assess grid dependence.
   - For single phase flows the variables chosen were the moment on the rotating walls and the velocity profiles at prescribed locations. For some cases additional parameters were picked whenever relevant. For example, in Chapter 6 where the effect of vortex shedding is investigated in single phase simulations, in addition to the velocity and the moment on the walls, the vorticity in the domain is also analysed for grid convergence.
   - For two phase flows, the variable chosen were the residence mass of oil and the capture efficiency.

3. The extrapolated values are calculated using:

$$\Phi_{ext}^{34} = \left(r_{M3M4}^{p}\Phi_4 - \Phi_3\right)/(r_{M3M4}^{p} - 1) \quad \textbf{(4.16)}$$

Similarly $\Phi_{ext}^{23}$and Φ_{ext}^{12} are calculated.

Where the apparent order, *p*, of the method is calculated using:

$$p = \frac{1}{\ln(r_{M3M4})}\left|ln|\varsigma_{M2M3} - \varsigma_{M3M4}|\right| \quad \textbf{(4.17)}$$

and $\varsigma_{M2M3} = \Phi_2 - \Phi_3$, and $\varsigma_{M3M4} = \Phi_3 - \Phi_4$

The extrapolated values, Φ_{ext}, that are calculated are an estimation of the exact numerical converged solutions when the size of the cell approaches zero. The apparent order, *p*, that is calculated is expected to be close to the formal order of the CFD code that is used to solve the governing equations when using the GCI method to evaluate errors[65]. For this thesis the formal order is 2 as most equations are solved in second order in ANSYS FLUENT. However, when calculating the apparent order, *p,* certain values of *p* may not be in close agreement with the formal order. For example in the work reported by Celik & Karatekin, the local values of the apparent order p are between 0.012 to 8.47[66] for the points that they used to monitor the velocity profile. Hence, when estimating the errors, an average value *p* is recommended to be used. The use of an average value of *p* instead of using local values will improve the accuracy of the uncertainty estimation [65].

4. The error estimates are calculated as follows.
The approximate relative error between the solutions of two consecutive grids is estimated using:

$$e_a^{M3M4} = \left|\frac{\Phi_{M4} - \Phi_{M3}}{\Phi_{M4}}\right| \quad \textbf{(4.18)}$$

The approximate relative error between the converged numerical solutions calculated using extrapolation and the solution on a grid is given by:

$$e_a^{M3M4} = \left| \frac{\Phi_{ext}^{M3M4} - \Phi_{M4}}{\Phi_{ext}^{M3M4}} \right| \quad \textbf{(4.19)}$$

5. The GCI for a grid is estimated as follows.

$$\mathrm{GCI}_{\mathrm{fine}}^{\mathrm{M3M4}} = \frac{1.25 e_a^{M3M4}}{r_{M3M4}^{p} - 1} \quad \textbf{(4.20)}$$

Low GCI values for a grid indicate that the error between the solution calculated and the exact numerical solution is small. However in order to achieve low GCI values the use of a fine grid is necessary and there is compromise between the accuracy and the computational costs associated in using a fine grid. Based on published results it can be seen that authors have used grids with GCI values in the range of 1.4% and 4.7% which are deemed to be acceptable[61] [63][67].

6. Error bars are reported on plots for the profile of the variable being reported using the GCI in conjunction with the average value of p as a measure of the global order of accuracy in order to compensate for local values of p that are not in agreement with the formal order of the CFD code.

Single phase grid dependence studies

When the sliding mesh model is used to simulate rotating components, the simulation has to be run as a transient one in ANSYS FLUENT and steady state simulations cannot be run in conjunction with the sliding mesh model. Hence a fixed number of time steps value was chosen for the simulations to achieve convergence with regards to the moment on rotating walls. It was seen that after 350,000 time steps (with $1x10^{-7}$s for the time step), the moment values achieved convergence. For each time step a maximum of 25 inner iterations were allowed. It was observed that for single phase simulations residuals for the flow parameters achieved convergence before the first 8 iterations and for two phase flow before 12 iterations. For all the cases in the grid dependence study for single phase flow, the simulations were run for exactly 350,000 time steps which is equivalent to 5.83 rotations.

Figure 4.12a) shows the position of the scoops after 350,000 time steps. Velocity profiles at arbitrary locations shown in Figure 4.12a) are taken and analyzed for each of the grids. The locations are 90^{o} apart from each other. From Figure 4.12b) it can be seen as the as the grid is refined from the coarse grid, M1, the velocity profiles begin to converge towards finest grid, M4. Table 4.4 presents the average GCI calculated for the grid based on the velocity and it can be seen that grids M3 and M4 have acceptable GCI values of 1.85% and 0.76% respectively.

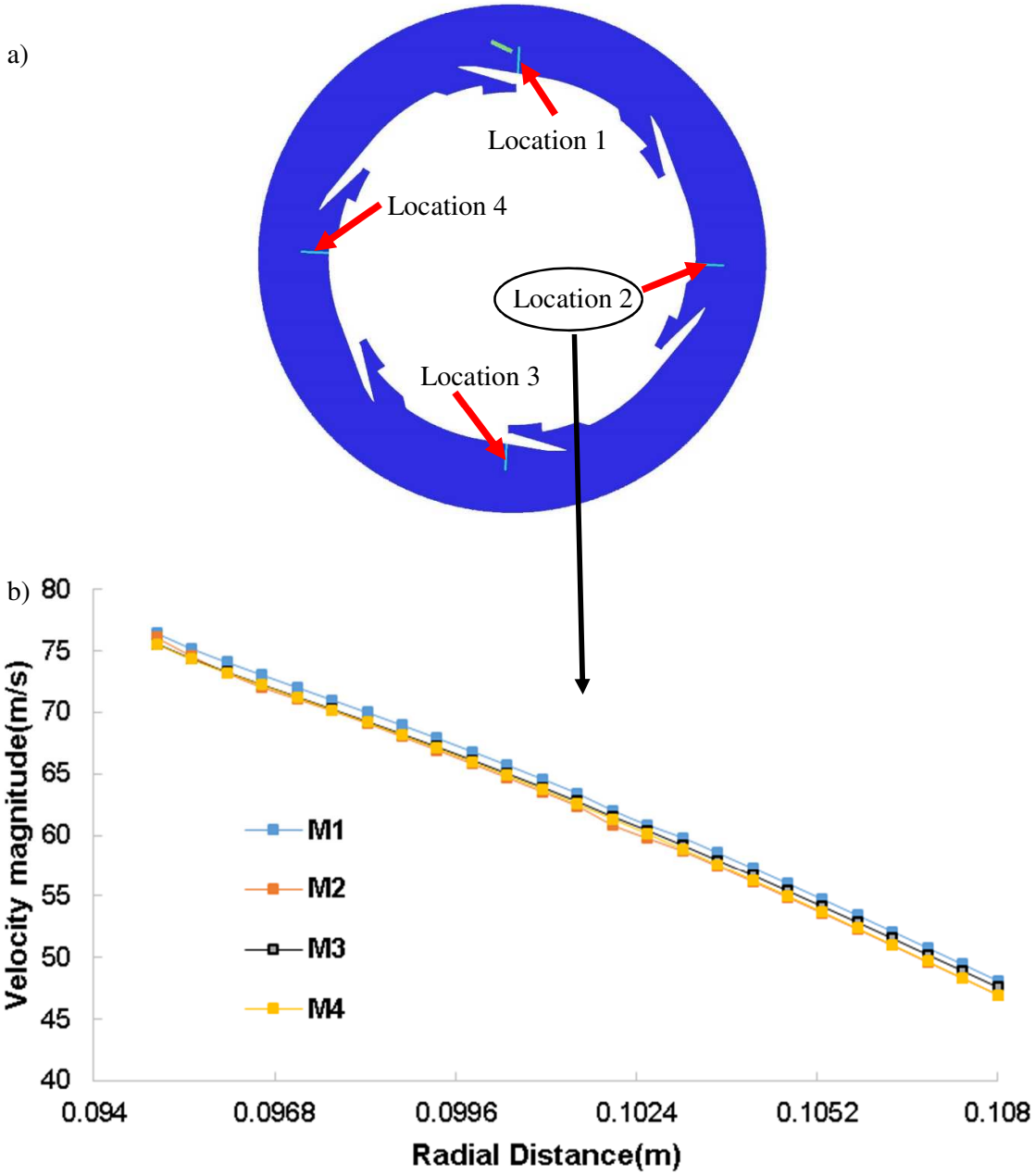


Figure 4.12 Chosen locations for velocity analysis and sample velocity plot shown for location 2

Table 4.4 Calculated average GCI values based on velocity magnitude for each of the grids

	M1	M2	M3	M4
Average GCI (%)	-	6.92	1.85	0.76

Figure 4.13a) shows the moment on the rotating walls vs. number of rotations. The error bars are not included for all the time steps for clarity purposes in presenting the plot Figure 4.13a as there were 350,000 time steps. Instead an average of the errors bars is considered for the last 110,000 time steps and included in Figure 4.13b and shown after the moment has achieved convergence for each of the grids that were analyzed. From the figure it can be seen that between the coarse mesh M1 and the finer grids there is a small difference in the values for the first 1.5 rotations. However beyond 1.5 rotations the moment values are similar for all the grids as they fluctuate with the number of rotations. Table 4.5 presents the calculated relative errors between two consecutive grids using eq. **(4.18)** and the average GCI values for each of the grids based on the moment after achieving convergence over the last 110,000 time steps. The maximum relative error between two consecutive grids is 1.71% which shows that there is very litte improvement in the convergence of the values when the grids are refined. Grids M3 and M4 have GCI values of less than 2% denoting low descritization errors compared to grid M2 which has a GCI of 4.1%.

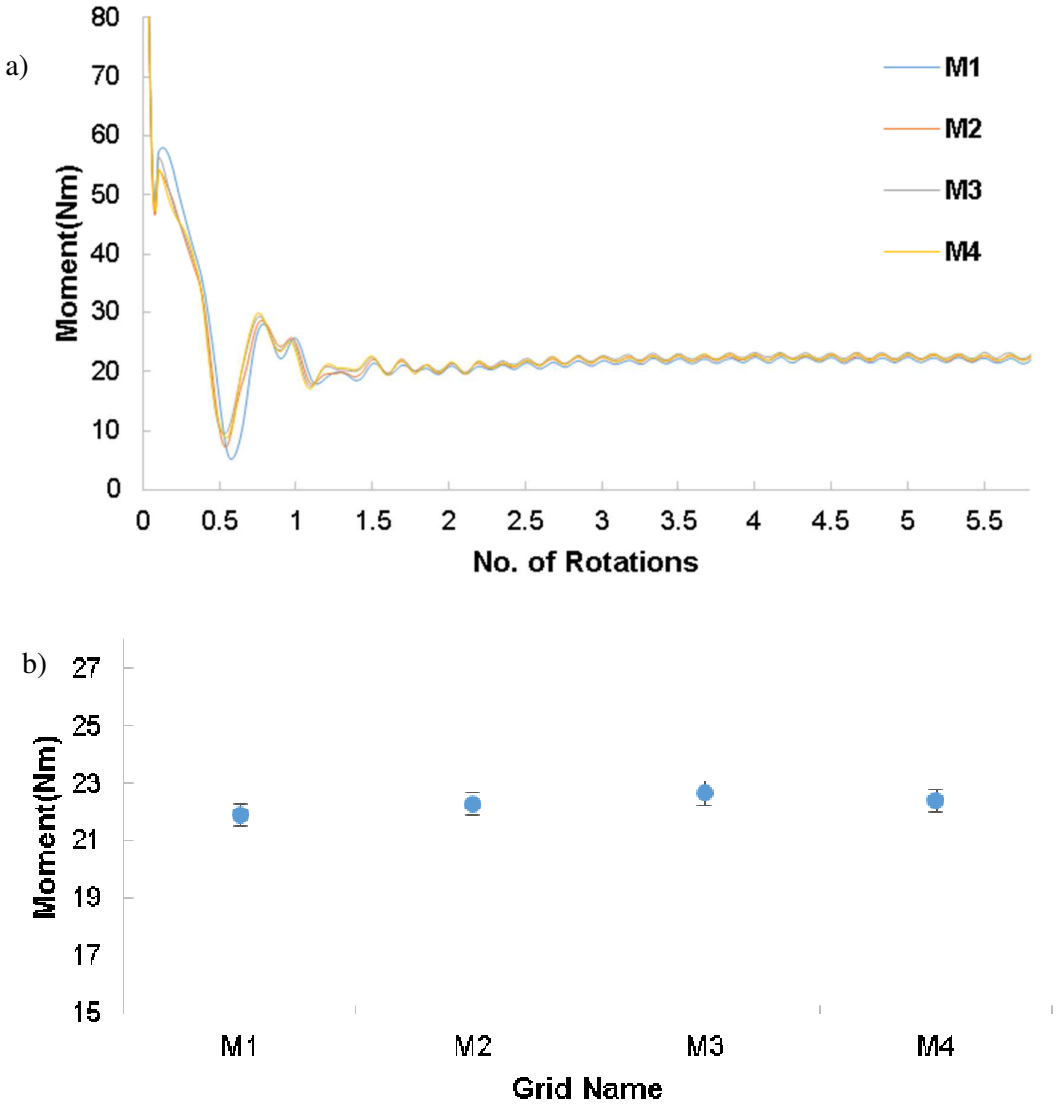


Figure 4.13 Moment on rotating walls of scoops a) vs. number of rotations b) values after achieving convergence

Table 4.5 Calculated average GCI values based on moment for each of the grids

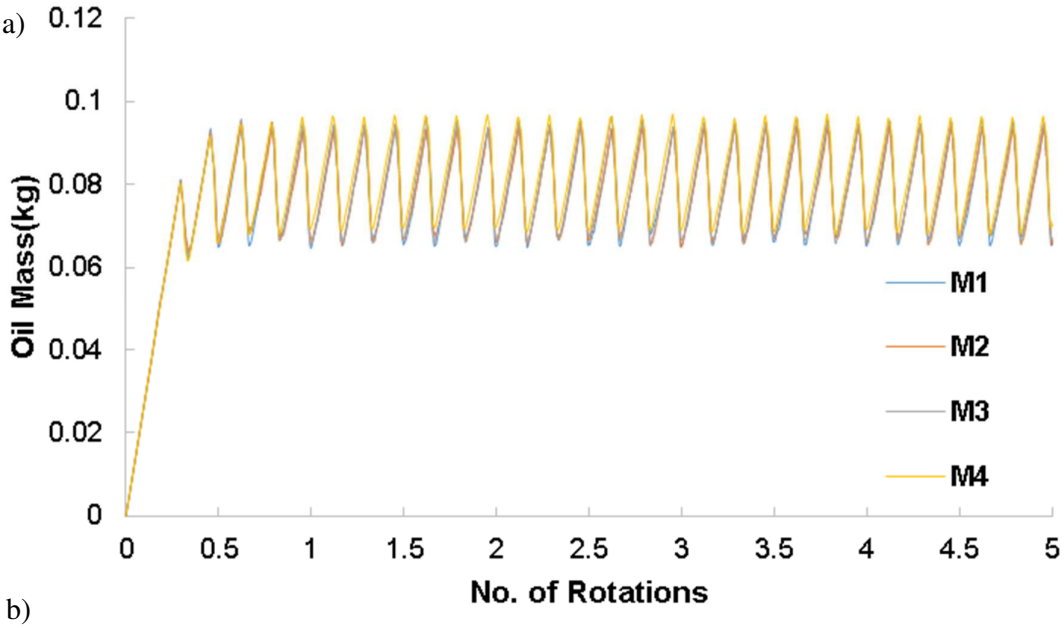
	M1	M2	M3	M4
Moment after convergence(Nm)	21.911	22.29	22.68	22.41
Relative error between converged values for two consecutive grids (%)	-	1.70	1.71	1.20
Average GCI considering last 110, 000 time steps (%)	-	4.10	1.74	1.12

Two phase grid dependence studies

For two phase studies the residence mass of oil in the domain and the oil capture efficiency of the scoops were chosen. It was observed that the residence oil mass in the system achieved convergence in few rotations compared to the capture efficiency. Figure 4.14a) shows the residence mass of oil in the system vs. number of rotations. The average of the errors bars is considered for the last 110,000 time steps and included in Figure 4.14b) after the oil residence mass has achieved convergence for each of the grids that were analyzed. From the figures it can be seen that there is very little difference between the grids as they are refined. However the coarsest grid, M1, tends to have values of the residence mass oil that deviate away from the values obtained on the finer grids.

Table 4.6 presents the calculated relative errors of the converged residence oil values between two consecutive grids using eq. (4.18) and the average GCI values for each of the grids based on the oil residence mass after achieving convergence over the last 110,000 time steps. It can be seen from table 4.6 that both the relative error and the GCI values are below 2% and this shows that the grids have acceptable values of discretization errors.

a)



b)

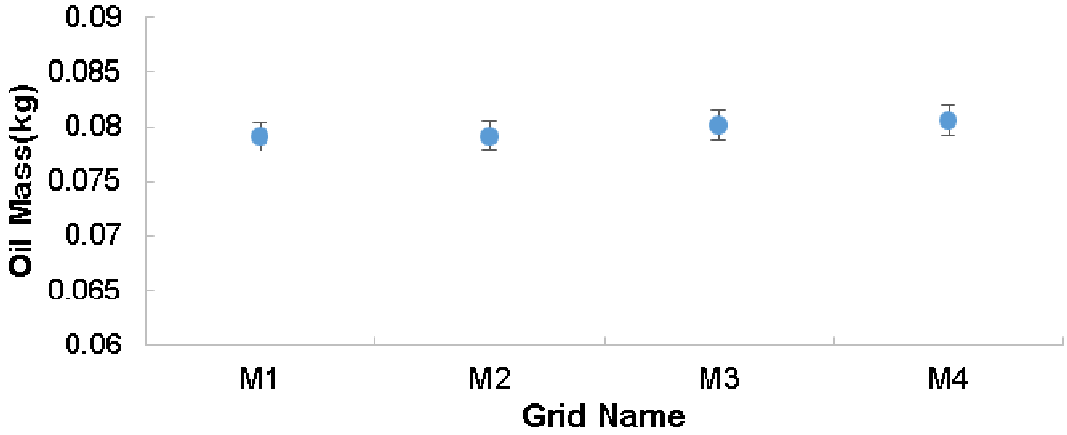


Figure 4.14 Oil Residence mass a) vs. number of rotations b) values after achieving convergence

Table 4.6 Calculated average GCI values based on oil residence mass for each of the grids

	M1	M2	M3	M4
Oil residence mass after convergence(kg)	0.0791	0.0792	0.0801	0.0805
Relative error between converged values for two consecutive grids (%)	-	0.126	1.12	0.497
Average GCI considering last 110, 000 time steps (%)	-	0.119	1.12	0.416

Figure 4.15a shows the capture efficiency of the scoops vs. number of rotations. The average of the errors bars is considered for the last 110,000 time steps and included in Figure 4.15b and shown after the capture efficiency of the scoops has achieved convergence for each of the grids that were analyzed. It is seen from Figure 4.15b) that between grids M3 and M4 there is very little difference in the values of the capture efficiency. Table 4.7 presents the calculated relative errors of the converged capture efficiency values between two consecutive grids using eq. (4.18) and the average GCI values for each of the grids based on the capture efficiency after achieving convergence. All the relative errors and the GCI values are close to 1% in table 4.7 which are considered to be acceptable.

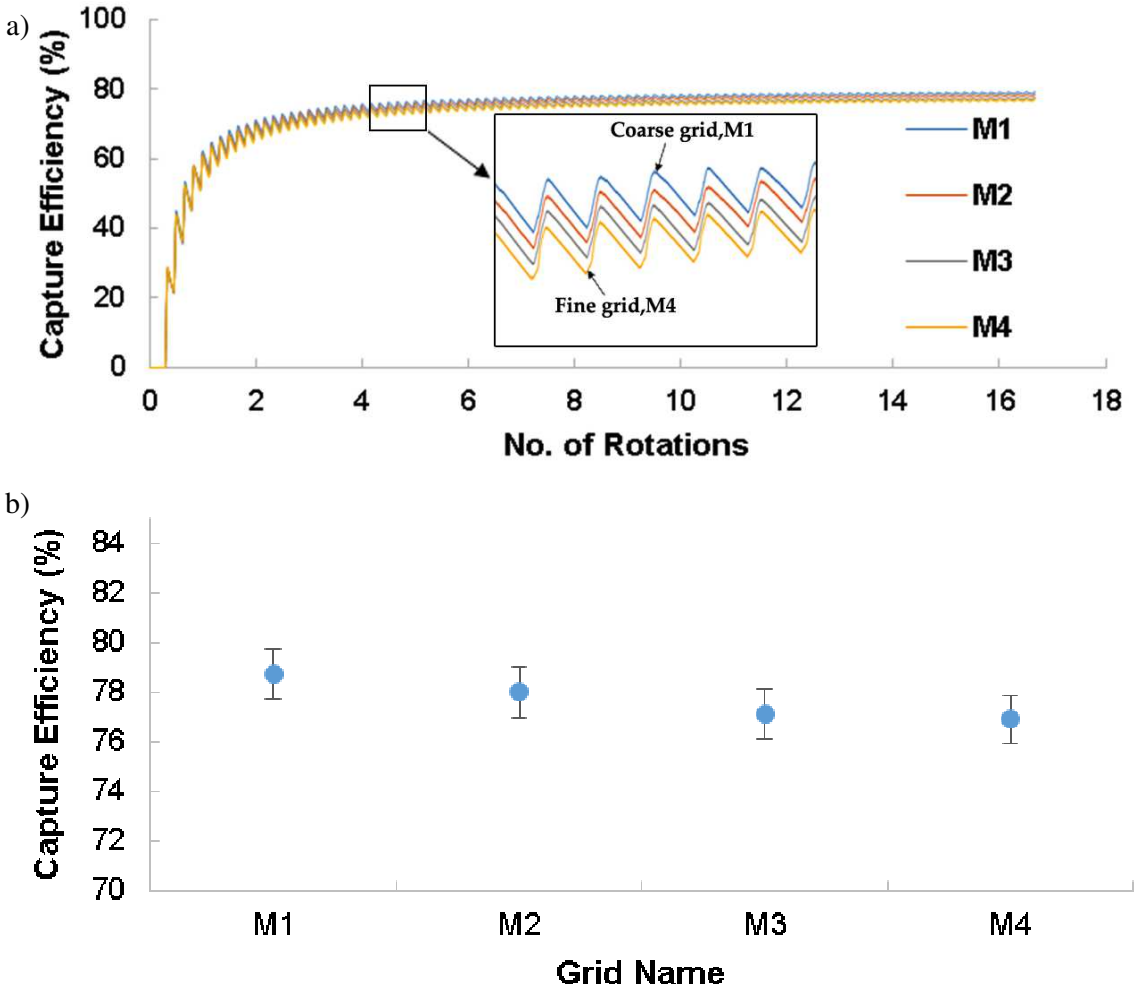


Figure 4.15 Capture Efficiency a) versus number of rotations b) values after achieving convergence

Table 4.7 Calculated relative errors and average GCI values based on capture efficiencies for each of the grids

	M1	M2	M3	M4
Capture Efficiency after convergence (%)	78.72	77.99	77.10	76.88
Relative error between converged values for two consecutive grids (%)	-	0.936	1.160	0.284
Average GCI considering last 110, 000 time steps (%)	-	0.914	1.010	0.261

It is observed from Figure 4.15a) that finer grids give slightly lower capture efficiencies. This is because of the oil droplet breakup process. With a coarse grid as seen in Figure 4.16 (which presents the slicing for different grids at the same time instant), the break of the droplets is less compared to using a finer grid. Hence there is more chance for the droplets to be uncaptured. Droplets that fall on the surface of the scoops tend to be centrifuged outwards. With a finer grid more droplets are centrifuged outwards and hence the capture efficiency is lower.

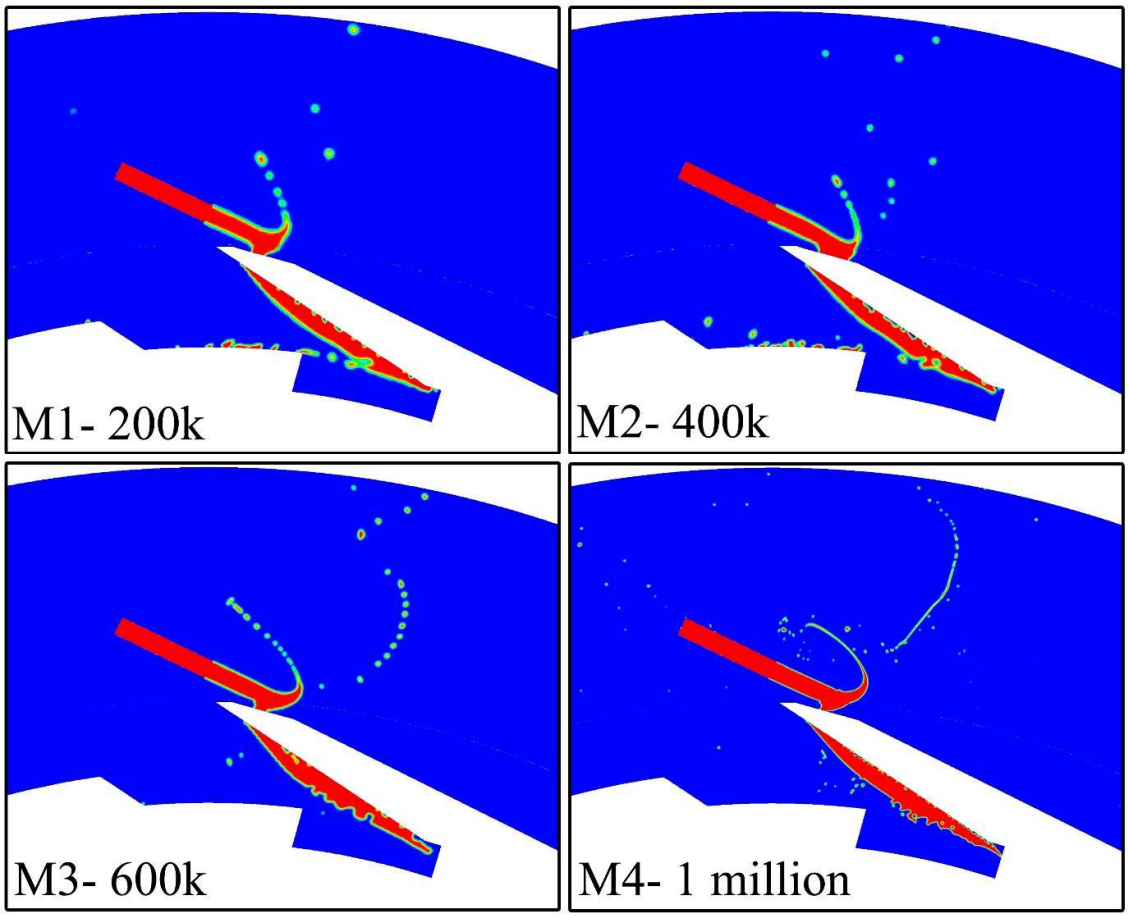


Figure 4.16 Slicing of oil jet for different grid sizes (red denotes 100% oil and blue 100% air).

4.4.2 Time dependence studies

In order to conduct time dependence studies grid M3 was chosen and simulations were conducted with 4 different time steps lower than $1x10^{-7}$s. The capture efficiency was analyzed for these four different time steps. However it was observed that there was no change in the capture efficiency when the time steps were lower than $1x10^{-7}$s. This is because the CFL condition is adhered to and the courant number is always less than 1 for all the time steps that were chosen. Since lower time step values did not change the capture efficiency, the highest time step value of $1x10^{-7}$s is chosen to carry out simulations.

4.4.3 Adopted grid

Based on grid dependence and time dependence studies grid M3 that comprised of 600k cells was chosen to carry the cases. When grid M3 is used there is a very slight over prediction of the capture efficiency when compared to using grid M4. The over prediction using M3 grid is quantified at around 0.284% as presented in table 4.7. This difference in the capture efficiency values between the two grids show that there is very little improvement in the prediction of the capture efficiency using a much finer grid. Furthermore the discretization error for grid M3 that is estimated using the GCI method is 1.01%. Hence it can be expected that the capture efficiencies predicted using grid M3 is not significantly away from the numerically converged solution. Although grid M4 offers better resolution in representing the oil jet breakup process there wasn't significant change in the capture efficiency values between M3 and M4 as seen in table 4.7. In order to minimize computational costs M3 was selected.

4.5 Computational Resources and HPC scaling study

Simulations were carried out using a high performance computing facility at the University of Nottingham. FLUENT was run in parallel using 40 computer nodes for each simulation. Each node consists of Two Intel Xeon E5 2670, 2.60 GHz (Sandy Bridge) Processors and 32Gbytes of RAM, with each processor providing 8 cores. It is important that optimum use of computational resources is done throughout the course of the PhD so that maximum number of cases can be run. Hence it was vital to conduct a HPC scaling study. Grid M3 was chosen to do this. The time required to compute 20 time steps for a two phase flow simulation is noted as the number of cores are increased. A plot showing the results is shown in Figure 4.17.

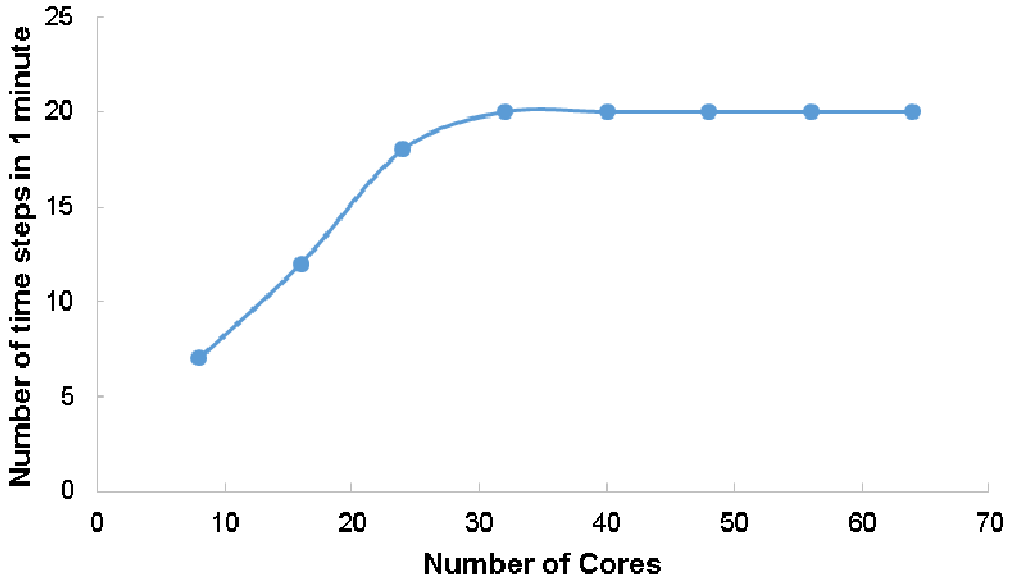


Figure 4.17 HPC scaling plot

It is seen that when the number of cores is above 40 there is no improvement in the calculation time and hence 5 machines which offer 40 cores is chosen to carry out simulations.

4.6 CFD analysis of the effect of shaft speed on capturing efficiency

A sample of the data obtained from the scoop outlet monitors at a shaft speed of 10000 rpm is presented in Figure 4.18. The flow of oil from each scoop creates pulses occurring at regular intervals. Summing the total mass outflow and dividing by the total mass inflow gives a value for capture efficiency that settles to a steady condition as the simulation progresses and this is illustrated by the sample plot in Figure 4.19. The section illustrated by η_{steady} is used to estimate the converged value of the efficiency.

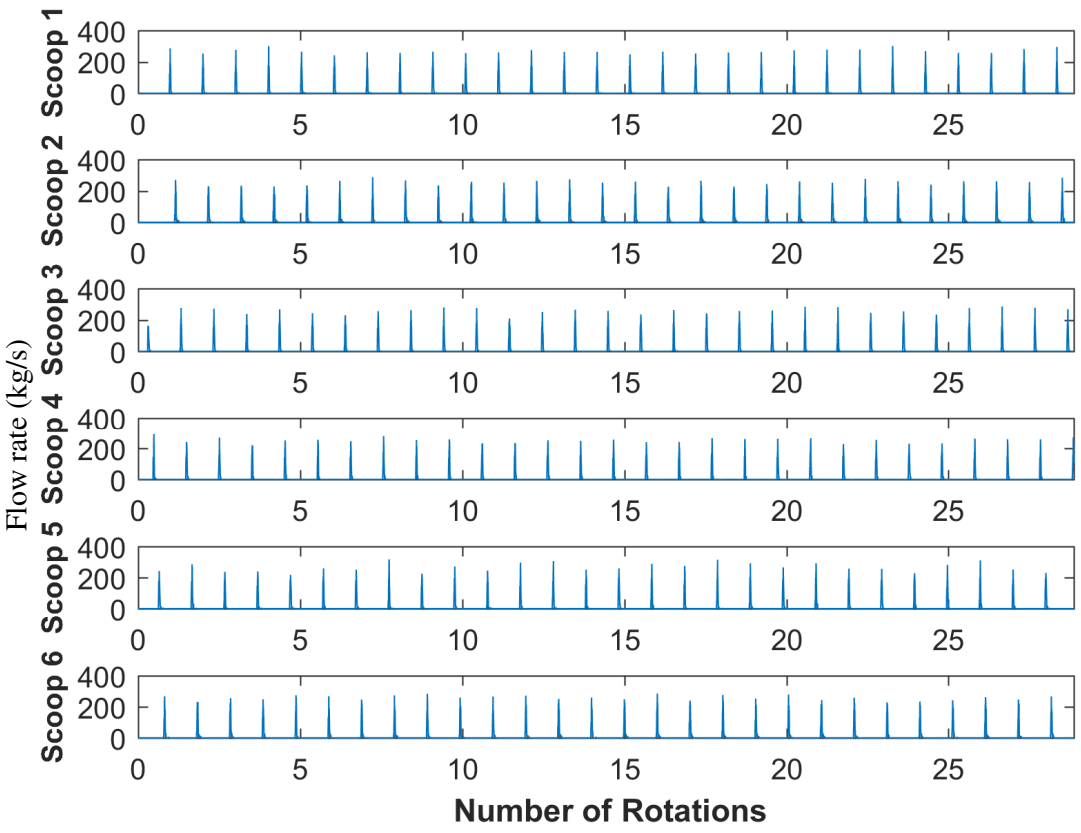


Figure 4.18 Mass flow rate from the 6 scoops at 10000rpm with a jet velocity of 22.381m/s

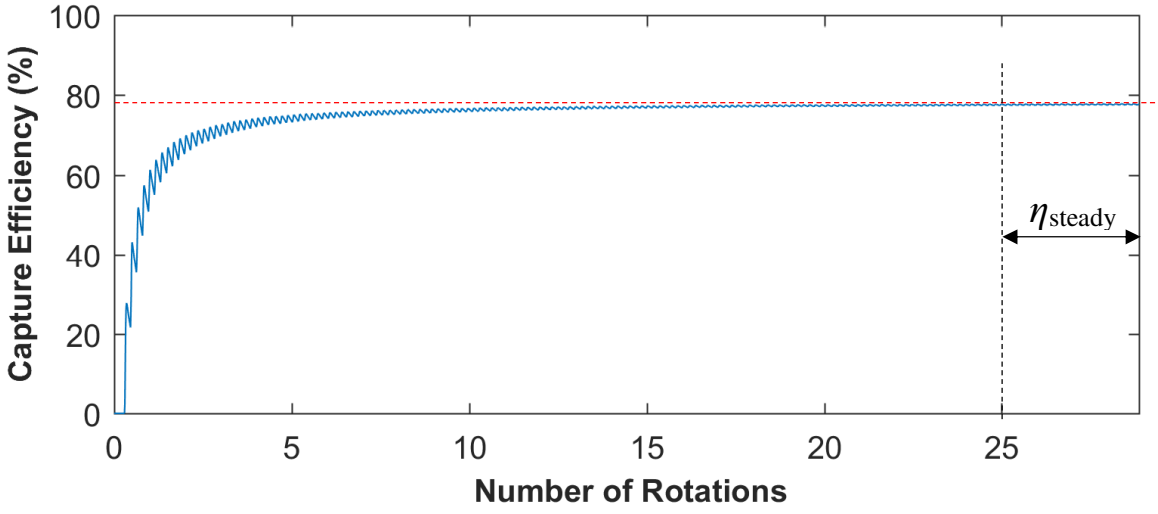


Figure 4.19 Capture efficiency vs. number of rotations at 10000rpm with a jet velocity of 22.381m/s

Contours of the oil phase volume fraction during capture are shown in Figure 4.20 for a shaft speed of 10000 rpm. The plume of oil noted by G2TRC researchers both computationally [41] and experimentally [5] is clearly seen following the slicing process. It is evident that an amount of oil primarily in the form of droplets formed during the slicing process of the jet is not captured. This loss reduces the capture efficiency below the 100% theoretically possible at this shaft speed. Oil droplets that have disintegrated from the core of the oil jet may interact with either the inner or outer rotor surfaces. They are then subjected to centrifugal forces and flung outwards. It is also observed that oil droplets that fall onto the surface of the rotor beneath the base of the scoop, centrifuge outwards and come into contact with the base of the scoop. The centrifugal effects induce them to slide out from the surface towards the tip of the scoop. Subsequently they exhibit a fountain like effect from the tip of the scoop as they slide out as shown in Figure 4.21.

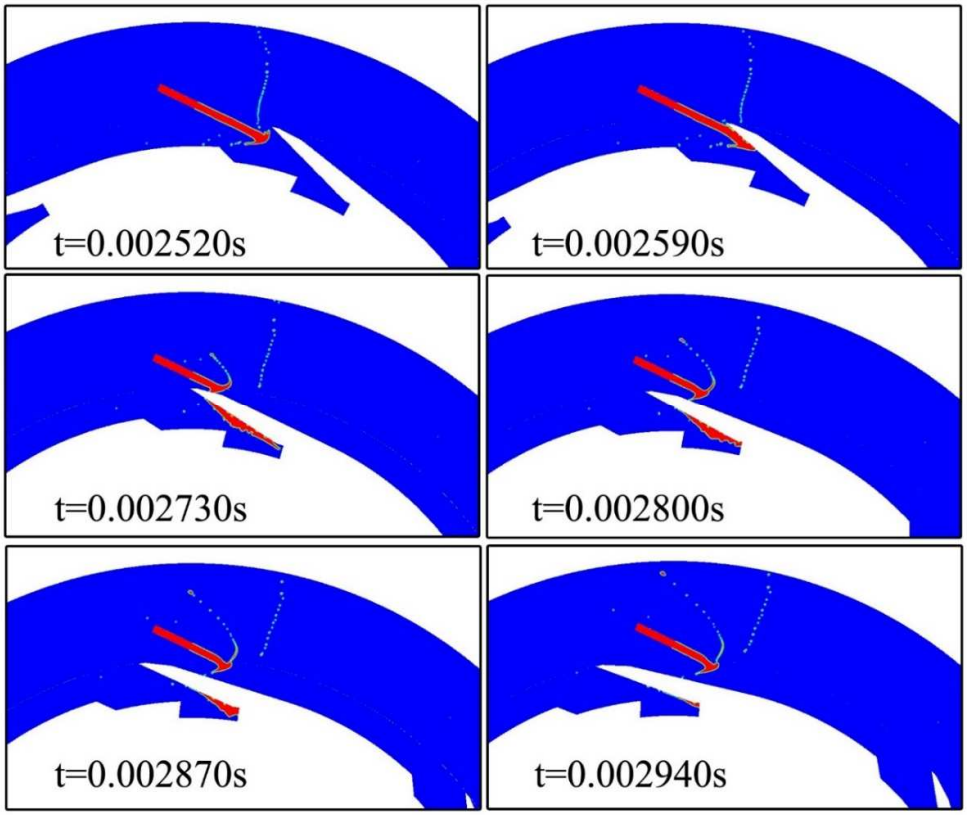


Figure 4.20 Sequence of oil volume fraction contours illustrating the slicing and capturing process at 10000rpm with a jet velocity of 22.381m/s (red denotes 100% oil and blue 100% air)

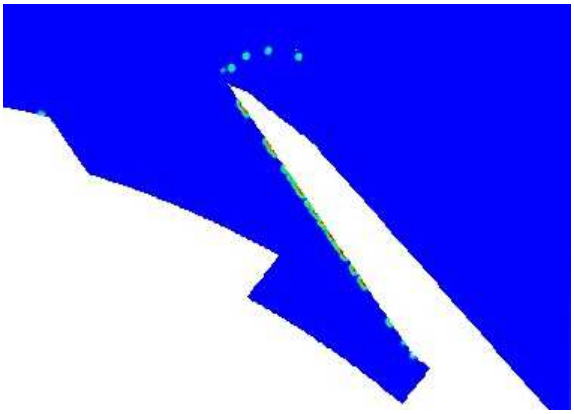


Figure 4.21 Oil being centrifuged out as the scoop rotates (red denotes 100% oil and blue 100% air).

Figure 4.22 shows the variation of capture efficiency with rotational speed obtained from CFD and experiments[5]. It observed that the efficiency of the scoop system increases sharply as the rotational speed increases towards the threshold speed and then decreases steadily with shaft speed. With reference to Figure 4.6 and Figure 4.7 we note that with increasing shaft speed, distance C_X decreases as does the angle over which the jet is in contact with a scoop. Both of these were noted as likely to lead to reduced capture efficiency as a consequence of more oil being deflected in the plumes associated with each slicing event[7] and more oil leaving the scoop through centrifugal effects.

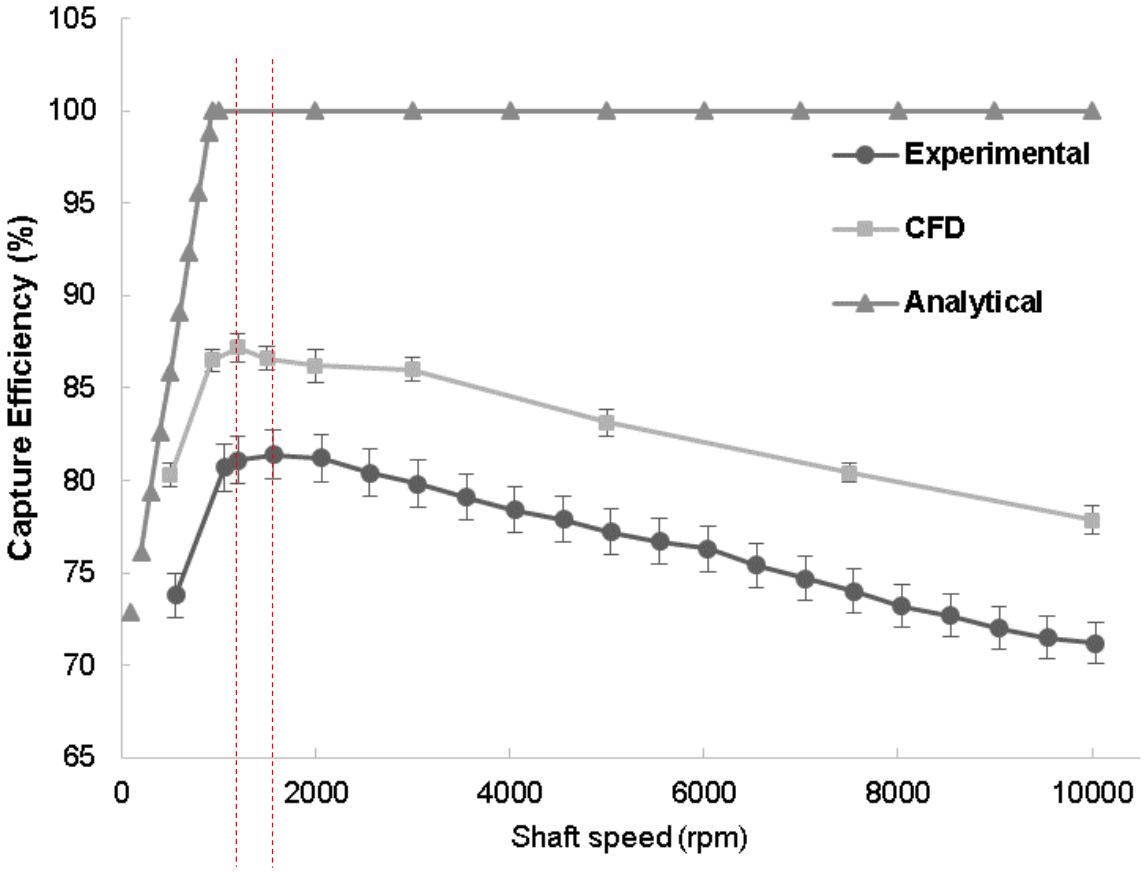


Figure 4.22 Capture Efficiency(from CFD, analytical study and experiments[5]) vs. shaft speed

As shown by the simplified analytical analysis in section 4.2 at low rotational speeds there is an angle, through which oil is uncaptured. This is illustrated in Figure 4.23 which shows part of the capturing process at 500 rpm. The oil jet crosses the outer radius of the scoop at two points as anticipated from the theoretical analysis presented. When the scoop slices the jet at the first point, there is a quantity of oil that is not captured as shown in Figure 4.23. Hence this leads to reduced captured efficiencies at low shafts speeds. It is also seen that as the oil jet interacts with the outer surface of the scoop system there is some alteration in its path and the jet is deflected.

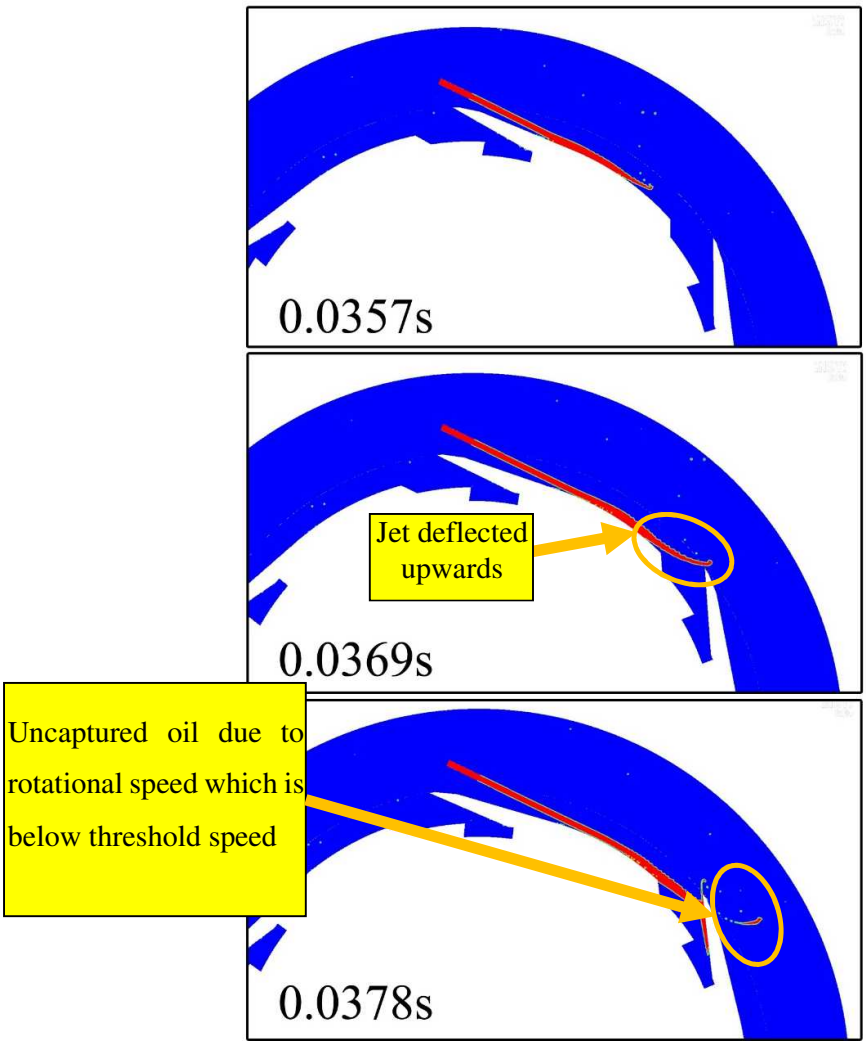


Figure 4.23 Oil loss at 500rpm (red denotes 100% oil and blue 100% air)

At shaft speeds above the threshold value, it is observed that as the shaft speed is increased, the strike point gradually shifts inboard relative to the tip of the scoop till the shaft speed is around 5000rpm. As the shaft speed is increased above 5000rpm, the point at which the jet strikes the scoop moves closer towards the tip of the scoop. There is a considerable difference between the C_x values estimated analytically and using CFD as seen in Figure 4.24. In CFD the values are much lower because the jet is deflected upwards due to the momentum of the air that pushes the jet upwards and deflects its path. Hence the jet strikes the scoop closer to the tip of the scoop in CFD and distance C_x estimated using CFD is smaller compared to analytical estimation. However both analytically and in CFD it is observed from Figure 4.24 that the values of C_x at the strike point reduce as the shaft speed is increased beyond 5000rpm. When

the jet strikes the scoops closer to the tip, it may lose momentum on its path to the outlet of the scoop where it is ingested. If the momentum of the jet is lost, then portions of the jet, which have not been ingested by the scoop may be centrifuged outwards without getting captured.

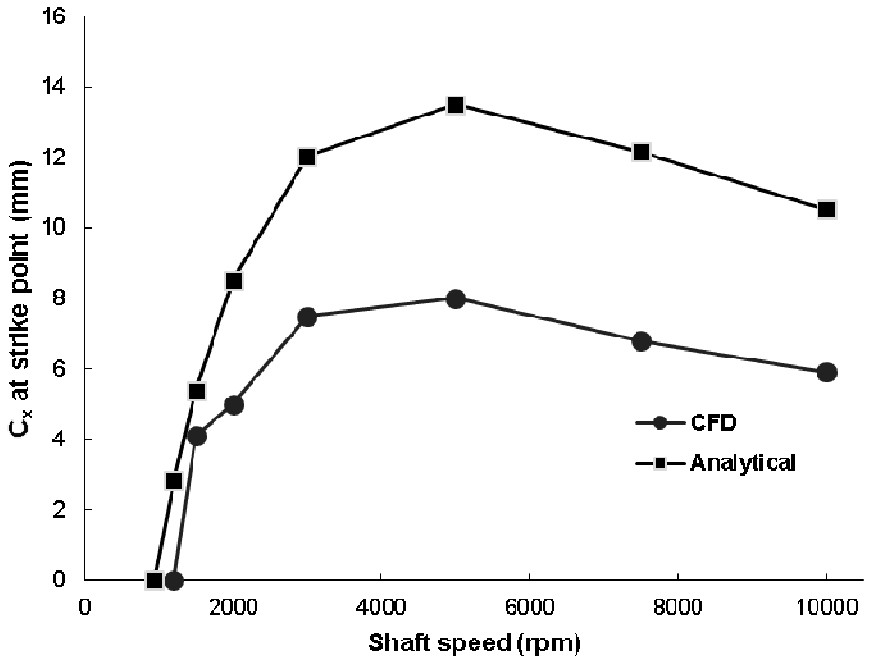


Figure 4.24 C_x at strike point for a jet velocity of 22.381m/s and a jet angle of 64.2°

The strike point for higher shaft speeds is illustrated by the contours images from CFD in Figure 4.25 which shows for shaft speeds of 5000, 7500 and 10000 rpm. It is seen that the strike point moves closer to the tip of the scoop as the shaft speed is increased.

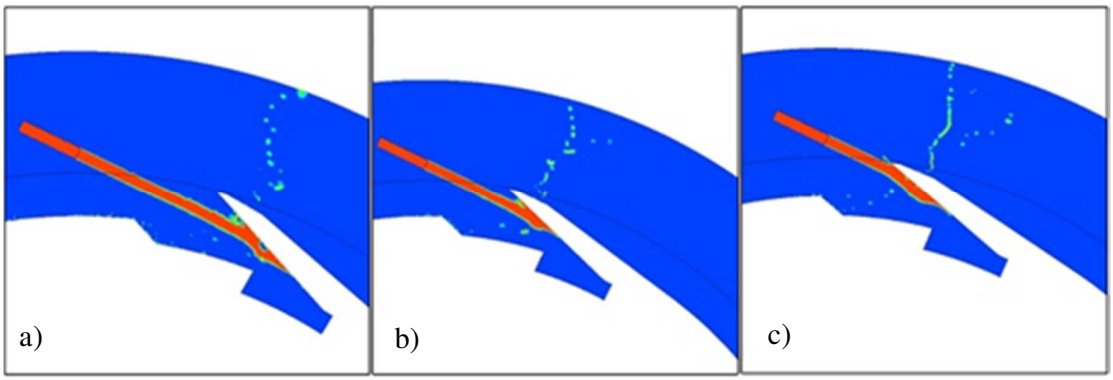


Figure 4.25 Collision points in CFD a) 5000rpm b) 7500rpm c) 10000rpm (red denotes 100% oil and blue 100% air)

A phenomena that is observed from CFD results is the pluming effect of the tip of the oil jet. In [7] this has been linked to the shedding of vortices from the scoop tips causing a pressure field that encourages pluming and scoop tip modifications are proposed to reduce vorticity. The frequency of vortex shedding from the tip of the scoop increases linearly with shaft speed as seen in [7] and has an associated Strouhal number of 0.13. This linear increase of vortex shedding leads to a linear decrease in capture efficiency as shaft speeds increase above the threshold shaft speed. The value of the CFD study is highlighted by the way oil loss mechanisms can be seen and examined. In particular the centrifugal and pluming losses identified using CFD are consistent with high speed imaging from the experiments. An illustrative image from the experimental study and CFD is shown in Figure 4.26 that shows the pluming of the oil jet.

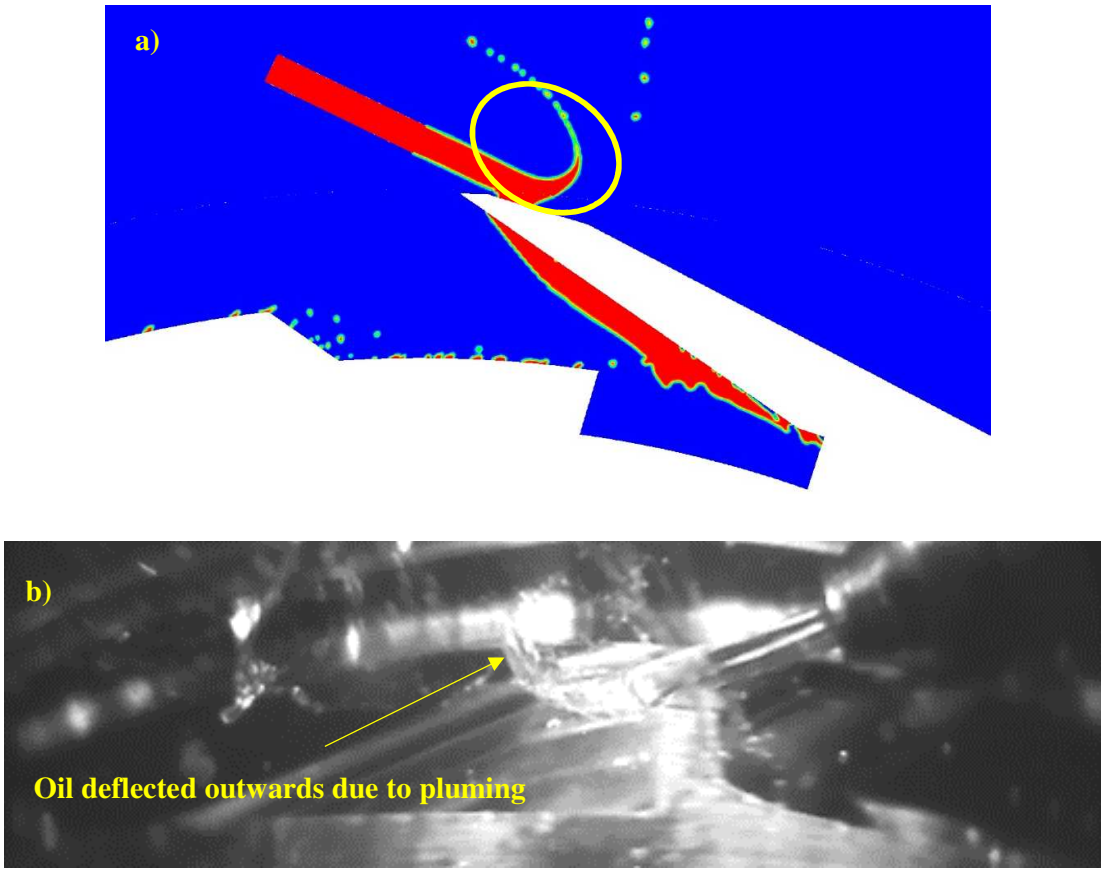


Figure 4.26 Illustrative image showing jet pluming a)CFD(red denotes 100% oil and blue 100% air) b)Experimental visualization[5]

CFD and experiments

The maximum difference in capture efficiencies predicted using the 2D CFD models is 5.5% compared to experimental data, noting experimental uncertainty is estimated as ± 1.6%[5]. Furthermore, it is noted that the CFD results follow a similar trend to the experimental results. Based on the theoretical analysis, it was calculated that the threshold speed is 934 rpm. However, both experimentally and using CFD it is seen that the capture efficiency continues to increase until 1500 rpm. At no point does capture efficiency reach 100%, neither experimentally nor in CFD. This indicates other factors as discussed contribute to reduced oil capture efficiency.

The numerical simulations, which were conducted in 2D, cannot have a good representation of the circular cross section jet of the experiments and this is likely one of the reasons why the CFD slightly over-predicts capture efficiency. The cross-sectional area of the jet in a 2D jet is in the shape of a rectangle and in 3D it is circular. For a jet of diameter, d, the cross-sectional area is greater in 2D than in 3D. Therefore the inlet flow rate is higher in 2D than in 3D and this could be a possible reason for the over prediction of the capture efficiency. Although 3D can eliminate this over prediction, the computational cost associated with a 3D simulation is infeasible for design purposes and it is therefore very encouraging to see trends well captured here and also that that the 2D model yields data only a few percent different to experimental data.

It is seen that the threshold speed of 934 rpm calculated from the analytical study is different from the threshold speed of 1500rpm and 1200rpm observed in experiments and CFD respectively. The most likely reasons for this are:

- Pluming of the jet due to vortex shedding [7] and jet deflection at low rotational speeds due to collision with the scoop drum are not taken into account in the analytical study. The contact of the jet with the drum causes the path of the jet to deflect from the theoretically predicted straight line path as seen in Figure 4.27. Hence the scoops have to rotate faster than the analytical threshold speed to capture portions of the jet which have been deflected further upwards.

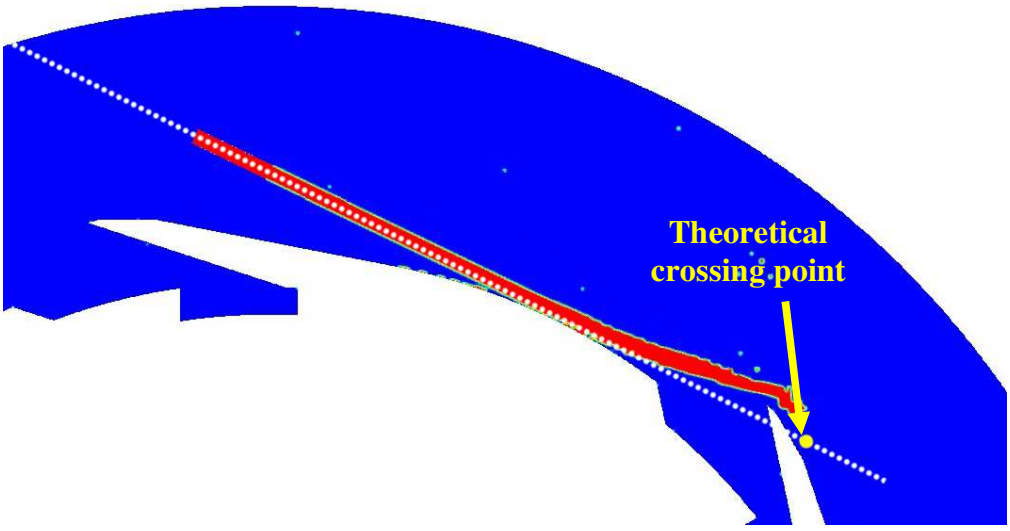


Figure 4.27 Jet deflected from the theoretical path at 1000rpm (red denotes 100% oil and blue 100% air)

- Jet diameter is not included in the analytical model. If the jet is considered to have a diameter, *d*, for the theoretical analysis as shown in Figure 4.28, there will be a portion of the jet that is not within the outer radius of the scoop, when the scoop meets the theoretical thin line representation of the jet (shown as a red line in Figure 4.28) at C (tip of scoop) at the threshold shaft. This portion of the jet within the region formed by the points A, B and C in Figure 4.28, will be uncaptured as the scoop rotates from point C to A. In order to fully capture this portion, the proceeding scoop should rotate faster that the threshold shaft speed that is estimated analytically.

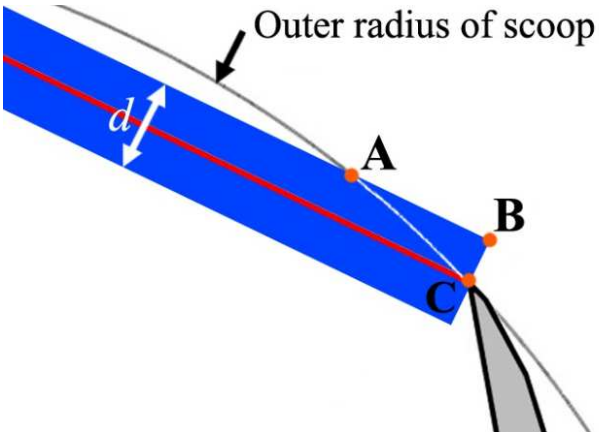


Figure 4.28 Consideration of jet diameter, *d*, for theoretical analysis

- Shaft speeds between 1000 rpm and 1500 rpm were not experimentally investigated and thus the peak could be closer to the analytical value. In CFD the maximum capture efficiency is observed at 1200rpm.

4.7 Significance of 2D studies

Figure 4.29 shows a 3D grid generated for the geometry that has been simplified for 2D studies presented in this chapter. A core cell sizing of 1mm and a tetrahedral mesh is used throughout this domain. The number of cells in the domain is 22 million. Based on the author's research work[68][69] and experience with 3D domains, when this sort of grid is converted into a polyhedral type grid, the grid size will reduce to around 5 million cells. It should be noted that when a tetrahedral mesh without any hexahedral type cells, the grid will reduce by a factor of around 4.5 when converted to a polyhedral mesh. Hexahedral cells cannot be converted to a polyhedral cell. Hence, if inflation layers are applied at the walls they will not be affected during the conversion process. A polyhedral mesh comprising of 5 million cells will take around 25mins to calculate 20 time steps for a two phase flow simulation using 192 cores of a HPC. To simulate 30 rotations of the system while maintaining a CFL number of less than 2 is computationally expensive.

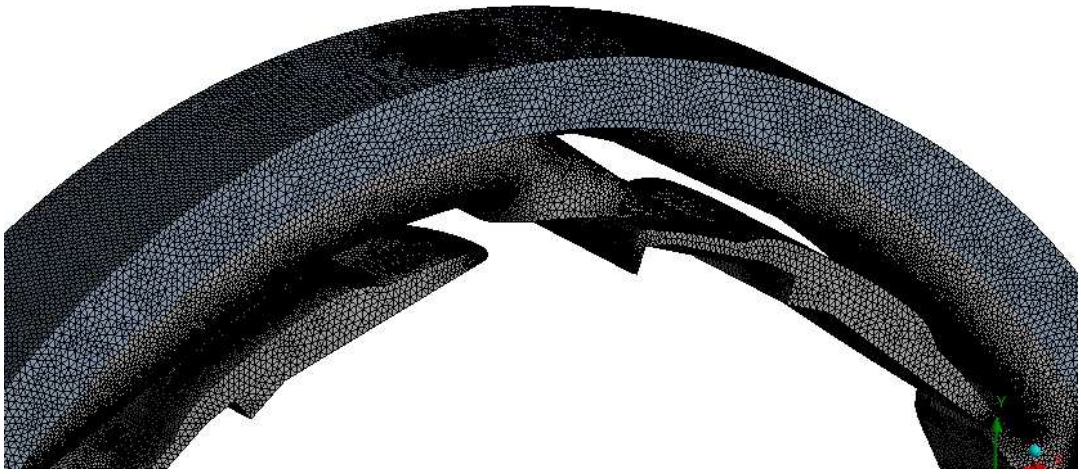


Figure 4.29 Tetrahedral grid of 3D scoops domain

Furthermore it should be noted that, a core cell size of 1mm is not sufficient to resolve the droplet break up process. In the grids used in 2D studies in this chapter, core cell sizes are 0.2mm. If a grid of 0.2mm core cell sizing is used in 3D the estimated total size of the domain

will be over 120 million cells when a tetrahedral mesh is generated. Following conversion to a polyhedral grid, the size will be over 24 million. Running simulations with the computational facilities that are accessible currently, it is practically impossible to simulate a case of this sort mainly due to the high computational costs and time that are involved.

Robust meshing softwares such as ANSYS ICEM offer great control for local meshing of the domain and can aid to reduce the overall size of the grid. Adaptive meshing in ANSYS FLUENT can also be used to coarsen and refine the grid dynamically at the expense of additional computational time as the simulation progresses. However despite these available features, the overall grid size cannot be reduced below 15 million very easily when a core cell size of 0.2mm is used.

This is where 2D simulations prove to be a major advantage. It can be argued that there are several discrepancies and many features of the flow such the circular jet being modelled as a rectangular one in 2D is too much of an oversimplification. However, the discrepancies from experimental results are within 6.6% for all the results produced using 2D simulations as observed in this chapter and the trends in behavior observed CFD is the same. Hence, throughout the course of this PhD, simulations are carried out in 2D and validated wherever possible with reliable experimental results.

Conducting simulations in 2D has also helped analyze several numerous types of geometries, configurations and operational conditions which would have not been possible if a 3D grid was used. If a 3D grid was opted for, only few cases could have been assessed throughout the course of this PhD.

4.8 Chapter conclusions on the effect of shaft speed on capture efficiency

In this study, the effects of shaft speed on the performance of a scoop based lubrication system are investigated in detail using analytical and numerical approaches. A scoop geometry investigated experimentally[5] at G2TRC was chosen for the modeling.

A simplified theoretical analysis was conducted to understand the relationship between the shaft speeds and capture efficiency. This yields insight with regard to the effect of shaft speed on the point of jet impact on the scoop and also the amount of oil collected by each scoop. A threshold velocity ratio is identified above which it is theoretically possible to capture 100% of the oil delivered by the jet. The shaft speed at which maximum capture efficiency occurs does not correspond with the threshold value, but occurs at a somewhat higher shaft speed. In the configuration examined here the threshold shaft speed was 934 rpm and the maximum capture efficiency was at around 1500 rpm. The observed trend of reduced capture efficiency with increasing shaft speed beyond the point of maximum capture is consistent with experimental data and can to some extent be linked to the geometric factors identified by simplified analytical approach.

The 2D CFD model consistently over predicts capture efficiency compared to experiment with a maximum difference of 6.64% for the 10000rpm case. However, trends are well represented and thus 2D CFD modelling can be regarded as sufficient for preliminary design purposes. The limitations of representing a round jet in 2D is identified as the most likely cause of the discrepancies. This chapter contains published data in Journal of Turbomachinery(doi:10.1115/1.4040812)[5] and ASME Turbo Expo 2018 proceedings in paper GT2018-76177[6] .

5 Effect of geometry and operating conditions on scoop capture efficiency

5.1 Overview

This chapter presents investigations done on various geometrical parameters which include the jet angle, constriction gap and the number of scoops. The jet angle and the constriction gap are shown in Figure 5.1. The effect of the jet velocity and also applying a low pressure in order to create a differential pressure across the scoops is investigated.

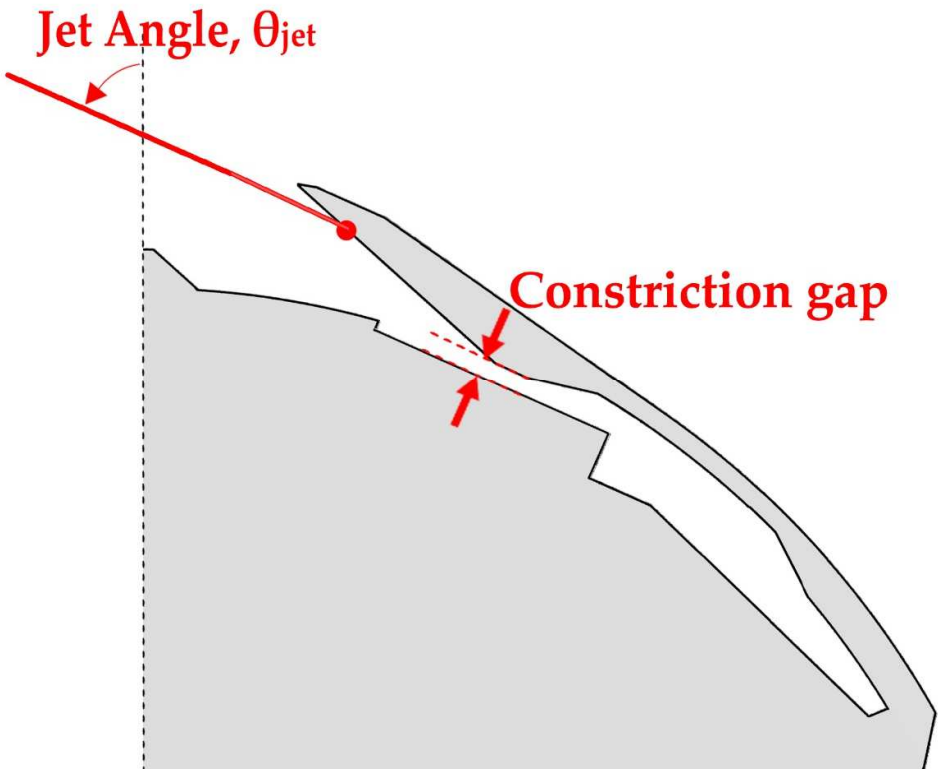


Figure 5.1 Constriction gap and Jet angle

Sufficient confidence in numerical modelling of the scoops has been gained due to observed trends in CFD that match with the trends in experiments as seen in Chapter 4. Hence other areas for which experimental results were not available were investigated using CFD. This included changing the number of scoops and simulating the effect of applying a low pressure at the scoop outlet. The significance of the work presented in this chapter lies in the advantage

of analyzing and highlighting the reasons as to why capture efficiencies vary with different geometrical conditions and operating conditions. This is not viable in experimental research due to the complications involved in installing the measuring and visualization equipment that would be needed.

Mesh and time dependence studies were conducted based on the method detailed in Chapter 4 and will not be presented again in this chapter. However, for all the plots shown error bars due to the discretization error are included.

5.2 Effect of constriction gap

The effect of the constriction gap shown in Figure 5.1 is investigated for three different values. This design variable is important because of the potential radial clearance and the reduction in the overall diameter of the scoops that might be achieved with a smaller constriction gap. This will eventually lead to a lower weight of the scoops. Although there is only a difference of 1mm between the values that have been investigated, it should be noted that 1mm reduction in the radius of the scoops is a reduction of 2mm on the overall diameter.

Figure 5.2 shows the variation in the capture efficiency as a function of constriction gap for different shaft speeds. The jet angle used is 64.2^{o} and the jet velocity is 22.381m/s. It can be seen that there is a similar trend in the capture efficiency increasing as the constriction gap is increased in both CFD and experiments. There is a slight increase in the capture efficiency as the constriction gap is increased from 2mm to 4mm.The lower capture efficiency observed in Figure 5.2 when using a gap of 2mm compared to 4mm is because of the droplets that are centrifuged outwards. The droplets that are centrifuged outwards are evident from volume fraction contours and CFD animations.

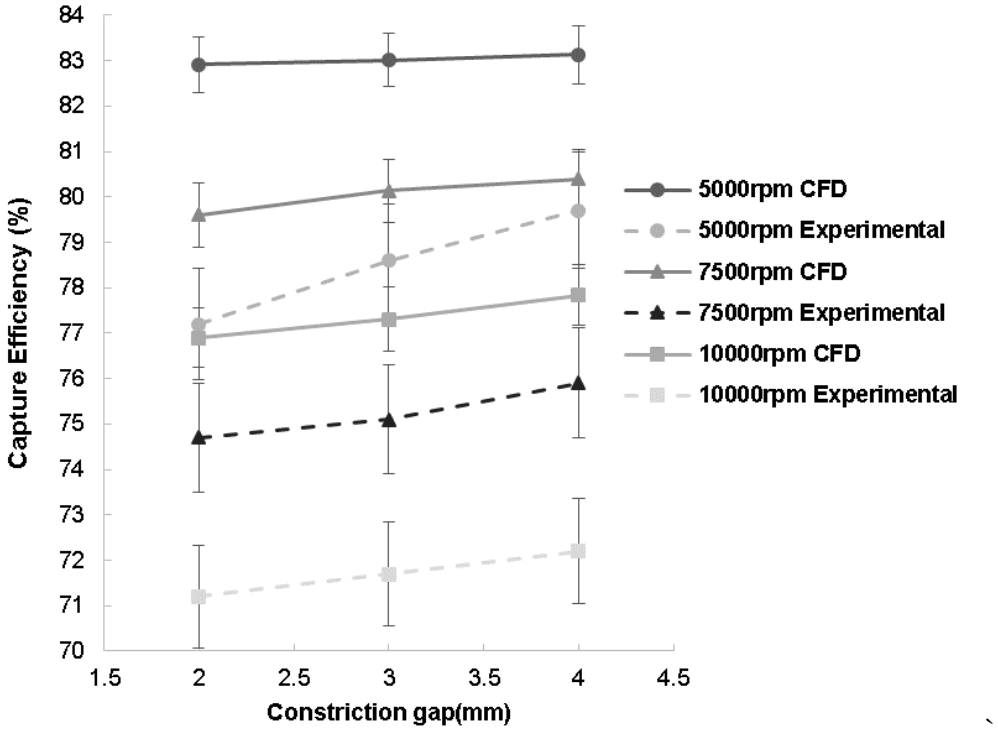


Figure 5.2 Effect of constriction gap on capture efficiency. Experimental data is obtained from[5]

Figure 5.3 shows the volume fraction and pressure contours at the same time instant for the different constriction gaps investigated. It is seen that when oil is captured by a scoop with a constriction gap of 2mm, there is restricted flow of oil from the outlet compared to all the other gaps which are larger. Due to the size of the constriction gap, there is a buildup of oil and a pressure increase at the outlet region. The high pressure region close to the outlet of the scoop restricts the flow of oil out from the scoop compared to when using a larger constriction gap. The oil loses considerable momentum as a result. Since oil is not emptied quickly, it leads to oil being rebound outwards and centrifuged as the scoops rotate. Figure 5.3 also shows that with constriction gaps of 3mm and 4mm the oil flows out the scoop without any disruption in the flow. This reflects on the lower pressure close to the outlet of the scoop when compared to using a gap of 2mm.

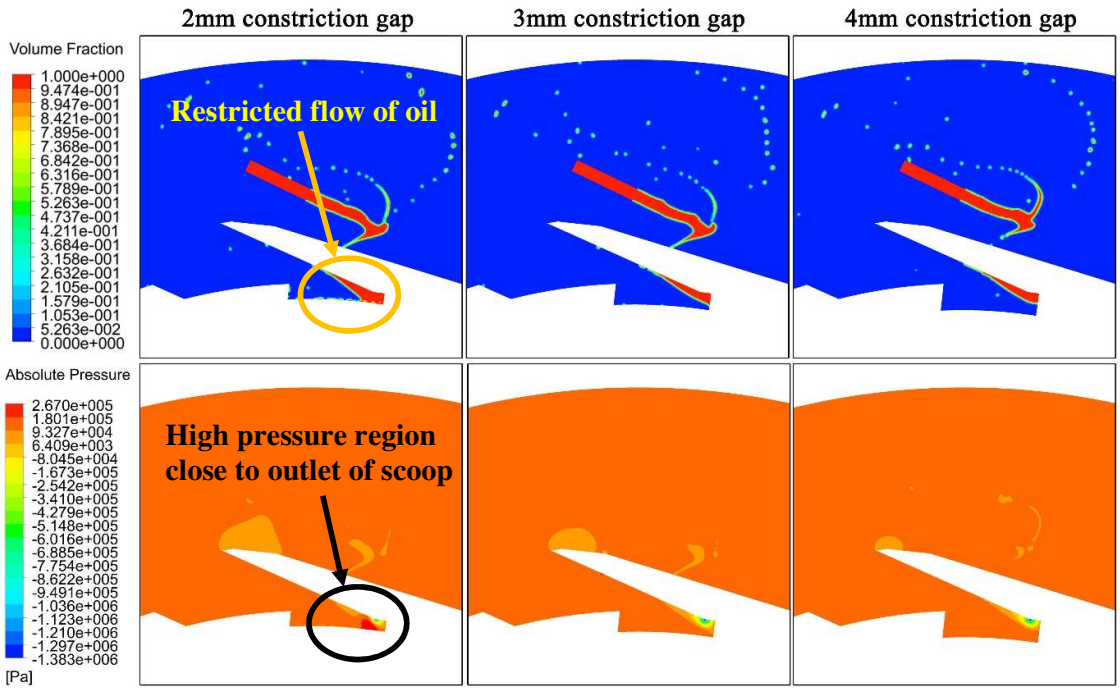


Figure 5.3 Volume fraction and pressure contours of oil after the slicing process of oil jet shown for the three gaps at 7500rpm at the same time instant.

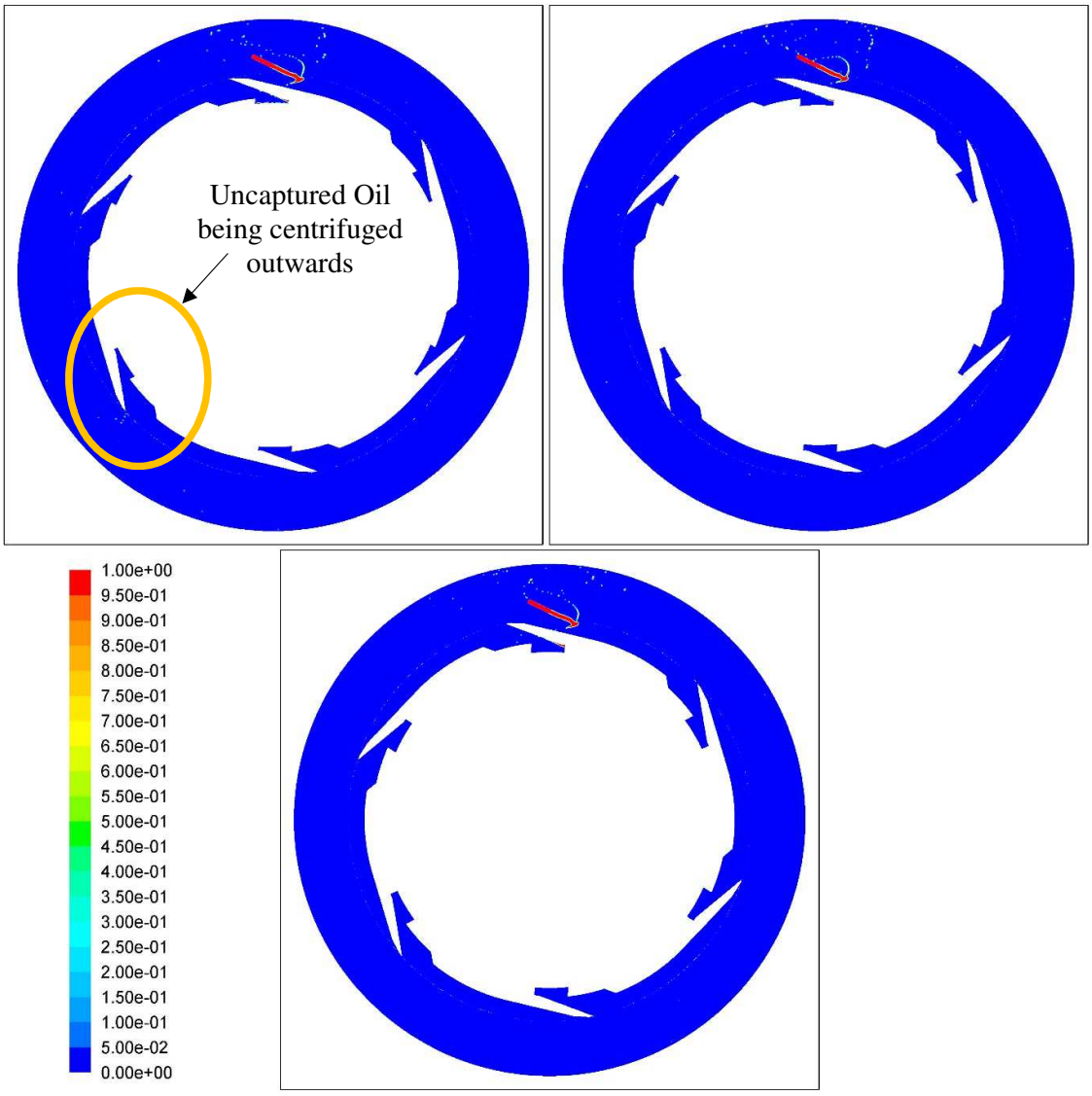


Figure 5.4 Scoops at the same time instant after capturing oil at 7500rpm shown using volume fraction contours of oil.

5.3 Effect of varying the jet velocity.

The effect of using a jet velocity lower than the threshold velocity for different shaft speeds is investigated in this section. Tests are conducted using a tandem jet configuration where an additional jet is placed in front of the existing jet with an angle of 10° circumferentially away. This is done to represent an alternate aero-engine configuration. Figure 5.5 shows the geometry and associated dimensions of the tandem jet configuration.

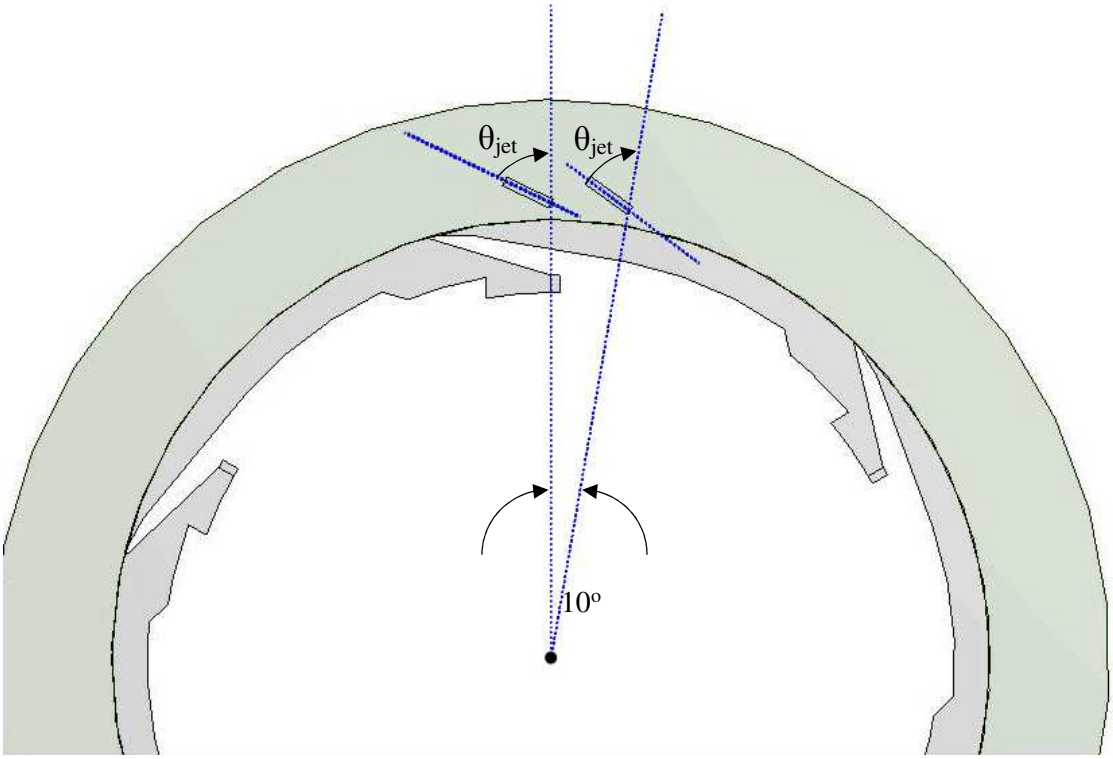


Figure 5.5 Geometry of single tandem jet that are 10° circumferentially apart.

Table 5.1 shows the velocity ratio and the corresponding jet velocities used for the shaft speed investigated in the experiments. It also states the analytical threshold jet velocity for each shaft speed. The jet velocity should be lower than this speed to ensure that there are no uncaptured portions of oil by the proceeding scoop due to the "loss angle" shown in section 4.2 from chapter 4. In all the experimental tests[5] the jet velocities used are significantly lower than the analytical threshold jet velocity. Hence, no portion of the jet is expected to be uncaptured by a proceeding scoop. In order to calculate the threshold jet velocity, with reference to Figure 4.1, the time for the jet to travel from A to B, should be equated to the time required for the

proceeding scoop to rotate through angle θ_4. It can be shown that the analytical threshold jet velocity is

$$V_{\text{jet}_{Thr}} = \frac{2R\omega sin\left(\frac{\theta_2}{2}\right)}{\theta_4} \quad \textbf{(5.1)}$$

It can be shown the analytical threshold jet velocity for the geometry investigated and a shaft speed of $\omega = 1047\ \text{rad/s}\ (10000\text{rpm})$ is 240.21 m/s.

In Table 5.1 it is seen that a velocity ratio of 4.80 is used for a shaft speed of 10000rpm compared to the velocity ratio for all other shaft speeds which are constant at 4.43. The reason for this is because the jet velocity is constrained by the experimental setup which has a limitation on the jet velocity.

Table 5.1 Tested experimental casses for investigations on varying the jet velocity[5]

Shaft speed(rpm)	**Velocity Ratio, VR=$\frac{r\omega}{V_{jet}}$**	**Jet velocity in experimental test (m/s)**	**Analytical threshold jet velocity for the shaft speed(m/s)**
500	4.43	1.23	12.14
1000	4.43	2.41	24.27
2000	4.43	4.82	48.55
3000	4.43	7.23	72.83
5000	4.43	12.10	119.74
7000	4.43	16.92	167.65
10000	4.80	22.25	240.21

Figure 5.6 shows the variation in the capture efficiency with the shaft speed and also the jet velocity that has been used. A jet angle of 64.2^o with the tandem configuration and a constriction gap of 4mm is used.

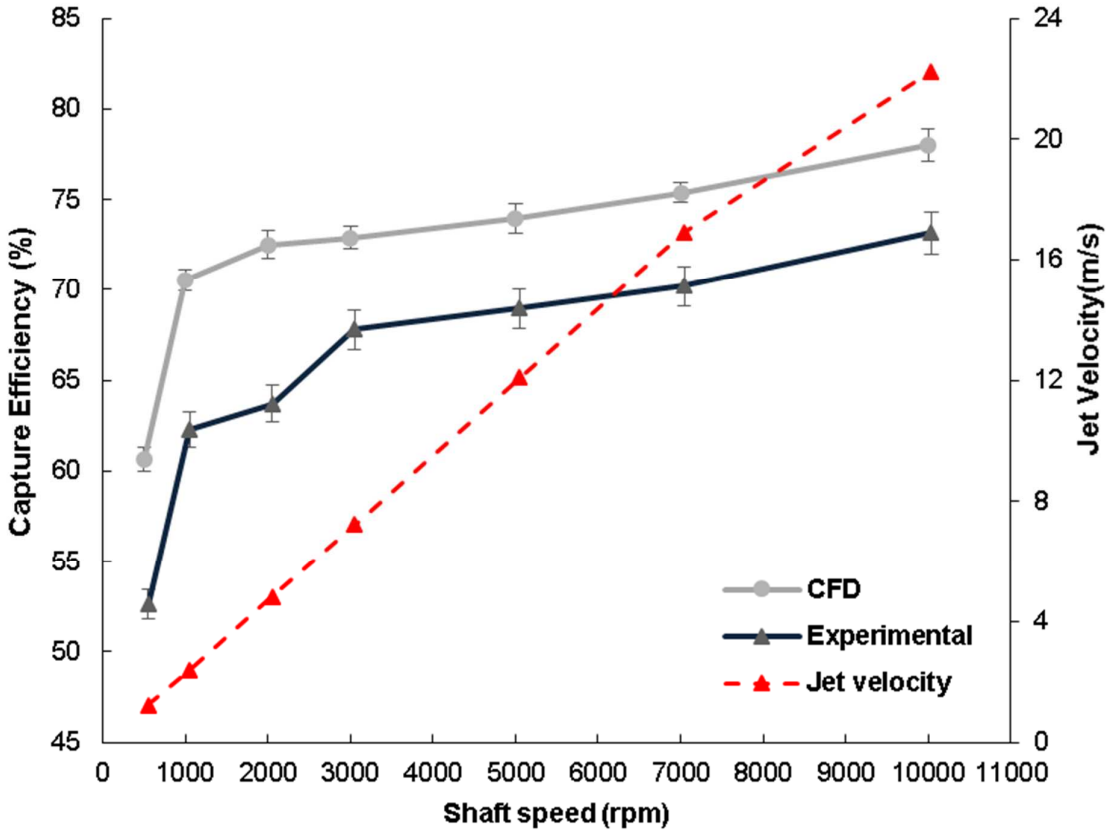


Figure 5.6 Capture Efficiency vs. shaft speed for varying jet velocity shown for CFD and experiments[5].

It is seen from Figure 5.6 that although at lower shaft speeds, where there is no uncaptured oil by the proceeding scoop after the slicing of the oil jet, the efficiency is still low compared to higher shaft speeds. There is sharp increase observed in the capture efficiency between 500rpm and 1000rpm both in CFD and experimentally. This is because at lower shaft speeds, when the scoops rotate too slowly, there is more chance for oil droplets and ligaments to be centrifuged outwards. At higher shaft speeds the scoops rotate very fast and capture more of the droplets and ligaments quickly giving them less time to be centrifuged outwards. Furthermore the jet velocity at higher shaft speeds is also higher and hence the momentum in the jet is higher. Hence the jet is driven through the scoop outlet more quickly at higher shaft speeds. This is illustrated in Figure 5.7 where the scoops are shown just after the slicing of the oil jet takes place. It is seen at 500rpm that for a particular scoop, after it captures oil, oil droplets that are disintegrated due to the slicing process are being centrifuged outwards even after it rotates through almost a full revolution and before it goes to slice the oil jet again. This shows

significant amount of oil that is being lost. The centrifuging of oil droplets at low shaft speeds is very clear in animations that are developed using volume fraction contours. Although centrifugal forces are relatively low when shaft speeds are low compared to high shaft speeds, the scoops rotate slowly at low shaft speeds giving enough time for oil droplets to gain momentum and get centrifuged outwards. At higher shaft speeds despite the fact that the centrifugal forces on the oil droplets are high, the droplets are captured by the scoop before they can be centrifuged outwards. Hence the losses due to centrifugal forces at higher shaft speeds is less significant.

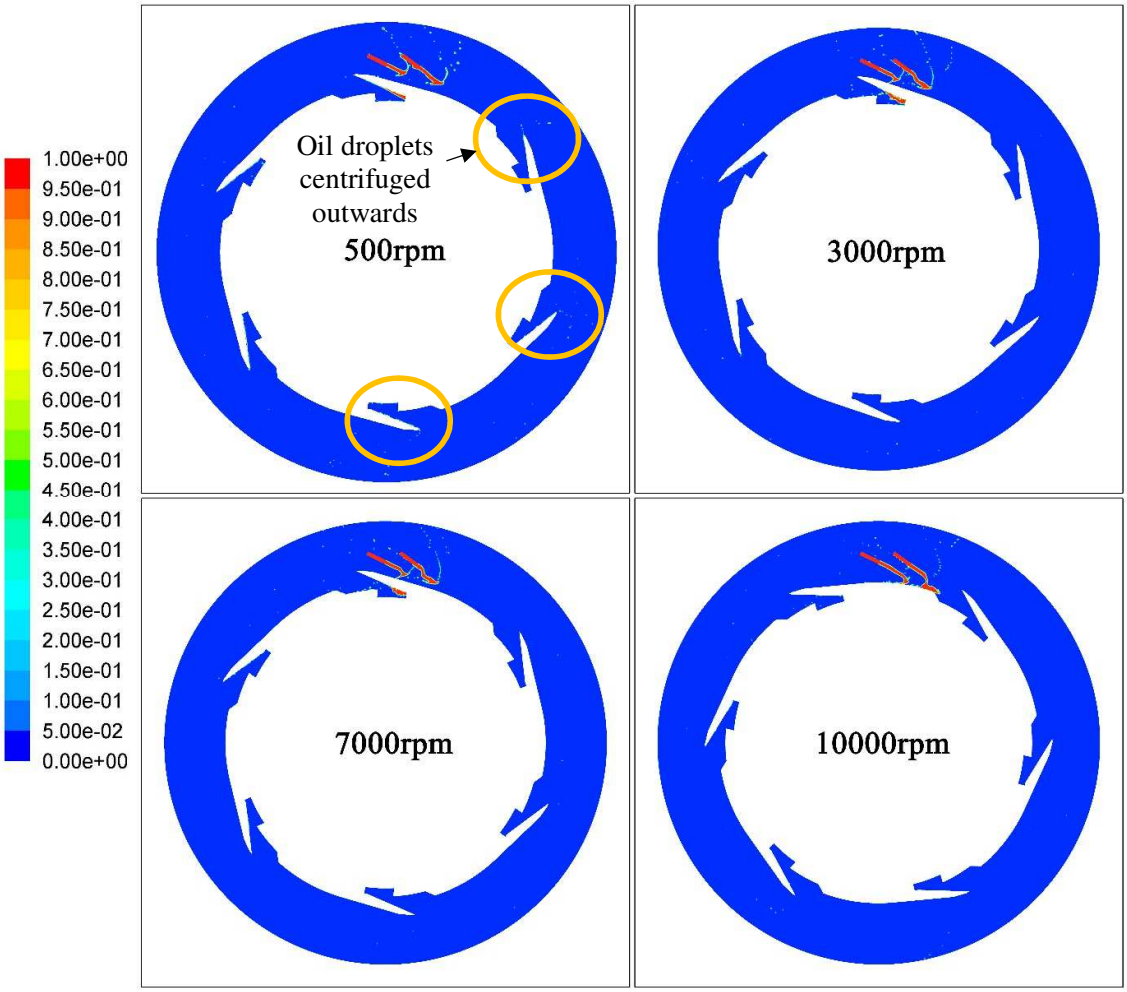


Figure 5.7 Oil droplets centrifuged outwards significantly at 500rpm following slicing of oil jet shown using volume fraction contours of oil.

Figure 5.8 shows a near jet view of a scoop after it has rotated few degrees after slicing the oil jets. The image shows the scoop approximately at the same position for both shaft speeds. It is seen that at 500 rpm there is far more oil that has not been ingested by the scoop compared to at 10000rpm. This oil eventually begins to get centrifuged outwards from the scoops as it rotates slowly at 500rpm. At 10000rpm, a scoop rotates much faster through a given angle compared to 500rpm and hence it can ingest oil more quickly. This gives less time for oil to be centrifuged outwards although the centrifugal forces on the oil droplets are higher at 10000rpm.

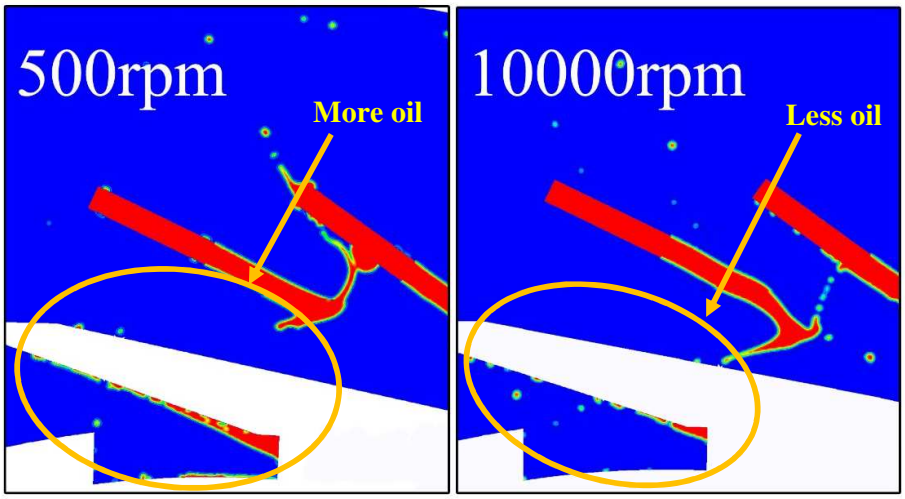


Figure 5.8 Near jet view at 500rpm and 10000rpm after the slicing of jet at approximately the same position (red denotes 100% oil and blue 100% air).

Another noteworthy variable that shows the difference at the two shaft speeds is the residence mass of oil in the domain. Residence mass of oil is the total mass of oil at any given time in the domain. It is perceived that when there is a higher residence mass in the domain, it can be captured by the scoops later. However, from animations developed using volume fraction contours, it can be evidently seen that the extra residence mass eventually gets lost in the form of oil droplets that are centrifuged from the scoops. Figure 5.9 shows the residence mass of oil in the system for the two different shaft speeds. With reference to Figure 5.7 it can be seen that almost after a rotation following the slicing of the oil jets, oil from the scoops is being centrifuged outwards. At 10000rpm before a scoop can rotate through half a revolution almost all the oil is captured and emptied from the scoop. The extra amount of residence oil at 500rpm in the domain is the uncaptured oil that will be centrifuged outwards from the scoops as they rotate.

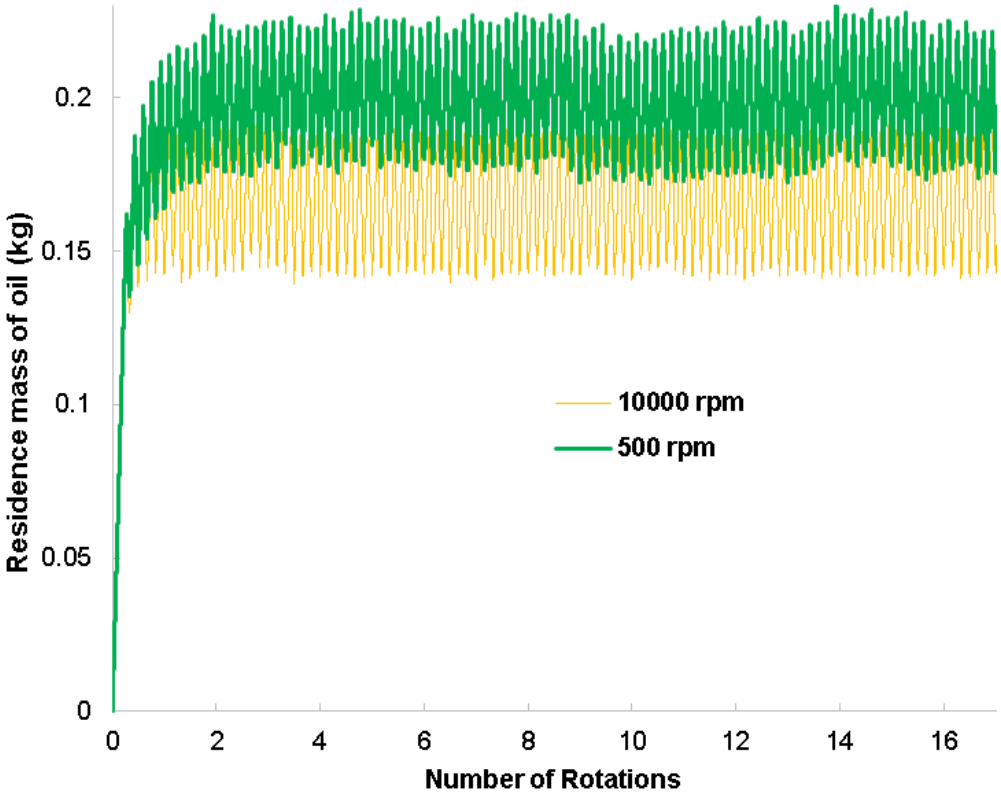


Figure 5.9 Residence mass of oil for 500rpm and 10000rpm

5.4 Effect of jet angle

The effect of the jet angle on the capture efficiency is investigated in this section. From the analytical study in chapter 4, it is seen that more radial jets give a larger C_x length and hence the collision point is closer to the outlets of the scoops. Therefore, it was anticipated from the analytical study that the capture efficiency is higher with radial jets. Hence in this study, θ_{jet} as shown in Figure 5.1, is reduced in steps of 5 degrees for three values and CFD study is conducted at four different shaft speeds for which experimental investigations have also been conducted. Jet angles 64.2^o, 59.2^o and 54.2^o are investigated in this study. Table 5.2 shows the velocity ratios, VR, and the jet velocities investigated in the test for the different shaft speeds.

Table 5.2 Tested experimental cases for investigations on varying the jet angle[5]

Shaft speed(rpm)	Velocity Ratio, VR=$\frac{r\omega}{V_{jet}}$	Jet velocity in experimental test (m/s)	Analytical threshold jet velocity for the shaft speed(m/s)
7000	4.43	16.88	167.65
8000	4.70	18.2	194.21
9000	5.22	18.41	218.48
10000	5.99	17.84	240.21

Figure 5.10 shows the variation in capture efficiency with jet angle at four different shaft speeds. It is very evident from the results of both CFD and experiments that when the jet is more radial, the capture efficiency of the scoops is higher.

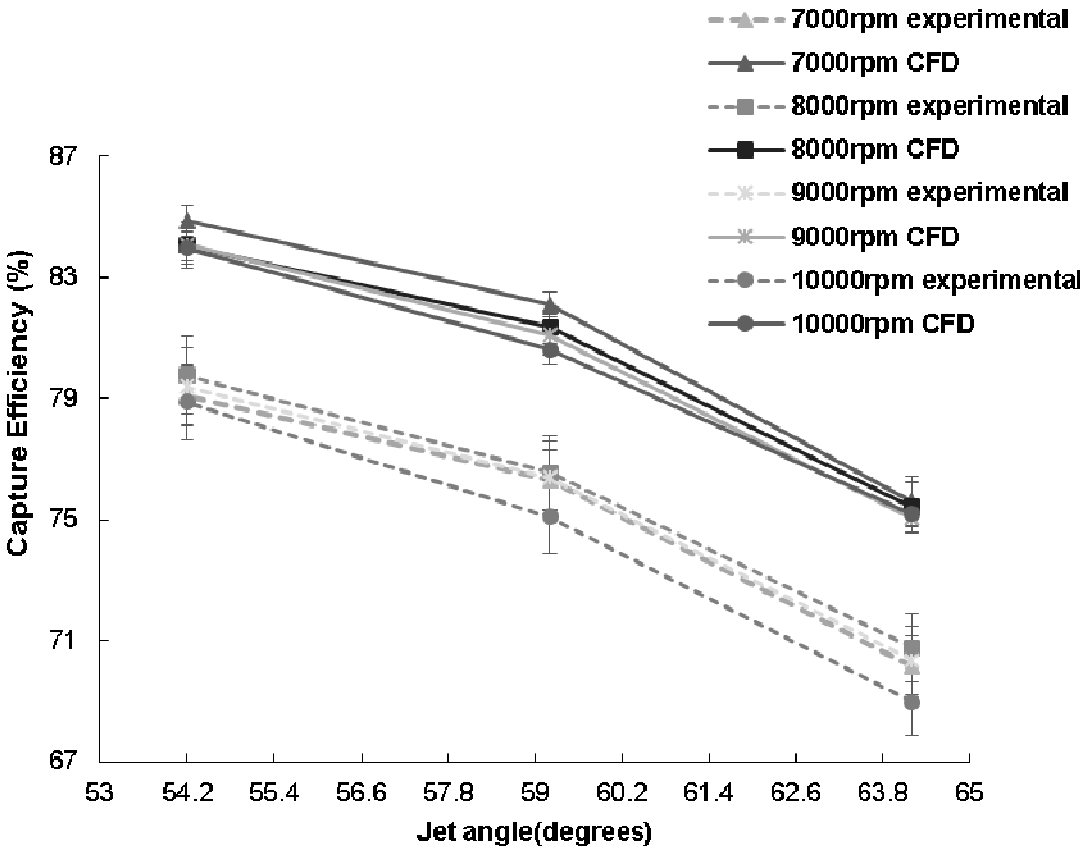


Figure 5.10 Effect of jet angle on the capture efficiency shown for CFD and experiments[5]

Although it is known that the length C_x is longer for more radial jets, contour plots of volume fraction using CFD results are not clear enough to illustrate and compare the difference in C_x

lengths for the three jet angles. This is because of the jet diameter and also the presence of two jets. Instead the distribution of the oil droplets after the slicing of the oil jet at the same time instant for the three jet angles is shown in Figure 5.11. The distribution of oil droplets gives a better idea as to why there is an increase in the capture efficiency for more radial jets. It can be seen from Figure 5.11 for the lowest value of θ_{jet} which is 54.2° the oil droplets are distributed closer to the scoop outlet and are most likely to be captured quickly as the scoop rotates. For the highest θ_{jet} of 64.2° the oil droplets are distributed further away from the outlet. Hence the droplets have a higher chance to be centrifuged outwards as the scoop continue to rotate. This eventually leads to a lower capture efficiency compared to the more radial jet.

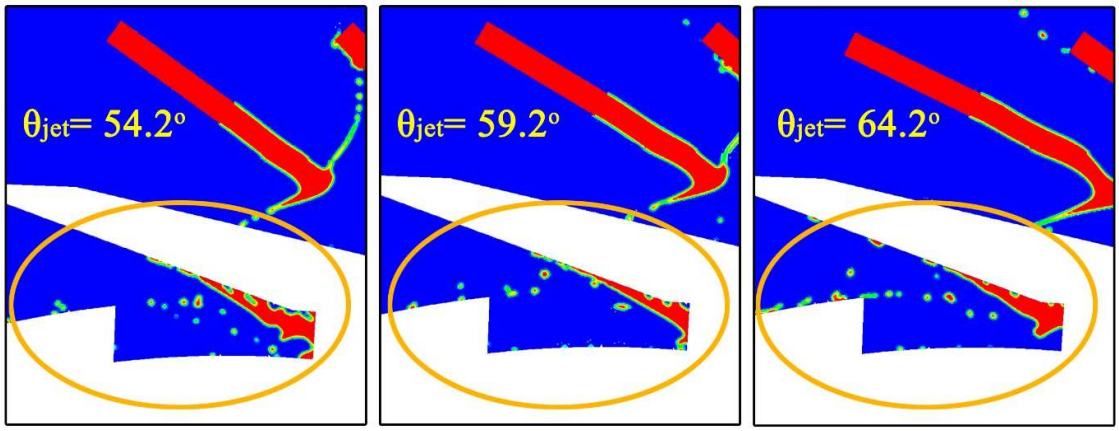


Figure 5.11 Distribution of oil droplets close to the scoop outlet highlighted for the three jet angles at the same time instant at 7000rpm a) 54.2° b) 59.2° a) 64.2°(red denotes 100% oil and blue 100% air)

With regards to more radial jets, it should be noted that the jet will start to collide with the outer surface of the scoops when the rotational speed is too low as seen in Figure 4.27. Once the jet collides with the drum, the oil droplets will rebound from the surface due to the momentum and some of them will also be centrifuged outwards. With greater values θ_{jet}(ie: more tangential jets), even if the VR is very low, the jet will not collide with the outer surface of the scoops. This is because the path of the jet does not intersect with the path of the scoops outer surface. However in experiments it has been shown that although the jet, impacts with the drum of the scoops, the capture efficiencies are not adversely affected[5].

5.5 Effect of differential pressure

It has been observed that for many of the configurations the droplets that are introduced in the vicinity of the scoops as a result of the disintegration of the oil jet, may be centrifuged outwards. This is particularly significant when a very low constriction gap like 2mm is used, at low shaft speeds and less radial jets such as $\theta_{jet} = 64.2^{o}$. Hence, potential ideas to enhance the scoops capture efficiency of these oil droplets were explored. One of the ideas was to impose low pressure at the outlet of the scoop so that a suction effect is created at the outlet of the scoops. This has not been assessed experimentally and only CFD will be used to assess the effect of creating a differential pressure across the scoops by imposing a significantly lower pressure than atmospheric pressure at the outlet of the scoop. The definition of differential pressure used in this investigation is:

$$\text{Differential Pressure} = \text{Atmospheric Pressure} - \text{Pressure at scoop outlet} \qquad \textbf{(5.2)}$$

Figure 5.12 shows the contours of the absolute pressure indicating the low pressure region relative to the surrounding at the scoop outlets when a differential pressure of 0.18bar is used. The value of the differential pressure is chosen arbitrarily such that the scoop outlet pressure is lower than the atmospheric pressure. The lower pressure seen at the outlet creates a suction effect that causes oil to be ingested more efficiently.

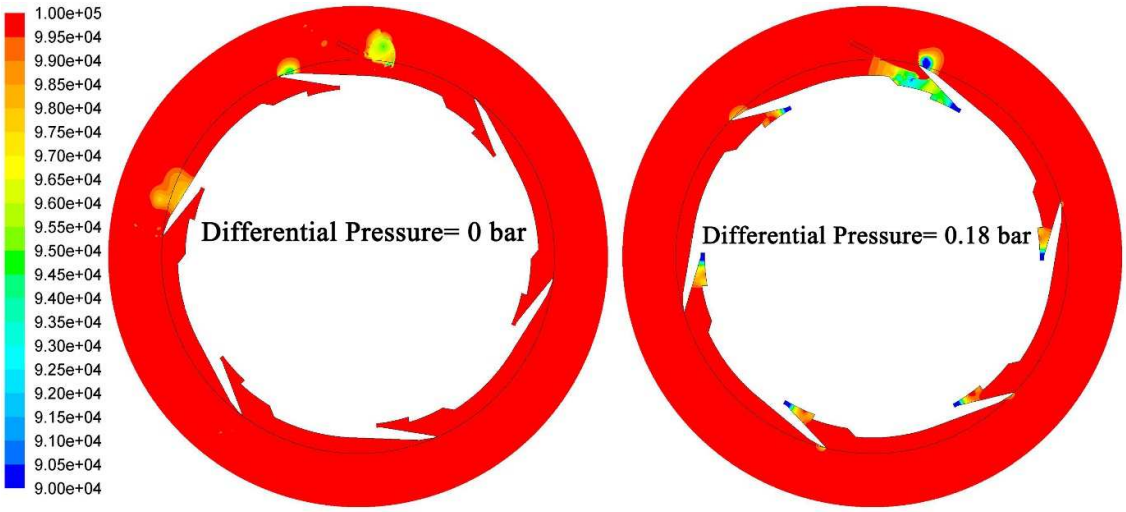


Figure 5.12 Absolute pressure contours indicating low pressure region at scoop outlets with a differential pressure of 0.18 bar (right).

The investigations are carried out for a geometry with a single jet using θ_{jet}=64.2^{o}, a constriction gap of 2mm, shaft speed of 7500rpm and jet velocity of 22.381m/s. A constriction gap of 2mm is used for the investigations because it was seen that there was restricted flow of oil due to size of the gap. Figure 5.13 shows the variation in the capture efficiency as a function of differential pressure. It is observed that the application of a low pressure at the outlet has an effect on the capture efficiency and gives improvement in the capture efficiency. However the increase in efficiency is not too significant. An increase in the differential pressure of 0.18 bar, results in an increase of close to 7% in the capture efficiency.

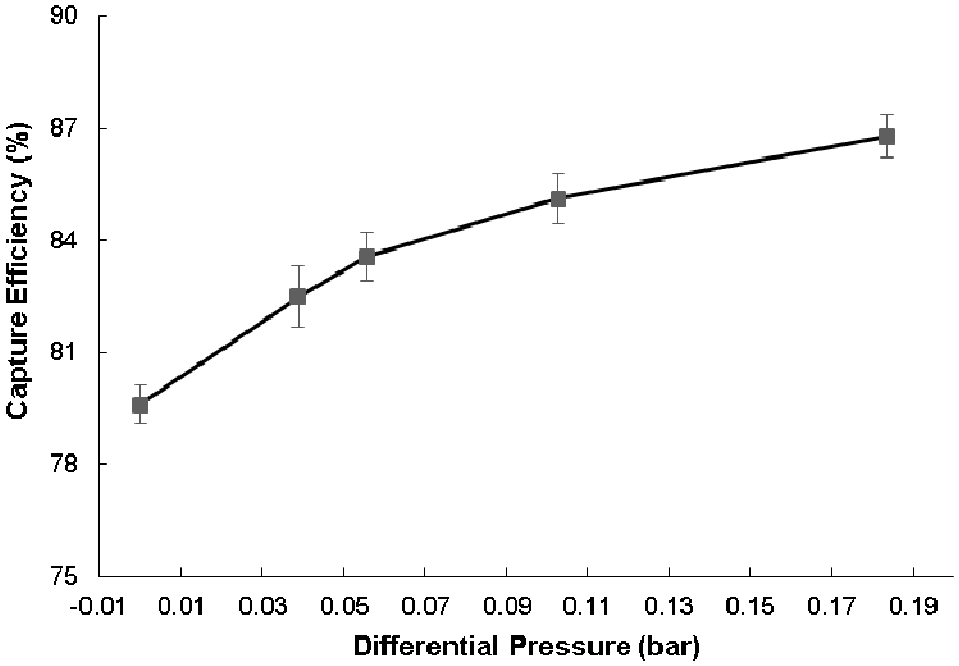


Figure 5.13 Capture efficiency vs. differential pressure for a shaft speed of 7500rpm, jet velocity of 22.381, jet angle of 64.2^{o} and constriction gap of 2mm.

Figure 5.14 shows the flow of oil into the scoops following the slicing of the oil jet for all the differential pressures investigated. It is seen that as the differential pressure is increased, the oil flow which was being restricted due to the small gap at the scoop outlets, flows more easily out from the scoops outlets. As oil flows more quickly from the outlet of the scoops there is lesser chance for oil droplets being centrifuged outwards without being captured and this leads to better capture efficiency at higher differential pressures.

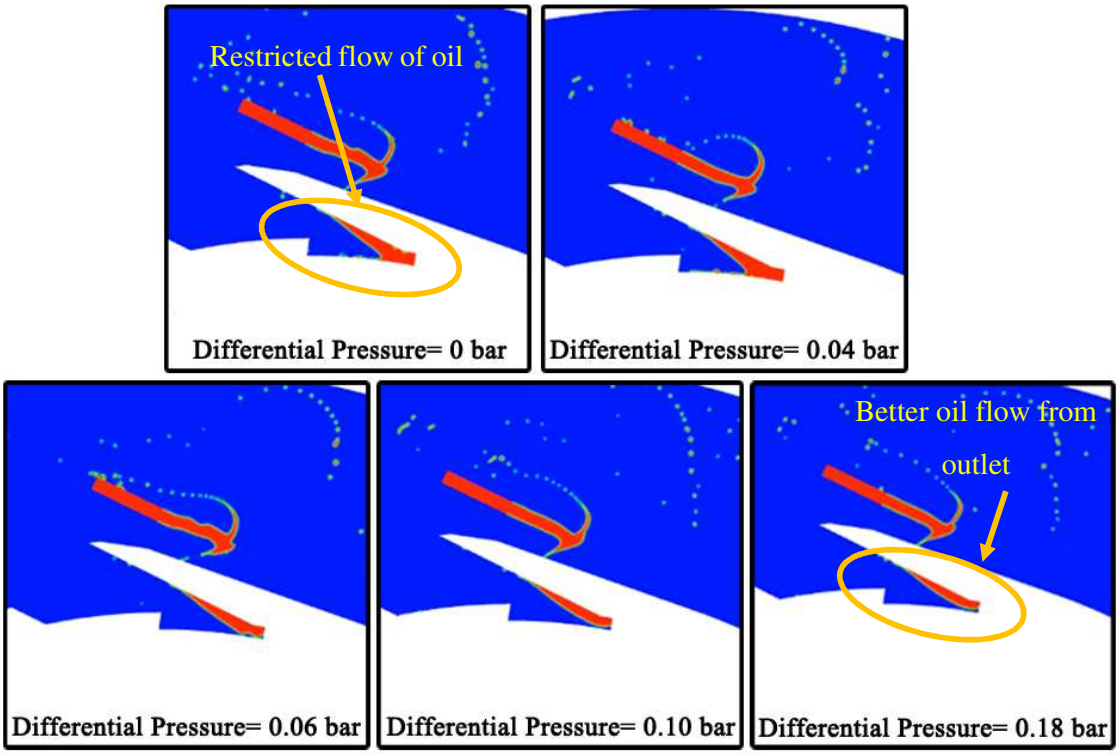


Figure 5.14 Ingestion of oil into scoop outlet using various differential pressures at a shaft speed of 7500rpm and a constriction gap of 2mm(red denotes 100% oil and blue 100% air)

Figure 5.15 shows the uncaptured oil droplets that are centrifuged outwards as the scoops rotate in a system where there is no differential pressure imposed. However, with a differential pressure of 0.18bar it is seen that there is no oil being centrifuged outwards as the scoops rotate after the capturing process.

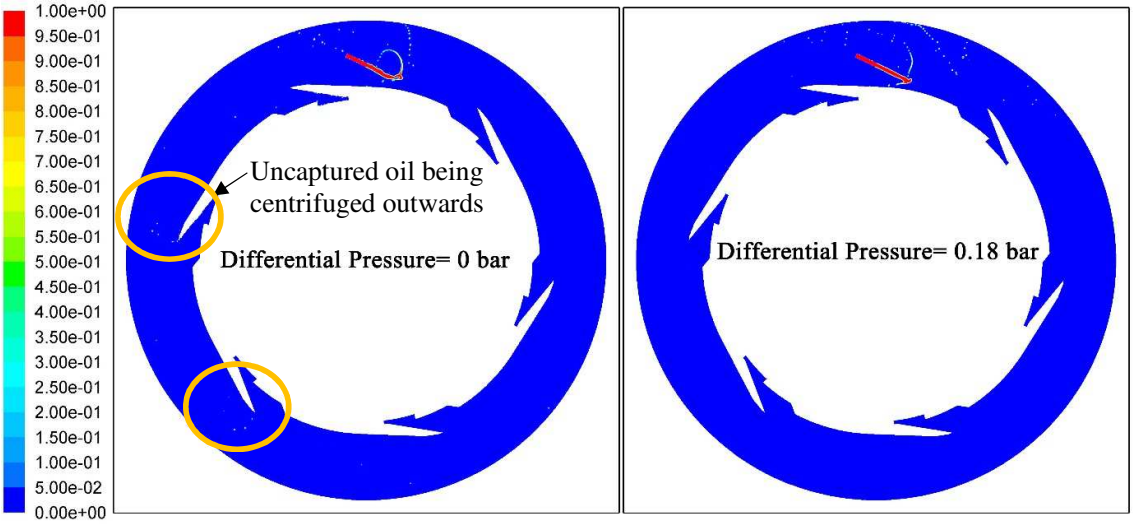


Figure 5.15 Volume fraction contours of oil without differential pressure (left) and with a differential pressure of 0.18bar (right).

5.6 Effect of Number of Scoops

Another geometrical investigation that was conducted is the effect of the number of scoops on the capture efficiency of the system. This parameter is given importance because reduction in the number of scoops could lead to reduced weight and also lower manufacturing costs. There are no experimental results available for this investigation and hence validation isn't possible. Figure 5.16 shows the variation of the theoretical capture efficiency as a function of the number of scoops. A jet velocity of 20m/s and a jet angle of 64.2^o is used to estimate the theoretical capture efficiency presented in Figure 5.16. It can be seen that when the number of scoops is below 3 for a shaft speed of 5000rpm and when using 1 scoop for both 5000rpm and 8000rpm, the efficiency is lower than 100%. This is because there are uncaptured portions of the jet due to the low rotational speed of the scoops as they rotate through a loss angle,θ_{Loss}as explained in section 4.2.1 in chapter 4. It can also be seen that as the shaft speed is increased while maintaining the same number of scoops, the theoretical capture efficiency increases as lesser portions of the jet are uncaptured.

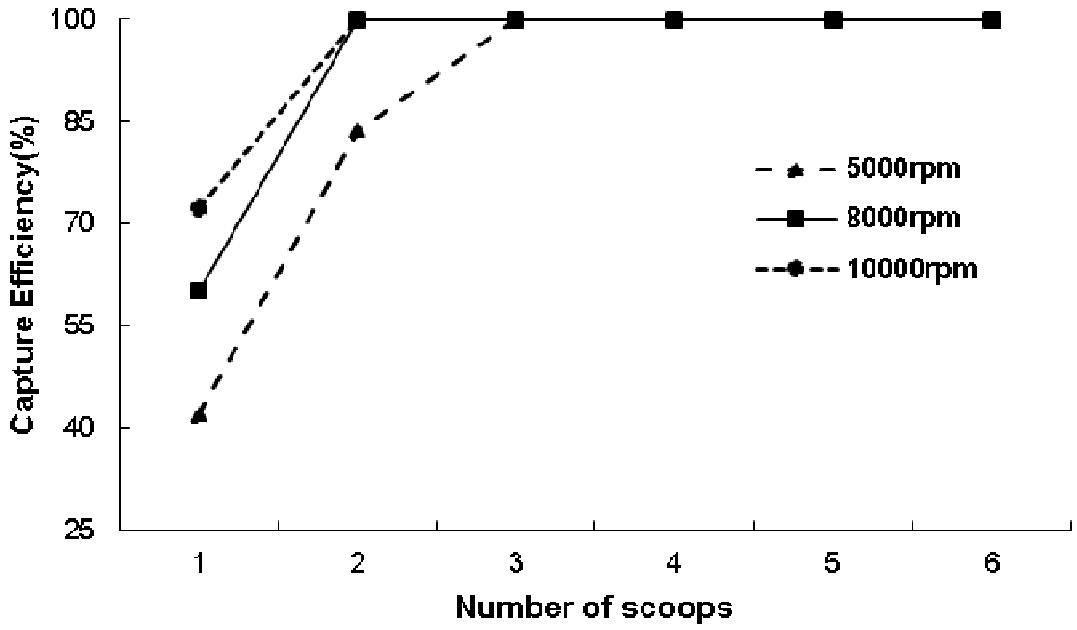


Figure 5.16 Theoretical capture efficiency for a jet velocity of 20m/s and a jet angle of 64.2^o

For a 1 scoop configuration rotating at 5000rpm, it can be calculated theoretically that the jet velocity should be lower than 6.9m/s in order to achieve 100% theoretical capture efficiency. When the jet velocity is lower than 6.9m/s there is no loss angle. Hence for all CFD investigations in this section a jet velocity of 6m/s is used. Two shaft speeds: 5000rpm and 8000rpm are investigated. The investigations are done with a jet angle of 64.2^{o} and a constriction gap of 4mm.

Figure 5.17 shows the variation in the capture efficiency of the scoops as a function of the number of scoops in the system. It is observed with 1 scoop the capture efficiency is extremely low. Although theoretically it can be expected 100% capture efficiency should be obtained for both 5000rpm and 8000rpm using 1 scoop, in reality the efficiency is much lower than this. This is because when using 1 scoop, the oil droplets that form as a result of the jet breakup are lost due to centrifugal forces, before they can be captured by the same scoop again.

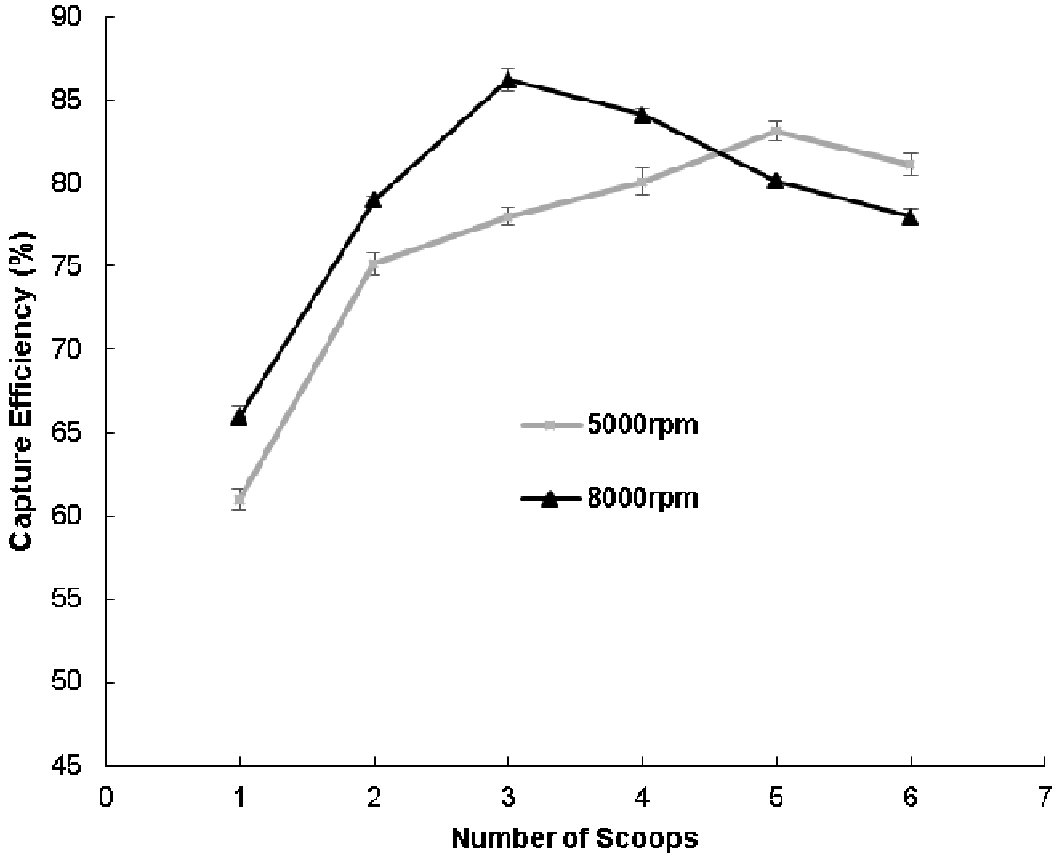


Figure 5.17 Capture efficiency vs. number of scoops for a jet velocity of 6m/s, a jet angle of 64.2^{o} and constriction gap of 4mm.

Figure 5.18 shows the oil volume fraction contours using a 1 scoop configuration right after the jet has impacted with the scoop. From the figure it can be seen that there are no uncaptured portions of the jet caused by a loss angle, as the jet velocity, 6m/s used in CFD investigations is significantly lower than the threshold jet velocity of 6.9m/s. However there is a large quantity of oil droplets that have collided with the drum and as the scoops rotate, the droplets are centrifuged away without being captured by the scoop. This can be clearly observed in animations developed using oil volume fraction contours.

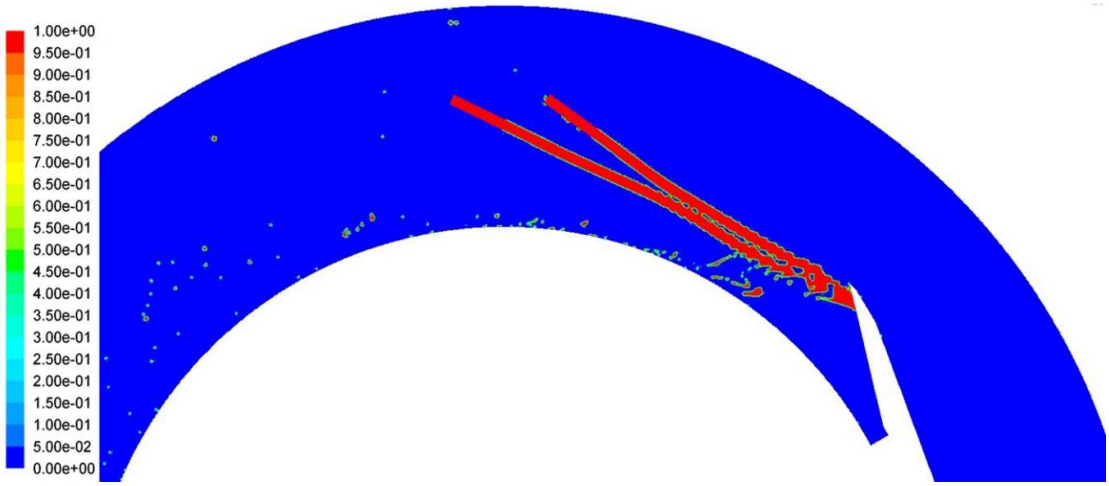


Figure 5.18 Oil volume fraction contours using 1 scoop just after impact with scoop

Figure 5.17 also shows that the efficiency increases when the shaft speed increases from 5000rpm to 8000rpm in a 1 scoop system. This is because more oil droplets are captured as the scoop rotates through a revolution more quickly at 8000rpm and giving lesser time for oil droplets to be centrifuged outwards compared to at 5000rpm.

At 5000rpm the maximum efficiency is obtained using 5 scoops and at 8000rpm the maximum efficiency is obtained using 3scoops. The difference in the optimum number of scoops for the two speeds is because at 5000rpm with 3 scoops there is a larger quantity of oil droplets that are uncaptured following the slicing process of the oil jet when compared to at 8000rpm with 3scoops. At 5000rpm more than 3 scoops are needed to capture the droplets that are lost due to centrifugal forces, because the scoops are not rotating fast enough.

Figure 5.17 shows that the peak efficiency at 8000rpm is observed when the number of scoops is 3. The capture efficiency increases as the number of scoops is increased towards 3 because

more oil droplets are captured. When the number of scoops is increased beyond 3 the efficiency begins to decline. It is believed that this is caused by the effect of vortex shedding that increases as the number of scoops increase. The effect of vortex shedding on the capture efficiency is shown in [7] and also presented in detail in chapter 6. Figure 5.19 shows the pressure contours for the different number of scoops investigated. It can be seen that the pressure at the tip of the scoop is lower compared to the surrounding region. This low pressure at the tip is associated with the formation of vortices from the tip of the scoop. The vortex at the tip of the scoop leads to a decrease in the capture efficiency as the scoop slices the oil jet. With more scoops the loss caused by the vortex at the tip of the scoop increases and hence the capture efficiency also decreases. Another possible contributing reason for this is the effect of turbulence that intensifies when more scoops are added. When there are lesser scoops, the average diameter of the scoop system is smaller. When more scoops are added, the average diameter increases and hence the Reynolds number of the flow also increases as a result leading to a more turbulent flow that causes greater breakup of the oil jet and introduces more droplets.

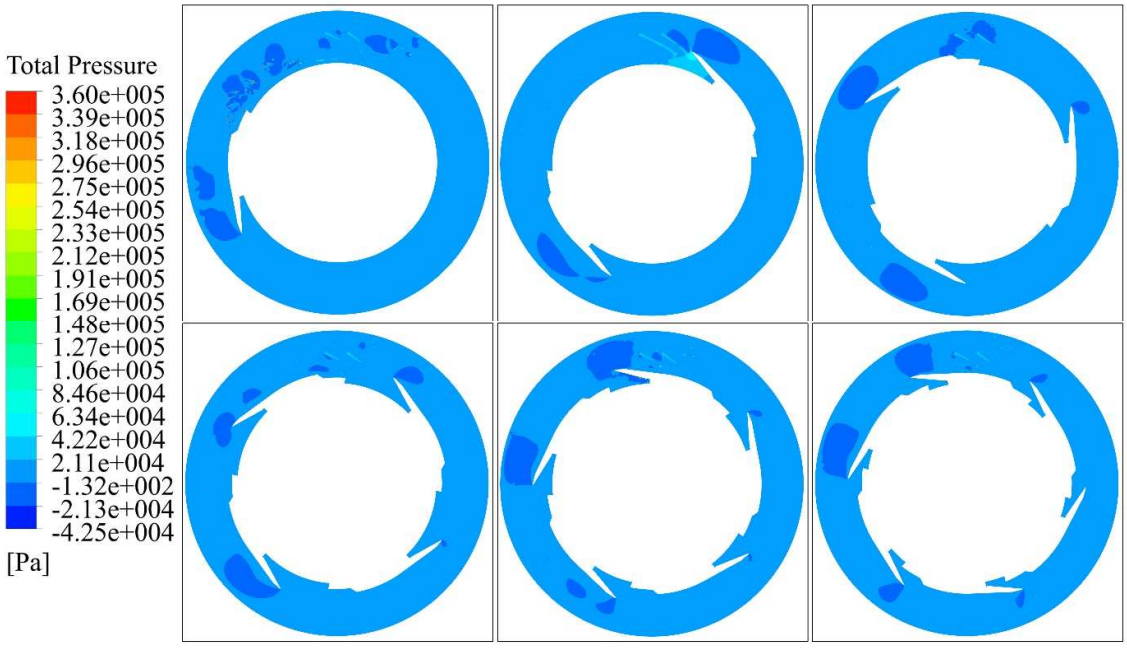


Figure 5.19 Pressure contours indicating low pressure at scoop tips due to vortex formation.

5.7 Chapter conclusions

In this chapter the effect of various geometrical parameters which included the constriction gap, jet angle and number of scoops were investigated. The effect of operating conditions such as using a jet velocity below the threshold velocity at various shafts speeds is investigated. In order to overcome the problem of having uncaptured oil droplets centrifuging outwards, reduced pressure at the scoop outlets is investigated.

It is seen that at a low value of the constriction gap there is restricted flow in the region close to the scoop outlet. This causes a delay in capturing oil droplets that are introduced after the slicing of the oil jet. Constriction gaps above 3mm overcome the problem of the restricted flow of oil at the outlet.

For jet velocities lower than the threshold jet velocity at various shaft speeds, it is seen at lower shaft speeds the capture efficiency is low. This is because of the low rotational speed that allow oil droplets to be centrifuged outwards before they can be captured leading to a decrease in the capture efficiency.

With regards to the jet angle, it is seen that the jet at 54.2^{o} to the vertical gives the highest efficiency. This is because the jet collides with the scoop closer to the outlet where the oil can be scooped more quickly leading to a better capture efficiency.

It is seen that when a larger differential pressure is used, the capture efficiency increases by almost 7% compared to when there is no differential pressure. Although there is a positive effect in the capture efficiency when a differential pressure is applied, the advantage is not too significant. The low pressure relative to the atmospheric at the outlet, aids the capturing of oil by the scoop as the oil is ingested more quickly by the scoops.

For a fixed jet velocity of 6m/s it is seen that at 8000rpm the optimum number of scoops required to achieve maximum capture efficiency is 3. With a higher number of scoops the capture efficiency decreases due to the increase in the vortex shedding frequency and the effect of turbulence that aggravate the oil jet break up process introducing more oil droplets. When the shaft speed is reduced to 5000rpm with the same jet velocity, the optimum number of scoops is 5. There is a shift in the optimum number of scoops because the scoops rotate slower

and more number of scoops are required to capture the oil droplets. Theoretically for the operating points investigated, it is expected that 100% capture efficiency should be obtained. However due to losses associated with uncaptured oil droplets, the capture efficiency is reduced.

The trend observed in CFD and experiments are very similar for all cases investigated in this chapter and the maximum difference between the experimental and CFD results was at 8.78% for the 2000rpm case that was investigated under the effect of jet velocity.

Based on the findings from this chapter some of the recommendations that can be made for scoop design and operation are:

- Use of a large constriction gap.
- If a lower constriction is essential due to space and weight constraints, applying a lower pressure at the scoop outlet should be considered in order to create a differential pressure across the scoop inlets and outlet.
- Use of more jet with lower perpendicular distance to the centre, O, with a jet velocity significantly lower than the threshold jet velocity so that the jet collides more closer to the scoop outlet.
- Higher shaft speeds should be used so that oil gets ingested more quickly.
- An optimum number of scoops should be chosen corresponding to the shaft speed at which the scoops are chosen to operate. For a particular shaft speed there exists a specific value for the number of scoops at which maximum capture efficiency is achieved.

6 Effect of vortex shedding on the performance of scoop based lubrication devices

6.1 Overview

From experiments and CFD it is observed that the capture efficiency of scoops gradually reduces as the shaft speed increases above the threshold shaft speed[5], although theoretically it is predicted that there should be 100% capture efficiency in this range. The reason for this is identified from CFD and experiments as being due to the loss of oil that is incurred when a scoop slices an oil jet and some oil from the plume is lost. When the shaft speed increases this loss of oil increases due to the pluming effects that become more pronounced. Using CFD it is seen that the pluming is linked to vortex shedding from the tip of the scoops.

None of the numerical or experimental studies (to the best of the author's knowledge) conducted in the past with regards to scoop based lubrication devices have addressed the vortex shedding phenomenon present in scoop based lubrication systems. In this chapter vortex shedding is analyzed to enhance understanding of its impact on the performance of scoop devices. The numerical methodology and details regarding grid dependence have been detailed in Chapter 3 and Chapter 4 and hence will not be presented in this chapter. A similar methodology was adopted for numerical work done in this chapter.

6.2 Vortex shedding from scoops

Figure 6.1 shows the images from the experiment[5] and 2D CFD results. It is seen that the tip of the jet begins to plume after the slicing process in both experiments and CFD.

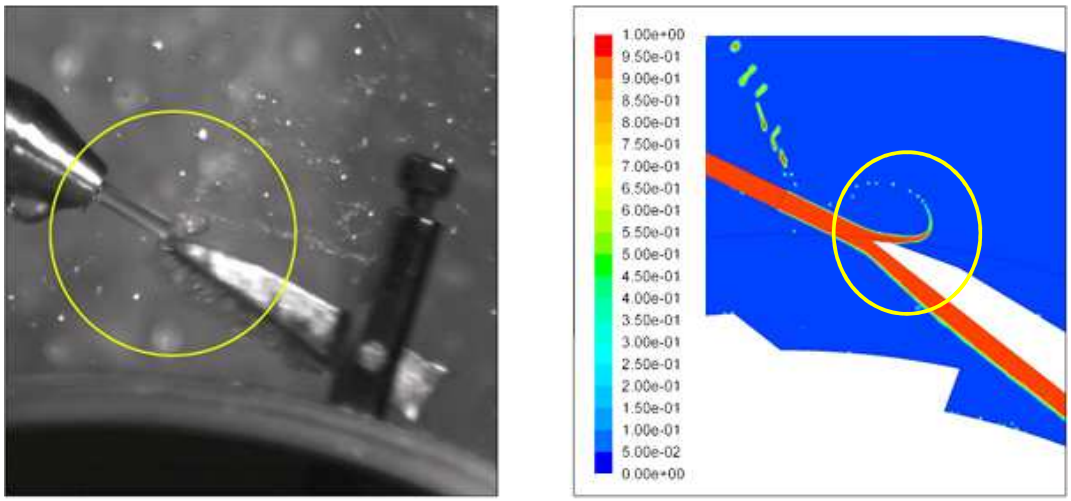


Figure 6.1 Experimental test on a wedge (left)[5] and CFD slicing of oil jet showing the formation of plume at the tip of jet after slicing using volume fraction contours of oil (right).

Based on in depth analysis of the CFD results from the work in this thesis, it has been identified that the vorticity arising at the tip of the scoop is linked to the pluming of the oil jet. The vorticity, ζ, which quantifies the extent to which the fluid is subjected to rotation about itself is given by

$$\zeta = \nabla \times \vec{u} \tag{6.1}$$

For the numerical work presented in this chapter a single jet with a jet angle of 64.2°, constriction gap of 4mm and a jet velocity of 22.381m/s is used. For the determination of the vortex shedding frequency, cases were carried out with a single phase simulation with the air phase only. For two phase simulations presented in the chapter the VOF multiphase model is used to model the flow between air and oil. The turbulence model used for all the cases investigated is the RNG k-ϵ model with standard wall conditions.

Figure 6.2 shows contours of vorticity that illustrate vortex formation for the scoop rotating at 10,000 rpm for a two phase simulation. It is seen that vortices form at the scoop tip and are shed forming a region of higher vorticity behind the scoop. The vortex grows from the tip of a scoop as it rotates and is eventually shed from the tip. Subsequently another vortex begins to form from the tip of the scoop, suggesting that the vortex shedding process is periodic in the system. Following the separation from the tip of scoop, the vortex reduces in strength and begins to diminish. This behavior of vortex shedding is comparable to the illustration presented by Ferreira[34] in Figure 2.13.

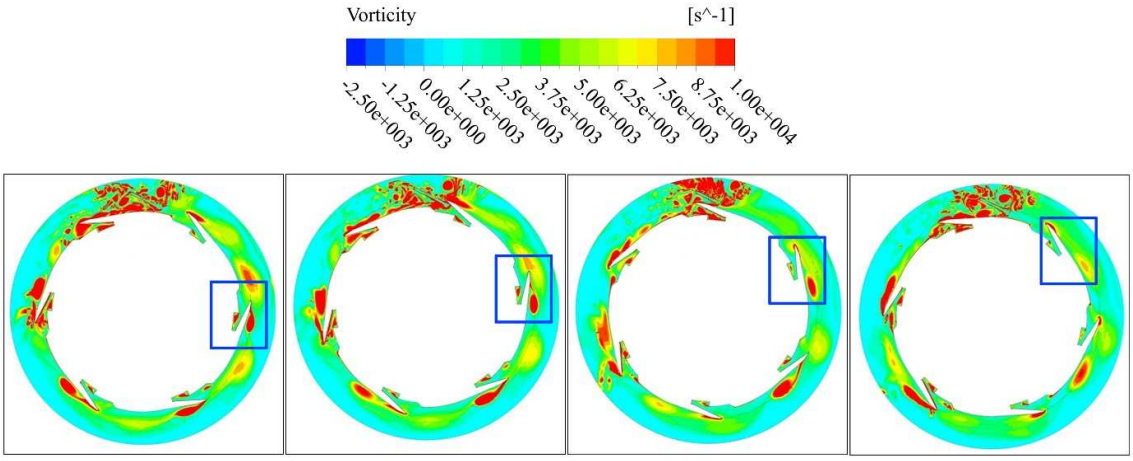


Figure 6.2 Vortex shedding progression highlighted for a scoop at 10000 rpm

Figure 6.3 shows vorticity contour plots for four shaft speeds, 3000 rpm, 5000 rpm, 7000 rpm and 10,000 rpm. CFD results reveal that vorticity increases with shaft speed in regions where sharp corners and high flow velocities are involved, particularly the tip of the scoops. This dictates that pluming effects at the jet tip substantially increase with shaft speed and this in turn leads to a reduction in the capture efficiency. Experimentally it is observed that for a fixed jet speed V_j the capture efficiency of the scoop lubrication systems decreased gradually as shaft speed increased over the range 2000rpm to 10,000 rpm as observed in Chapter 4.

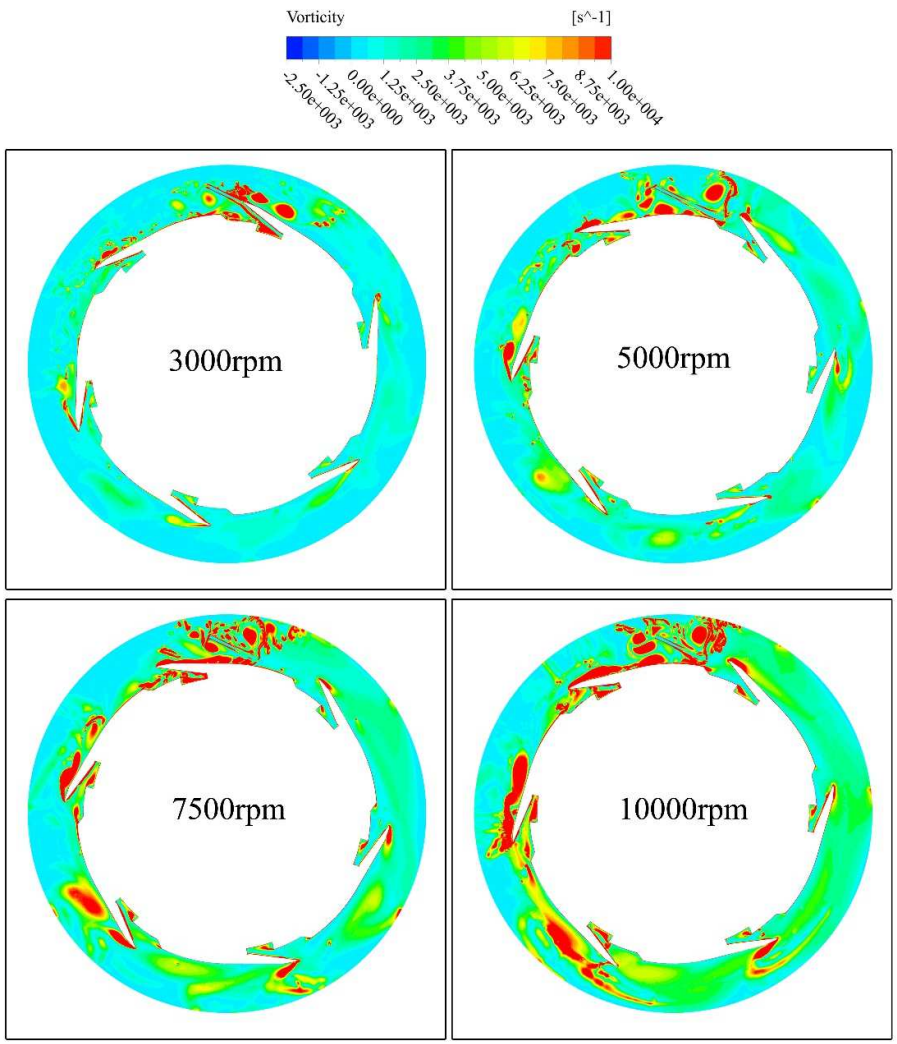


Figure 6.3 Vorticity increasing progressively with shaft speed

In their numerical study of wind turbines Trivellato & Castelli [70] found a vortex shedding frequency linked to blade passing frequency. Similarly, in this system there is a frequency associated with the shaft speed of the scoops. A noteworthy parameter is the Strouhal number *St* which describes the unsteady nature of vortex shedding. It is given by

$$\mathrm{St} = \frac{fL}{V} \tag{6.2}$$

where *f, L* and *V* are the frequency of vortex shedding, length scale and velocity scales.

In order to determine vortex shedding frequency using the CFD model, a single phase system (air only) is simulated. The two phase (oil and air) model is not utilized due to the noise introduced in the data by oil droplets, which are centrifuged outward from the surface of the scoops, as was witnessed in results from preliminary simulations. In order to estimate the frequency of vortex shedding the pressure, velocity and vorticity are monitored at a cell-vertex monitor placed behind the tip of each scoop. Monitoring of the selected variables was carried out at each time step and hence the sampling frequency, $f_S=1/t_i$ where t_i is the corresponding value of the time step size for each case investigated.

Table 6.1 Sampling frequency, f_s, for each case

Shaft Speed (rpm)	Sampling Frequency, f_s (MHz)
2000	0.76
3000	1.21
5000	2.16
7500	3.12
10000	4.44

The fluctuations in the data are converted to Power Spectral Density (PSD) using the Fast Fourier Transform(FFT) Utility in FLUENT[55] and analyzed. The PSD_ϕ of a signal for a variable, Φ, that fluctuates with time and is monitored at discrete intervals, spaced by a time step, t_i, can be written as a function of the frequency,f, as:

$$\mathrm{PSD}_\Phi = \frac{{t_i}^2}{N t_i}\left|\sum_{n=1}^{N} \Phi(nt_i)e^{-i2\pi f t_i}\right|^2 \qquad \textbf{(6.3)}$$

Where, N, is the total number of data points, n is number of timesteps and t_i is the value of the time step.

Figure 6.4 shows part of a sample of the pressure signal and Figure 6.5 shows the associated PSD plot. The data is for a case at 10,000 rpm but is typical of all those investigated. The first peak at the lower frequency corresponds to the interaction of the scoop with the jet tube walls

for each revolution (f = 166 Hz for the 10,000 rpm case). The other peaks are at frequencies slightly above 2f, 3f, 4f and 5f. The peak associated with the vortex shedding frequency is identified with the aid of the PSD and animations of vorticity that are used to count the number of vortices that are being shed in one revolution. The number of samples used to develop the PSD plot for the 10000rpm case is 190,000 and the sampling frequency is f_S=4.44MHz.

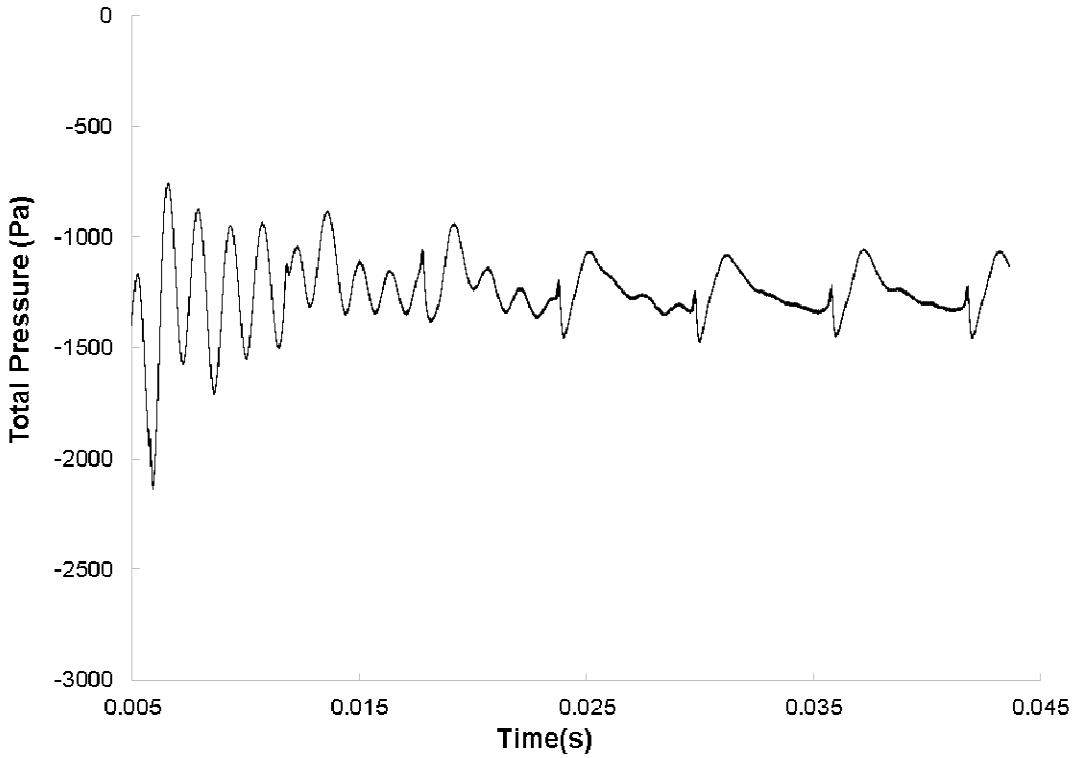


Figure 6.4 Pressure data from vertex point behind scoop tip at 10000rpm

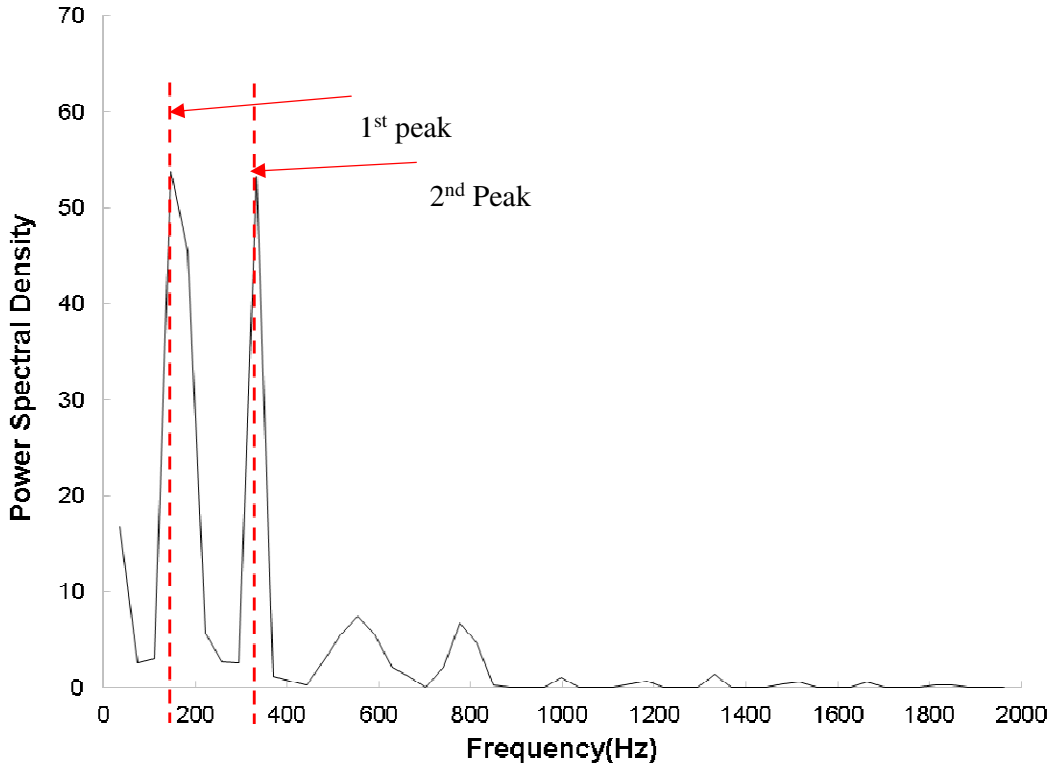


Figure 6.5 PSD plot using total pressure data at 10000rpm

The associated Strouhal number for each case can be calculated by utilizing the velocity at the tip of the scoop, the characteristic length and the frequency given by the second peak on each PSD plot. For comparison the geometry is quite similar to vortex shedding from an inclined flat plate and in such a case the characteristic length would be the length of the plate as shown in Figure 6.6 (which was used in the work of Lam & Wei [71]).

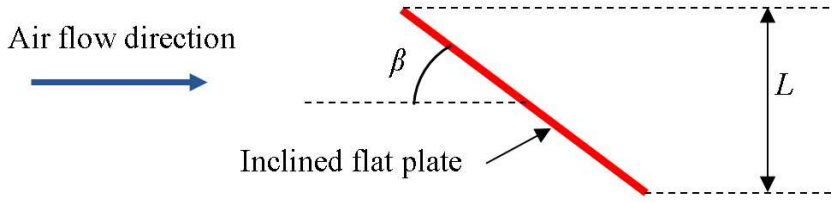


Figure 6.6 Characteristic length, *L*, for an inclined flat plate as used in the work of Lam & Wei [71]

Here the characteristic length, L, is taken as the scoop length as illustrated in Figure 6.7. The calculated frequency for each of the single phase calculations is tabulated in Table 6.2. The

associated Strouhal number was calculated for the five cases and the average Strouhal number was found to be 0.132. This compares to values of 0.15 found for inclined flat plates [71] at comparable angles of inclination.

Table 6.2 Shaft speeds with associated vortex shedding frequencies and Strouhal numbers

Shaft Speed (rpm)	Vortex Shedding Frequency, *f* (Hz)	Strouhal Number, *St*
2000	67	0.1302
3000	106	0.1360
5000	168	0.1306
7500	257	0.1332
10000	340	0.1322

Pressure contours, shown in Figure 6.7 were plotted to aid understanding of the pluming effect caused at the tip of the jet. The pressure contours highlight that regions where vortices are formed and shed, have a lower pressure compared to the surrounding regions. This is similar to that seen in published results[36]. The vortices circulate the system in a direction opposing the direction of the jet because they are driven by the rotation induced airflow. During the slicing process, the tip of the jet is subjected to high pressure which imposes a force on the tip of the jet, causing it to plume. This can be seen very clearly in Figure 6.10 which shows a close-up of the pressure field, volume fraction and vorticity contours as the jet interacts with a scoop.

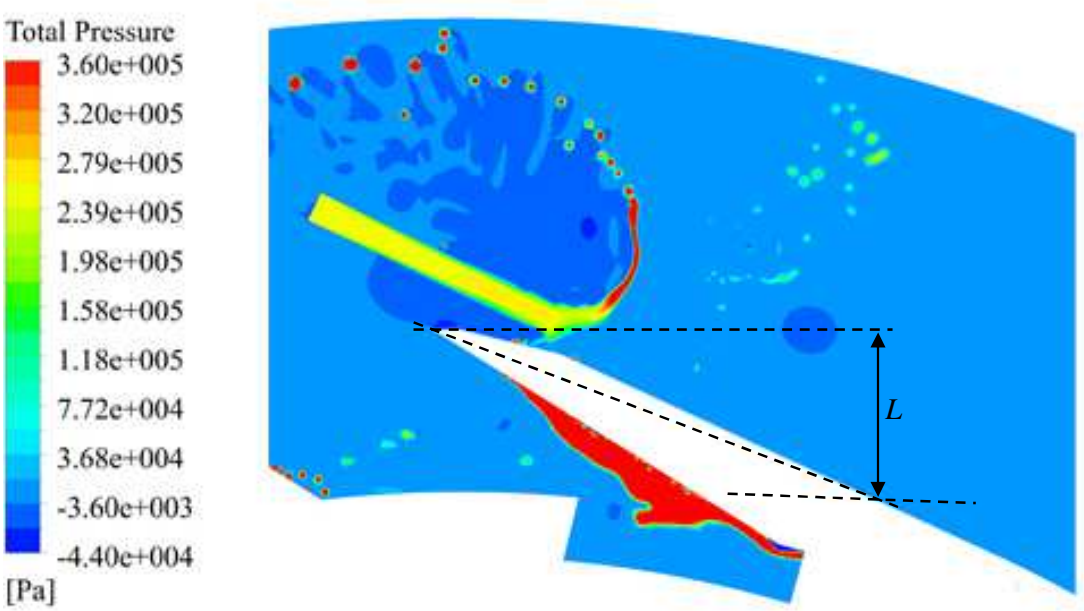


Figure 6.7 Total gauge pressure illustrating the pluming effect.

The velocity vectors in Figure 6.8 show how the flow is in the vicinity of the scoop tip. The swirl is comparable to the illustration of the vectors seen at the tip of a turbine in the work of Mclaren[35].The swirl causes the tip of the jet to bend upwards when a scoop approaches to commence the slicing process. Following the slicing process the surrounding high pressure region aggravates the pluming effect at the tip of the jet, by deforming it.

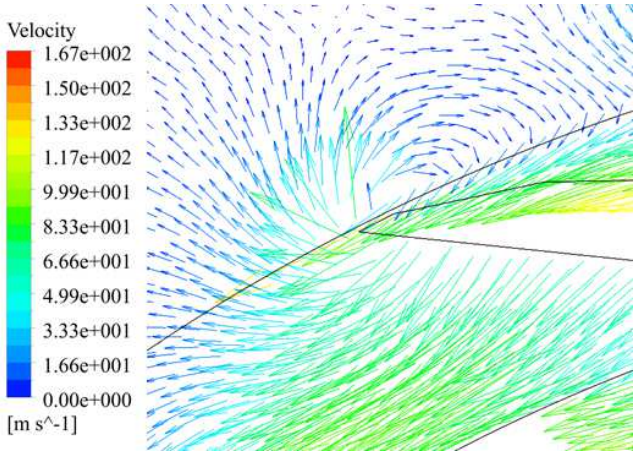


Figure 6.8 Velocity vectors in the stationary frame of reference at the tip of the scoop indicating a swirl

As the jet progresses following the slicing process, it retains the deformed shape, which eventually stretches at the tip and disintegrates into smaller droplets. A significant quantity of oil in the form of droplets is lost and not captured by the following scoop, due to the pluming effect caused by the preceding scoop. This is illustrated in Figure 6.9.

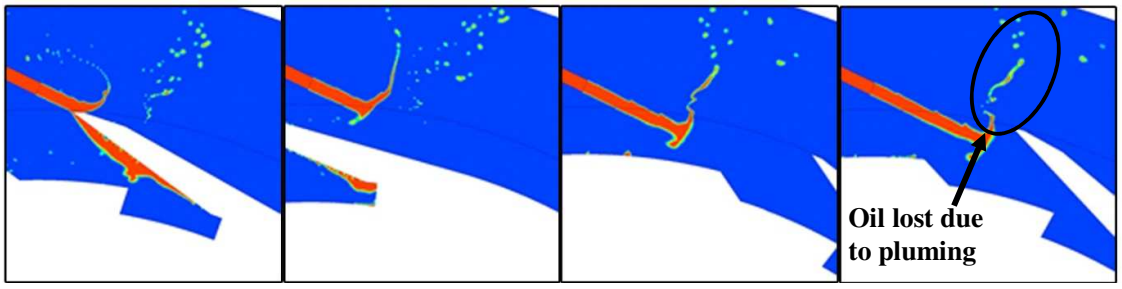


Figure 6.9 Volume fraction contours (red- oil and blue-air) showing formation of plume at tip of jet which eventually gets stretched out and is uncaptured by the proceeding scoop.

6.3 Geometry optimization to minimize vortex shedding effects

Having identified blade tip vortex shedding as one of the mechanisms likely responsible for reduction in capture efficiency two geometrical modifications were evaluated to see if they could minimize this effect. In the first test, the sharp edge of the scoop was rounded off or sharpened and in the second the jet direction was reversed. Gandhi et al have shown that vortices shed from a sharp body are more stronger compared to that of a bluff body in their study[72] and hence it was decided to assess the performance of blunt tipped scoops. A reversed direction was chosen based on the patent of Dins et al [73] that permits a reversed direction jet in their scoop design of curved blade oil scoops.

Figure 6.10 compares volume fraction contours and vorticity contours obtained for the blunt and extremely sharp-edged blades. It is seen that pluming effects are far higher when sharp scoop tips are used for the slicing process, compared to blunt scoops. It is witnessed that blunt scoops lower the pluming effects as well as causing the tip of the jet to bend inwards towards the scoops. The variation in the shape of the jet tip following the slicing event using various top geometries shows the effect of the vorticity on the jet tip and hence the capture efficiency is also affected subsequently. Although the vorticity field looks higher with a blunt tip, it should be noted that the vortex shed is further downstream from the tip of the scoop using a blunt tip

compared to a sharp tip. Hence the plume is deflected inwards using a blunt tip and oil loses associated with the slicing event is lower compared to when using a sharp tip.

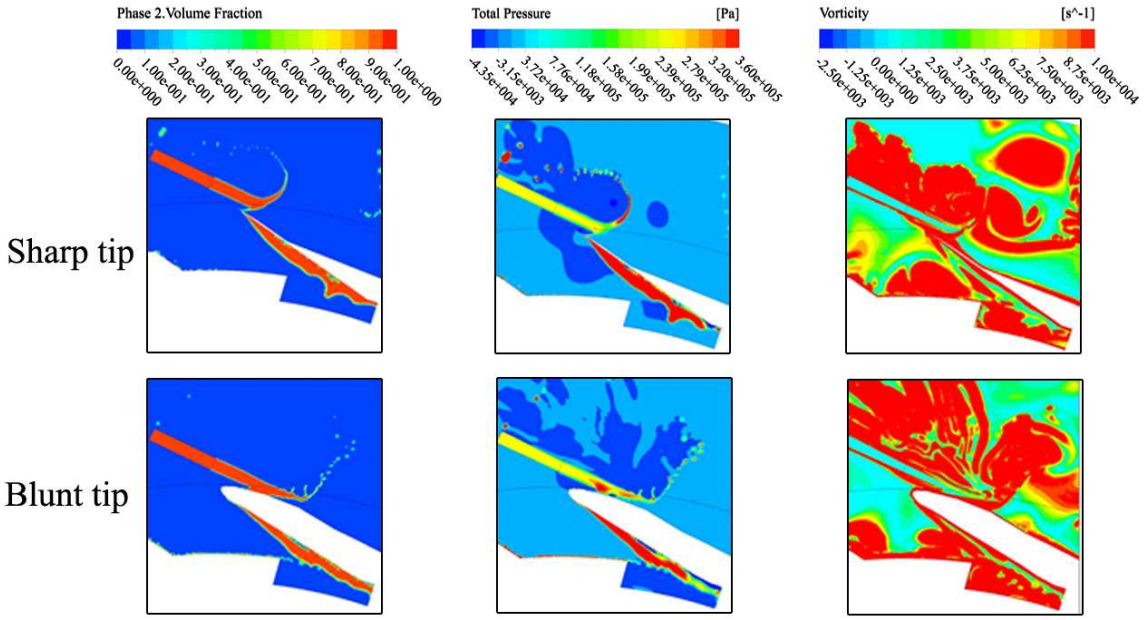


Figure 6.10 Volume fraction contours of oil, Total pressure and Vorticity contours for sharp tip (top row) and blunt tip (bottom row) at 7500rpm

Figure 6.11 compares the capture efficiency for the two scoop tip geometries at 7500 rpm. Compared to the baseline geometry it is seen that scoops with blunt tips give an increase of 2% in the overall capture efficiency. There is a slight decrease in capture efficiency with a sharp tip scoop. When sharp scoop tips are used, vortices are formed from the tip of the scoop and vorticity levels are high close to the tip of the scoops. Blunt scoop tips shed vortices further away from the tip (leading edge), along the walls, reducing vorticity levels at the tip of the scoops. This eventually reduces the pluming effect on the tip of the jet, as the slicing process commences.

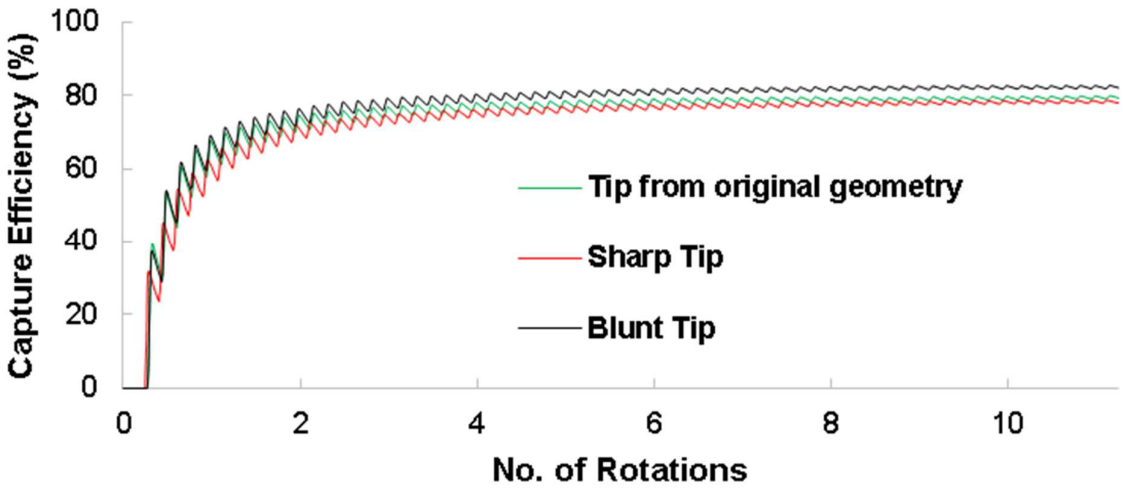


Figure 6.11 Capture efficiency for three different tip geometries of scoop

A reverse jet configuration was investigated where the shaft rotates in the same direction as the jet. The jet was created using a mirror image of the jet used in the original configuration. So, the value of the jet angle is the same. The shaft speed used for the simulation was 10,000 rpm and the jet velocity 22.381m/s. Figure 6.12 shows the computed oil capturing process using the volume fraction and vorticity contours, at four time intervals. It is observed that the pluming effect on the tip of the jet is almost eliminated. This is because vortices move in a similar direction to the jet during the slicing process and are circulating at a higher velocity compared to the jet velocity. Hence the tip of the jet is not subjected to a pressure gradient that deforms its tip from the surrounding regions.

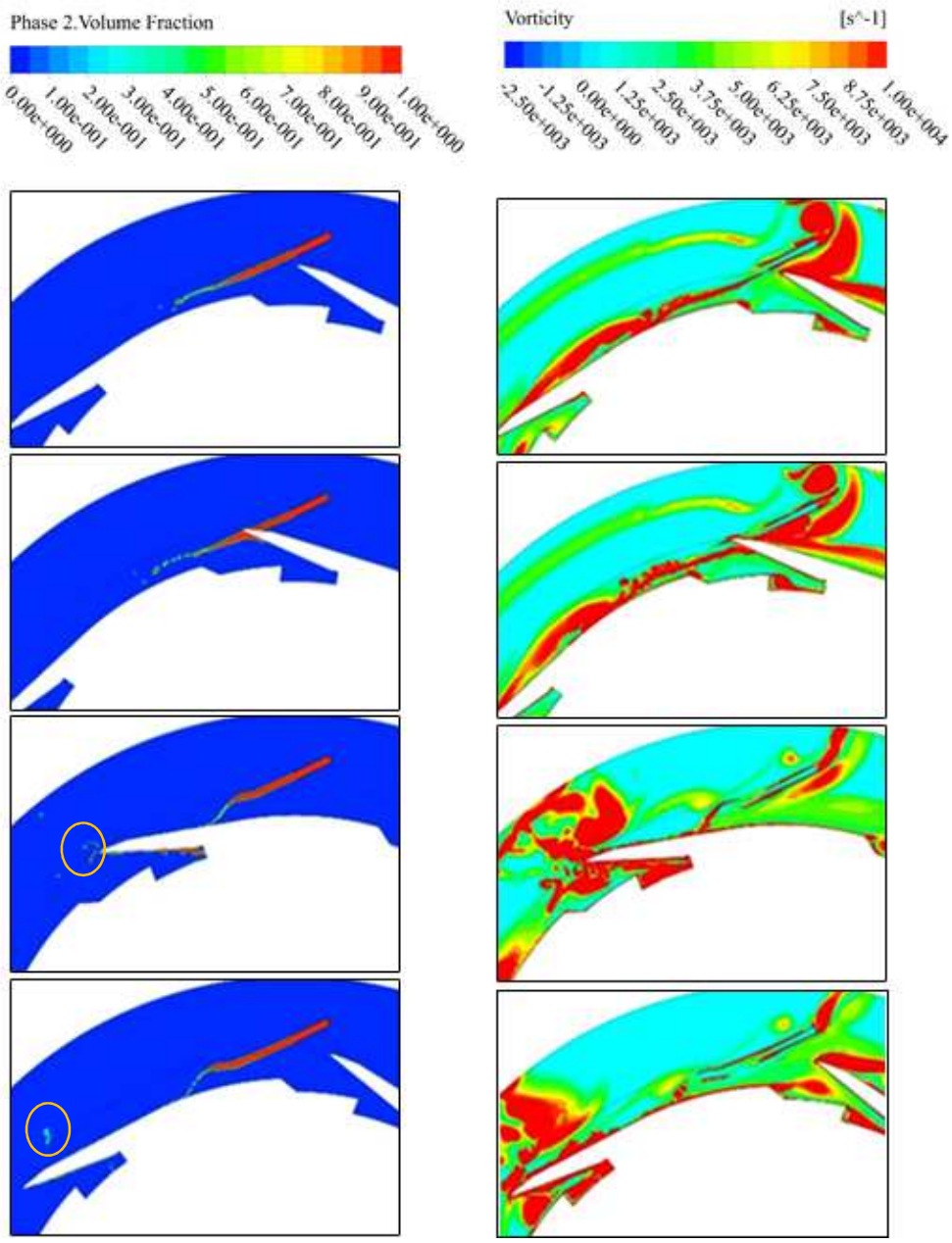


Figure 6.12 Volume fraction contours of oil (left) and vorticity contours (right) for the progression of oil jet slicing process using a reverse jet configuration.

Despite the fact that the reverse jet configuration eliminates pluming at the jet tip, the overall capture efficiency was found to decrease by 10%. This is because oil losses occur in the form of droplets centrifuging after hitting the outer surface of the scoops and other areas (such as close to the scoop outlets). Oil droplets that are centrifuged outwards without being captured are indicated with a circle on Figure 6.12. Hence an alternate geometry must be adopted to

compensate for oil loses occurring from other sections of the scoop system, if the reverse jet configuration is intended to be used. An alternate geometry should be capable of capturing the loses associated with the reverse jet configuration.

6.4 Chapter conclusions

In the study presented in this chapter it was identified that vortex formation from the scoop tip leads to a modified pressure field and consequent jet deflection and pluming, reducing capture efficiency. The study found that the extent of the region affected by this vorticity increased with increasing shaft speed, and that vortex shedding frequency had an associated Strouhal number of 0.132.

Two geometrical modifications to reduce jet pluming were identified and investigated using CFD. Blunting the sharp edge of the scoop reduced vorticity and increased capture efficiency by 2% at 7500 rpm. Reversing the jet direction so that it was with rotation instead of against rotation almost eliminated jet deflection and pluming but reduced capture efficiency by 10%. A modified scoop system geometry would be required to capitalize benefits from reverse jet configurations.

The results of the study presented in this chapter has given vital insight into the effects of vortex shedding on the capture efficiency of a scoop system. It is suggested that future designs may not need sharp tipped scoops and that somewhat better capture efficiency may be possible with a blunted leading edge.

Work presented in this chapter has been published in the proceedings of ASME Turbo Expo 2017 in the paper GT2017-63444[74].

7 Conclusions

7.1 Attainment of objectives

The aim of the project was to develop a computationally efficient multiphase CFD model to predict and assess the performance of the particular scoop device that has been experimentally investigated by G2TRC. All the objectives stated in chapter 1 were achieved. In addition to that additional work concerning the prediction of vortex shedding was also done. A summary of the key finding for each of the chapters where results were produced is given in this section.

7.2 Conclusions on the effect of shaft speed on capture efficiency presented in chapter 4

The objectives of the thesis fulfilled in this chapter include the achievement of a CFD model that predicts capture efficiencies in close agreement with experimental results, assessing the effect of shaft speed and explaining qualitatively for the factors affecting the capture efficiency due the variation in the shaft speed. An analytical and 2D CFD study was conducted to assess the effect of shaft speed on the capture efficiency of the scoop device in 2D. The chapter also presents grid dependency studies that were conducted prior to simulation so that a grid independent solution is achieved. The CFD study showed the existence of a threshold shaft speed for a fixed jet velocity at which optimum capture efficiency can be obtained. For the geometry and operating conditions investigated using CFD, the optimum velocity ratio identified was 0.477 which corresponds to a shaft speed of 1000rpm and a jet velocity of 22.38m/s. CFD results are within 6.64% from experimental results. In-depth discussion about the contributing factors to variation is presented and reasons for discrepancies between analytical, CFD and experimental results are also given.

7.3 Conclusions on the effect of geometry and operating conditions on scoop capture efficiency presented in chapter 5

The objectives of the thesis that are achieved in this chapter are mainly geared towards investigating the effects of various geometrical changes and operating conditions on the capture efficiency. In chapter 5 investigations were carried out to assess the change in performance when changes to geometry operating conditions are done. The findings are as follows:

- A constriction gap of 4mm gives the best capture efficiency compared to gaps of 3mm and 2mm for a jet velocity of 22.381m/s and in the shaft speed in the range of 5000rpm to 10000rpm. A gap of 2mm leads to a choked flow at the outlet of the scoops which causes a significant reduction in the capture efficiency of the scoops. There is no significant increase in the capture efficiency between 3mm and 4mm because there is no choked flow with a gaps of 3mm and 4mm.
- When factored flow rates (such that the jet velocity is below the threshold velocity for the corresponding shaft speed) are used, it is observed that the capture efficiency increases linearly with shaft speed. This is because at low shaft speeds, oil droplets have sufficient time to be centrifuged outwards. At higher shaft speeds, oil droplets have less time and get captured by scoops quickly
- With more jets that make a shorted perpendicular distance to the centre, O,(jets that make a smaller angle to the vertical), the capturing efficiency is higher, because the jet impinges the scoop closer to the outlet where there is less chance for resulting oil droplets to be centrifuged outwards as the scoops rotate.
- An increase of 7% in the capturing efficiency is seen when a differential pressure of 0.18bar is applied across the outlet of scoops, due to quicker removal of oil from the scoops.
- It is observed that there is a specific value for the number of scoops that is required for optimum capture efficiency for a fixed jet and shaft speed. The capture efficiency increases as the number of scoops are increased towards the optimum value, beyond which the capture efficiency decreases. It is also observed that as the shaft speed is increased the number of scoops necessary to give a higher capture efficiency reduces.

7.4 Conclusions on the effect of vortex shedding on the capture efficiency presented in chapter 6

The objectives of the thesis that are achieved in this chapter include the identification of the vortex shedding which is a factor that effects the capture efficiency as shaft speeds are increased for a constant jet velocity and investigating various geometrical changes that may improve the capture efficiency. Chapter 6 presents in-depth investigations of the effect of vortex shedding on the capturing efficiency. It was identified that vortex formation from the scoop tip leads to a modified pressure field with consequent jet deflection and pluming, reducing capture efficiency. The study found that the extent of the region affected by this vorticity increased with increasing shaft speed, and that vortex shedding frequency had an associated Strouhal number of 0.132. Further studies done to assess the effect of the tip shape show that scoops with blunt tip give higher capturing efficiency compared to sharp tipped scoops.

7.5 Contribution to science and novelty in work

The work presented in this thesis has been published in papers including the Journal of Turbomachinery(doi:10.1115/1.4040812)[5]), Proceedings of Turbo Expo 2017(paper no: GT2017-63444[74]) and Turbo Expo 2018(paper no: GT2018-76177[6]). Published work will be useful for researchers who work in modelling of scoops and also for researchers who use different geometries. Guidelines in the published work can be used by researchers to adopt a suitable modelling strategy for their investigations. The work done in this PhD is in 2D. CFD results were within 6.64% of experimental results showing that the model used here is computationally efficient and sufficiently accurate. Hence the modelling strategy can be used by future researchers also to assess their scoop devices in 2D (based on appropriate geometry simplifications). It should be noted that not all scoop geometries can be simplified to a 2D one.

In-depth investigations for some of the operating conditions and geometries not used by previous researchers using CFD and experiments has been presented. This part of the work will help researchers and engineers understand and consider the factors that contribute to variations and reduction in the capture efficiency of scoops devices.

The effect of vortex shedding in scoop devices has been studied in this research and the associated Strouhal number and vortex shedding frequencies have also been estimated. To the best of the author's knowledge, this is the first time such research has been done either by the use of CFD or experiments.

7.6 Future Work

Contribution from this PhD and published research papers (on CFD work and experiments) is still not sufficient to fill the gaps in research concerning scoop work. Some of the potential areas that have to be researched are highlighted as follows:

1. 3D simulation of scoop devices with grid refinements comparable to that of 2D used in this chapter. This has not been done in the past and previous researchers have only done work with coarse grid that still give results with discrepancies compared to experimental data. A 3D simulation of this sort can be done only if access to a powerful computational facility is available due to the grid size that will be involved.
2. Efforts with regards to turbulence modelling should be geared towards the use of more accurate turbulence models such as Large Eddy Simulations (LES) and Direct Numerical Simulations (DNS). Currently efforts have been devoted towards LES turbulence modelling and preliminary results have been produced by the author of this thesis.
3. Different scoop geometries (such as blunt) and configurations (like a reverse jet configuration presented in Chapter 6) could be assessed experimentally with the intention of eliminating the pluming at the tip of the oil jet.
4. Experimentally determining the vortex shedding frequency should be done in order to validate the CFD findings presented in chapter 6.
5. Some investigations involving lower pressure at the outlets to create a differential pressure across the scoops (as suggested in chapter 5) can be investigated experimentally to validate results found in CFD.
6. The usage of various number of scoops have to be investigated experimentally. It is deduced from CFD work that there is an optimum number of scoops beyond which capture efficiency decreases.

References

[1] R. J. Parker, "Lubrication of Rolling-element bearings," *NASA Tech. Memo. 81449*, 1980.

[2] K. Kovaleski Stanley, "Radial Scoop Construction," U.S. Patent 4648485, 1987.

[3] K. L. Fisher, H. F. Demel, and R. Hazeley, "Methods and apparatus for supplying oil to bearing assemblies," US patent 6409464, 2002.

[4] K. L. Fisher, "Bi-directional oil scoop for bearing lubrication," U.S. 6,682,222, 2004.

[5] P. P. Cageao, K. Simmons, A. Prabhakar, and B. Chandra, "Assessment of the oil scoop capture efficiency in high speed rotors," *J. Eng. Gas Turbines Power*, pp. 1–14, 2017.

[6] A. Prabhakar, Y. A. Abakr, and K. Simmons, "Numerical Investigations to Assess the Impact of Shaft Speed on the Performance of Scoop Devices," in *Proceedings of the ASME Turbo Expo*, 2018, p. GT2018-76177.

[7] A. Prabhakar, Y. A. Abakr, and K. Simmons, "Effect of Vortex Shedding on the Performance of Scoop Based Lubrication Devices," no. 50923. p. V07AT34A008, 2017.

[8] O. E. Diemuodeke and I. Sher, "Mechanistic Model for the Breakup Length in Jet Atomization," *SAE Int. J. Engines*, vol. 9, no. 2, pp. 1314–1319, 2016.

[9] J. Becker and C. Hassa, "Breakup and Atomization of a Kerosene Jet in Crossflow at Elevated Pressure," *Atomization and Sprays*, vol. 12, no. 1–3. pp. 49–68, 2002.

[10] C. Aalburg, G. M. Faeth, and K. A. Sallam, "Primary Breakup of Round Turbulent Liquid Jets in Uniform Crossflows," *AIAA J.*, vol. 734, no. January, pp. 1907–1916, 2005.

[11] R. E. Phinney, "The breakup of a turbulent liquid jet in a gaseous atmosphere," *J. Fluid Mech.*, vol. 60, no. 4, pp. 689–701, 1973.

[12] H. Grosshans, A. Movaghar, L. Cao, M. Oevermann, R. Z. Szász, and L. Fuchs, "Sensitivity of VOF simulations of the liquid jet breakup to physical and numerical parameters," *Comput. Fluids*, vol. 136, pp. 312–323, 2016.

[13] P. Paleo Cageao, K. Simmons, A. Prabhakar, and B. Chandra, "Experimental investigation into Gas Turbine Oil Scoop Capture Efficiency," *J. Eng. Gas Turbines Power*, no. GTP171167, 2018.

[14] D. Fuster *et al.*, "Simulation of primary atomization with an octree adaptive mesh refinement and VOF method," *Int. J. Multiph. Flow*, vol. 35, no. 6, pp. 550–565, 2009.

[15] S. Khosla and C. Smith, "Detailed Understanding of Drop Atomization by Gas Crossflow Using the Volume of Fluid Method," *19th Annu. Conf. Liq. At. Spray Syst.*

Toronto, 2006.

[16] R. Reddy and R. Banerjee, *Simulation of a gas blasted liquid sheet on GPU architecture*. 2014.

[17] R. Reddy and R. Banerjee, "Study of Disintegration of a High Speed Liquid Jet Using VOF Method," in *Procedia IUTAM*, 2015, vol. 15, pp. 305–312.

[18] G. Anirban, R. M. Barron, and R. Balachandar, "Numerical simulation of high-speed turbulent water jets in air," *J. Hydraul. Res.*, vol. 48, no. 1 EXTRA ISSUE, pp. 119–124, 2010.

[19] B. Guo, T. A. G. Langrish, and D. F. Fletcher, "An assessment of turbulence models applied to the simulation of a two-dimensional submerged jet," *Appl. Math. Model.*, vol. 25, no. 8, pp. 635–653, 2001.

[20] H. Hajikandi and A. Mansoori, "A comparative assessment of turbulence models for axisymmetric confined jet with back pressure," *J. Appl. Sci.*, vol. 7, no. 1, pp. 121–126, 2007.

[21] B. Jafarzadeh, A. Hajari, M. M. Alishahi, and M. H. Akbari, "The flow simulation of a low-specific-speed high-speed centrifugal pump," *Appl. Math. Model.*, vol. 35, no. 1, pp. 242–249, 2011.

[22] Y. I. Wei-lin and C. Jiang, "Coupled Fluid-Thermal-Solid Simulation of Axial Through-Flow Rotating Cavities," in *ASME Turbo Expo 2013*, 2013, pp. 1–9.

[23] A. J. Turner, "Application of CFD to model an aeroengine internal gearbox, PhD Thesis," University of Nottingham, 2015.

[24] T. A. Webb, "Power losses in spiral bevel gears. PhD thesis," University of Nottingham, 2010.

[25] L. Li and H. Versteeg, "Numerical investigation on fluid flow of gear lubrication," … *Fuels Lubr.*, vol. 1, pp. 1056–1062, 2009.

[26] S. Rapley, "Computational investigation of torque on spiral bevel gears, PhD Thesis," University of Nottingham, 2009.

[27] C. Gorla *et al.*, "Hydraulic losses of a gearbox: CFD analysis and experiments," *Tribol. Int.*, vol. 66, pp. 337–344, 2013.

[28] C. Gorla *et al.*, "CFD simulations of splash losses of a gearbox," *Advances in Tribology*, 2012.

[29] H. Arisawa, M. Nishimura, H. Imai, and T. Goi, "Computational Fluid Dynamics Simulations and Experiments for Reduction of Oil Churning Loss and Windage Loss in Aeroengine Transmission Gears," *J. Eng. Gas Turbines Power*, vol. 136, no. 9, pp. 92604–92609, May 2014.

[30] F. Concli, E. Conrado, and C. Gorla, "Analysis of power losses in an industrial planetary speed reducer: Measurements and computational fluid dynamics calculations," *Proc. Inst. Mech. Eng. Part J J. Eng. Tribol.*, vol. 228, no. 1, pp. 11–21, 2014.

[31] F. Concli and C. Gorla, "Computational and experimental analysis of the churning power losses in an industrial planetary speed reducer," in *WIT Transactions on Engineering Sciences*, 2012, vol. 74, pp. 287–298.

[32] F. Concli and C. Gorla, "Influence of lubricant temperature, lubricant level and rotational speed on the churning power loss in an industrial planetary speed reducer: computational and experimental study," *Int. J. Comput. Methods Exp. Meas.*, vol. 1, no. 4, pp. 353–366, 2013.

[33] F. Concli and C. Gorla, "Oil squeezing power losses in gears: A CFD analysis," in *WIT Transactions on Engineering Sciences*, 2012, vol. 74, pp. 37–48.

[34] C. S. Ferreira, "The near wake of the VAWT 2D and 3D views of the VAWT aerodynamics," *T.U.Delft Thesis*, 2009.

[35] K.W. McLaren, "Unsteady loading of high solidity vertical axis wind turbines," *PhD Thesis*, 2011.

[36] C. Li, S. Zhu, Y.-L. Xu, and Y. Xiao, "2.5D large eddy simulation of vertical axis wind turbine in consideration of high angle of attack flow," *Renew. Energy*, vol. 51, pp. 317–330, 2013.

[37] Y. Chen and Y. Lian, "Numerical investigation of vortex dynamics in an H-rotor vertical axis wind turbine," *Eng. Appl. Comput. Fluid Mech.*, vol. 9, no. 1, pp. 21–32, 2015.

[38] K. M. Lam and M. Y. H. Leung, "Asymmetric vortex shedding flow past an inclined flat plate at high incidence," *Eur. J. Mech. B/Fluids*, vol. 24, no. 1, pp. 33–48, 2005.

[39] D. L. Sondak and D. J. Dorney, "Simulation of Vortex Shedding in a Turbine Stage," *J. Turbomach.*, vol. 121, no. July, pp. 428–435, 1999.

[40] S. K. Prasad, P. Sangli, O. Buyukisik, and D. Pugh, "Prediction of Gas Turbine Oil Scoop Capture Efficiency," in *ASME 2014 Gas Turbine India Conference, American Society of Mechanical Engineers*, 2014, p. GTINDIA2014-8329.

[41] E. Korsukova, A. Kruisbrink, H. Morvan, P. P. Cageao, and K. Simmons, "Oil Scoop Simulation and Analysis using CFD and SPH," in *Proceedings of the ASME Turbo Expo*, 2016, p. GT2016-57554.

[42] K. Simmons, L. Harrison, E. Korsukova, and P. P. Cageao, "CFD Study Exploring Jet Configurations and Jet Pulsing for an Aeroengine Scoop-Based Oil Delivery System," in *Proceedings of the ASME Turbo Expo*, 2018, p. GT2018-76182.

[43] L. Yaguo, J. Le, L. Zhenxia, and H. Jianping, "Simulation and Analysis of Oil Scoop Capture Efficiency," in *Proceedings of the ASME Turbo Expo*, 2018, p. GT2018-75989.

[44] A. Prabhakar, Y. A. Abakr, and K. Simmons, “First year PhD progress report-Numerical Investigations to assess performance of scoop devices,” 2015.

[45] A. Prabhakar, Y. A. Abakr, and K. Simmons, “Second year PhD progress report-Numerical Investigations to assess performance of scoop devices,” 2016.

[46] S. Yuan, K. Guo, J. Hu, and Z. Peng, “Study on Aeration for Disengaged Wet Clutches Using a Two-Phase Flow Model,” *J. Fluids Eng.*, vol. 132, no. 11, p. 111304, 2010.

[47] H. Liu, J. Wang, N. Kelson, and R. J. Brown, “A study of abrasive waterjet characteristics by CFD simulation,” *J. Mater. Process. Technol.*, vol. 153–154, no. 1–3, pp. 488–493, 2004.

[48] Q. Peng, L. Gui, and Z. Fan, “Numerical and experimental investigation of splashing oil flow in a hypoid gearbox,” *Eng. Appl. Comput. Fluid Mech.*, vol. 12, no. 1, pp. 324–333, Jan. 2018.

[49] M. Angioletti, E. Nino, and G. Ruocco, “CFD turbulent modelling of jet impingement and its validation by particle image velocimetry and mass transfer measurements,” *Int. J. Therm. Sci.*, vol. 44, no. 4, pp. 349–356, 2005.

[50] J. U. Brackbill, D. B. Kothe, and C. Zemach, “A continuum method for modeling surface tension,” *J. Comput. Phys.*, vol. 100, no. 2, pp. 335–354, 1992.

[51] M. Raciti Castelli, A. Englaro, and E. Benini, “The Darrieus wind turbine: Proposal for a new performance prediction model based on CFD,” *Energy*, vol. 36, no. 8, pp. 4919–4934, 2011.

[52] R. Barrio, J. Fernndez, E. Blanco, and J. Parrondo, “Estimation of radial load in centrifugal pumps using computational fluid dynamics,” *Eur. J. Mech. B/Fluids*, vol. 30, no. 3, pp. 316–324, 2011.

[53] D. A. Arias and T. A. Shedd, “CFD analysis of compressible flow across a complex geometry venturi,” *J. Fluids Eng. Trans. ASME*, vol. 129, no. 9, 2007.

[54] D. A. Arias and T. A. Shedd, “CFD analysis of flow field and pressure losses in carburetor venturi,” *SAE Technical Papers*, 2006.

[55] a Fluent, “ANSYS Fluent 12.0,” *ANSYS Fluent Theory Guid.*, vol. 15317, no. November, pp. 1–2498, 2009.

[56] N. Y. Gnedin, V. A. Semenov, and A. V. Kravtsov, “Enforcing the Courant–Friedrichs–Lewy condition in explicitly conservative local time stepping schemes,” *J. Comput. Phys.*, vol. 359, pp. 93–105, 2018.

[57] H. A. Jakobsen, “Numerical convection algorithms and their role in eulerian CFD reactor simulations,” *Int. J. Chem. React. Eng.*, vol. 1, no. 1, 2002.

[58] D. C. Wilcox, *Turbulence modeling for CFD*, vol. 93. 1993.

[59] B. E. Launder and D. B. Spalding, “The numerical computation of turbulent flows,” *Comput. Methods Appl. Mech. Eng.*, vol. 3, no. 2, pp. 269–289, 1974.

[60] V. Yakhot, S. a. Orszag, S. Thangam, T. B. Gatski, and C. G. Speziale, “Development of turbulence models for shear flows by a double expansion technique,” *Phys. Fluids*, vol. 4, no. 7, pp. 1510–1520, 1992.

[61] A. Rezaeiha, I. Kalkman, and B. Blocken, “CFD simulation of a vertical axis wind turbine operating at a moderate tip speed ratio: Guidelines for minimum domain size and azimuthal increment,” *Renew. Energy*, vol. 107, pp. 373–385, 2017.

[62] M. Karimi, G. Akdogan, K. H. Dellimore, and S. M. Bradshaw, “Quantification of numerical uncertainty in computational fluid dynamics modelling of hydrocyclones,” *Comput. Chem. Eng.*, vol. 43, pp. 45–54, 2012.

[63] F. Mortazavi, A. Riasi, and A. Nourbakhsh, “Numerical Investigation of Back Vane Design and Its Impact on Pump Performance,” *J. Fluids Eng.*, vol. 139, no. 12, pp. 121104–121109, Sep. 2017.

[64] J. of F. Engineering, “Journal of fluids engineering editorial policy. statement on the control of numerical accuracy, editorial,” *J. Fluids Eng.*, vol. 115, pp. 339–342, 1993.

[65] T. S. Phillips and C. J. Roy, “Richardson Extrapolation-Based Discretization Uncertainty Estimation for Computational Fluid Dynamics,” *J. Fluids Eng.*, vol. 136, no. 12, p. 121401, 2014.

[66] I. Celik and O. Karatekin, “Numerical Experiments on Application of Richardson Extrapolation With Nonuniform Grids,” *ASME J. Fluids Eng.*, vol. 119, no. 3, p. 584, 1997.

[67] S. Alimohammadi, D. B. Murray, and T. Persoons, “Experimental validation of a computational fluid dynamics methodology for transitional flow heat transfer characteristics of a steady impinging jet,” *J. Heat Transfer*, vol. 136, no. 9, 2014.

[68] M. Stephen, Ambrose, Arun, Prabhakar,PVS Kumar, Kiran, Kakimpa, Bruce, Herve, “Oil flow in an epicyclic gearbox,” *FF159/SA/024/issue01*, 2017.

[69] H. Prabhakar, Arun, Ambrose, Stephen, Morvan, “Two phase flow in a DERWENT scavenge gearbox,” *FF 202/AP/issue01*, 2018.

[70] F. Trivellato and M. Raciti Castelli, “Appraisal of Strouhal number in wind turbine engineering,” *Renew. Sustain. Energy Rev.*, vol. 49, pp. 795–804, 2015.

[71] K. Lam and C. Wei, “Numerical simulation of vortex shedding from an inclined flat plate,” *Eng. Appl. Comput. Fluid Mech.*, vol. 4, no. 4, pp. 569–579, 2010.

[72] B. Gandhi, N. Singh, V. Seshadri, and J. Singh, “Effect of Bluff Body Shape on Vortex Flow-meter Performance,” *Indian J. Eng. Mater. Sci.*, vol. 11, pp. 378–384, 2004.

[73] D. Jonathan, H. John, and K. Arun, “Curved blade oil scoop,” US7244096B2, 2007.

[74] A. Prabhakar, Y. A. Abakr, and K. Simmons, “Effect of vortex shedding on the performance of scoop based lubrication devices,” in *Proceedings of the ASME Turbo Expo*, 2017, vol. 7A–2017, p. GT2017-63444.

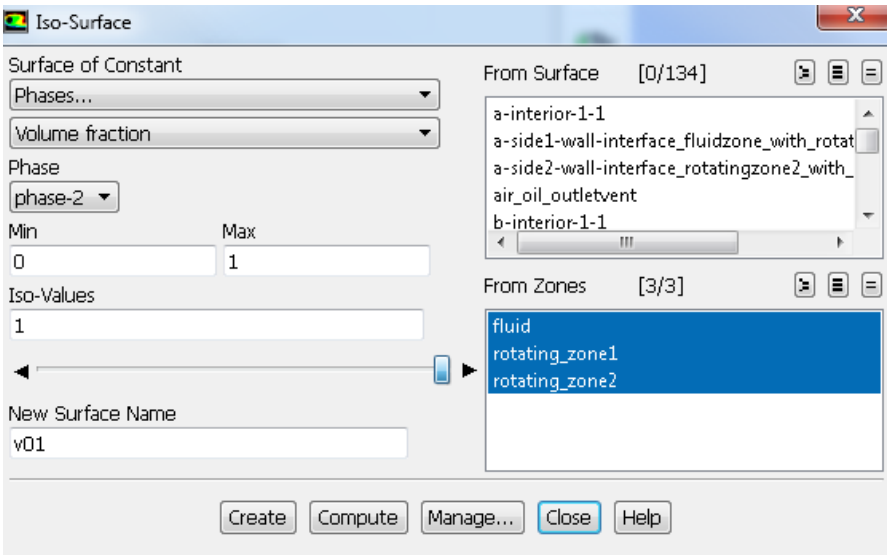
8 Appendix

8.1 Post-Processing and exporting images using FLUENT while running on high performance computing (HPC)

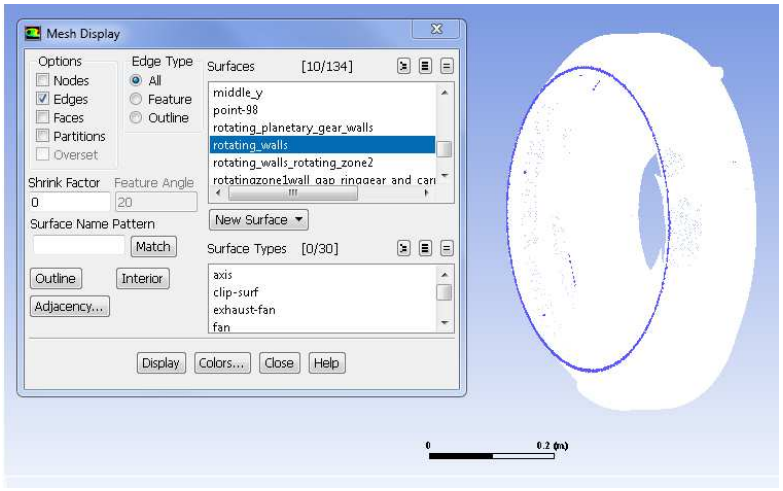
FLUENT was used to export images while simulations were progressing on the HPC. This method of exporting simulations allowed to analyze the flow of oil while the simulations were running and also eliminated the time in downloading a case and a data file and then opening it with CFD-Post. The method of saving images using FLUENT is not presented in any ANSYS tutorial or online forums. Hence will be presented here which might help users of FLUENT.

Saving VOF contour images in 3D.

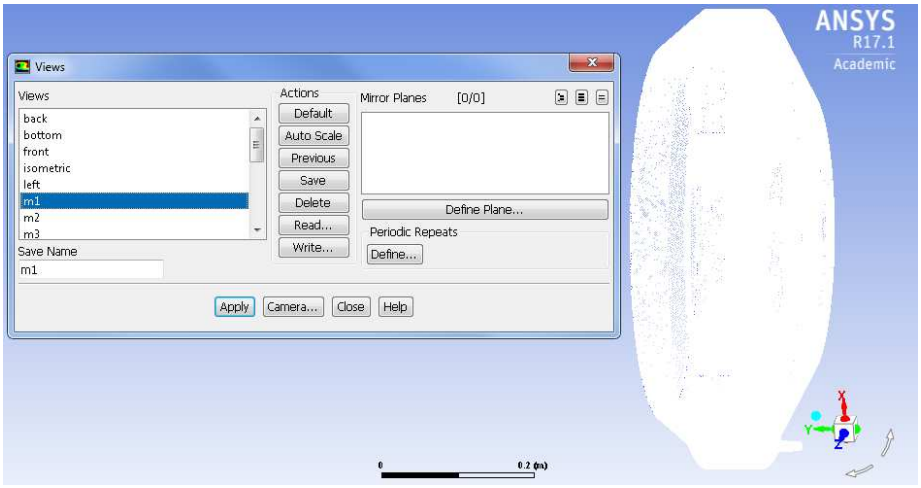
1. After the initialization of the case file, create an iso-surface of the volume fraction of oil for all the fluid zones using a value of 1. Similarly create iso-surfaces for volume fraction values of 0.9, 0.8, 0.7, 0.6, and 0.5.



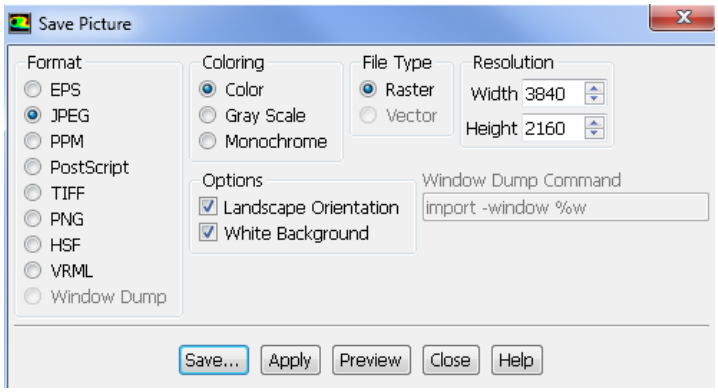
2. Use mesh display and display the surfaces of all the walls, inlets and pressure outlets only.



3. Under the "Viewing" tab click on views and create the necessary camera views at which images should be created. Use the camera view tools to change the orientation of the view.



4. Under File>Save picture, set the resolution of the image to the values (or higher) shown. Use the preview button to see the image that will be exported from FLUENT for a view that was saved in Step 3. Adjustments to the view might be needed.



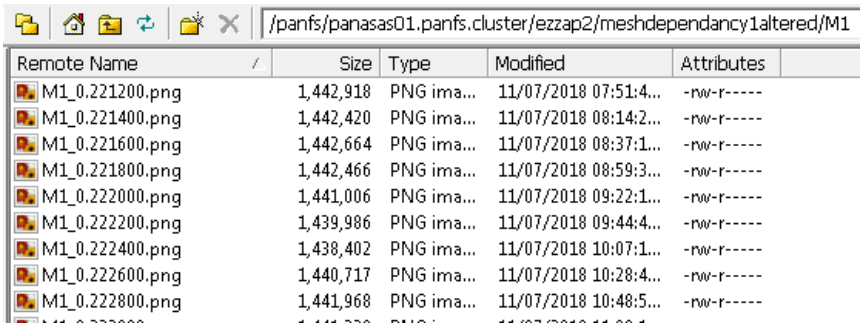
5. Click on Solution> Calculation Activities> Execute commands and enter the following commands and execute them at every 20 time-steps(or as preferred):

No	Command	Command Description
1	display open-window 6	Open a new window in FLUENT
2	display set-window 6	Sets the window for graphical outputs(such as plots).
3	display set lights headlight-on? no	Sets graphics related to mesh and the scene
4	display set contours filled-contours yes	
5	display set contours node-values no	
6	display set contours render-mesh yes	
7	display set contours surfaces 43 44 45 46 47 48 49 50()	Chose the iso-surfaces on which volume fraction contours will be displayed based on their ID that were created in Step 1
8	display surface-mesh 15 22 12 2 19 1 0 3 6 10 17 21 4 5 11 9 24 23 ()	Displays the surface mesh of surfaces with the ID's stated that will be used to represent the geometry of the case (walls, inlets, pressure outlets, etc).
9	display contour phase-2 vof 1 1	Range of volume fraction to be displayed. Although iso-surfaces for values less than 1 were created, the minimum limit here is used as 1 and all the iso-surfaces will be shown with the same color.
10	display set windows scale visible yes	Displays the color scale for the volume fraction values
11	display set windows text visible yes	Display text such as simulation time, case details and other text such as ANSYS version details
12	display update-scene select-geometry yes casing_walls1 yes casing_walls2 yes walls_pipes yes wall_end2_fluidzone yes walls_sump yes	This command selects the surfaces stated here. Surfaces can be selected only if they were mentioned in command No. 8

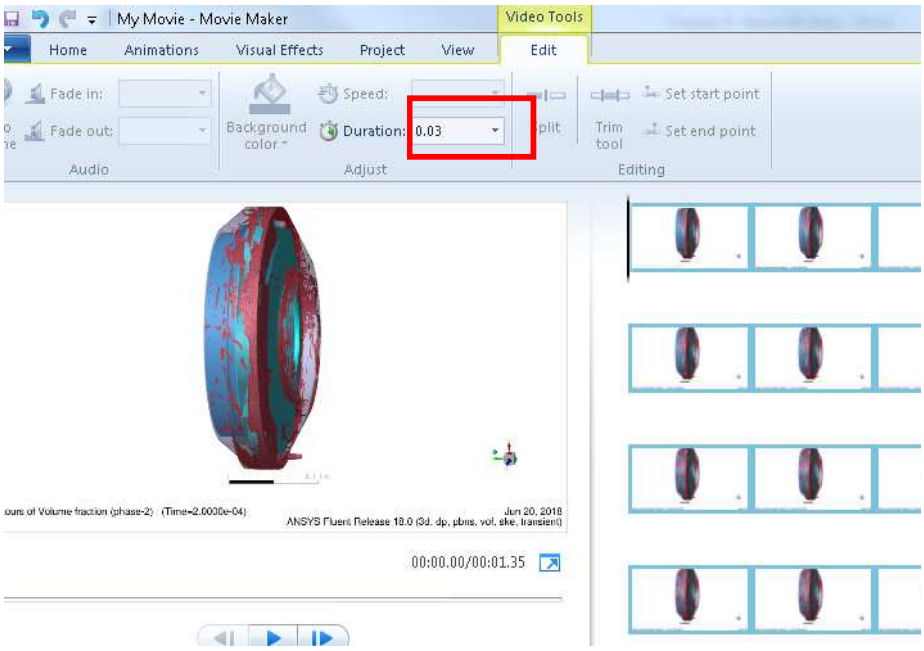
	wallend_rotatingzone2 yes scavenge_outlet no no	
13	display update-scene display Object Name:Group yes yes yes yes no no no no no 192 201 255 54	This command adds color and set the transparency to the selected surfaces in the previous step. The last 4 numbers (192 201 255 54) are used to add the color and transparency. 192 201 255 is the RGB color and 54 stands for the transparency of the surface. Note that different colors for the surface can be achieved using the same RGB color but using different transparency values.
14	display update-scene select-geometry yes bearing_inlet_flow_on_rotatingzone 1 yes rotating_walls_rotating_zone2 yes rotating_walls yes stationary_planetary_gear_walls yes rotating_planetary_gear_walls yes sun_gear_walls yes rotatingzone1wall_gap_ringgear_and _carrierplate no no	Similar explanation as for commands **12** and **13**
15	display update-scene display Object Name:Group yes yes yes yes no no no no no 0 255 255 0	
16	display update-scene select-geometry yes inlet_planetary_gear yes inlet_ring_gear yes inlet_sungear_plus_annulusfraction no no	
17	display update-scene display Object Name:Group yes yes yes yes no no no no no 0 0 0 0	
18	display update-scene select-geometry yes contour-43-phase-2-vof yes contour-44-phase-2-vof yes contour-45-phase-2-vof yes contour-46-phase-2-vof yes contour-47-phase-2-vof yes contour-48-phase-2-vof yes contour-49-phase-2-vof yes contour-50-phase-2-vof no no	
19	display update-scene display Object Name:Group yes yes yes yes no no no no no 0 0 0 0	
20	display update-scene select-geometry yes rotating_walls_rotating_zone2 yes	

	rotatingzone1wall_gap_ringgear_and _carrierplate no no	
21	display update-scene display Object Name:Group yes yes yes yes no no no no no 0 160 255 0	
22	display update-scene select-geometry yes mesh_walls no no	
23	display update-scene display Object Name:Group yes yes yes yes no no no no no 255 255 0 85	
24	display view restore-view m1	This command sets the view m 1that was created and saved in step 3
25	display save-picture M1/M1_%6f.png	This command saves the view of m1 in the folder M1. Note that folder M1 should be created before the simulation commences.
26	display view restore-view m2	Similar explanation as for commands **24** and **25**
27	display save-picture M2/M2_%6f.png	
28	display view restore-view m3	
29	display save-picture M3/M3_%6f.png	
30	display view restore-view m4	
31	display save-picture M4/M4_%6f.png	

Commands can be run in the text to user interface (TUI) in FLUENT before the simulation is run to confirm that all the commands are working. After all 5 steps are completed, the simulation can be run on the workstation or HPC as usual after the creation of the necessary folders corresponding to commands **24-31**. Images will be saved in each folder as shown with the simulation time:



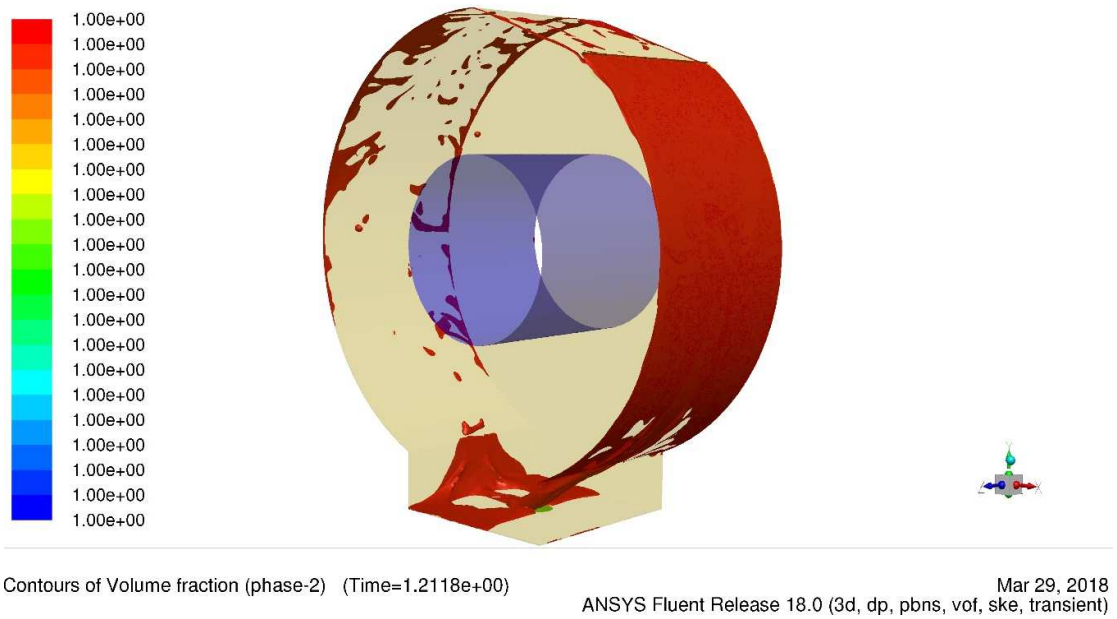
6. After the images are downloaded, they should be imported into Microsoft movie maker. Select all the images after they have been imported and then under Edit, change the duration of the images to anywhere between 0.03s to 0.2s based on the desired frame rate.



7. Export the movie from movie maker in the desired movie format (example: mp4 or wmv). Animations will be created from the images that were exported from FLUENT.

Sample images that are post-processed using FLUENT only while the simulation was running are shown below:



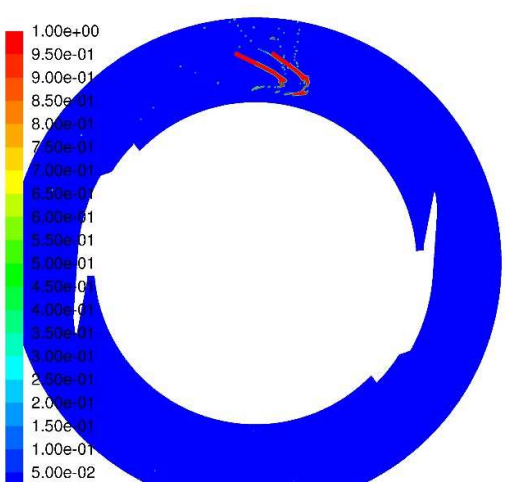


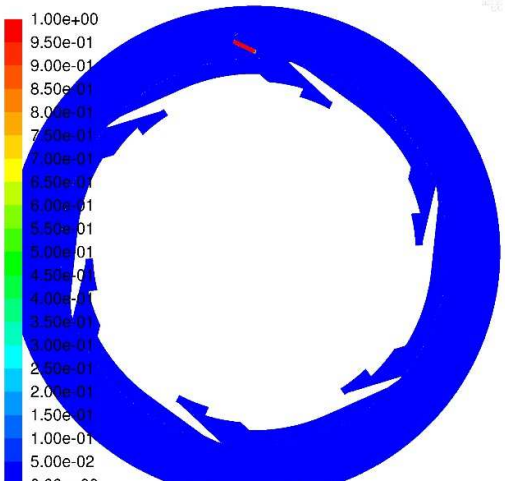
Saving VOF contour images in 2D or at planes in a 3D simulation.

1. Follow steps 2 to 4 as mentioned for 3D images. Then Click on Solution> Calculation Activities> Execute commands and enter the following commands and execute them every 20 time-steps(or as preferred:

No	Command	Command Description
1	display open-window 5	Open a new window in FLUENT
2	display set-window 5	Sets the window for graphical outputs(such as plots)
3	view camera projection orthographic	Sets graphics related to mesh and the scene
4	display set contours filled-contours yes	
5	display set contours node-values yes	
6	display set contours render-mesh yes	
7	display set contours surfaces ()	Chose the surfaces on which volume fraction contours will be displayed based on their IDs stated. If no ID's are given in this command, all the surfaces present in the case. If volume fraction contours at a plane in a 3D case is required. The plane should be created beforehand and the ID should be stated in this command.
8	display surface-mesh ()	Displays the surfaces with the ID's stated that will be used to represent the geometry (walls, inlets, pressure outlets, etc).
9	display contour phase-2 vof 0 1	Range of volume fraction to be displayed.
10	display set windows scale visible yes	Displays the color scale for the volume fraction values
11	display set windows text visible yes	Display text such as simulation time, case details and other text such as ANSYS version details
12	display view restore-view front	Restores the saved view
13	display save-picture Front_%6f.png	Saves the picture of the view in command **12**
14	display view restore-view nearjet	Similar explanation as for commands **12** and **13**
15	display save-picture nearjet%6f.png	

Images will be saved as the simulations are running. The images can be used to created animations using movie maker (as shown for a 3D case). Sample images in 2D acquired from FLUENT are shown below:


1.00e+00
9.50e-01
9.00e-01
8.50e-01
8.00e-01
7.50e-01
7.00e-01
6.50e-01
6.00e-01
5.50e-01
5.00e-01
4.50e-01
4.00e-01
3.50e-01
3.00e-01
2.50e-01
2.00e-01
1.50e-01
1.00e-01
5.00e-02


1.00e+00
9.50e-01
9.00e-01
8.50e-01
8.00e-01
7.50e-01
7.00e-01
6.50e-01
6.00e-01
5.50e-01
5.00e-01
4.50e-01
4.00e-01
3.50e-01
3.00e-01
2.50e-01
2.00e-01
1.50e-01
1.00e-01
5.00e-02

8.2 MATLAB codes

8.2.1 Analytical modelling calculations (iterative calculations and plots)

```
clc
close all
Haxis=3.85;
R=102;
Theeta_jet=64.2;
Theeta_scoop=33.05858717;
v=22.381;
w=10000;

format long
Theeta_3=asind(((R+Haxis)*sind(Theeta_jet))/R);
Theeta_2=180-(2*Theeta_3);
Theeta_1=Theeta_3-Theeta_jet;
Theeta_4=60-Theeta_2;
Theeta_5=30-Theeta_1;
Ratio=(Theeta_4*sind(Theeta_3))/(6*R*sind(Theeta_2))*1000;
Epsilon=(27.352000000000000);
AB=R*(sind(Theeta_2)/sind(Theeta_3));

% Contact Point
Epsilon1=0:0.001:Theeta_2;
Theeta_scoop_jet1=(Theeta_jet+Theeta_scoop)-(Theeta_4+Theeta_5+Epsilon1);
OY1=(R.*((sind(90-(Theeta_2/2))))).(sind(90+(Theeta_2/2)-Epsilon1));
YZ1= R-OY1;
Q1=90-Theeta_jet+(Theeta_4+Theeta_5+Epsilon1);
Q2222=Epsilon1+Theeta_3;
CX1=((sind(Q1).*YZ1)./((sind(Theeta_scoop_jet1))));
YX1=((sind(90-Theeta_scoop).*YZ1)./((sind(Theeta_scoop_jet1))));
OX1=((R.^2)+(CX1.^2)-(2.*R.*CX1.*cosd(90-Theeta_scoop))).^0.5;
gamma1=asind((YX1./OX1).*(sind(90+Theeta_jet-Theeta_4-Theeta_5-Epsilon1)));
Beta1=Epsilon1-gamma1;
AX1=(((R.*sind(Theeta_2))-(OX1.*sind(Beta1)))./(sind(Theeta_3)));

Epsilon1_iterate=(AX1./(v*1000))-((Theeta_4+Epsilon1)/(6*w));
Epsilon1_iterate=abs(Epsilon1_iterate);
[min_num, min_idx]=min(Epsilon1_iterate(:));
[X1,Y1]=ind2sub(size(Epsilon1_iterate),min_idx);
contact_angle_1=Epsilon1(1,Y1);

% Contact Point vs w
Theeta_jet_contact=58.2:3:70.2;
Theeta_3_contact=asind(((R+Haxis)*sind(Theeta_jet_contact))/R);
```

```
Theeta_2_contact=180-(2*Theeta_3_contact); Theeta_1_contact=Theeta_3_contact-
Theeta_jet_contact;
Theeta_4_contact=60-Theeta_2_contact;
Theeta_5_contact=30-Theeta_1_contact;

Theeta_jet_loop_counter=size(Theeta_jet_contact,2);

for j =1:1:Theeta_jet_loop_counter

w_contact=0:25:12000;
w_loop_counter=size(w_contact,2);

for i=1:1:w_loop_counter;
   Epsilon2=0:0.001:Theeta_2_contact(1,j);
   Theeta_scoop_jet=(Theeta_jet_contact(1,j)+Theeta_scoop)-
(Theeta_4_contact(1,j)+Theeta_5_contact(1,j)+Epsilon2);
   OY=(R.*((sind(90-(Theeta_2_contact(1,j)/2))))./(sind(90+(Theeta_2_contact(1,j)/2)-
Epsilon2));
   YZ= R-OY;
   Q=90-Theeta_jet_contact(1,j)+(Theeta_4_contact(1,j)+Theeta_5_contact(1,j)+Epsilon2);
   CX=((sind(Q).*YZ)./((sind(Theeta_scoop_jet))));
   YX=((sind(90-Theeta_scoop).*YZ)./((sind(Theeta_scoop_jet))));
   OX=((R.^2)+(CX.^2)-(2.*R.*CX.*cosd(90-Theeta_scoop))).^0.5;
   gamma=asind((YX./OX).*(sind(90+Theeta_jet_contact(1,j)-
(Theeta_4_contact(1,j)+Theeta_5_contact(1,j)+Epsilon2))));
   Beta=Epsilon2-gamma;
   AX=(((R.*sind(Theeta_2_contact(1,j)))-(OX.*sind(Beta))))./(sind(Theeta_3_contact(1,j))));
   Epsilon2_iterate=(AX/(v*1000))-((Theeta_4_contact(1,j)+Epsilon2)/(6*w_contact(1,i)));
   Epsilon2_iterate=abs(Epsilon2_iterate);
   [min_num, min_idx]=min(Epsilon2_iterate(:));
   [X2,Y2]=ind2sub(size(Epsilon2_iterate),min_idx);
   contact_angle_angularspeed(j,i)=Epsilon2(1,Y2);

contact_angle_reference_angularspeed(j,i)=Epsilon2(1,Y2)+Theeta_4_contact(1,j)+Theeta_5
_contact(1,j);
   capture_angle_angularspeed(j,i)=Theeta_2_contact(1,j)-Epsilon2(1,Y2);

   Theeta_scoop_jet_contact(j,i)=(Theeta_jet_contact(1,j)+Theeta_scoop)-
(Theeta_4_contact(1,j)+Theeta_5_contact(1,j)+Epsilon2(1,Y2));


   Q_epsilon(j,i)=90-
Theeta_jet_contact(1,j)+(Theeta_4_contact(1,j)+Theeta_5_contact(1,j)+Epsilon2(1,Y2));
Theeta_scoop_jet_epsilon(j,i)=(Theeta_jet_contact(1,j)+Theeta_scoop)-
(Theeta_4_contact(1,j)+Theeta_5_contact(1,j)+Epsilon2(1,Y2));
OY_epsilon(j,i)=(R.*((sind(90-
(Theeta_2_contact(1,j)/2))))./(sind(90+(Theeta_2_contact(1,j)/2)-Epsilon2(1,Y2)));
YZ_epsilon(j,i)= R-OY_epsilon(j,i);
```

```
CX_epsilon(j,i)=((sind(Q_epsilon(j,i)).*YZ_epsilon(j,i))./((sind(Theeta_scoop_jet_epsilon(j,i
)))));
end
end
contact_angle_with_omega=contact_angle_angularspeed;
capture_angle_with_omega=capture_angle_angularspeed;
contact_angle_with_omega(Theeta_jet_loop_counter+1,:)=w_contact;
capture_angle_with_omega(Theeta_jet_loop_counter+1,:)=w_contact;

figure(1)
plot(w_contact,capture_angle_angularspeed,'LineWidth',3);
legend({'\theta_j_e_t= 58.2^{\circ} ','\theta_j_e_t= 61.2^{\circ}','\theta_j_e_t=
64.2^{\circ}','\theta_j_e_t= 67.2^{\circ}','\theta_j_e_t= 70.2^{\circ}'})
 set(gca,'fontsize',15)
 xlabel('Shaft Speed (rpm)')
ylabel('Contact Angle (degrees)')
ylim([0 58])
axis square
print(gcf,'Figure1.png','-dpng','-r300');

figure(2)
plot(w_contact,contact_angle_reference_angularspeed,'LineWidth',3);
legend({'\theta_j_e_t= 58.2^{\circ} ','\theta_j_e_t= 61.2^{\circ}','\theta_j_e_t=
64.2^{\circ}','\theta_j_e_t= 67.2^{\circ}','\theta_j_e_t= 70.2^{\circ}'})
set(gca,'fontsize',15)
xlabel('Shaft Speed (rpm)')
ylabel('Strike angle (degrees)')
axis square
print(gcf,'Figure2.png','-dpng','-r300');



figure(3)
Q_642=90-
Theeta_jet_contact(1,3)+(Theeta_4_contact(1,3)+Theeta_5_contact(1,3)+contact_angle_angu
larspeed(3,:));
Theeta_scoop_jet_642=(Theeta_jet_contact(1,3)+Theeta_scoop)-
(Theeta_4_contact(1,3)+Theeta_5_contact(1,3)+contact_angle_angularspeed(3,:));
OY_642=(R.*((sind(90-(Theeta_2_contact(1,3)/2))))./(sind(90+(Theeta_2_contact(1,3)/2)-
contact_angle_angularspeed(3,:)));
YZ_642= R-OY_642;
CX_642=((sind(Q_642).*YZ_642)./((sind(Theeta_scoop_jet_642))));
plot(w_contact,CX_642,'r','LineWidth',3);
set(gca,'fontsize',15)
 xlabel('Shaft Speed (rpm)')
ylabel('C_X at strike point (mm)')
axis square
ylim([0 30])
```

```
print(gcf,'Figure3.png','-dpng','-r300');

figure(4)
plot(w_contact,Theeta_scoop_jet_contact,'LineWidth',3);
legend({'\theta_j_e_t= 58.2^{\circ} ','\theta_j_e_t= 61.2^{\circ}','\theta_j_e_t=
64.2^{\circ}','\theta_j_e_t= 67.2^{\circ}','\theta_j_e_t= 70.2^{\circ}'})
set(gca,'fontsize',15)
xlabel('Shaft Speed (rpm)')
ylabel('Angle Between Jet and Scoop at contact point (degrees)')
axis square
print(gcf,'Figure4.png','-dpng','-r300');

figure(6)
plot(w_contact,CX_epsilon,'LineWidth',3);
legend({'\theta_j_e_t= 58.2^{\circ} ','\theta_j_e_t= 61.2^{\circ}','\theta_j_e_t=
64.2^{\circ}','\theta_j_e_t= 67.2^{\circ}','\theta_j_e_t= 70.2^{\circ}'})
set(gca,'fontsize',15)
xlabel('Shaft speed (rpm)')
ylabel('C_X  at strike point (mm)')
axis square
print(gcf,'Figure6.png','-dpng','-r300');
```

8.2.2 MATLAB Post-processing code for FLUENT data

```
%Clear Workspace, close all open figures and switch of all warning messages
clear all
clc
close all
warning('off','all')

%Reading the mass flow rates
data= xlsread('data.xlsx');
%Inlet flow rate
Y = abs(data(:,1));
%Scoop 1 Data
X1= abs(data(:,2));
%Scoop 2 Data
X2= abs(data(:,3));
%Scoop 3 Data
X3= abs(data(:,4));
%Scoop 4 Data
X4= abs(data(:,5));
%Scoop 5 Data
X5= abs(data(:,6));
%Scoop 6 Data
X6= abs(data(:,7));

%compensate for download error from HPC computer
a1=size(Y,1);
a2=size(X1,1);
a3=size(X2,1);
a4=size(X3,1);
a5=size(X4,1);
a6=size(X5,1);
a7=size(X6,1);
b1=[a1 a2 a3 a4 a5 a6 a7];
b1=min(b1);

Y=Y(1:b1,:);
X1=X1(1:b1,:);
X2=X2(1:b1,:);
X3=X3(1:b1,:);
X4=X4(1:b1,:);
X5=X5(1:b1,:);
X6=X6(1:b1,:);

%calculating the mass flow in using numerical integration.
n=size(Y,1);
Time=Y(:,2);
```

```
inlet_massflowrate=Y(:,3);
mass_in = trapz(Time,inlet_massflowrate);

Time_steps=diff(Time);
Time_steps=([Time_steps(1,1);Time_steps]);
mass_flowedin_per_timestep=inlet_massflowrate.*Time_steps;
mass_flowed_in= cumsum(mass_flowedin_per_timestep);

%calculating the mass flow out using numerical integration.
X=X1+X2+X3+X4+X5+X6;
outlet_massflowrate=X;
outlet_massflowrate= abs(outlet_massflowrate);
mass_out = trapz(Time,outlet_massflowrate);

mass_flowedout_per_timestep=outlet_massflowrate.*Time_steps;
mass_flowed_out= cumsum(mass_flowedout_per_timestep);

%A loop to find the position of first non-zero mass flow rate at outlet
for i=1:1:n;
   if outlet_massflowrate(i,1)==0;
         i=i+1;
   elseif outlet_massflowrate(i,1)>1;
      i=i-1;
   break
   end
end

% Effciency and Flow time display and Rotation Speed

for i1=1:1:n;
   if X3(i1,1)==0;
         i1=i1+1;
   elseif X3(i1,1)>1;
      i1=i1-1;
   break
   end
end

for i2=1:1:n;
   if X4(i2,1)==0;
         i2=i2+1;
   elseif X4(i2,1)>1;
      i2=i2-1;
   break
   end
end
```

```
for i3=1:1:n;
   if X5(i3,1)==0;
         i3=i3+1;
   elseif X5(i3,1)>1;
      i3=i3-1;
   break
   end
end

for i4=1:1:n;
   if X6(i4,1)==0;
         i4=i4+1;
   elseif X6(i4,1)>1;
      i4=i4-1;
   break
   end
end

for i5=1:1:n;
   if X1(i5,1)==0;
         i5=i5+1;
   elseif X1(i5,1)>1;
      i5=i5-1;
   break
   end
end

t1=Time(i2,1)-Time(i1,1);
t2=Time(i3,1)-Time(i2,1);
t3=Time(i4,1)-Time(i3,1);
t4=Time(i5,1)-Time(i4,1);
t1t2t3t4avg=(t1+t2+t3+t4)/4;
t6scoops=t1t2t3t4avg*6;
RPM=(1/t6scoops)*60;
Number_of_Rotations=(RPM/60)*max(Time);
Number_of_Rotations=num2str(Number_of_Rotations);
RPM=num2str(RPM);
Flow_time = num2str(max(Time));
Efficiency_scoop= (mass_out/mass_in)*100;
Efficiency_scoop = num2str(Efficiency_scoop);


fprintf('SIMULATION INFORMATION...\r\n');
fprintf('The current flow time is %s seconds.\n',Flow_time);
fprintf('The Rotational Speed is approximately %s RPM.\n',RPM);
fprintf('The Wedges have completed %s rotations.\n',Number_of_Rotations);
fprintf('The current efficiency of the system is estimated to be %s%%.\n',Efficiency_scoop);
```

```
%Efficiency Graph Calculations
%Inputs

inlet_massflowrate_mod=inlet_massflowrate(1:n);
Time_steps_mod=Time_steps(1:n);
mass_flowedin_per_timestep_mod=inlet_massflowrate_mod.*Time_steps_mod;
mass_flowed_in_mod= cumsum(mass_flowedin_per_timestep_mod);
mass_flowed_out_mod=mass_flowed_out(1:n);
efficiency_p=(mass_flowed_out_mod./mass_flowed_in_mod)*100;

%Dotted line at the converged efficiency
eff_lim=(max(efficiency_p)*0.1)+max(efficiency_p);
Time_mod=Time(1:n);
Average_efficiency_settling=efficiency_p(round(size(efficiency_p)):end,1);
Time_eff=Time(round(size(efficiency_p)),1);
Time_eff=Time_eff(1,1);
Time_line_y=0:50:100;
Time_line_x=(ones(1,3))*Time_eff;
Average_Efficiency= mean(Average_efficiency_settling);
Average_Efficiency_line_x=0:((max(Time))/2):max(Time);
Average_Efficiency_line_y=(ones(1,3))*Average_Efficiency;
max_efficiency=max(efficiency_p);
max_efficiency_line_x=0:((max(Time))/2):max(Time);
max_efficiency_line_y=(ones(1,3))*max_efficiency;

%Plotting Codes
figure(1)
plot(Time,inlet_massflowrate,':r','LineWidth',2.5)
hold on
plot(Time,outlet_massflowrate,'b')
legend('Inlet Flow Rate','Outlet Flow Rate')
xlim([0 (max(Time))])

% x-axis limits
%xlim([(i*dt_int)*(1e-07) (n*dt_int)*(1e-07)])

% x-axis label
xlabel('\bf Time (s)','FontSize',10)
% y-axis label
ylabel({'Total flow rate (kg/s)                '},'rot',360,'FontSize',10,'fontweight','bold')
set(get(gca,'YLabel'),'Rotation',90);

%Tick for inlet mass_flow_rate
ytick_inlet=mean(inlet_massflowrate);
set(gca, 'YTick', sort([ytick_inlet, get(gca, 'YTick')]));
print('1- Mass Flow Rate','-dpng','-r150')

axis square
```

```
figure(2)
plot(Time,mass_flowed_in,':r','LineWidth',2.5)
hold on
plot(Time,mass_flowed_out,'b')
legend(' Mass Supplied at Inlet','Total Mass at Outlet','Location', 'NorthWest')

% x-axis limits
xlim([0 (max(Time))])
% x-axis label
xlabel('\bf Time (s)','FontSize',10)
% y-axis label
ylabel({' Mass (kg)'},'rot',360,'FontSize',10,'fontweight','bold')
 print('2- Mass Flow','-dpng','-r150')

set(get(gca,'YLabel'),'Rotation',90);

axis square

figure(3)
plot(Time_mod,efficiency_p);
xlim([0 (max(Time))])
ylim([0 100])
% x-axis label
xlabel('\bf Time (s)','FontSize',10)
% y-axis label
ylabel({'Capture Efficiency (%)'},'rot',360,'FontSize',10,'fontweight','bold')
hold on
set(get(gca,'YLabel'),'Rotation',90);
axis normal
print('3- Efficiency','-dpng','-r150')


figure(4)
%Wedges Flowrates
subplot(6,1,1)
plot(Time,X1);
xlim([0 (max(Time))])
ylabel({'Scoop 1';'Flow Rate (kg/s)'},'rot',90,'FontSize',10,'fontweight','bold')
subplot(6,1,2)
plot(Time,X2);
xlim([0 (max(Time))])
ylabel({'Scoop 2';'Flow Rate (kg/s)'},'rot',90,'FontSize',10,'fontweight','bold')
subplot(6,1,3)
plot(Time,X3);
xlim([0 (max(Time))])
ylabel({'Scoop 3';'Flow Rate (kg/s)'},'rot',90,'FontSize',10,'fontweight','bold')
subplot(6,1,4)
```

```
plot(Time,X4);
xlim([0 (max(Time))])
ylabel({'Scoop 4';'Flow Rate (kg/s)'},'rot',90,'FontSize',10,'fontweight','bold')
subplot(6,1,5)
plot(Time,X5);
xlim([0 (max(Time))])
ylabel({'Scoop 5';'Flow Rate (kg/s)'},'rot',90,'FontSize',10,'fontweight','bold')
subplot(6,1,6)
plot(Time,X6);
xlim([0 (max(Time))])
ylabel({'Scoop 6';'Flow Rate (kg/s)'},'rot',90,'FontSize',10,'fontweight','bold')
xlabel('\bf Time (s)','FontSize',10)
 print('4- Individual Flow Rates of Wedges','-dpng','-r150')

figure(5)
hold on
plot(Time,X1,'b')
plot(Time,X2,'k')
plot(Time,X3,'Color',[0,0.5,0])
plot(Time,X4,'r')
plot(Time,X5,'Color',[0.5,0,0.9])
plot(Time,X6,'Color',[0.8,0.5,0])
ylabel({'Flow Rate                ';'(kg/s)                '},'rot',360,'FontSize',10,'fontweight','bold')
xlabel('\bf Time (s)','FontSize',10)
legend('Wedge1','Wedge2','Wedge3','Wedge4','Wedge5','Wedge6','Location','NorthEastoutsid
e')
 print('5- All Wedges Flow Rates','-dpng','-r150')
```

8.3 Experimental Paper with published results for validation.

Journal of Engineering for Gas Turbines and Power. Received May 12, 2017;
Accepted manuscript posted July 11, 2018. doi:10.1115/1.4040812
Copyright (c) 2018 by ASME

Assessment of the oil scoop capture efficiency in high speed rotors

Paloma Paleo Cageao
Paloma.Paleo@nottingham.ac.uk
Gas Turbine and Transmissions Research Centre
University of Nottingham, UK

Kathy Simmons *
kathy.simmons@nottingham.ac.uk
Gas Turbine and Transmissions Research Centre
University of Nottingham, UK

Arun Prabhakar
arun.prabhakar@nottingham.ac.uk
Gas Turbine and Transmissions Research Centre
University of Nottingham, UK

Budi Chandra
budi.chandra@uwe.ac.uk
University of West England, UK

Accepted Manuscript Not Copyedited

Experimental research was conducted into a scooped rotor system that captures oil from a stationary jet and directs it through passages within the shaft to another axial location. Such a system has benefits for delivering oil via under-race feed to aeroengine bearings where direct access is limited. Oil capture efficiency was calculated for three jet configurations, a range of geometric variations relative to a baseline and a range of operating conditions. Flow visualization techniques yielded high-speed imaging in the vicinity of the scoop leading edge.

Overall capture efficiency depends on the amount of oil initially captured by the scoop that is retained. Observation shows that when the jet hits the tip of a scoop element, it is sliced and deflected upwards in a 'plume'. Ligaments and drops formed from this plume are not captured. In addition, some oil initially captured is flung outwards as a consequence of centrifugal force. Although in principle capture of the entire supply is possible over most of the shaft speed range, as demonstrated by a simplified geometric model, in practice 60% to 70% is typical.

Significant improvement in capture efficiency was obtained with a lower jet angle (more radial) compared to baseline. Higher capture efficiencies were found where the ratio of jet to scoop tip speed was lower.

This research confirms the capability of a scoop system to capture and retain delivered oil. Additional numerical and experimental work, is recommended to further optimise the geometry and increase the investigated temperature and pressure ranges.

NOMENCLATURE

α	Jet deflection angle (deg)
η	Capture efficiency (%)
θ_2	Angle (defined in Fig. 4) (deg)
θ_4	Angle (defined in Fig. 4 (deg)
θ_{jet}	Jet orientation angle (deg)
θ_{loss}	Angle related to uncaptured jet oil jet (defined in Fig. 4) (deg)
θ_{ref}	Baseline jet orientation angle (deg)
ν	Oil kinematic viscosity ($m^2 s^{-1}$)
ρ	Oil density at 30 °C ($kg m^{-3}$)
ρ_j	Oil density at observation j ($kg m^{-3}$)
σ	Oil/air surface tension ($N m^{-1}$)
ω	Rotational shaft speed (rpm)
ω_{max}	Maximum shaft speed tested (rpm)

*Address all correspondence to this author.

Downloaded From: http://gasturbinespower.asmedigitalcollection.asme.org/ on 08/31/2018 Terms of Use: http://www.asme.org/about-asme/terms-of-use

Journal of Engineering for Gas Turbines and Power. Received May 12, 2017;
Accepted manuscript posted July 11, 2018. doi:10.1115/1.4040812
Copyright (c) 2018 by ASME

A,B,C	Positions defined in Fig. 4
d_c^{ref}	Baseline size of oil scoop constriction (m)
d_c	Size of oil scoop constriction (m)
d_c*	Non-dimensional size of oil scoop constriction
fps	Frames per second
n_j	Sample size
n_{scoops}	Number of scoop blades
Q_{jet}	Oil jet flow rate ($1\,min^{-1}$)
$\overline{\dot{M}}_{jet}$	Average of oil jet mass flow rate ($kg\,s^{-1}$)
$\dot{M}_{scoop}$	Oil mass flow rate through scoop ($kg\,s^{-1}$)
$\dot{M}_{jet}$	Oil jet mass flow rate ($kg\,s^{-1}$)
R_{tip}	Rotor outer radius (m)
R_{jet}	Radial distance to oil injector (m)
$R_c{}^2$	Coeffcient of determination
ROI	Region of interest
T_{jet}	Feed oil temperature (°C)
V_j	Oil jet velocity ($m\,s^{-1}$)
VR	Jet to scoop tip velocity ratio
VR_{thr}	Threshold velocity ratio

1 Introduction

Lubrication and cooling of transmission systems components in a gas turbine engine is a prime concern. This is particularly important for the bearings where appropriate oil supply will ensure safe, reliable and efficient engine operation and a long life expectancy. The oil lubrication system is designed to minimize the effects of friction and wear and to provide cooling both to the bearings and to the surrounding bearing chambers. In civil aero-engines, which have shafts rotating at high speeds up to 15.000 rpm, it is common practice to use jet lubrication for bearings. Oil is targeted at the annulus gap between the inner and outer race [1] or at collection scallops for under-race feed. These are illustrated conceptually in Fig. 1. As speeds rise, centrifugal forces increase and it becomes more difficult for oil targeted directly at the bearing to penetrate to the critical surfaces. Consequently, in high duty conditions (high speeds, loads and operating temperatures) to ensure the oil flow to the bearings is effective and efficient, under-race lubrication is often preferred [1, 2, 3]. With under-race feed, oil moves outwards through feed holes within the shaft to lubricate the inner race surfaces of the bearing under the influence of centrifugal force. Under-race lubrication presents several advantages for higher speed applications, but in a confined space there may not be sufficient axial access for the jet to target the under-race location directly and in such case it is desirable to supply the oil at a different axial location to that of the feed, transporting the oil to the bearing through slots in the rotor. In such cases, one configuration proposed is a rotating 'scoop geometry' device, where each scoop captures a charge of lubricant as the shaft rotates delivering it to a bearing as an under-race feed. Such a geometry is illustrated conceptually in Fig. 2 and 3.

The concept of a scoop delivery system is not new; Brown [3] in 1970 described a scoop system where an oil jet is targeted axially at a channel that delivers oil to under-race

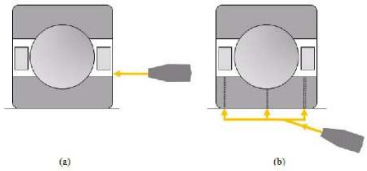


Fig. 1: Oil jet targeted directly at bearing a) shows oil targeted directly at a bearing but b) shows under-race feed.

feed holes at a different axial location, but development has been relatively slow as in most cases a scoop delivery system is not necessary. An early scoop design for a gas turbine is described in the 1987 patent of Kovaleski [4]. The invention described is a scoop system that directs specific proportions of oil axially, forward and rearward from the scoop to lubricate bearings located on opposite sides of the scoop itself. Over the years, scoop geometry design has evolved. The patents of Fisher et al. [5] and Fisher [6] are for conventional flat bladed scoops whereas that of Dins et al [7] describes a scoop comprising a curved blade intended to maximize fluid capture. In 2016 Rolls-Royce patented the concept of a bi-directional scoop [8] where the key difference to previously patented scoop designs is that the oil inlet path through the scoop follows a path angled such that it is turning throughout its journey rather than travelling first perpendicular to the shaft and then parallel to it.

Continuously increasing demands on gas turbine engines for increased fuel efficiency and lower environmental impact are leading to more compact and lighter engines [9]. Without a doubt, the desire for increased compactness leads to more crowded components making an appropriate, effective and efficient lubrication system even more challenging. Where bearing lubrication is concerned it is therefore important that as much as possible of the oil delivered by the jet subsequently arrives at the bearing. The ratio of the oil captured by the scoop to the amount directed at the scoop from the stationary nozzle is commonly termed the oil scoop capture efficiency. In the ideal scenario all the oil exiting the nozzle would travel to the target component. Capture efficiency can depend on a wide range of parameters such as the shaft speed, oil jet characteristics (including configuration, orientation, velocity, distance travelled by the oil jet and flow rate) and the geometry of the scoop device (including number, angle and profile of the blades/scoops and the geometry of the oil passages along the shaft). Oil scoops with higher efficiency could permit a decrease in the total amount of oil that must be delivered to the jet which may in turn allow reduction in the size and weight of parts of the oil system.

In this paper the results from an experimental investigation into a scoop geometry are presented. Geometric variations of the nozzle and scoop geometries are investigated over a range of operating conditions using a test module mounted to a single shaft test facility at the University of Nottingham's Gas Turbine and Transmissions Research Centre (G2TRC). The value of such data is two-fold with numer-

Downloaded From: http://gasturbinespower.asmedigitalcollection.asme.org/ on 08/31/2018 Terms of Use: http://www.asme.org/about-asme/terms-of-use

Journal of Engineering for Gas Turbines and Power. Received May 12, 2017;
Accepted manuscript posted July 11, 2018. doi:10.1115/1.4040812
Copyright (c) 2018 by ASME

ical and visualisation data providing direct design insight and also supporting modelling capability through qualitative and quantitative validation.

2 Previous Work

There are a couple of published Computational Fluid Dynamics (CFD) investigations into aero-engine scoops. The first of these is by Prasad et al. [10] where a system involving two scoops and two nozzles was investigated. The paper gives very little geometric data but the scoop is sharp edged and does not look too dissimilar to those investigated here. For fixed shaft speed the effect of increasing the oil flow rate (through increasing the jet velocity) was to increase capture efficiency but the effect was quite small with only 5% increase in capture efficiency for a fivefold increase in jet velocity. For fixed jet velocity and increasing shaft speed up to 4 times baseline, the capture efficiency increased to a peak value, 8% above baseline when the shaft speed was double the baseline shaft speed. The authors also found that increasing the scoop system width by 50% increased capture efficiency by 12%. Another result presented is that a 60% increase in capture efficiency could be obtained by reducing the scoop outer diameter by 10%, this being attributed to reduced magnitude of centrifugal force. Although no experimental data is included in the paper the authors state that their CFD data matches experiment to within 2%.

Korsukova et al. [11] conducted a numerical investigation on a geometry very similar to that investigated experimentally here using both CFD and smooth particle hydrodynamics (SPH). The 2-D, 2-D extrusion and 3-D models provide significant insight into flow behaviour near the scoops. The paper highlights a couple of key features, that were also seen experimentally. First, the formation of plume, droplets and ligaments after the oil jet is sliced by the scoop that are not captured by the scoop system. Second, part of the oil initially captured is subsequently expelled as a consequence of centrifugal forces. Both represent losses and reduce the capture efficiency. In the paper the simulation data is compared with included experimental data showing good qualitative agreement and a quantitative agreement to within 10%.

There does not appear to be any published experimental work relating to scoop systems similar to the one investigated here. In particular the experimental work mentioned in [10] is not currently in the public domain.

3 Oil scoop geometry investigated

In the scoop geometry investigated here a rotating radial scoop similar in geometry to that proposed in US patent 6,682,222 [6] is used to capture oil from a stationary oil jet. In the patented scoop, oil is directed towards the scoops on a trajectory dictated by the nozzle orientation, with the nozzle axis mounted at an angle θ_{jet} to the extended radius as illustrated in Fig. 2. The intention for the patented device is that some oil is captured by the scoops and some is reflected back into the chamber for a second lubrication purpose. In the current investigation the intention is to capture as much oil as possible in the scoops.

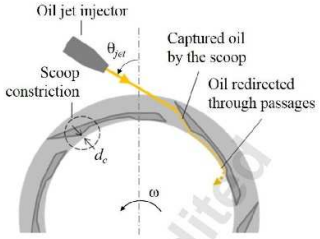


Fig. 2: Side view of scoop system (illustrative geometry).

This leads to the concept of capture efficiency as the ratio of oil captured by the scoops to oil delivered by the jet. There are two elements to be considered with regard to oil capture. The first is how much of the oil from the jet could potentially be captured; this is essentially the amount of oil that falls within the zone swept by the scoops. Dependent on many geometric and operational parameters this value can be 100% of the delivered oil. The second element is how much of this initially captured oil is ultimately delivered along the axial passages. Not all the oil initially captured is retained by the scoop system; some will flow back out of the scoops as centrifugal forces overcome initial fluid momentum.

Once captured the oil is directed axially and in a potential application of the device it would subsequently be delivered to an engine component such as a bearing via under-race feed as conceptually illustrated in Fig. 3. In the experimental investigation conducted here, captured oil was delivered to a measurement system, not to a bearing.

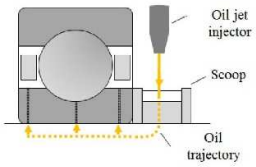


Fig. 3: Front view of scoop system (illustrative geometry).

As shown in Fig. 2, the oil injector ejects a jet of oil across open space toward the scoop and against rotation ω taking advantage of the oil's inertia to drive the oil inwards towards the axial passages. Because the scoops are rotating, centrifugal forces act to drive the oil outwards and an identified element of the scoop system is the constriction labelled on Fig. 2. As identified in [6] this constriction is not just a barrier to oil flowing backwards out of the oil passages, it

Downloaded From: http://gasturbinespower.asmedigitalcollection.asme.org/ on 08/31/2018 Terms of Use: http://www.asme.org/about-asme/terms-of-use

Journal of Engineering for Gas Turbines and Power. Received May 12, 2017;
Accepted manuscript posted July 11, 2018. doi:10.1115/1.4040812
Copyright (c) 2018 by ASME

also creates an adverse centrifugal pressure gradient to further deter escape of captured oil. The effect on scoop capture efficiency of the radial size of the narrowest part of the constriction, d_c, is one of the parameters investigated in this study. The jet angle, θ_{jet}, is another experimentally investigated parameter.

In this study a geometry comprising 6 scoops was chosen. Over the parametric range of shaft speeds and oil flowrates three jet angles were investigated and these are the baseline θ_{ref} (64.2°), $\theta_{ref} - 5°$ and $\theta_{ref} - 10°$.

3.1 Simplifed model

In seeking to better understand how the scoop system works and what are the key parameters, a simplified model has been developed. The simplified scoop system geometry is illustrated in Fig. 4, where the scoop blades are represented by a simple wedge shape. In this geometrical analysis the jet is represented as a line, having neither width nor spread angle. The formation of plumes, drops and ligaments is not considered and all the oil initially captured by the scoop is assumed retained. The jet is sliced when the scoop tip is at point A, while the next scoop is at point C (light grey wedges). As the scoop system rotates (dark grey wedges) the jet grows from point A to point B.

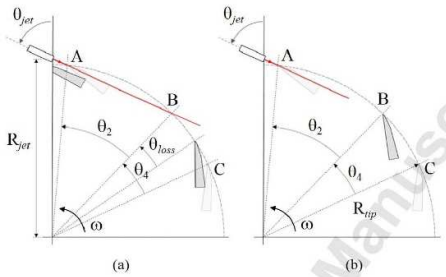


Fig. 4: Capture criterion. (a) At $VR < VR_{thr}$, the oil jet passes point B before next scoop reaches there. The oil jet is not entirely captured. (b) At $VR \geq VR_{thr}$, the scoop passes point B before the oil jet. The oil jet is entirely captured.

It is useful here to introduce the velocity ratio VR, a dimensionless parameter defined as the ratio of the scoop tip velocity to the jet velocity:

$$VR = \frac{\omega R_{tip}}{V_j}, \tag{1}$$

where R_{tip} is the rotor outer radius, V_j the oil jet velocity and R_{jet} is the distance of the oil injector from the centre of the rotor.

At low velocity ratios the jet cuts the circle formed by the outer radius of the scoop at point B before the next scoop has reached there (Fig. 4a). The section of the jet outside of the sweep of the scoop is not captured; this oil loss is represented by θ_{loss} in Fig. 4a. At a threshold capture velocity ratio VR_{thr}, the tip of the next scoop meets point B at the same instant as the jet. This threshold velocity ratio is given by

$$VR_{thr} = \frac{\theta_4 V_j}{\omega_{thr} 2R_{tip} \sin\left(\frac{\theta_2}{2}\right)}. \tag{2}$$

Above VR_{thr}, the jet is theoretically fully captured and for the investigated geometry $VR_{thr} = 0.44$, calculated using Eq. (2).

As long as the scoops are rotating (shaft speed $\omega > 0$) the oil capture efficiency in the region $VR < VR_{thr}$ is given by:

$$\eta = \frac{\frac{2\pi}{n_{scoops}} - \theta_{loss}}{\frac{2\pi}{n_{scoops}}}, \tag{3}$$

where n_{scoops} is the number of scoop blades and $2\pi/n_{scoops} = \theta_2 + \theta_4$ is the angle between scoops (see Fig. 4). θ_{loss} is defined as

$$\theta_{loss} = \theta_4 - 2\,VR_{thr} \sin\left(\frac{\theta_2}{2}\right), \tag{4}$$

and the angle θ_2 is

$$\cos\left(\frac{\theta_2}{2}\right) = \frac{R_{jet}}{R_{tip}} \sin(\theta_{jet}). \tag{5}$$

Thus it can be seen that in the low speed region the capture efficiency depends on the number of scoops, jet angle and velocity ratio.

This simplified geometrical model was developed to give insight into the oil capture process. The model does not include any losses due to pluming, droplet and ligament formation or centrifugal forces and because it is a 2D model it is equally valid for any of the jet configuration tested in this work: single jet, twin jets and tandem jet (jet configurations are discussed in Section 4.3). The twin jet configuration is two single jets side by side and the tandem jets are two single jets with an angular offset. If jet interaction effects are neglected then the model can be applied additively for these two-jet configurations.

Accepted Manuscript Not Copyedited

Downloaded From: http://gasturbinespower.asmedigitalcollection.asme.org/ on 08/31/2018 Terms of Use: http://www.asme.org/about-asme/terms-of-use

Journal of Engineering for Gas Turbines and Power. Received May 12, 2017;
Accepted manuscript posted July 11, 2018. doi:10.1115/1.4040812
Copyright (c) 2018 by ASME

4 Experimental test rig

The laboratory experiments were conducted using a scoop test module mounted onto the G2TRC single shaft test facility. The facility consists of a bed plate, gearbox and 130 kW DC motor that can rotate the bearing-mounted shaft up to 15.000 rpm dependent on the installed test module. In these tests the maximum shaft speed (ω_{max}) was limited to 10.000 rpm. A schematic diagram of the facility with test module mounted is shown in Fig. 5. In these tests shaft speed was set as a direct setpoint input to the motor drive, with an estimated uncertainty of ± 4 rpm at all setpoints based on measured data analysis.

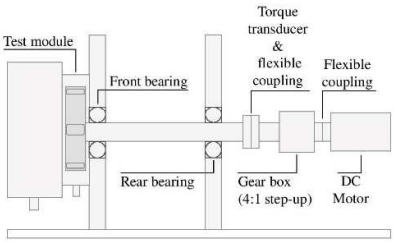


Fig. 5: Schematic illustration of the single shaft test facility with scoop module mounted.

The scoop test module consisted of two chambers, the scoop chamber containing the jet and scoop geometry and the front chamber. Oil caught by the individual scoops was directed axially along the shaft through passages and collected in the front chamber. Each chamber has its own scavenge port so that oil passing through the scoops is separated from oil not captured by the system. A schematic illustration of the oil scoop test module and associated hydraulic circuit is shown in Fig. 6. The first build of the test module had a front chamber that was too small in diameter leading to scavenge issues and a larger Perspex^{TM} chamber was added outside the original stainless steel front chamber. Both can be seen in the photographs of the test module shown in Fig. 7.

A positive displacement pump delivers oil to the oil jet manifold at the required flow rate Q_{jet}. The flow rate was changed manually as required for each test as an input value to the pump inverter and measured using an Kral flowmeter (OME24) that has a range up to 50 l min^{-1}. For these experiments MIL-PRF 7808 turbine oil type was used, with the steady state feed temperature T_{jet} controlled to be close to 30 °C. The kinematic viscosity and density of the oil at 30 °C are 2.71×10^{-5} m^2 s^{-1} and 933.4 kg m^{-3} respectively and oil/air surface tension is 3.12×10^{-2} N m^{-1}.

The front chamber contains an exit port at the bottom through which oil exits under the effect of gravity via a flexible pipe into a container standing on electronic scales. The mass of oil on the scales is logged during testing and that data is used to calculate the captured oil flowrate. The oil

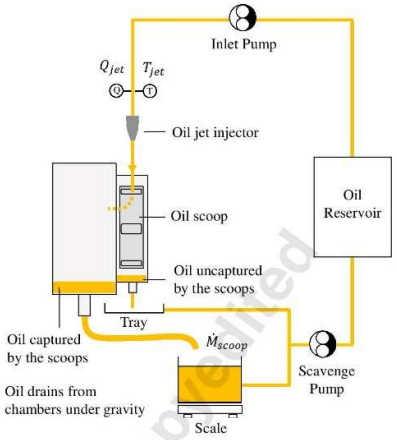


Fig. 6: Schematic illustration of the oil scoop module and associated hydraulic circuit.

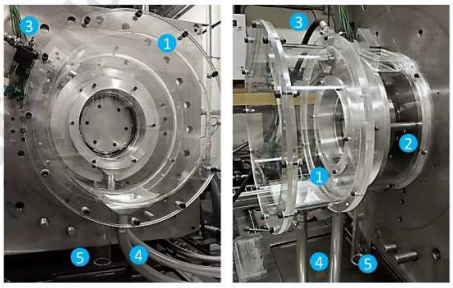


Fig. 7: Oil scoop test module: side view (left) and front view (right). 1-Front chamber, 2-Scoop chamber, 3- Oil jet injector, 4-Front chamber exit and 5-Scoop chamber drain.

flow rate out of the front chambers was measured at each test point. A positive displacement pump was used to empty the container after each test returning the oil to the oil reservoir.

The scoop chamber houses the rotating scoop element and the housing contains an exit port that provides gravity drainage for the oil not passing through the scoops. Lubrication oil for the rig front bearing also exits here. Oil leaving through the scoop chamber housing is collected in a tray and pumped back to the oil reservoir. The top of the circular cross-section scoop chamber contains an opening with a cover for an access to the interior of the chamber allowing easy access with the borescope for flow visualization.

Downloaded From: http://gasturbinespower.asmedigitalcollection.asme.org/ on 08/31/2018 Terms of Use: http://www.asme.org/about-asme/terms-of-use

Journal of Engineering for Gas Turbines and Power. Received May 12, 2017;
Accepted manuscript posted July 11, 2018. doi:10.1115/1.4040812
Copyright (c) 2018 by ASME

4.1 Oil scoop capture efficiency calculation method

At first start-up the rig was allowed to warm-up and was then observed to operate in a steady, stable condition at each setpoint. At each test point, after changing the operating conditions, 1-2 minutes of settling time were allowed to reach a stable operating condition. Rig monitors were used to assess when conditions had stabilised. Once the rig was stabilised at the setpoint oil was collected in the collection tank for a period of 5-8 minutes. Throughout the test, oil flowrate and temperature were logged along with the mass of oil on the scales.

The oil scoop capture efficiency is the ratio of the oil mass flow captured (and retained) by the scoop $\dot{M}_{scoop}$ to the average of the overall mass flow of oil that was injected to the scoop during the test $\overline{\dot{M}}_{jet}$, that is

$$\text{Efficiency}[\%] = \frac{\dot{M}_{scoop}[\text{kg s}^{-1}]}{\overline{\dot{M}}_{jet}[\text{kg s}^{-1}]}, \tag{6}$$

The mass of the collected oil through the scoops (m) was measured and recorded at a sampling rate of 4 Hz. A simple linear regression analysis using the least squares method was calculated to determine the oil mass flow rate $\dot{M}_{scoop}$, represented by the slope or regression coefficient of the fitted line. The coefficient of determination ${R_c}^2$ obtained in the tests varied between 0.999 and 1 indicating that the line fit was straight with an excellent fit and therefore the mass flow rate was steady throughout the test.

The electronic scales were calibrated to $\pm 5g$ and at the lowest flowrate the minimum mass collected over the duration of a test was 4kg. Combining uncertainties we find the maximum uncertainty in $\dot{M}_{scoop}$ to be 0.1%.

The average mass flow rate of oil injected to the scoops is expressed by

$$\overline{\dot{M}}_{jet} = \sum_{j=1}^{n_2} \dot{M}_{jet_j} = \sum_{j=1}^{n_2} \rho_j Q_{jet_j}, \tag{7}$$

where $\rho_j = f(T_{jet_j})$ is the density of the oil at observation j; a function of the oil feed temperature T_{jet_j}. Q_{jet_j} is the oil jet manifold flow rate at observation j of n_j measurements at a sampling rate of 1 Hz to ensure the system was steady stable through each test.

Calibration data for the flowmeter gives a maximum uncertainty in volume flowrate of 0.6%. The uncertainty in density is the product both of the variation in supply temperature and also the accuracy of the correlation used to give density as a function of temperature. Oil supply temperature was measured using K-type thermocouples with a quoted accuracy of $\pm 2K$ and our data shows the supply temperature to have varied by less than 0.6K over the duration of the tests. Using available oil property data gives us an uncertainty in density of 1.5% based primarily on thermocouple accuracy. Combining the uncertainties in volume flowrate and density yields an uncertainty of around 1.6% in $\overline{\dot{M}}_{jet}$. Combining the uncertainties in jet mass flowrate and scoop captured mass flowrate gives a representative upper limit on uncertainty in capture efficiency of around 1.6%, dominated by the uncertainty in supply oil density.

An additional consideration for an experimental study of this kind is repeatability, a measure of the extent to which identical results would be produced at the same nominal set point if a test were repeated. The time available for testing precluded the possibility of any kind of full statistical analysis. However, to give an indication, one of the tests (twin jet, constriction ratio 1 and $\theta_{ref} - 5°$) was repeated on two different days, before and after a rig rebuild. The two data sets are shown plotted in Fig. 8 where it can be seen that the points are almost indistinguishable. The average difference between values is 0.5% with the maximum difference of 1.5% occurring at $\omega/\omega_{max} = 0.1$. This value is less than the estimated measurement uncertainty. The only parameters that would vary from test to test not accounted for in the measurements made are the air properties.

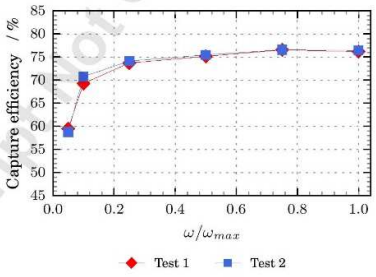


Fig. 8: Repeat test indicating level of repeatability. Test configuration: Tandem jet, d_c^*= 1 and $\theta_{jet} = \theta_{ref} - 5$.

4.2 Visualization

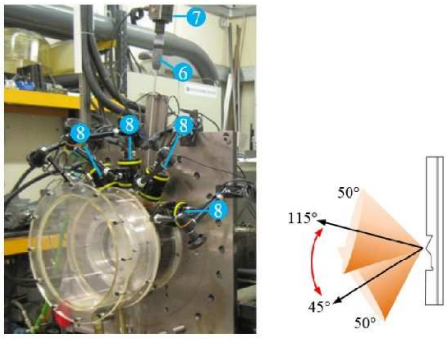
Visualization of the oil jet behaviour in the vicinity of the leading edge of the scoop was also conducted. Fig. 9a shows the set-up for the visualization during the experiments. For the image acquisition a high speed camera (manufactured by IDT, model OS4-S3-M-04) was used. The camera is 12 bit monochrome, with 1024x1024 pixel resolution and can acquire images at up 6000frames per second (fps). Higher frame rates can be obtained if the image resolution is reduced. The camera has 8GB onboard RAM and 512GB Solid State Memory. The images were recorded using IDT's Motion Studio software. To improve the resolution and quality of images of the interior of the scoop chamber an Olympus series 5 zoom swing prism rigid borescope was attached to the camera. The borescope has an 8mm diameter and 54cm working length; the direction of view is 45° to 115°

Downloaded From: http://gasturbinespower.asmedigitalcollection.asme.org/ on 08/31/2018 Terms of Use: http://www.asme.org/about-asme/terms-of-use

Accepted Manuscript Copy Only

Journal of Engineering for Gas Turbines and Power. Received May 12, 2017;
Accepted manuscript posted July 11, 2018. doi:10.1115/1.4040812
Copyright (c) 2018 by ASME

downwards from the borescope axis and the field of view is 50° as shown in Fig. 9b. For illumination four white lights, Model 120E Veritas, were used. They were synchronized and pulsed with the high speed camera. Each light offered 22 000 lumens output when pulsed.



(a) (b)

Fig. 9: (a) Visualization set up. 6-Borescope, 7-Camera and 8-Lights. (b) Direction and field of view of the borescope.

The selection of the image resolution, the image acquisition rate and the illumination must be optimised at each condition. For higher shaft speeds a higher frame rate is desirable and this requires the number of pixels per frame to be reduced. With a higher frame rate it becomes harder to get enough light in the frame. During imaging, the region of interest (ROI) was adjusted appropriately, within the capability of the boroscope field of view as shown in Fig. 10. The image acquisition rate was chosen considering the shaft speed of each test in order to be able to visualize the jet flow with a good resolution, avoiding blurred images. As an example, at low shaft speeds a typical image resolution would be 512x260 pixels and a frame rate of 10 000 fps selected and at high speeds an image size of 512x128 pixels with a frame rate of 44 000 fps was employed. Visualization of the flow for high jet flow rates and/or high shaft speeds was difficult because under those circumstances, the borescope lens was constantly covered with splashed oil.

At low shaft speeds and low oil flowrates, a good understanding of flow features affecting oil scoop capture efficiency was gained by observing the oil jet interaction with the scoop leading edge. However, the visualization of the process of structural change of the jet was limited.

To observe the process of structural change of the jet including the surrounding scoop geometry a series of tests involving a simplified test module were undertaken. The simplified module consisted of a cylinder – with same inner diameter as the scoop device test module and six solid wedge elements representing the scoops. The rear end of the

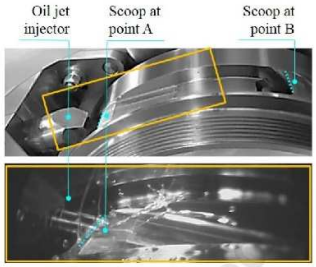
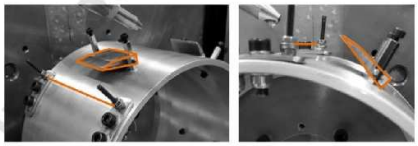


Fig. 10: Images of the scoop device and the oil jet injector. Top: The ROI is marked with a rectangle. Bottom: Frame showing the ROI from the recorded high speed filming using the borescope connected to the high speed camera.

scoop circumferential outer surface was represented by a thin wire. This geometrically simplified test module is shown in Fig. 11.



(a) (b)

Fig. 11: Geometrically simplified scoop test module. Highlighted with orange are the wedge shape and the thin wire.

4.3 Test matrix

A number of different tests were conducted on the scoop test module and these are detailed along with the relevant parametric ranges in each of the following subsections. All testing was conducted on a scoop unit consisting of 6 scoop elements similar to those illustrated in Fig. 2. A table summarising the testing conducted is included as Section 4.3.5.

4.3.1 Effect of jet to scoop velocity ratio

In the first set of tests a jet consisting of two nozzles as illustrated in Fig. 12a was used. The flowrate was set to a constant value corresponding to the highest jet velocity tested and the shaft speed ratio, defined as $\frac{\omega}{\omega_{max}}$, was varied from 0.05 to 1 in steps of 0.05. The baseline jet angle θ_{ref} was used along with a baseline scoop constriction d_c. A non-dimensional scoop constriction d_c^* is defined as the scoop constriction ratio with reference to the baseline d_c.

Downloaded From: http://gasturbinespower.asmedigitalcollection.asme.org/ on 08/31/2018 Terms of Use: http://www.asme.org/about-asme/terms-of-use

Journal of Engineering for Gas Turbines and Power. Received May 12, 2017;
Accepted manuscript posted July 11, 2018. doi:10.1115/1.4040812
Copyright (c) 2018 by ASME

4.3.2 Effect of scoop constriction

Using the same geometric configuration as in Section 4.3.1 scoop constrictions ratios $d_c{}^*$ of 1, 1.5 and 2 were investigated. As with the investigation of Section 4.3.1 the flowrate was set to a constant value (highest jet velocity tested) and shaft speed ratio was varied from 0.05 to 1 in steps of 0.05.

4.3.3 Jet velocity varying with shaft speed

In most current aero-engines the amount of oil delivered to bearing chambers and bearings is not a fixed amount but varies as a function of the speed of the shaft driving the pumps. Consequently, the velocity ratio (jet velocity to scoop tip velocity) may vary very little with shaft speed. A series of tests was conducted with an almost constant velocity ratio over a range of shaft speeds and for three scoop constriction ratio values, 0.5, 1 and 2. In these tests a different jet arrangement was used where there were two nozzles in tandem (two single orifice jets 10° apart circumferentially) as shown in Fig. 12b but the jet baseline angle was retained. To see whether the jet configuration was a significant factor the test with a constriction ratio of 1 was repeated for three jet configurations, single jet, twin jets (a nozzle with two orifices axially aligned) and tandem jets as shown in Fig. 12.

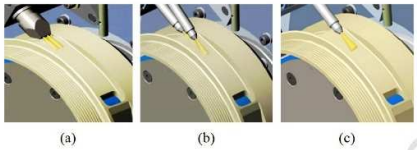


Fig. 12: Jet configurations tested: (a) twin jets, (b) tandem jets and (c) single jet.

4.3.4 Effect of jet angle

For the tandem jets configuration, tests were conducted with three different jet orientations: θ_{ref} as the baseline angle (see Fig. 13), $\theta_{ref} - 5°$ and $\theta_{ref} - 10°$.

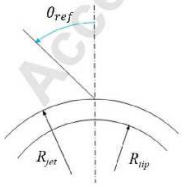


Fig. 13: Baseline oil jet orientation, θ_{ref}. Arrow defines the positive direction of the angle.

4.3.5 Summary of tests conducted

For completeness and ease of reference Section 4.3.5 is included here, summarising the conditions associated with each of the tests conducted.

5 Results and discussion

5.1 Effect of velocity ratio, fixed jet velocity

For a fixed jet velocity Fig. 14 shows how the capture efficiency varied with velocity ratio. The capture efficiency initially increases with shaft speed, reaching a maximum value at a velocity ratio between 0.8 and 1.0 with around 81% of the oil being captured by the scoops and then decreasing as shaft speed is further increased. Also on the graph is shown the theoretical maximum oil capture efficiency for an ideal scoop system. Above the total capture threshold (i.e., VR_{thr}, where $VR = 0.44$), the theoretically efficiency is 100% .

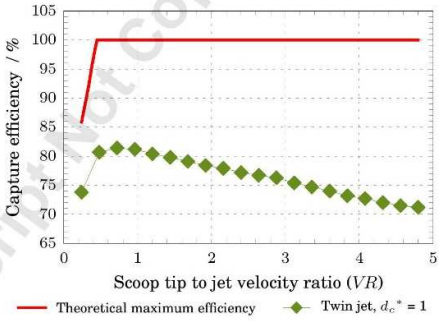


Fig. 14: Variation in capture efficiency with velocity ratio for a fixed jet velocity and varying shaft speed.

The amount of oil captured by the scoop system depends not only on how much is initially scooped but also how much is retained. Analysis of the video imaging shows that i) as the scoop approaches the jet there is an amount of oil that is deflected by the pressure field creating a flow away from the scoop and ii) as the scoop rotates a portion of oil initially scooped will be accelerated outwards through centrifugal force and will leave the scoop. These factors both increase with increasing speed thus reducing capture efficiency. Figures 15 (images from the geometrically simplified test module) and 16 (images from the representative test module) illustrate these two factors. In Fig. 15, when the jet is sliced by the wedge leading edge, the oil jet is deflected with a jet deflection angle α of approximately 135 ° from the axis line of the jet (Fig. 15b). The head of the sliced oil scrolls up gradually forming a plume (blue arrows in Fig. 15b-j). Just before the jet interacts with the next scoop, the jet deflection angle decreases to about 45 ° (Fig. 15j). The plume extends

Downloaded From: http://gasturbinespower.asmedigitalcollection.asme.org/ on 08/31/2018 Terms of Use: http://www.asme.org/about-asme/terms-of-use

Accepted Manuscript Not Copyedited

Journal of Engineering for Gas Turbines and Power. Received May 12, 2017;
Accepted manuscript posted July 11, 2018. doi:10.1115/1.4040812
Copyright (c) 2018 by ASME

Table 1: Parameters and conditions of the conducted tests

Test Assess effect of:	Shaft speed $\frac{\omega}{\omega_{max}}$	Velocity ratio VR	Set up configuration	Cross reference
Velocity ratio, fixed jet speed	0.05 to 1	0.3 to 5	Jet angle [θ_{jet}]: θ_{ref} Constriction [d_c^*]: 1 Jet configuration: Twin jet	Section 4.3.1 Section 5.1 Fig. 14
Scoop constriction	0.05 to 1	0.3 to 5	Jet angle [θ_{jet}]: θ_{ref} Constriction [d_c^*]: 1, 1.5, 2 Jet configuration: Twin jet	Section 4.3.2 Section 5.2 Fig. 17
Jet velocity varying with shaft speed VR almost constant	0.05 to 1	4.4 to 4.8	Jet angle [θ_{jet}]: θ_{ref} Constriction [d_c^*]: 1 Jet configuration: Twin jet	Section 4.3.3 Section 5.3 Fig. 18
Jet velocity varying with shaft speed Higher VR	0.5 to 1	4.4 to 6	Jet angle [θ_{jet}]: θ_{ref} Constriction [d_c^*]: 0.5, 1, 2 Jet configuration: Tandem jets	Section 4.3.3 Section 5.3 Fig. 19
Jet configuration	0.05 to 1	4.4 to 4.8	Jet angle [θ_{jet}]: θ_{ref} Constriction [d_c^*]: 1 Jet configuration: Twin, tandem, single	Section 4.3.3 Section 5.3 Fig. 20
Jet angle	0.5 to 1	4.4 to 6	Jet angle [θ_{jet}]: θ_{ref}, $\theta_{ref} - 5°$, $\theta_{ref} - 10°$ Constriction [d_c^*]: 1 Jet configuration: Tandem jet	Section 4.3.4 Section 5.3 Fig. 23

upwards and small ligaments and drops are formed. A significant portion of the ligaments and drops are not captured by the scoop and this represents a capture inefficiency of the scoop system. In addition, Fig. 15j shows ligaments of oil expelled from the edge of the scoop as it rotates.

In Fig. 16, when the scoop edge is approaching the jet (Fig. 16a-e), the deflected plume is observed (in Fig. 16a this is marked with a circle). Ligaments of oil leaving the edge of the scoop are well captured on the images of Fig. 16e-h. In Fig. 16e, just before the jet starts to slide along the inner scoop surface, ligaments of oil are expelled and these are marked with a ellipse. Both these factors contribute to the capture efficiency being less than 100% even though it is geometrically feasible under these conditions.

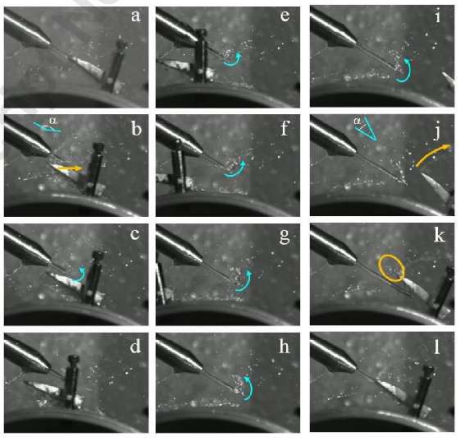


Fig. 15: Visualization of the jet flow at increments of 1×10^{-3}s with single jet for a simplified geometry of the scoop device. Angle jet is θ_{ref}, scoop construction ratio of 1 at the shaft speed ratio of 0.05 and VR of 4.3.

5.2 Effect of scoop constriction, fixed jet velocity

The results of the tests run with constant jet velocity and 3 constriction sizes are shown in Fig. 17. The graph shows that constriction size makes no difference to the shaft speed at which the maximum capture efficiency occurs but it does make a difference to the capture efficiency itself with the highest values occurring for the larger constriction value. The data for scoop constriction ratios d_c^* of 1.5 and 2 is very similar with slightly lower values for the d_c^* of 1 although in most cases the difference falls within experimental uncertainty. Overall capture efficiency is made up from the proportion of oil entering the scoops in the first place and the proportion of that, that is retained. In all three of these cases the amount of oil entering the scoop is the same and so the differences in capture efficiency can be attributed to differences in retention. As jet momentum and centrifugal forces do not vary with constriction we can conclude that the tighter constriction does limit the rate at which oil flows into the axial channels a little.

Copyright © 2018 by ASME
Unauthorized reproduction prohibited.

Downloaded From: http://gasturbinespower.asmedigitalcollection.asme.org/ on 08/31/2018 Terms of Use: http://www.asme.org/about-asme/terms-of-use

Journal of Engineering for Gas Turbines and Power. Received May 12, 2017;
Accepted manuscript posted July 11, 2018. doi:10.1115/1.4040812
Copyright (c) 2018 by ASME

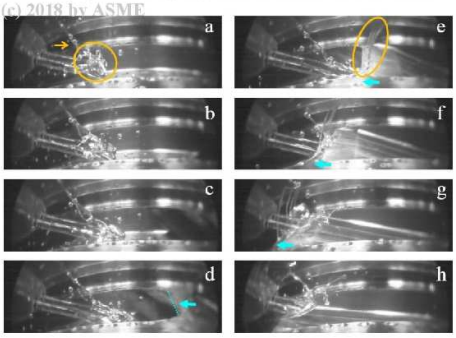


Fig. 16: Visualization of the jet flow evolution at increments of 2×10^{-3}s for a twin jet configuration. Angle jet is θ_{ref}, scoop constriction ratio of 1 at shaft speed ratio of 0.05 and VR of 4.3. The blue arrow points to the leading edge of the scoop.

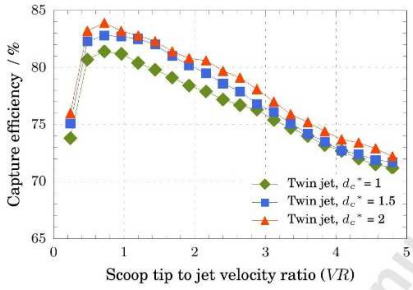


Fig. 17: Effect of constriction on capture efficiency for fixed jet velocity and varying shaft speed.

5.3 Jet velocity varying with shaft speed

In these tests the velocity ratio ($VR = \frac{R_{tip}\omega}{V_j}$) had values between 4.4 and 4.8 as shown in Fig. 18. Over a significant portion of the shaft speed range the velocity ratio was constant at around 4.4. The measured capture efficiency over the range of shaft speeds increases with shaft speed and is slightly higher when the scoop constrictions ratio d_c^* is 2 compared to 1 or 0.5 (73% at ω/ω_{max}=1 compared to 71% for the smaller constrictions). Capture efficiency values are around 60% to 70%, slightly lower than the values obtained for the same velocity ratio (but a higher jet velocity) as shown in Fig. 17 where a velocity ratio of 4.4 corresponds to a capture efficiency of around 72% in the case of constriction ratio of 1. Fig. 18 provides confirmation that constriction does not make a lot of difference to capture efficiency. The fact that the larger constriction ratio of 2 has slightly better capture efficiency than the smaller values 1 or 0.5 would suggest that there is an element of the constriction preventing oil moving past the constriction as fast as it would like to but that this is a minor effect.

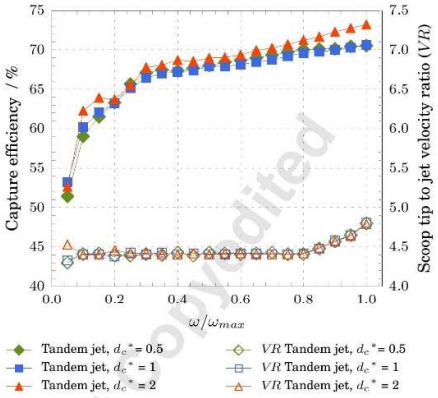


Fig. 18: Graph showing how capture efficiency varies with shaft speed for three constriction values. Velocity ratios as plotted on the chart.

A second set of tests was done with a somewhat higher velocity ratio at higher shaft speeds and the data is shown on Fig. 19. As can be seen, with the higher velocity ratios the capture efficiency falls a little. This is indicative that for the same shaft speed, slightly less oil is retained by the scoops when the jet velocity is lower. This is consistent with the findings of Prasad et al [10] and with the identified importance of jet momentum in opposing centrifugal force.

All three jet configurations are compared in the data shown in Fig. 20, for a constriction ratio of 1 and velocity ratios as shown on the chart. Here it is clear that the twin and tandem jets behave in a very similar fashion but lower capture efficiencies are obtained for the single jet. As shown in Fig. 15 the front part of the jet deflects after hitting the scoop and is then flattened by the aerodynamic forces creating a low pressure region in the vicinity of the scoop tip. With the tandem jet the second jet does not see the same pressure field as the front jet and the deflection a) happens earlier and b) much of the deflected oil meets the front jet and is still captured. To some extent this can be seen in Fig. 21, which shows images for all three jets at a shaft speed ratio of 1. With the twin jet, although behaviour is less clear, it seems that the deflection of the two jets is reduced because of their proximity. At higher speed the still images are less clear as can be seen in Fig. 22 where the shaft speed ratio is 0.8, but it can be seen that the single jet case shows a more sheet-like deflection of the jet compared to the twin jet. It is suggested that the interaction of the jets creates a flow less susceptible to deflection.

Accepted Manuscript Not Copyedited

Downloaded From: http://gasturbinespower.asmedigitalcollection.asme.org/ on 08/31/2018 Terms of Use: http://www.asme.org/about-asme/terms-of-use

Journal of Engineering for Gas Turbines and Power. Received May 12, 2017;
Accepted manuscript posted July 11, 2018. doi:10.1115/1.4040812
Copyright (c) 2018 by ASME

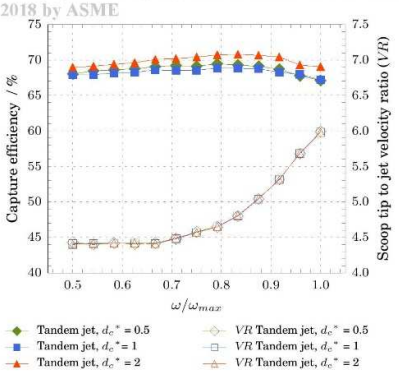


Fig. 19: Capture efficiency as a function of shaft speed for three constrictions values and velocity ratios as indicated on the chart.

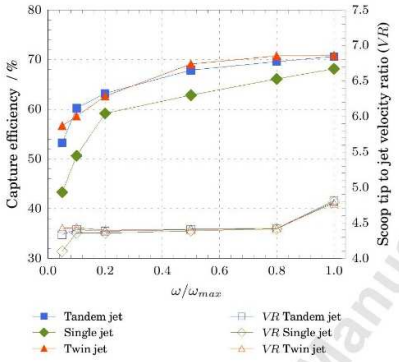


Fig. 20: Graph showing the effect of jet configuration for a case with 2mm constriction and velocity ratios as shown in Fig. 18.

5.4 Effect of jet angle

The effect of jet angle was evaluated for the baseline jet orientation, θ_{ref}, and the angles $\theta_{ref}-5^\circ$ and $\theta_{ref}-10^\circ$. Three scoop constrictions were assessed over shaft speeds ratios from 0.5 to 1, at the same velocity ratios as indicated in Fig. 19. The capture efficiency characteristics are shown in Fig. 23. It can be seen that decreasing the jet angle from baseline increases the capture efficiency with maximum values around 79% being obtained at $\theta_{ref}-10^\circ$ and 76% at $\theta_{ref}-5^\circ$ compared to the maximum around 69% for baseline θ_{ref}. These three values are valid for the constriction ratio of 1.

The increase of the capture efficiency with decreasing jet angle, may be attributed to changes of a) the momentum

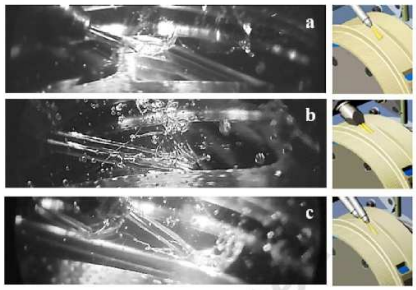


Fig. 21: Visualization of the jet flow behaviour at the shaft speed ratio of 0.1 for three different jet configurations: a) single jet, b) twin jet and c) tandem jet.

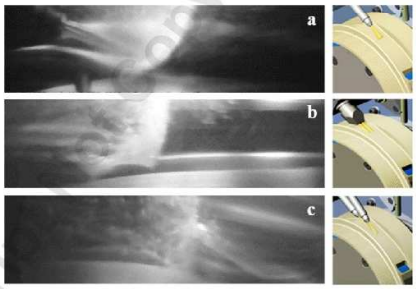


Fig. 22: Visualization of the jet flow behaviour at the shaft speed ratio of 0.8 for three different jet configurations: a) single jet, b) twin jet and c) tandem jet.

and b) the deflection of the oil jet.

With regard to momentum, the simplified diagrammatic representation of Fig. 24 shows how the location where the oil jet impacts on the scoop changes with the jet angle. Reducing the jet angle from the baseline, the oil jet strikes more inboard from the scoop tip and closer to the constriction as is illustrated in Fig. 24a. In that case the flow path of the oil film spread against the scoop is shorter, before it reaches the constriction. It may therefore be expected that the oil film loses less momentum and is therefore less likely to be ung back off the scoop. Thus the amount of lost oil is reduced, which could partially account for the increase in the capture efficiency.

With regard to oil jet deflection it is found that after slicing the jet is less deected at lower jet angles, as is shown by the images of Fig. 25. Fig. 25a (i) shows the jet when it is about to hit the edge of the scoop. It is notable that in the region radially outside the scoop that is approaching the jet, there is a cloud of ligaments and drops of oil (highlighted in a circle) and these are the oil coming from the plume created during the previous scoop-jet interaction. This is oil which

Downloaded From: http://gasturbinespower.asmedigitalcollection.asme.org/ on 08/31/2018 Terms of Use: http://www.asme.org/about-asme/terms-of-use

Journal of Engineering for Gas Turbines and Power. Received May 12, 2017;
Accepted manuscript posted July 11, 2018. doi:10.1115/1.4040812
Copyright (c) 2018 by ASME

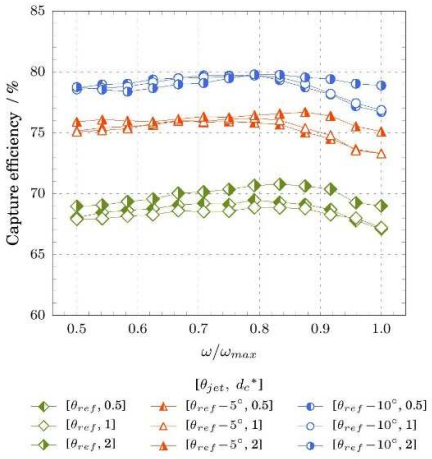


Fig. 23: Effect of jet angle on capture efficiency for three scoop constrictions for the tandem jet configuration.

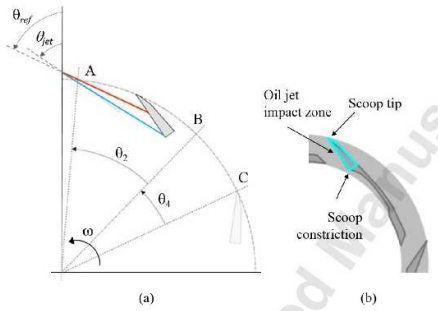


Fig. 24: Position where oil jet impacts on the scoop at different angles. Scoop operating with $VR \geq VR_{thr}$ (a) at the baseline jet angle θ_{ref} (red line) and at a jet angle lower than the baseline, $\theta_{jet} < \theta_{ref}$ (blue line). (b) Key zones of the simplified scoop geometry.

has not been captured by the scoop and is now mixing with the expelled oil. Fig. 25a (iii) shows how the jet after hitting the scoop evolves into a big plume with a jet deflection angle α of approximately 135 ° from the baseline jet angle. This plume expands outwards with formation of ligaments that will not be captured by the next scoop. When the baseline jet angle is reduced by 5° as shown in Fig. 25b(i) there is no trace of oil escaping as a consequence of plume formation, and there is only expelled oil visible. After hitting the scoop edge (Fig. 25b(iii)), the jet deflection angle is about zero and therefore the plume is much less deflected and so travels along with the jet. The same holds for the ligaments which move parallel to the jet and are therefore captured by the next scoop.

The capture efficiency was also measured for a shaft speed ratio of 0.05, VR of 4.3 and constriction ratio of 1 yielding 51% and 59% for the baseline jet angle and for θ_{ref} $-5°$ respectively.

From visualization at high speed it was also observed that for the baseline jet angle the flow was deflected more severely than for lower jet angles. At the higher speeds the flow visualization was hindered by splashing which affects the quality of the still images which are therefore not shown in the paper but considerable insight was obtained through viewing the movies.

It is also interesting to note that whereas at baseline jet angle θ_{ref} there is roughly a 2% advantage of the constriction ratio of 2 over 1, this is not seen for $\theta_{ref}-10°$ except at the highest shaft speeds where the velocity ratios were highest.

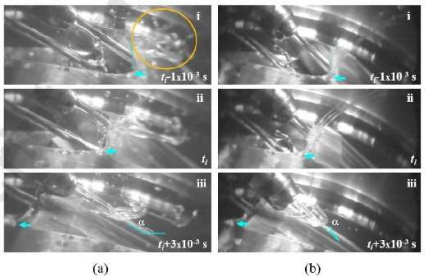


Fig. 25: Comparison of oil deflected after hitting the edge of the scoops for the tandem jet configuration and two jet angles: (a) Baseline jet angle θ_{ref} and (b) $\theta_{ref}-5°$ jet angle. The evolution of the jet flow is shown 1×10^{-3}s before the jet hits the edge of the scoop, during the slicing action at t_i and 3×10^{-3}s after hitting the edge of the scoop. Images arfe for shaft speed ratio 0.05, VR 4.3 and constriction ratio 1. The blue arrow points to the leading edge of the scoop.

5.5 Further considerations and future work

For the experiments conducted in this study air conditions were ambient and oil supply temperature was lower than would be found in an aeroengine bearing chamber. This facilitated the high quality visualisation central to the experimental work conducted. However, it is necessary to evaluate how the flow behavior might be different at more engine representative conditions. Taking generic representative bearing chamber conditions of pressure 2.6 bar, air temperature

Downloaded From: http://gasturbinespower.asmedigitalcollection.asme.org/ on 08/31/2018 Terms of Use: http://www.asme.org/about-asme/terms-of-use

Journal of Engineering for Gas Turbines and Power. Received May 12, 2017;
Accepted manuscript posted July 11, 2018. doi:10.1115/1.4040812
Copyright (c) 2018 by ASME

280° and oil temperature 160° we obtain a test rig oil Weber number around 16% lower than in an engine and an air Weber number around 50% lower. The oil Reynolds number is around 90% of the engine value. These differences primarily arise due to reduced oil viscosity at higher temperatures. The biggest influence of these differences will be in the number and size of droplets produced by jet-scoop impact. Primary oil jet capture by the scoop is not dominated by droplet splashing and so there is no reason to doubt the applicability of the main findings presented here.

One of the important benefits of this experimental work comes from data made available for numerical model validation and indeed G2TRC have conducted both CFD and SPH modelling on scoops. Consequently, building on the work of [11] a CFD model with modified oil and air properties could relatively easily be created. Future experimental work could be conducted at higher temperature and pressure but a new test module (likely with significantly reduced visual access) would be required and so future CFD investigation is recommended prior to future experiments. It is also worth noting that a numerical investigation using smooth particle hydrodynamics has investigated the effect of oil viscosity and shown it to have a negligible effect on predicted capture efficiency [12].

The work presented here shows that a scoop system of this type is capable of capturing the majority of the oil delivered by the jet over a range of representative shaft speeds and oil flowrates. It can be argued that 100% capture is not desirable in any case as some oil may be required for wetting the walls of the chamber where the oil is delivered. The size of the constriction has been shown to be important but results are not so sensitive that differential thermal expansion will prevent adequate oil delivery over an engine operation envelope. It seems therefore that the proposed system has considerable promise for future engine applications and future work may involve testing on an engine or a more engine representative test rig.

6 Conclusions

An experimental investigation into a scoop geometry has been conducted to measure the capture efficiency of a system with the potential for delivering oil to transmissions components in a gas turbine engine at a different axial location to the feed jet. Geometric variations of the oil jet injector and the scoop over a range of operating conditions have been examined.

A simplified geometrical model is presented that introduces the capture criterion and provides valuable insight into how geometric and operational parameters affect the system's behaviour. This model shows that for any scoop operating at a velocity ratio above the total capture threshold $VR \geq VR_{thr}$, the oil jet is theoretically entirely captured and thus the theoretical capture efficiency is 100%. In practice total capture is not achieved, with the highest observed value being 81% occurring at a velocity ratio between 0.8 and 1. This was measured at high jet velocity with the twin jet configuration and baseline jet angle and constriction. At higher velocity ratios (further increase of shaft speed) there is reduced capture efficiency. The cause of reduction from the theoretical efficiency is that in this latter case, the motion of the fluid is described without consideration of effects such as oil deflection, plume formation, oil shedding as ligaments and drops nor oil ejected outwards from the scoop as a consequence of centrifugal forces all of which represent oil lost to the system.

Effect of scoop constriction, fixed jet velocity. Increasing the constriction from the baseline case to constriction ratios of 1.5 and 2, for fixed high jet velocity was investigated using the twin jet configuration. Capture efficiencies show similar behaviour presenting the maximum efficiency at similar velocity ratios between 0.8 and 1. The effect of increasing the constriction has a very small impact on the maximum capture efficiency particularly in going from 1.5 to 2, where the difference falls within experimental uncertainty. There is an improvement of 2.5% from baseline case to constriction ratio of 2.

Jet velocity varying with shaft speed. With an almost constant velocity ratio of around 4.4 the capture efficiency increases with increasing shaft speed attaining values around 60% to 70%. These values are slightly lower than those obtained for the same velocity ratio but a higher jet velocity (for example 72% when constriction ratio was 1). When the velocity ratio was increased by reducing the jet velocity for the same shaft speed, the capture efficiency reached its maximum value at a velocity ratio of around 4.8 and then fell for higher shaft speeds. Less oil is retained when the jet velocity is lower. A tentative conclusion from these results is that if a smaller nozzle diameter can be tolerated (maintaining flowrate and thus increasing velocity) then higher capture efficiencies will be achieved. Reducing the constriction ratio from 1 to 0.5 did not have any significant effect on the measured capture efficiency. Slightly higher values were obtained when the constriction ratio was increased to 2.

Comparison of jet configurations. For the three jet configurations investigated the two-jet configurations (tandem and twin jets) presented similar capture efficiency while for the single jet configuration the efficiency was lower by around 10% at low shaft speeds and 3% at high shaft speeds. Therefore jet configurations involving two jets are recommended for a higher capture efficiency.

Effect of jet angle. The angle of the oil jet is identifed as a key parameter to consider when designing a scoop feed system. The capture efficiency increased by around 11% when the jet baseline angle was reduced by 10°. Funding in this project did not permit exploration of other jet angles so further work is recommended to identify the optimum jet angle for the scoop system.

Overall this study establishes the capability of a scoop system of this kind to capture and retain oil delivered via a feed jet. The work shows that it is not viable to capture all the jet oil because of jet pluming and splashing but careful choice of geometric and operational parameters can yield signficant improvement. In particular lower velocity ratio (higher jet velocity) is shown to be advantageous and choice of jet angle is a key design parameter. Further investigation

Downloaded From: http://gasturbinespower.asmedigitalcollection.asme.org/ on 08/31/2018 Terms of Use: http://www.asme.org/about-asme/terms-of-use

Journal of Engineering for Gas Turbines and Power. Received May 12, 2017;
Accepted manuscript posted July 11, 2018. doi:10.1115/1.4040812
Copyright (c) 2018 by ASME

starting with numerical modelling is recommended but the authors see no reason why such a system should not be trialled at engine-representative conditions.

Acknowledgements

The authors would like to thank Rolls-Royce plc for its financial and technical support and the UK Technology Strategy Board for its financial support of the SILOET 2 Program.

References

[1] Zaretsky, E. V., 1997. "Rolling Bearing and Gear Lubrication". *Tribology for Aerospace Applications*. Society of Tribologists and Lubrication Engineers, Park Ridge, Ill., US, pp. 207-323.

[2] Brown, P. F., 1970. "Bearings and Dampers for Advanced Jet Engines". SAE Technical Paper No. 700318, Warrendale, Pennsylvania, US.

[3] Lee, C. W., Johnson, G. R., Palma, P. C., Simmons, K., and Pickering, S. J., 2004. "Factors Affecting the Behaviour and Efficiency of a Targeted Jet Delivering Oil to a Bearing Lubrication System". Proceedings of ASME Turbo Expo 2004, Vienna, Austria, ASME Paper No. GT2004-53606, Vol. **2**, pp.191–199.

[4] Kovaleski, S., 1987. "Radial Scoop Construction". US Patent 4,648,485.

[5] Fisher, K., Demel, H., and Hazeley, R., 2002. "Methods and Apparatus for Supplying Oil to Bearing Assemblies". US Patent 6,409,464.

[6] Fisher, K., 2004. "Bi-Directional Oil Scoop for Bearing Lubrication". US Patent 6,682,222.

[7] Dins, J., Hogan, J., and Kumar, A., 2007. "Curved Blade Oil Scoop". US Patent 7,244,096.

[8] Mcdonagh, S., 2016. "A Liquid-Capturing Shaft". US Patent 2016/0069186 A1.

[9] RAEng, 2014. "Innovation in Aerospace". Royal Academy of Engineering in association with the Royal Aeronautical Society, London, UK, http://www.raeng.org.uk.

[10] Prasad, S. K., Sangli, P., Buyukisik, O., and Pugh, D., 2014. "Prediction of Gas Turbine Oil Scoop Capture Efficiency". Proceeding of ASME 2014 Gas Turbine: Power for Land, Sea and Air, New Delhi, India, ASME Paper No. GTINDIA2014-8329, pp. V001T05A004 1-8.

[11] Korsukova, E., Kruisbrink, A., Morvan, H., Cageao, P. P., and Simmons, K., 2016. "Oil Scoop Simulation and Analysis using CFD and SPH". Proceding of ASME Turbo Expo 2016: Turbine Technical Conference and Exposition, Seoul, South Korea, ASME Paper No. GT2016-57554, Vol. **7B**, pp. V07BT31A027 1-8.

[12] Kruisbrink, A., Korsukova, E., Evans, K., and Morvan, H. P., 2017. "SILOET 2 Project 18.4: CFD and SPH Work on the Compound Scoop". Gas Turbine and Transmissions research centre, University of Nottingham.

Accepted Manuscript Not Copyedited

Downloaded From: http://gasturbinespower.asmedigitalcollection.asme.org/ on 08/31/2018 Terms of Use: http://www.asme.org/about-asme/terms-of-use